CIAL PUBLICATION 748

U.S. DEPARTMENT OF COMMERCE / National Bureau of Standards

Technical Digest
Symposium on Optical Fiber Measurements, 1988

Sponsored by the National Bureau of Standards
in cooperation with the IEEE Optical Communications Committee
and the Optical Society of America

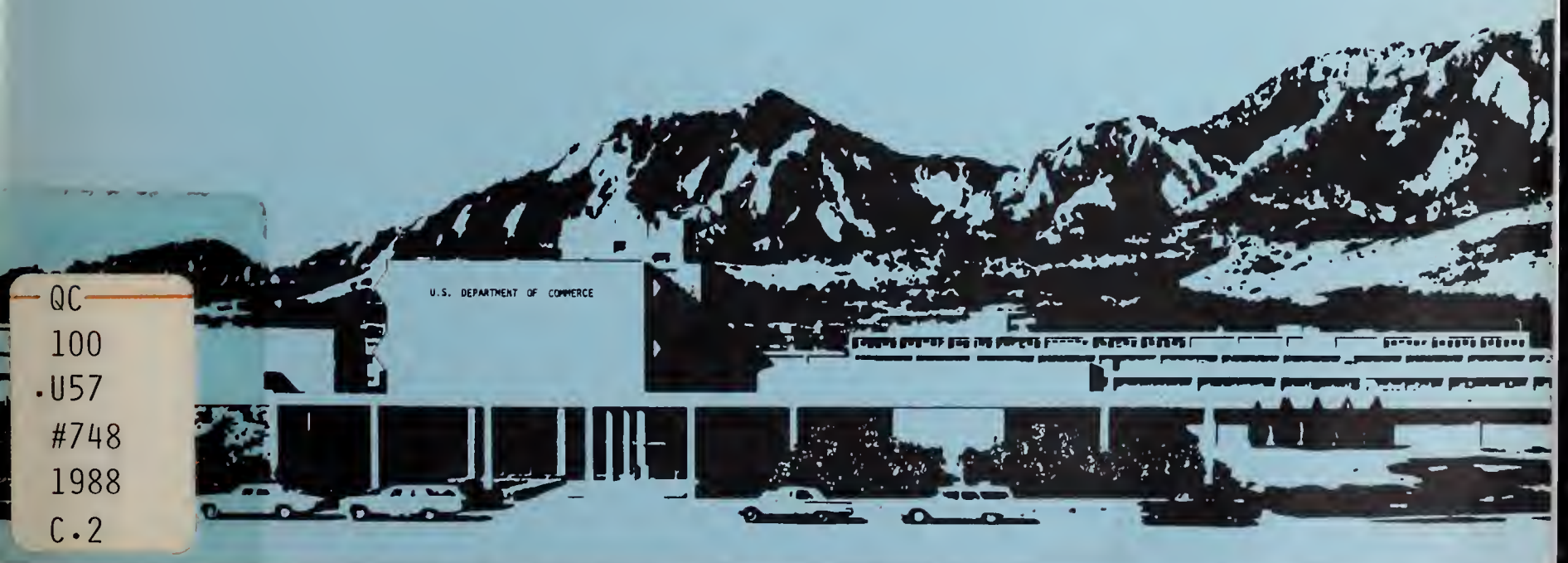

The National Bureau of Standards[1] was established by an act of Congress on March 3, 1901. The Bureau's overall goal is to strengthen and advance the nation's science and technology and facilitate their effective application for public benefit. To this end, the Bureau conducts research to assure international competitiveness and leadership of U.S. industry, science and technology. NBS work involves development and transfer of measurements, standards and related science and technology, in support of continually improving U.S. productivity, product quality and reliability, innovation and underlying science and engineering. The Bureau's technical work is performed by the National Measurement Laboratory, the National Engineering Laboratory, the Institute for Computer Sciences and Technology, and the Institute for Materials Science and Engineering.

The National Measurement Laboratory

Provides the national system of physical and chemical measurement; coordinates the system with measurement systems of other nations and furnishes essential services leading to accurate and uniform physical and chemical measurement throughout the Nation's scientific community, industry, and commerce; provides advisory and research services to other Government agencies; conducts physical and chemical research; develops, produces, and distributes Standard Reference Materials; provides calibration services; and manages the National Standard Reference Data System. The Laboratory consists of the following centers:

- Basic Standards[2]
- Radiation Research
- Chemical Physics
- Analytical Chemistry

The National Engineering Laboratory

Provides technology and technical services to the public and private sectors to address national needs and to solve national problems; conducts research in engineering and applied science in support of these efforts; builds and maintains competence in the necessary disciplines required to carry out this research and technical service; develops engineering data and measurement capabilities; provides engineering measurement traceability services; develops test methods and proposes engineering standards and code changes; develops and proposes new engineering practices; and develops and improves mechanisms to transfer results of its research to the ultimate user. The Laboratory consists of the following centers:

- Applied Mathematics
- Electronics and Electrical Engineering[2]
- Manufacturing Engineering
- Building Technology
- Fire Research
- Chemical Engineering[3]

The Institute for Computer Sciences and Technology

Conducts research and provides scientific and technical services to aid Federal agencies in the selection, acquisition, application, and use of computer technology to improve effectiveness and economy in Government operations in accordance with Public Law 89-306 (40 U.S.C. 759), relevant Executive Orders, and other directives; carries out this mission by managing the Federal Information Processing Standards Program, developing Federal ADP standards guidelines, and managing Federal participation in ADP voluntary standardization activities; provides scientific and technological advisory services and assistance to Federal agencies; and provides the technical foundation for computer-related policies of the Federal Government. The Institute consists of the following divisions:

- Information Systems Engineering
- Systems and Software Technology
- Computer Security
- Systems and Network Architecture
- Advanced Computer Systems

The Institute for Materials Science and Engineering

Conducts research and provides measurements, data, standards, reference materials, quantitative understanding and other technical information fundamental to the processing, structure, properties and performance of materials; addresses the scientific basis for new advanced materials technologies; plans research around cross-cutting scientific themes such as nondestructive evaluation and phase diagram development; oversees Bureau-wide technical programs in nuclear reactor radiation research and nondestructive evaluation; and broadly disseminates generic technical information resulting from its programs. The Institute consists of the following Divisions:

- Ceramics
- Fracture and Deformation[3]
- Polymers
- Metallurgy
- Reactor Radiation

[1]Headquarters and Laboratories at Gaithersburg, MD, unless otherwise noted; mailing address Gaithersburg, MD 20899.
[2]Some divisions within the center are located at Boulder, CO 80303.
[3]Located at Boulder, CO, with some elements at Gaithersburg, MD

Technical Digest—Symposium on Optical Fiber Measurements, 1988

Digest of a Symposium sponsored by the
National Bureau of Standards
in cooperation with the
IEEE Optical Communications Committee
and the Optical Society of America

September 20-21, 1988
National Bureau of Standards
Boulder, Colorado 80303

Edited by
G.W. Day
D.L. Franzen

Electromagnetic Technology Division
Center for Electronics and Electrical Engineering
National Engineering Laboratory
National Bureau of Standards
Boulder, Colorado 80303

Stimulating America's Progress
1913-1988

U.S. DEPARTMENT OF COMMERCE, C. William Verity, Secretary
NATIONAL BUREAU OF STANDARDS, Ernest Ambler, Director

Issued September 1988

Library of Congress Catalog Card Number: 88-600561

National Bureau of Standards Special Publication 748
Natl. Bur. Stand. (U.S.), Spec. Publ. 748, 202 pages (Sept. 1988)
CODEN: XNBSAV

U.S. GOVERNMENT PRINTING OFFICE
Washington: 1988

For sale by the Superintendent of Documents, U.S. Government Printing Office, Washington, DC 20402

PREFACE

It is our pleasure to present here summaries of all of the papers given at the fifth biennial Symposium on Optical Fiber Measurements. Forty-two papers, eight invited and thirty-four contributed, are included. This is a substantial increase over the 1986 Symposium, made possible by the elimination of workshops from the program.

As always, certain themes appear in the program. This year, we see the largest ever group of papers on optical time domain reflectometry (OTDR), apparently motivated in large part by concern about reflections and their effects on source behavior. The second largest group of papers concerns the measurement of cut-off wavelength. And for the first time, we see a significant number of papers on the characterization of planar optical waveguides.

The Symposium continues to enjoy broad international support. This year's program includes participants from 25 organizations in 8 countries; more than 40 percent of the papers are from outside the United States.

G. W. Day
D. L. Franzen
Boulder, Colorado
September 1988

SYMPOSIUM COMMITTEE

D. L. Franzen, NBS, General Chairman

G. W. Day, NBS, Program Chairman

A. H. Cherin, AT&T Bell Laboratories

P. DiVita, CSELT

R. L. Gallawa, NBS

A. H. Hartog, York Technology

W. T. Kane, Corning Glass Works

F. P. Kapron, Bell Comm. Research

P. Lovely, Photon Kinetics

M. Ogai, Furukawa Electric

W. A. Reed, AT&T Bell Laboratories

P. R. Reitz, AMP

CONTENTS

Except where attributed to NBS authors, the content of individual sections of this volume has not been reviewed or edited by the National Bureau of Standards. NBS therefore accepts no responsibility for comments or recommendations therein. The mention of trade names in this volume is in no sense an endorsement or recommendation of the National Bureau of Standards.

Advances in OTDR

Mitsuhiro Tateda and Tsuneo Horiguchi
NTT Transmisssion Systems Laboratories
Tokai-mura, Ibaraki-ken, 319-11 Japan

1. Introduction Barnoski and Jensen[1] first demonstrated that detection and analysis of Rayleigh backscattered light from an optical probe pulse propagating down a fiber gives the attenuation characteristics of the fiber. Using this technique, we can also evaluate the splice losses and fault location in an optical transmission line, composed of several optical fiber cables, at one endface of it nondestructively. Hence this technique, so called optical time domain reflectmetry (OTDR), has become a strong and helpful tool in all the fields of manufacturing, testing and installation of optical fiber cables. The gated detection technique greatly increased the ability of the OTDR technique[2],[3], which enables the detection of weak scattered light preventing detector sensitivity saturation by the strong Fresnel reflection light.

2. Recent progress in the OTDR technique

(1)Enlargement of the dynamic range The OTDR technique has enlarged its application target from multimode fibers at a short wavelength (~0.8 μm) to singlemode fibers at a longer wavelength (1.3-1.5μm). However, the backscattered light in singlemode fibers is as small as a tenth of that in multimode fibers. To overcome this difficulty, two kinds of approach have been developed to enlarge the dynamic range. First, to increase the input optical power (approach A) and second to decrease the minimum detectable optical power (approach B). They are listed in Table 1 after Healey[4]. In approach A, various kinds of high

power laser light sources such as Q-switched Nd:YAG laser[5] (λ =1.32μm), Er^{+++}:glass laser[6] (λ =1.55μm) and P_2O_5 doped fiber Raman laser[7] (λ =1.59μm) are used. In the Raman OTDR technique[8], Rayleigh backscattered lights accompanied by Stokes lights with wavelength ranging from 1.2 to 1.7 μm converted from the strong input pumping light in the fiber under test is detected (Fig. 1). Hence, this technique is used only for fault location. Effectively improved optical signal power is utilized in the correlation technique by signal processing[9]. In approach B, cryogenic detectors and data-averaging processing are effectively used. A semiconductor laser is used both as an optical pulse generator and as a backscattered optical signal amplifier, without a directional coupler, whose operation mode is switched by a drive circuit (Fig. 2)[10]. In the photon counting technique, photons in the backscattered light are detected digitally[11],[12]. In the heterodyne detection method[13]-[15], we can expect to approach the shot-noise limit by increasing the local oscillator power (Fig. 3[13]), although problems of fading and polarization noise are high-lighted.

(2)Enhancement in resolution Small resolution (ΔL$\sim$ 5mm) significant in fault location is obtained by a narrow optical pulse (τ =46 ps).[16] However, 1/N times narrow pulse (τ /N) requires an N times broad bandwidth with an N times large noise power, and it also diminishes the backscattered optical power to 1/N, which result in dynamic range decrease (7.5 log N dB). Resolution as high as 15 μm was reported by nonlinear detection, in conjunction with a mode-locked dye laser[17](Fig. 4). An optical reflectometer with a low coherence light source realizes submillimeter[18] and micrometer[19] resolution in the application area of optical circuit diagnostics (Fig. 5).

(3)Reduction of single mode fiber OTDR noise Besides the weak Rayleigh backscattered light, single-mode fiber OTDR has the problem of polarization dependent amplitude fluctuation due to small birefringence in the fiber under test. An acoustooptical deflector without polarization dependence[3] and polarization scrambler[20] are effective in preventing this. Birefringent launching fiber[21] composed of polarization maintaining fiber(s) drastically diminishes the fluctuation (Fig. 6). The fading phenomenon intrinsic to a coherent light source is reduced by a nonlinear signal averaging operation[22].

(4)User friendliness As the potential of the OTDR technique has become recognized, requests from users, for ease of operation, have been increasing. OTDR for both 1.3 μm and 1.5 μm fulfills one need in testing wideband optical fibers. Automated OTDR waveform processing, eliminating cursor handling procedure, is attractive because of constant measurement repeatability by a nonskilled person, and the possibility of remote controlled measurement (Fig. 7). The key point is in judging the splice points, where time, and space averaging processes, least square approximation and difference calculas processes are used.

3. Future technology We have already realized the first stage of the optical transmission systems of trunk lines[23]. It is expected that the second stage, that is the era of the optical subscriber lines, will begin in the near future, where several demands for the OTDR technique will be emphasized. For example, diminishing the dead zone will be essentially important in diagnosing complicated optical networks such as Local Area Networks. Furthermore, in testing the broadcasting type branching networks, light source power for testing will be

limited so as not to destroy the adjacent equipment connected to the system. To overcome these problems, new techniques in a wider field must be developed for the OTDR technique.

References

(1) M. K. Barnoski et al., Appl. Opt., 15, 2112, 1976.

(2) S. D. Personick, Bell Syst. Tech. J., 56, 355, 1977.

(3) T. Horiguchi et al., J. Lightwave Tech. LT-2, 108, 1984.

(4) P. Healey, J. Lightwave Tech. LT-3, 876, 1985.

(5) M. P. Gold et al., 10th ECOC, 128, 1984.

(6) M. Nakazawa et al., Optics Lett., 9, 312, 1984.

(7) K. Suzuki et al., Electron. Lett., 22, 1273, 1986.

(8) K. Noguchi, J. Lightwave Tech., LT-2, 1, 1984.

(9) J. J. Bernard et al., 10th ECOC, 84, 1984.

(10)K. Suzuki, Electron. Lett., 20, 714, 1984.

(11)P. Healey, Electron. Lett., 17, 751, 1981.

(12)B. F. Levine et al., Electron. Lett., 21, 194, 1985.

(13)S. Wright et al., 9th ECOC, 177, 1983.

(14)S. Wright et al. Optical Fiber Sensors Conference, 347, 1984.

(15)P. Healey et al., Electron. Lett., 18, 862, 1982.

(16)"A technical note on 00S-01 (in Japanese)", Hamamatsu Photonics Inc., Hamamatsu, Japan, 1987.

(17)J. J. Fontaine et al., Opt. Lett., 6, 405, 1981.

(18)K. Takada et al., Appl. Opt., 26, 1603, 1987.

(19)B. L. Danielson et al., Appl. Opt., 26, 2836, 1987.

(20)K. Aoyama et al., IEEE, J. Quantum Electron., QE-17, 862, 1981.

(21)T. Horiguchi et al., J. Opt. Soc. Amer. A, 2, 1698, 1985.

(22)P. Healey et al., Electron. Lett., 20, 360, 1984.

(23)T. Uenoya, Japan Telecommunication Review, 101, 1985.

Table 1 Data of the top dynamic range of OTDR

* code length $2^{15}-1$ ** cooled by liquid N_2

Approach	Technology		Wave-length λ (μm)	Pulse width T (μs)	Band-width B (MHz)	Input optical power Pin (dBm)	Minimum detectable powere Pd (dBm)	Postdetection S/N Improvement SNIR (dB)	Dynamic range L (dB)	Reference Year
A Increase of Input optical power	High Power Laser	YAG laser	1.32	0.5	0.3	+30	-75	60	41	(5) 1984
		Er***laser	1.55	1	1	+36	-70 **	36	34	(6) 1984
		Raman laser	1.59	0.8*	0.3	+34	-70 **	54	35	(7) 1986
	Raman OTDR		1.06	0.2	2	—	-68 **	39	30	(8) 1984
	Correlation Method		1.3	0.1	—	—	—	—	15	(9) 1984
B Decrease of minimum detectable optical power	Optical preamplifier		1.29	1	1	+ 3	-62	30	13.5	(10) 1984
	Photon counting		1.32	1	—	-15	-93 **	34	20	(11) 1981
			1.52	1	—	-26	-75	63	12.5	(12) 1985
	Heterodyne detection		1.15	0.8	1.2	- 9	-81	53	32	(13) 1983
			1.3	2	—	-15	—	57	24	(14) 1984
			1.52	1	3	-23	-90	45	10	(15) 1982

Table 2 Advances in OTDR technique other than dynamic range

Subject	Technique	Feature	Reference Year
Resolution ΔL	Narrow pulse	ΔL=5mm, pulse width=46ps	(16) 1987
	Nonlinear detection	ΔL=15μm, pulse width=0.12 ps, 300W at λ=600 nm	(17) 1981
	Low coherence interferometry	ΔL=38μm, coherence length=50μm	(18) 1987
		ΔL= 1μm, spectral width=130nm	(19) 1987
Polarization noise reduction	Acoustooptic deflector	$\eta \parallel / \eta \perp$<1.18 ($\eta$:diffraction efficiency)	(3) 1984
	Polarization scrambler	Time averaging by twisting the test fiber	(20) 1981
	Birefringent launching fiber	Fluctuation of 0.73 dB is reduced to 0.06 dB	(21) 1985
Fading reduction	Nonlinear signal averaging	Modulus and multichannel averaging	(22) 1984
User friendliness	Two wavelength measurement	λ=1.3, 1.5μm	—
	Automated waveform processing	Without cursor handling	—

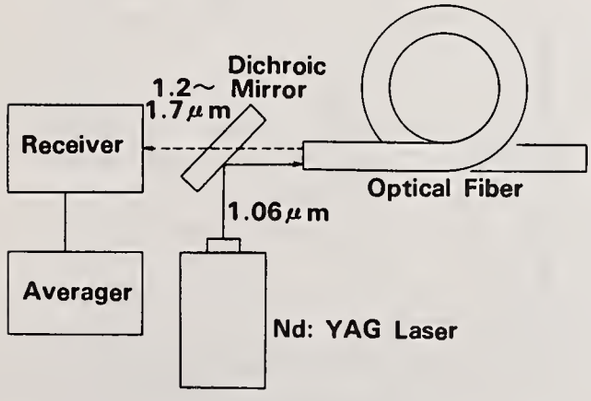

Fig. 1 Raman OTDR technique (8)

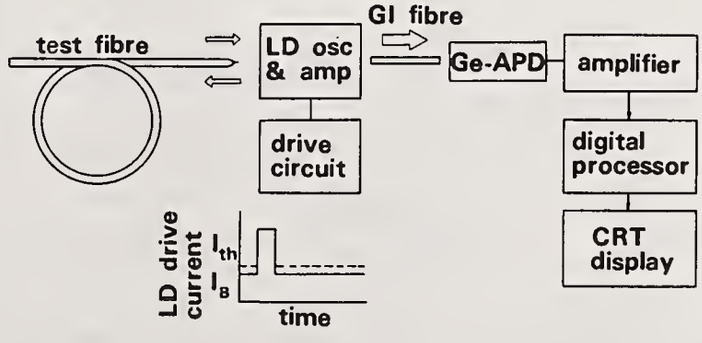

Fig. 2 Laser-diode amplifier OTDR (10)

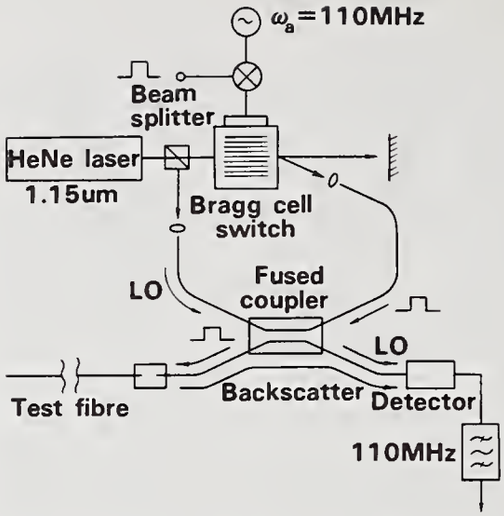

Fig. 3 Heterodyne detection method (13)

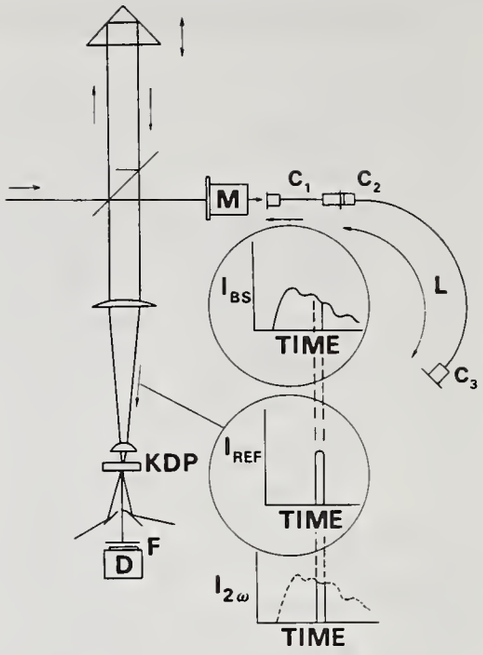

Fig. 4 Nonlinear detection (17)

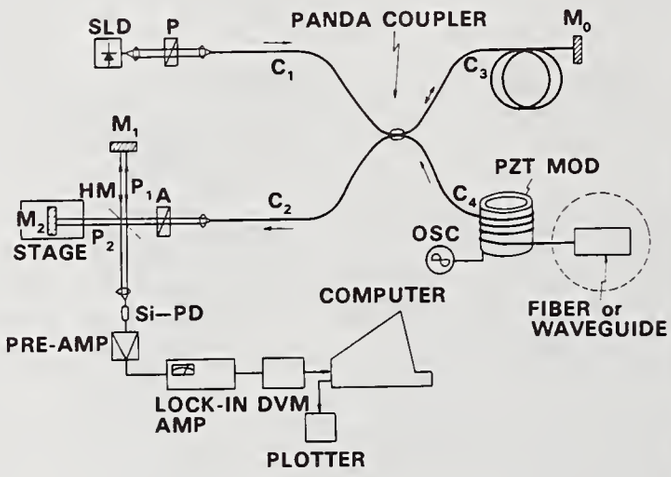

Fig. 5 Low coherence interferometry (18)

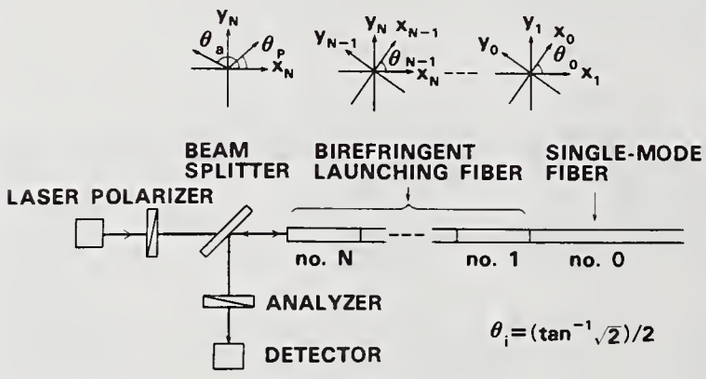

Fig. 6 Birefringent launching fiber (21)

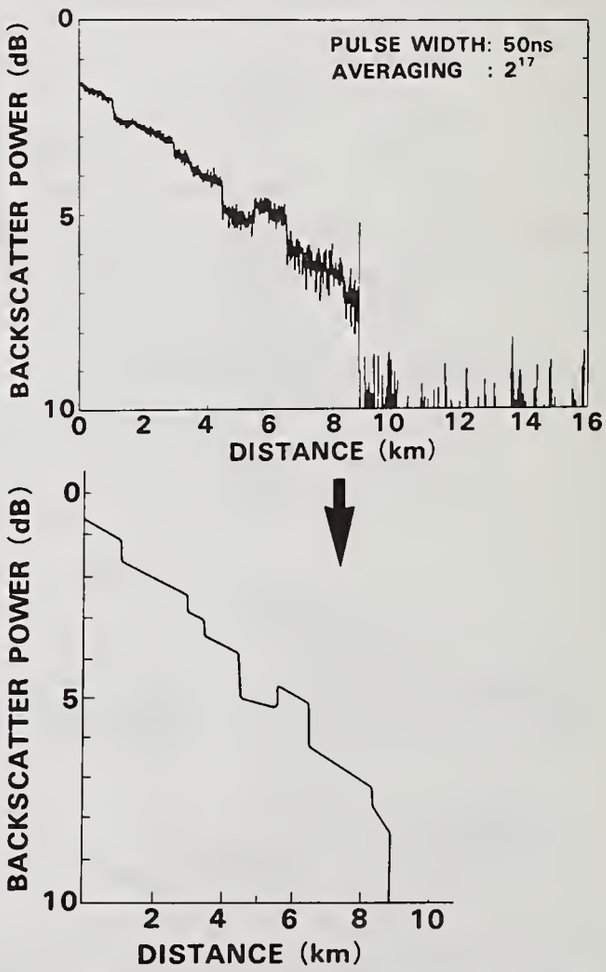

Fig. 7 Automated waveform processing

INVESTIGATION OF OPTICAL COMPONENTS IN MICROMETER RANGE USING AN OTDR SYSTEM WITH THE BALANCED HETERODYNE DETECTION

R.P. Novàk, H.H. Gilgen and R.P. Salathé
Swiss PTT, Technical Centre, 3000 Bern

W. Hodel, P. Beaud, J. Schütz and H.P. Weber
University of Berne, 3000 Berne

Switzerland

1. Introduction

Optical time domain reflectometry is a well known method for the diagnostics of fiber optics systems. The new small structures such as integrated optical devices require nevertheless the resolution in the micrometer range.

In our previous work [1] we have reported on the development of an infrared subpicosecond OTDR system and its first applicability as a diagnostic tool for the investigations of integrated optical devices. The light source was delivering pulses of 300 fsec duration and 70 mW average power at the wavelength of 1.3 μm. Together with the intensity correlation detection technique the achieved dynamic range was 75 dB with the spatial resolution of 60 μm in air.

In this paper we describe a significant improvement of this system on the detection side. The detection of the weak backscattered light is performed with a Mach-Zehnder type interferometer combined with the balanced heterodyne detection, resulting in an improvement of 30 dB compared to the intensity correlation technique.

2. OTDR set-up

Fig. 1 shows the experimental arrangement. The light source consists of a CW mode-locked Nd:YAG laser, fiber/grating-pair pulse compressor and an infrared dye laser (dye Nr. $26^{+}HFB^{-}$) in linear configuration [1]. It delivers pulses of 300 fsec duration at the repetition rate of 82.00 MHz. The wavelength of the dye laser is tunable between 1.25 and 1.35 μm. The output beam is split by a dielectric beam splitter (BS1) into the Local Oscillator (LO) part and the Signal Beam (SB). The signal beam is fed through the beam splitter (BS2) and the lens (L) to the structure under investigation. The back reflected signal (RS) from the sample passes back to the BS2 and is directed to the heterodyne balanced detection system consisting of the third beam splitter (BS3) and the InGaAs Detectors D_1-D_2. The LO beam is first fed to an acousto optic modulator (AOM) in order to impose a frequency shift needed for the heterodyne detection. In the experiment the AOM (Bragg cell) is operating at 40.99 MHz. The LO beam passes the AOM twice being reflected by a 100% mirror (M) mounted on a precision translation stage (TS). The total frequency shift is therefore 81.98 MHz. This leads to a convenient detection of a beat signal at a frequency of 20 kHz. The movement of the mirror M serves to impose a delay for the LO pulses and achieve in this way the time coincidence with the RS signal (layer sampling).

The beam splitter BS3 (50%) is combining at a time two resulting beams - RS and LO and directs them to two detectors. The electrical beat signals from these detectors are exactly 180 degrees out of phase due to the phase shift introduced by the reflection on the beam splitter BS3. Finally the detector outputs are processed by a differential amplifier (balanced detection) and spectral analyser.

The induced photocurrents I(T) of the two detectors (D_1, D_2) are given by the sum of the two Gaussian bandwidth limited pulses:

$$I_{\pm}(T) \propto \frac{P_{SB} + P_{LO}}{2} \pm 2\sqrt{P_{SB}\,P_{LO}} \cdot e^{-\frac{\pi^2 T^2 \Delta\nu^2}{4 \ln 2}} \cos\left[2\pi(\nu t + \nu_o T) + \Phi\right] \qquad 1)$$

where P_{LO} and P_{SB} are the corresponding powers of the LO and SB at the beat frequency, $\Delta\nu$ the spectral width, ν_o the center frequency, ν the beat frequency of 20 kHz, T the delay and Φ the phase between two beams [2].

If the splitting ratio of the beam splitter BS3 is exactly 1/2, the difference of the two photocurrents I_+ and I_- will be given by the doubled interference term only. A small difference of this ratio can be additionally adjusted by two polarisers P1, P2.

The heterodyne detection of very short pulses allows a very high spatial resolution.

3. Experimental results

a) Linearity and sensitivity:
Fig. 2 illustrates the sensitivity and linearity of the system. The sample is a BK7 mirror substrate of 3 mm thickness. Two highest peaks (-14 dB) correspond to 4% reflections of the front (F) and back (B) surface. Further, three echos (E1-E3) can be identified resulting in a sensitivity of more than 100 dB. All peaks lie on a straight line demonstrating the linearity of the system over the whole range.

b) Two reflections, small separation:
Fig. 3 illustrates the case, where the separation of two reflections was smaller than the pulse width in the material. The investigated pellicle had the thickness of 6.4 µm. This leads to the interferences between the pulses reflected from the front and the back surfaces. These interference effects combined with the tunability of the dye-laser allows to determine such small separations. It can be shown that the optical separation d_{opt} is given by:

$$d_{opt} = \frac{\lambda max \cdot \lambda min}{4\,(\lambda max - \lambda min)}$$

where λmax and λmin are the wavelength where the maximum positive (one peak) or maximum negative (two peaks) interference occurs, respectively. The tuning range (100 nm) allows therefore to resolve two reflections with a separation of less than 10 µm.

c) Measurement on Integrated Optical Devices:
Fig. 4 shows an example of a measurement on an integrated optical device. The structure is a rib-waveguide Mach-Zehnder interferometer on GaAs substrate. Different peaks corresponding to the entrance face (F) -14 dB, end face (B) - 41 dB, waveguide splitting (Y) -58 dB and echo of the back-end face (E) -88 dB, can be detected. Assuming the losses to be distributed evenly, an average loss coefficient α can be calculated from

$$\alpha = - \frac{1}{2L} \ln \left(R_F \cdot R_B \cdot \frac{P_E}{P_B} \right)$$

where L is the length of the waveguide and R_F and R_B are the reflection coefficients of the front and end face, respectively. The power ratio P_E/P_B of the first echo (E) and back reflex (B) can be taken from the figure.

4. Conclusions

A new OTDR system using an infrared (1250 - 1350 nm) ultrashort (300 fsec) pulse source in conjunction with balanced heterodyne detection has been developed. The resolution is about 60 µm in air with the possibility to resolve two scattering centres separated by less than 10 µm. The dynamic range is better than 100 dB. The applicability of the system for the investigation of integrated optical devices has been shown. The work is in progress and more examples (optical connectors, splices, couplers etc) will be presented at the symposium.

5) References

[1] R.P. Novàk, H.H. Gilgen, R.P. Salathé, B. Zysset, P. Beaud, and H.P. Weber.
Time domaine reflectometer in the micrometer range. Proceedings of ECIO 87, Glasgow.

[2] R. Stierlin, R. Bättig, P.-D. Henchoz and H.P. Weber.
Excess-noise suppression in a fibre optics balanced detection system.
Optical and Quantum Electronics 18, pp. 445-454, 1986.

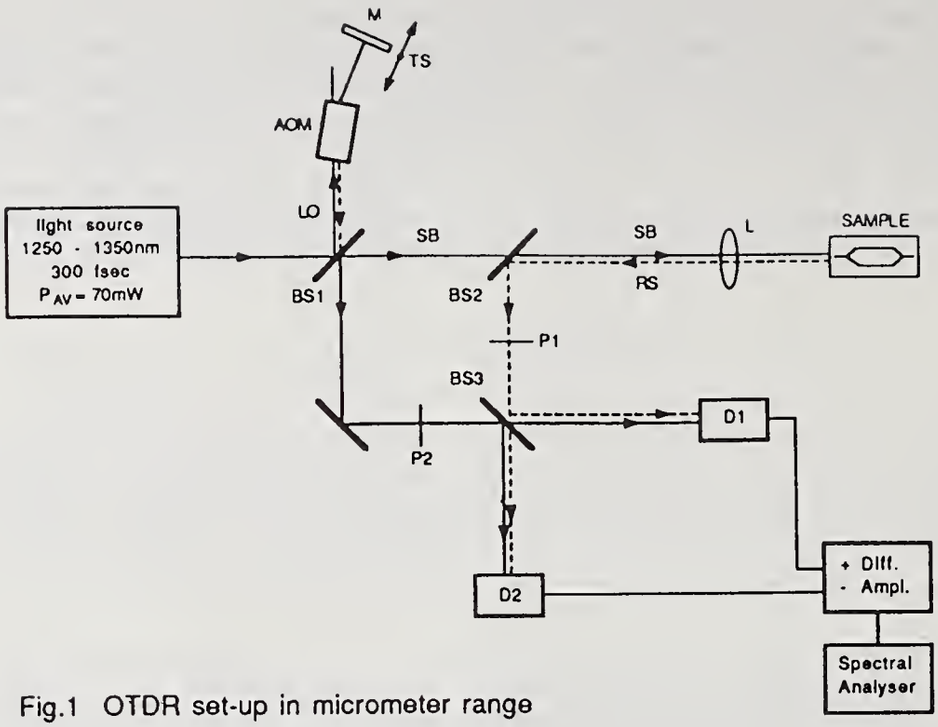

Fig.1 OTDR set-up in micrometer range

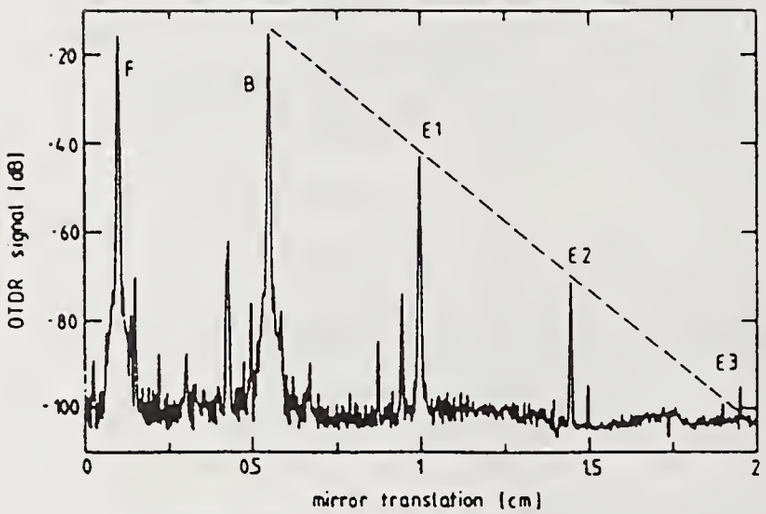

Fig.2 Linearity and sensitivity

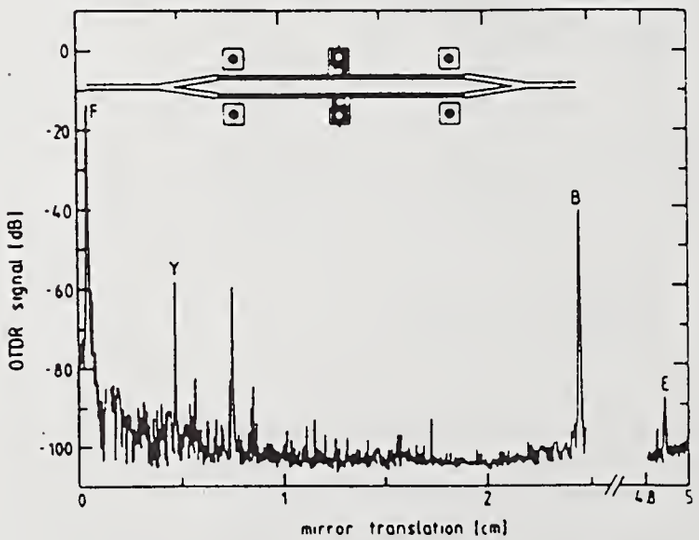

Fig.4 Reflections from a Mach-Zehnder Interferometer

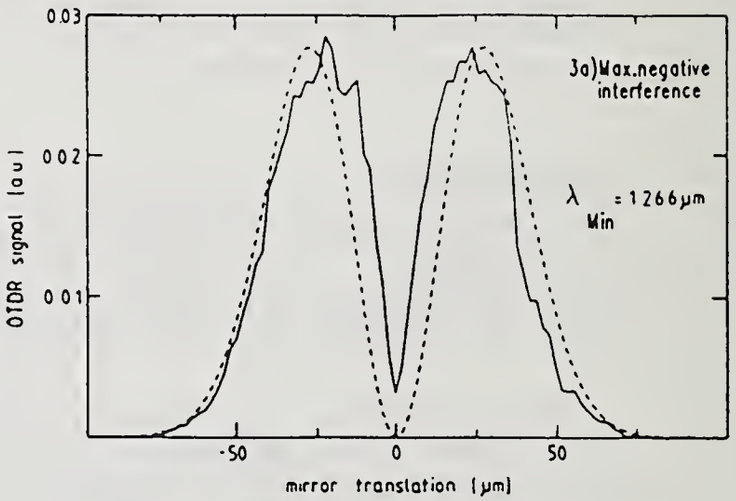

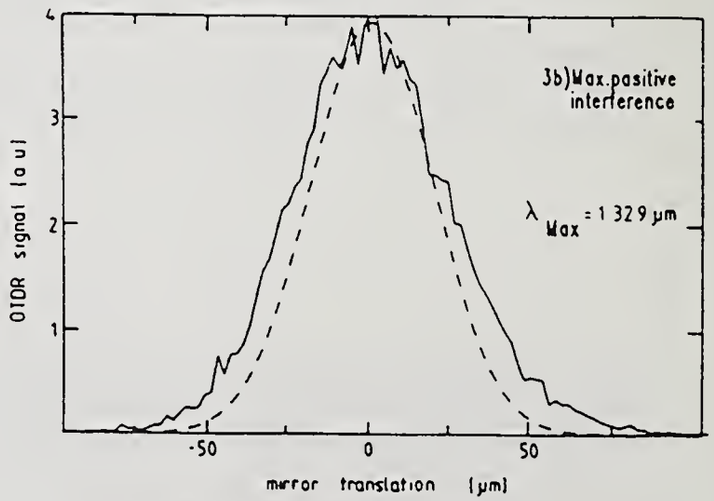

Fig.3 Two reflections. Small separation.

155 km LONG-RANGE OTDR MEASUREMENT AT 1.55 μm WAVELENGTH REGION

Y. NAMIHIRA, Y. HORIUCHI, and H. WAKABAYASHI,

KDD Meguro Research & Development Laboratories,
2-1-23, Nakameguro, Meguro-ku, Tokyo, 153, Japan.

T. OSHIMI, K. KITAGAWA, and T. OOKA

Anritsu Corporation, Atsugi, Kanagawa, 243 Japan.

INTRODUCTION : Since the silica-based single-mode fibers (SMFs) have their minimum loss in the 1.55 μm wavelegnth region [1], 1.55 μm range, long-haul optical fiber submarine cable systems have been developed [2]. In optical fiber systems, the repeater spacing is expected to be over a 120 km ; therefore, practical long-range, optical time-domain reflectometry (OTDR) is indispensable for the measurement of the loss distributions and the fault location along such long optical fiber cables. Untill now, to improve the measuring system dynamic range, several techniques have been reported, such as using a high power Nd : YAG laser [3] and cooling a Ge-PIN photodiode to 77 k (-196 ^{o}C) with liquid nitrogen [4]. Other techniques using a semiconductor laser (LD) and a Ge-avalanche photodiode (APD) have been widely used, however ; it is difficult to achieve any improvement in the dynamic range because of the large dark current of a Ge-APD. Accordingly, a InGaAs/InP-APD [5] with a small dark current promises to achieve a large dynamic range OTDR in 1.55 μm wavelength region. So far, in 1.55 μm wavelength range OTDR using a cooled InGaAs/InP-APD with a peltier's thermodevice, a Rayleigh backscattered signal over a 64 km SMF with fiber loss of 0.21 dB/km and a one-way backscattered dynamic range of around 24 dB have been reported [6]. Recently, using high power LD and InGaAs/InP-APD, a 147 km OTDR measurement and a one way backscattered dynamic range of 29.3 dB have been presented [7]. However, there are few reports on OTDR

with a one-way backscattered dynamic range of more than 30 dB.

This letter presents the first measurement results of a Rayleigh backscattered signal and a Fresnel reflection (with mirror surface) over a 154.80 km and a 225.45 km SMFs with fiber loss of 0.187 dB/km by 1.55 μm long-range OTDR using a InGaAs/InP-APD with a small dark current, a high-power LD and a low noise receiver [8].

A one-way backscattered dynamic range of 32.97 dB at room temperature has been successfully achieved.

RESULTS AND DISCUSSIONS : To improve the backscattered dynamic range of the OTDR, signal/noise ratio (SNR) and receiver sensitivity, the following items were examined :

(a) A InGaAs/InP-APD with a small dark current (~8 nA) was used.
(b) A high-power LD module (~+ 14.8 dBm) was used.
(c) To increase the multiplication factor M of InGaAs/InP-APD, M was set to 40.
(d) The noise floor level of the receiver was reduced to improve SNR.
(e) The one-way backscatterd dynamic range of the OTDR using InGaAs/InP-APD was increased by + 9.8 dB comparing with that using Ge-APD.

Table 1 shows the comparison of the Ge-APD with the InGaAs/InP-APD parameters at room temperature used in the experiment. From Table 1, it can be seen that the dark current I_d of the InGaAs/InP-APD has a small value of 8 nA (at $0.9V_B$) [5], and when the multiplication factor increases to $M \cong 40$, the value is greater than that of Ge-APD ($M \cong 10$). A buried hetero-structure InGaAsP/InP-LD at 1.548 um wavelength is driven at an effective peak power of + 14.8 dBm (~ 30 mW) at the pigtail fiber output end. The pulse width is variable and the maximum width is 10 μs. The long-range OTDR parameters are shown in Table 2. The averaging time was 3.8×10^5 times, and the receiver sensitivity improvement in optical power level was about 12.4 dB.

Fig.1 shows the OTDR measuring system. Fig.2 represents the Rayleigh backscattered signal and Fresnel refrection (with mirror surface) along a 154.80 km and a 225.45 km low-loss pure silica-core SMFs [1] with a total fiber loss at 1.55 μm of 0.187 dB/km as measured by OTDR using InGaAs/InP-APD.

Fig.3 indicates the one-way backscattered dynamic range against fiber length for the pure silica-core SMF and the segmented-core, dispersion shifted fiber (DSF) [9]. The fiber parameters are shown in Table 3. In Table 3 the group index N_g was 1.462 for the pure silica-core SMF and 1.475 for the segmented-core DSF [7]. These values were obtained from the relation between the fiber mechanical length and the optical group delay time measured by the phase shift technique.

It was confirmed from Fig.3 that the one-way backscattered dynamic range of OTDR was about 32.97 dB. Also, it can be seen that the difference between the fiber loss measurement results by the OTDR and the cutback method for the pure silica-core SMF and the segmented-core DSF are 0.008 dB/km and 0.009 dB/km, respectively. From these results it is found that loss measurement by OTDR is in good agreement with that of the cutback method.

CONCLUSIONS : A Rayleigh backscattered signal and Fresnel reflection (with mirror surface) over a 154.80 km and a 225.45 km pure silica-core SMF with fiber loss of 0.187 dB/km was successfully observed by long-range OTDR using a 1.55 μm high-power LD and InGaAs/InP-APD with a small dark current at room temperature. Long range 1.55 μm wavelength region OTDR with one-way backscattered dynamic range of 32.97 dB at room temperature was developed.

ACKNOWLEDGEMENT : The Authors would like to Dr. T. Muratani and Dr. T. Yamamoto of KDD Meguro R & D Laboratories for their encouragement.

REFERENCES :

[1] Y. Namihira et al., : Electron. Lett., 23, pp.963-964, 1987.
[2] S. Yamamoto et al.,: Suboptic '86, France, Communication 13.2, pp.369-376, 1986.
[3] M. Nakazawa : Electron. Lett., 17, pp.783-785, 1981.
[4] M. Fujise et al.,: Electron. Lett., 6, pp.232-233, 1984.
[5] Y. Matsushima et al., : IEEE Electron Device Letters, vol. EDL-2, No.7, pp.179-181, 1981.
[6] K. Shimizu et al., : IEICE, National Convention Record, vol.70, No.4, pp.294-296, 1987.
[7] Y. Namihira et al.,:Electron. Lett., 23, pp.1219-1220, 1987.
[8] K. Okada et al., : Electron. Lett., 16, pp.629-630, 1980.
[9] T. D. Croft et al.,: IEEE, vol.LT-3, No.5, pp.931-934, 1985.

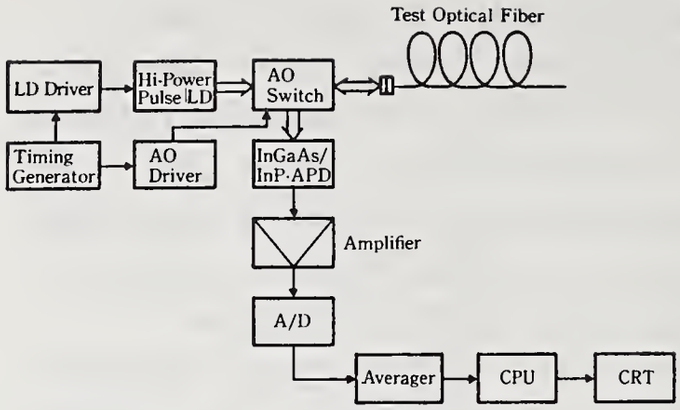

Fig.1 Long-range OTDR measuring system.

Table 1 Comparison of Ge-APD with InGaAs/InP-APD parameters at room temperature (~300 K).

	Ge-APD	InGaAs/InP-APD
Dynamic range [One way], (dB)	~23.13	~32.97
Breakdown voltage V_{B_t} (V)	~33.7	~79.9
Multiplication factor, M	~10	~40
Dark current [at $0.9V_B$], I_d, (nA)	~200	~8
Excess noise figure, x	~1.0	~0.7
Quantum efficiency, (%)	~70	~93

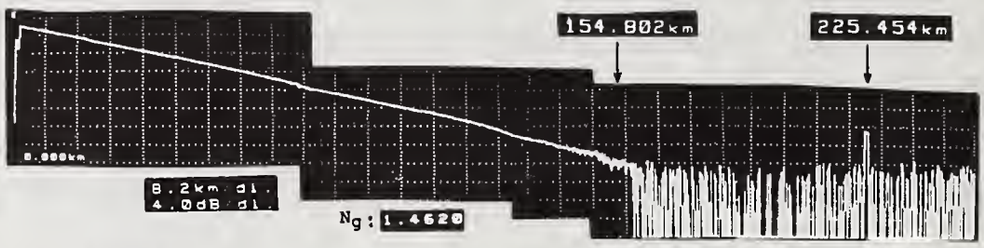

Fig.2 Rayleigh backscattered signal and Fresnel reflection (with mirror surface) along a 154.80 km and a 225.45 km pure silica-core SMFs with fiber loss 0.187 dB/km at 1.55 μm.
Fiber loss : 0.195 dB/km (OTDR), 0.187 dB/km (cutback)
Vertical scale : 4.0 dB/div, horizontal scale : 8.2 km/div

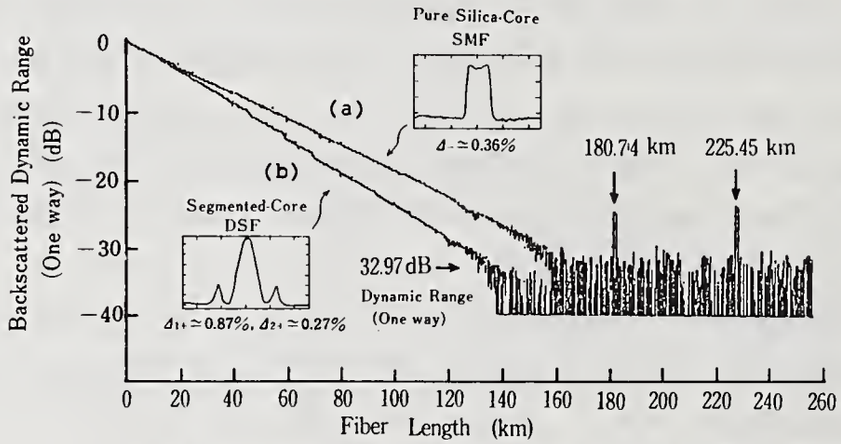

Fig.3 One-way backscattered dynamic range against fiber length in the case of pure silica-core SMF and segmented-core DSF.
(a) Pure silica-core SMF :~0.195 dB/km (OTDR), ~0.187 dB/km (cutback),
(b) Segmented-core DSF :~0.228 dB/km (OTDR), ~0.219 dB/km (cutback)

Table 2 Long-range OTDR parameters.

(a) LD	Wavelength (μm)	Pulse width W (μs)	Pulse rept. rate T_p (ms)	Effective peak power (within fibres) P_o (mW)
	~1.548	~10	~3.28 (305 Hz)	~+30 (+14.8 dBm)
(b) AMP	Load resistance R (kΩ)		Band width B (MHz)	
	~10		~3.5	
(c) Averager	Sampling period S (μs)		Averaged number N	
	~1.6		~3.8 x 10^5	

Table 3 Fiber parameters at 1.55 μm wavelength

	Pure silica -core SMF	Segmented -core DSF
Total fibre length (km) [Total fibre loss, dB]	~274.24 [51.42]	~193.07 [42.33]
Fibre loss (including splice loss, dB/km) [Averaged fibre loss, dB/km]	~0.187 [0.185]	~0.219 [0.207]
Refractive index difference, (%)	~-0.36	~+0.87 ~+0.27
Group index N_g	~1.462	~1.475

BIDIRECTIONAL OTDR MEASUREMENTS UTILIZING AN IMPROVED FOLDED-PATH TECHNIQUE

E. L. Buckland and M. Nishimura
Sumitomo Electric Fiber Optics Corporation
Research Triangle Park, NC 27709 USA

INTRODUCTION

For accurate attenuation and defect analysis using Optical Time Domain Reflectometry (OTDR), averaging of measurements taken in both directions through a fiber is necessary. The use of a mirrored surface at the far end of a fiber to facilitate a simultaneous two-way measurement has been proposed [1,2]. However, a noise contribution arising from the finite reflectivity at the fiber-OTDR interface can significantly degrade the results of attenuation measurements in the mirrored trace. In this paper, we expand on the theory of the "folded-path" OTDR and present a practical system, including a correction algorithm, for significantly improving the performance of the two-way OTDR measurement technique.

THEORY

The theory of single-mode fiber backscatter has been thoroughly developed [3,4]. The time dependent signal detected by the OTDR is a function of the total attenuation scattered and confined in the counterpropagating fundamental mode. Material and structural variations along the fiber length result in scattering factor variations which lead to the bidirectionality phenomena in OTDR measurements.

With the folded path OTDR, the impulse is to treat the mirrored trace as an ideal representation of the reverse fiber signature. This is inadequate, however. Though the reflectivity at the fiber-OTDR interface is very small, it is not negligible in the analysis of the mirrored signal. As shown in Figure 1, additional contributions arise due to the finite reflectivity of the input end of the fiber.

By analyzing various trace components one can effectively eliminate this unacceptable signal contribution. Figure 2 shows a typical trace of three concatenated fibers through a time t=6*L/Vg, where L is the total link length and Vg is the propagation group velocity. The forward and initial mirrored trace (through t=4*L/Vg) are represented by the following equations:

Eqn. 1. $0 < t \leq 2\,L/Vg$ (T1):

$$P(t) = Eo\ Vg\ e^{-2\alpha_T z}\ B(z)$$

Eqn. 2. $2\ L/Vg < t \leq 4\ L/Vg$ (T2):

$$P(t) = Eo\ Vg\ e^{-2\alpha_T L}\ R_e^{\,2} \left[e^{-2\alpha_T z'}\ B(z') + 2e^{-2\alpha_T z}\ B(z)\ \frac{R_i}{R_e} \right]$$

Eo is the input signal, α_T is the total attenuation contribution, z and z' are positions along the fiber axis as measured from the input and the far end mirror, respectively. B(z) is the local scattering factor. R_e and R_i are the reflectivities of the mirrored end and the fiber-OTDR interface, respectively. Similar equations are easily derived for greater times t by recognizing the effect of multiple reflections.

The mirrored fiber trace of interest is the z' component of Eqn. 2. This signal is obtained from the measured trace by subtracting out an attenuated replication of the forward trace (T1), appropriately time correlated. Letting D0 be the total link attenuation to the beginning of T2, D1 be the return loss between T1 and T2 and D2 be the return loss between T2 and T3, the attenuation factor for the forward trace contamination of T2 is

Eqn. 4 $$-10 \log \left[2e^{-2\alpha_T L}\ R_e\ R_i \right] = D0 + (D2 - D1) + \epsilon$$

where ϵ is a small error term dependent on the scattering factors B(0) and B(L), and the end reflectivities.

MEASUREMENT AND ANALYSIS

The measurement system consists of the test link spliced between two reference fibers , R1 and R2 as shown in Figure 1. R1 and R2 are depressed cladding single-mode fibers, chosen long enough to suppress effects of Fresnel reflection detector saturation. Additionally, R1 and R2 have the same mode field diameter, effectively eliminating the error term in Eqn. 4. A thin layer of gold has been sputtered onto the end of R2 to provide a mirror surface having greater than 93% reflectivity, R_e. R2 is a permanent system component, so that R_e is a constant for all measurements.

Backscatter measurements were performed using a commercially available OTDR, utilizing a masking function to further minimize effects of detector saturation. The large peak at the end of T1 in Figure 2 is the mirror reflection from the end of the termination fiber. Similarly, the reflected peak at the end of T2 is caused by the non-zero reflectivity, R_i, at the input end of the system. Figure 3 shows an enlargement of T2 from the previous graph before and after application of the correction algorithm

To verify the improvement in measurement accuracy using this correction routine , 12 cabled depressed cladding single-mode fibers were measured using the described system. The splices to R1 and R2 were mechanical V-groove splices with index matching liquid. Attenuation measurements from the averaged bidirectional OTDR traces were compared with standard cut-back method results at 1.3μm and 1.55μm before and after correction. The results are shown in Table 1. Recognition of the input reflectivity R_i allows for significant improvement of attenuation measurements.

	1.30μm		1.55μm	
	$\bar{x}$	σ	$\bar{x}$	σ
uncorrected trace	.036	.032	.031	.036
corrected trace	-.008	.015	.011	.017

Table 1. Attenuation error: OTDR - cutback (dB/km)

An additional advantage of designing the system with known reference fibers is the ability to measure mode field diameter (MFD) directly with the OTDR. With the MFD of R1 and R2 measured by the far field pattern (FFP) method [5], the MFD at either end of the test fibers were calculated directly from the splice losses S1 and S2 (fig. 1). Figure 4 shows the excellent agreement achievable between the FFP technique and the simultaneous two-way OTDR measurement at both 1.3μm and 1.5μm. The repeatability of the MFD measurement using this folded-path technique was measured to have a standard deviation of σ = 0.1μm or better at both wavelengths.

CONCLUSIONS

We have presented a practical system for performing simultaneous bidirectional OTDR measurements using a reflective termination fiber. A correction algorithm has been introduced to account for the finite input reflectivity for improved attenuation measurements.. We have also demonstrated the feasibility of measuring fiber MFD in the same measurement, greatly increasing the utility of the OTDR for routine product evaluation or field use.

REFERENCES

1] L. Faltin, J. Opt. Commun., Vol 9, No. 1, 1988, pp.24-6.
2] M.P. Gold and A.H. Hartog, Proc. 10th ECOC, Stuttgart, 1984, pp.128-9.
3] D. Philen et.al., IEEE Trans., Vol. MTT-30, No. 10, 1982, pp.1487-96.
4] M.E. Fermann et.al., J. of Lightwave Technology, Vol. LT-6, No. 4, 1988, pp.545-51.
5] E.L. Buckland and M. Nishimura, Electron. Lett., Vol. 21, No. 24, 1985, pp.1149-51.

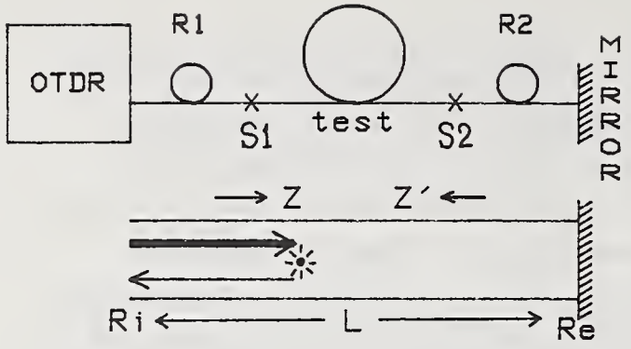

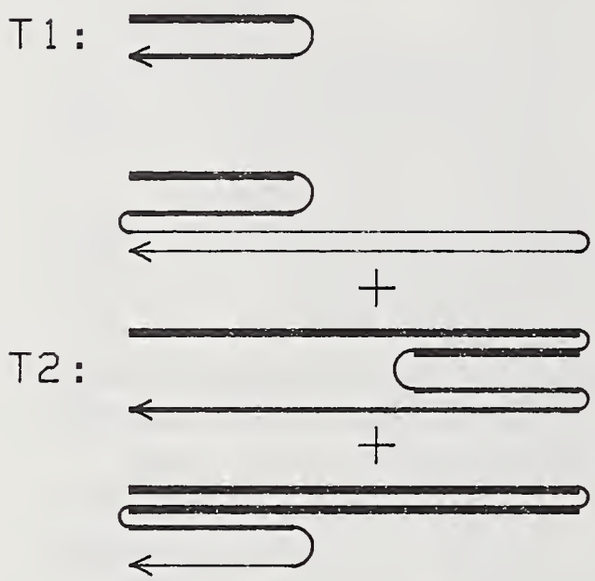

Fig. 1

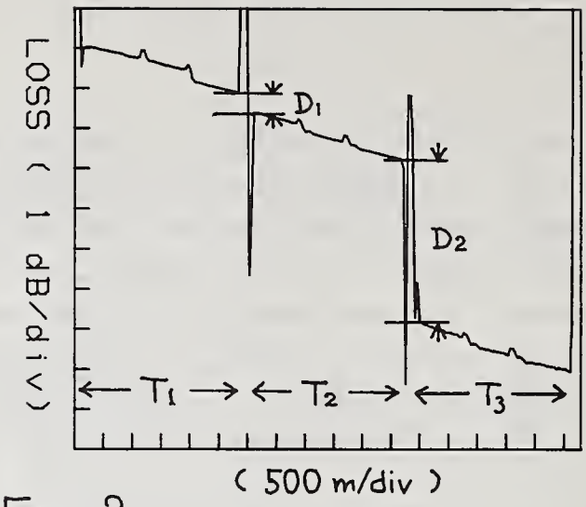

Fig. 2

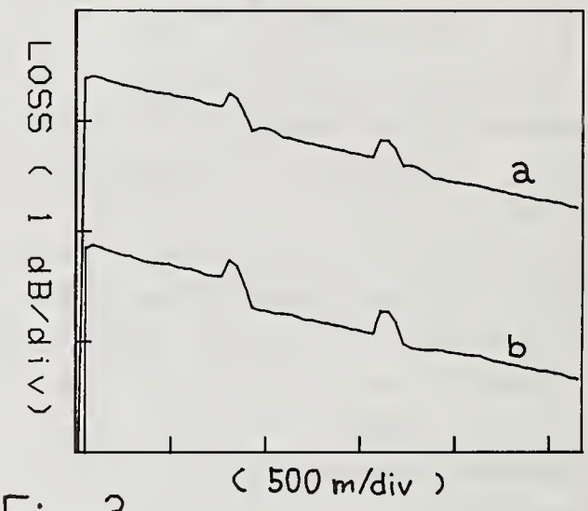

Fig. 3

FIGURE 1. Measurement system and optical signal paths. T1 is the backscattered signal from a point z in the forward trace. T2 shows possible paths for a scattered signal arriving at the detector after an additional round-trip through the fiber. The desired reverse trace is from the signal at z'.

FIGURE 2. Folded-path OTDR trace through three round-trip traverses of the input signal.

FIGURE 3. Reverse OTDR signature a) before correction for the reflectivity Ri and b) after correction.

FIGURE 4. Mode field diameter measurements: Far field pattern vs. bidirectional OTDR at 1300nm and 1550nm.

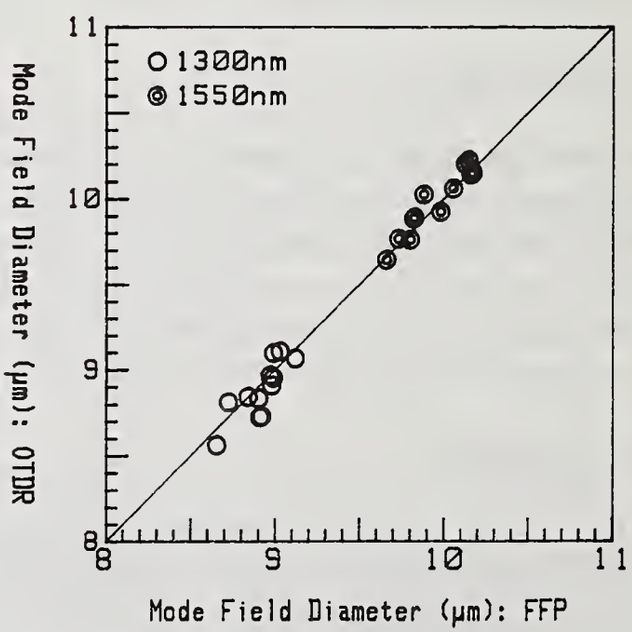

Fig. 4

OTDR EXPERIMENT FOR GLASS OPTICAL WAVEGUIDES BY USING INTERFEROMETRIC TECHNIQUE WITH 1.3 μm SLD

K. Takada, H. Nagai*, N. Takato, and J. Noda

NTT Opto-Electronics Laboratories,
Nippon Telegraph and Telephone Corporation
Tokai, Ibaraki-ken, 319-11, Japan
Tel. 0292-87-7515, Fax. 0292-87-7877
* Morino-sato, Atsugi-shi,3-1, Kanagawa-ken, 243-01,Japan
Tel. 0462-40-2751, Fax. 0462-40-7863

Abstract

First demonstration of OTDR experiments on the glass optical waveguides is presented by using a newly proposed OTDR system based on a Michelson interferometer. To obtain high spatial resolution less than 0.1 mm, an 1.3 μm-wavelength superluminescent diode is adopted. Scattering centers produced by waveguide irregularity are observed clearly in silica based waveguides.

Introduction

Optical time domain reflectometers (OTDRs) are now widely used for testing optical fiber cables. The spatial resolution of the conventional OTDRs using optical short pulses is relatively low, about 1m, because of limit in pulse width and the frequency characteristics of the electrical circuits. Therefore, the conventional OTDRs are not applicable for characterizing miniaturized optical waveguides. In this paper, we present a new type of the OTDR based on the interferometric technique and discuss experimental results on application to silica-based optical waveguides.

Experimental setup

The proposed OTDR system is shown schematically in Fig. 1.[1] The system is composed of the superluminescent diode (SLD), a Mach-Zehnder interferometer and a Michelson interferometer. To achieve high spatial resolution, the incoherent and high power SLD is used as a light source. The SLD light oscillating at the center wavelength of 1.3 μm is launched into the fiber-optic Mach-Zehnder interferometer, i.e., into one arm C_1 of a polarization-maintaining PANDA fiber coupler.[2] The launched

light is divided into two arms C_3 and C_4. Light in the arm C_3 reflects at a mirror M_0, and the reflected light is used as the reference light in the interferometer. The fiber arm C_4 is connected to a test waveguide through a cylindrical piezoelectric phase modulator (PZT MOD) which modulates the propagating light beam at a frequency of 10 kHz. The Mach-Zehnder interferometer with the fiber coupler is necessary for coupling the light into the test waveguide without excess loss, and for superimposing the backscattered light with the reference light. Here the polarization maintaining fiber coupler ensures the stable performance little dependent on the polarization noise.

The superimposed light at the coupler is guided into the bulk-type Michelson interferometer through the arm C_2. The output signal from the Michelson interferometer is detected by a lock-in amplifier at the frequency of $f+\Delta f$, where f is the modulation frequency and Δf is a Doppler shift caused by the scanning of a mirror M_2.

Principle

When a light propagates in a waveguide, a fraction of the light is back-scattered at arbitrary positions in the waveguide. The optical path difference $\Delta\ell$ between the particular two reflected waves is twice the distance ΔS between the two scattering points multiplied by the refractive index n_c of the waveguide material, i.e., $\Delta\ell = 2\Delta S n_c$. The two waves become independent of each other when $\Delta\ell$ is longer than the coherence length ℓ_c of the light source. These two waves interfere independently with the reference light. To make these light waves interfere, the Michelson interferometer is necessary for giving the corresponding delay.

In the Michelson interferometer shown in Fig. 1, optical path P_1 of the first arm is held constant, while optical path P_2 of the second arm is variable. When P_2 is varied, the interference envelopes appear in the Michelson interferometer. As the reflected light is phase-modulated with f=10 kHz, only the interference signal between the reference light and the returning light from the test waveguide can be detected by the lock-in amplifier. The interference peak produced at a given mirror position is proportional to γ, where γ is the amplitude of the returning light at the corresponding back-scattering point. The relative power at this point is described by γ^2, or logarithmically, by $C=-20\log\gamma$ (dB).

Results

Figure 2 shows the I-L characteristic of the SLD operating at λ =1.3 μm wavelength.[3] The output light power is 1.2 mW at I=140 mA and its spectrum is almost continuous with $\delta\lambda$ =40 nm spectral width. The output power was very stable and no spectral changes were observed while the OTDR experiments were made. The coherence length was $\ell_c = \lambda^2/\delta\lambda$ =42 μm, and then the spatial resolution of the present OTDR was $\ell_c/2n_c$ =15 μm.

Test silica glass optical waveguides are single-mode embedded straight waveguides fabricated by a combination of flame hydrolysis deposition and reactive ion etching processes.[4] The cross-sectional view of the glass waveguide is shown in Fig. 3. The core consisting of TiO_2 doped SiO_2 was 8 μm in both width and height. The buffer and cladding glass layers made of SiO_2 were 8 μm and 32 μm in thickness, respectively. The refractive indices of the buffer and the cladding layers were almost the same, and were lower by 0.25 % than that of the core.

Figure 4 shows the measured amplitude Γ vs. the optical path difference in the interferometer, where the test waveguides are 1.8-cm long SiO_2 glass optical waveguides. These two optical waveguides were fabricated under different process conditions, although their waveguide parameters were the same. Both ends of the test waveguides were immersed in matching oil to reduce the end reflection. For the single-mode fiber, the reflected power at both ends were reduced to lower than -70 dB relative to the propagating light power.[1] However, the reflected power did not decrease to lower than -40 dB for the glass optical waveguides with the same matching oil. This difference may be due to the refractive index difference between the waveguides and the matching oil and/or due to imperfect end preparation of the waveguides. Thus the relatively-large end reflections were observed for these glass waveguides.

In the single mode fibers there are no scattering centers except for Rayleigh scattering centers. Correspondingly, no peaks were observed at the detection range of $\Gamma = 10^{-5}$ when a short piece of a single mode fiber was used as a test waveguide. However, a few scattering centers were observed for one glass optical waveguide as shown in Fig. 4(a), while no scattering centers were observed for another as shown in Fig.4(b). Therefore, it is clarified that the scattering centers are produced in the silica based optical waveguides under slightly different process conditions. The detection level is set at one order of magnitude higher than Rayleigh-backscattered signal

level. Therefore, these observed peaks may be produced by the so-called Mie scattering. The origins of the scattering centers are inhomogeneity in the waveguides produced during etching and/or consolidation.

Conclusion

We have proposed a new type of OTDR system for characterizing miniaturized optical waveguides by using interferometric techniques with a 1.3 μm SLD. Scattering centers in the waveguides were made clear. Therefore, the system is useful for finding the scattering centers and for clarifying loss mechanism in the optical waveguides.

Acknowledgment

The authors would like to express their sincere thanks to I. Yokohama for supplying the PANDA coupler and to E. Noguchi for fabricating 1.3-μm SLDs. They also thank to N. Uchida for his continuous encouragement.

References

1) K. Takada et al., Appl. Opt. vol. 26, pp. 1603-1606 (1987).
2) I. Yokohama et al.,Electron. Lett. vol. 22, pp.929-930(1986).
3) H. Nagai et al., submitted to Electron. Lett.
4) N. Takato et al., Electron. Lett. vol.22, pp.321-322 (1986).

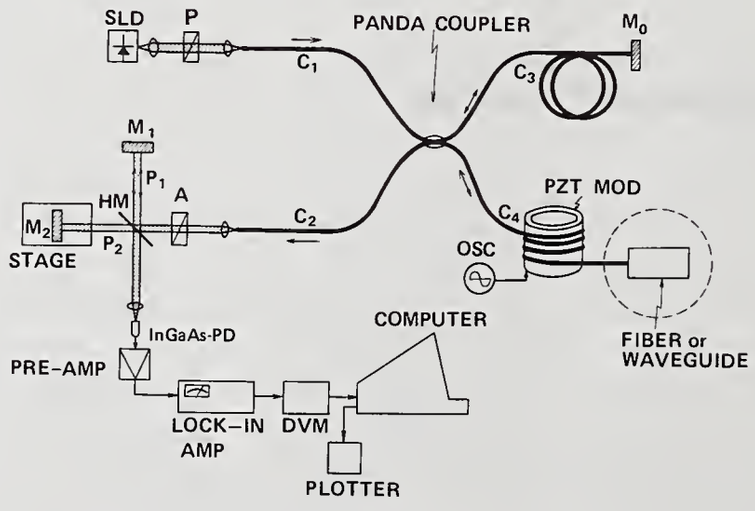

Fig. 1. Experimental setup.

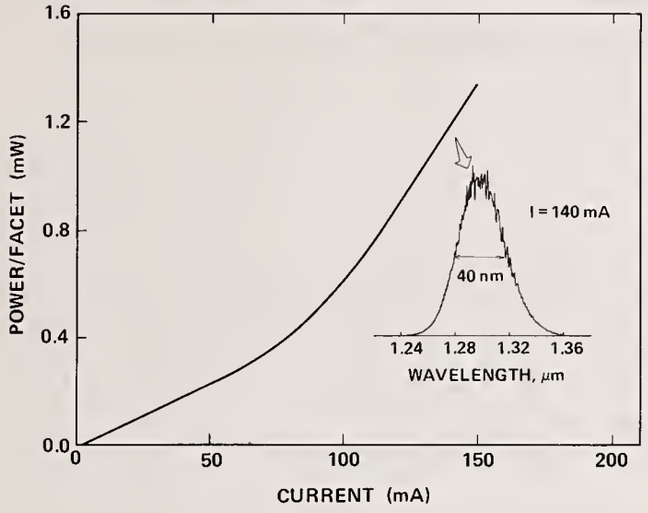

Fig.2. I-L characteristic of SLD.

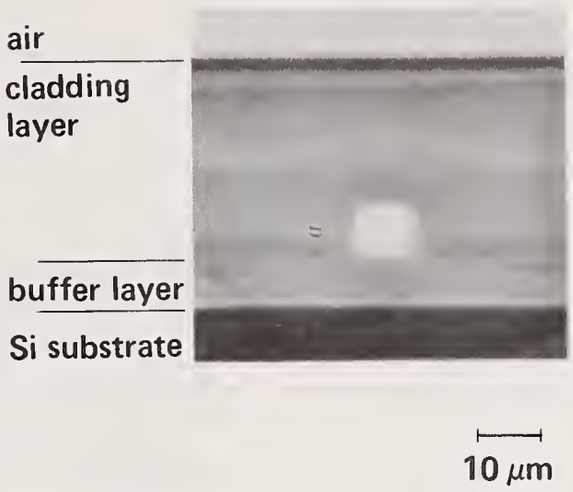

Fig.3. Cross sectional view of SiO_2 glass waveguide.

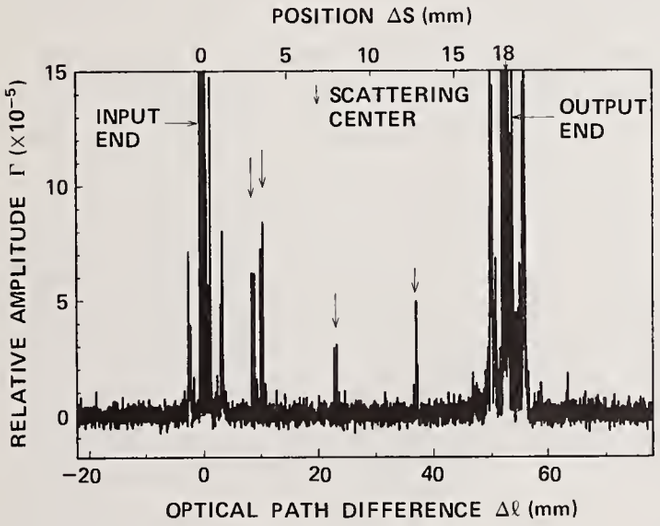

Fig.4(a). Amplitude Γ vs. optical path difference for 1.8cm-long SiO_2 glass waveguide.

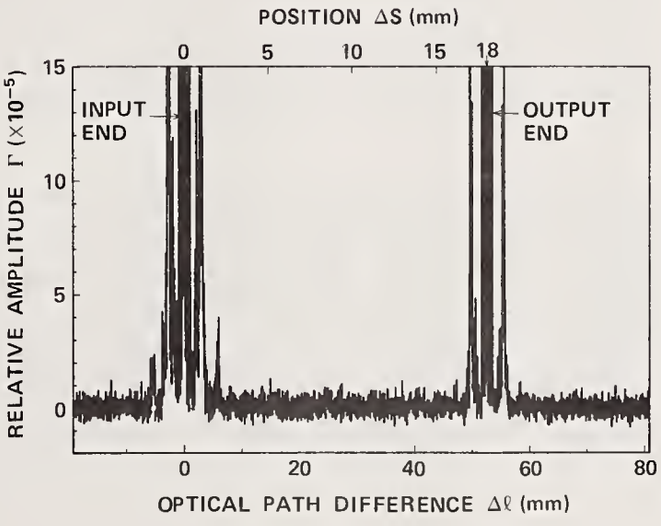

Fig.4(b). Amplitude Γ vs. optical path difference for 1.8cm-long SiO_2 glass waveguide.

Reflectance Measurement in Lightwave Systems: A Comparison of Various Techniques

S. K. Das, A. F. Judy, G. M. Alameel, R. M. Jopson, T. F. Adda

AT&T Bell Laboratories

1. Introduction

The measurement of the reflectance of fiber optic components is increasing in importance as operating systems push the performance limits of fiber. For example, the performance of semiconductor lasers, especially single-line ones, can be either degraded or improved by optical feedback[1][2][3] from nearby connectors or from fiber backscatter.[4] Both coherent and direct detection systems can be effected by intensity noise caused by multi-path interference between two or more large reflections.[5] Likewise bi-directional systems[6] and analog systems[7] may be sensitive to large reflections.

This paper overviews the principle methods for measuring reflections and discusses their applications and limitations. It also presents a comparative "round-robin" study between five different measurements at three AT&T Bell Laboratories locations: Whippany, Crawford Hill and Atlanta. Close agreement has been obtained between these measurements and estimates are derived for the repeatability and accuracy of the various test methods. We conclude with identification of problem areas and recommendations.

2. Types of Optical Reflection Measurements

The typical method for measuring reflections uses a separate light source and detector connected by a coupler. (Fig. 1(a)) The coherence length of the source must be much shorter than the distance between the components so that coherent interference will not occur. Also the system, especially the coupler, must be free of polarization sensitivity. (We note that the evaluation of polarization effects is the least developed in the literature.) Similarly, mode dependent coupling must be negligible in multimode couplers that are used to measure reflectance in multimode fiber systems.

The type of modulation of the light source can be used to divide optical reflectometry into three subtypes: optical continuous wave reflectometry (OCWR) which is often called the "coupler method", optical time domain reflectometry (OTDR), and optical frequency domain reflectometry (OFDR). The first two are the most commonly used and will be discussed in detail below. OFDR, which is also called optical network analysis, is not widely used at the present. It may become popular for analog systems applications since it operates by frequency modulation of a rf/microwave subcarrier onto the light source and detecting (and displaying) the magnitude and phase of the reflectance as a function of the modulation frequency.[8] However we will not treat it extensively here.

2.1 OCWR: Description

OCWR is perhaps the simplest and most developed of the reflectometry methods. At least two measurement standards have been proposed to standardize it.[9][10] However both require an inconvenient making-and-breaking of fusion splices to perform the test. Here we describe a more general procedure and theory which is inclusive of the original methods while eliminating this restriction.

The OCWR method functions by generating an essentially unmodulated, CW signal. (A very low frequency modulation for lock-in detection is equivalent.) Thus the detector measures the sum of the power from: (1) the coupler crosstalk, (2) the reflections from all the components-under-test, and (3) any spurious reflections. The following procedure describes the measurements and calculations needed to separate these contributions.

2.2 OCWR: Theory

The power transfer between the four ports of a bidirectional 2x2 coupler, can be represented by a symmetric 4x4 matrix $[\eta]$. For an application such as measuring unknown reflectance values, port 4 is unused and hence terminated inside the coupler with a suitable index matching epoxy. This is shown in Fig. 1 (a). Port 3 is connected to the test system; ports 1 and 2 are connected to a light source (preferably a laser) TX and a power meter RX, respectively. Fig. 1 (b) shows a test connector C_x connected to port 3 of the coupler via an intermediate connection C_i. Assuming that no reflection is coherent with any other, the received power P_{R1} at RX is given by

$$P_{R1} = P_T \left[\eta_{12} + \eta_{13}\eta_{32}R_i + \eta_{13}\eta_{32}\eta_i^2 R_x + \eta_{13}\eta_{32}\eta_i^2\eta_x^2 R_{T1} + \eta_{14}\eta_{42}R_4 \right] \quad . \quad (1)$$

where P_T=laser power output, R_i=reflection from connection C_i, R_x=reflection from connection C_x, R_4=residual reflection of fiber termination at port 4, R_{T1}=residual reflection from termination T1, η_i=power coupling efficiency of C_i, and η_x=power coupling efficiency of C_x. The test connector C_x is opened and the leading connector/splice is terminated as shown in Fig. 1 (c). (Alternately, the fiber before test connection C_x may be looped in a small diameter to attenuate the reflection from C_x.) The received power at the RX is

$$P_{R2} = P_T \left[\eta_{12} + \eta_{13}\eta_{32}R_i + \eta_{13}\eta_{32}\eta_i^2 R_{T2} + \eta_{14}\eta_{42}R_4 \right] \quad (2)$$

where R_{T2} is the residual reflection from end termination T2. The power emerging from T2 is given by $P_3 = P_T\eta_{13}\eta_i$. Subtracting (2) from (1) and rearranging the terms one gets

$$R_x = R'_x + [R_T(1-\eta_x^2)] \quad , \quad (3)$$

where the raw reflectance is given by

$$R'_x = \frac{P_{R1}-P_{R2}}{P_3\eta_i\eta_{32}}$$

and R_T=R_{T1}=R_{T2} has been assumed. (This assumption has been verified, to a limited extent, in experiments involving a given batch of connectors polished in a similar fashion.) From (3) it is clear that the crosstalk η_{12} and the reflections R_4 or R_i have no influence in the measurement of R_x. Hence, index matching C_i is unnecessary, unless R_i is so high that it masks the sensitivity of the measurement of P_{R1} and P_{R2}. What is important, however, is the end reflection R_T which has traditionally been ignored. R'_x is an easily measurable quantity and so is η_x. The "correction" ΔR_x in dB is given by

$$\Delta R_x\,(dB) = 10 \log R_x - 10 \log R'_x = 10 \log \left[1 + \frac{R_T(1-\eta_x^2)}{R'_x} \right] \quad (4)$$

and is plotted in Fig. 2. It is found that for a test connection loss L_x=-10 log η_x=0.5 dB, 10 log R_T=-30 dB and 10 log R'_x=-40 dB, the correction $\Delta R_x\,(dB)$ is $\approx$ 5 dB. The correct reflectance is then -40+5=-35 dB.

2.2.1 Example : OCWR Measurement of Fresnel References. It will be shown that the OTDR methods for measuring reflectances rely on either of the two references, Rayleigh backscatter or a glass-to-air Fresnel reflection. The OCWR provides a simple and accurate means ($\pm$0.5 dB) to measure Fresnel reflections. This is done as follows. In Fig. 3 (a), jumper BC has a reference Fresnel reflection at the end C. With B connected to port 3 of the coupler one obtains

$$P_{R1} = P_T \left[\eta_{12} + \eta_{13}\eta_{32}R_i + \eta_{13}\eta_{32}\eta_i^2 R_F + \eta_{14}\eta_{42}R_4 \right] \quad (5)$$

where R_F is the reference Fresnel reflection. Now the end C is index matched as in Fig. 3 (b), and the power

P_{R2} at RX is:

$$P_{R2} = P_T \left[\eta_{12} + \eta_{13}\eta_{32}R_i + \eta_{13}\eta_{32}\eta_i^2 R_T + \eta_{14}\eta_{42}R_4 \right] \quad (6)$$

where R_T is the residual reflection from the termination. Subtracting (6) from (5), and using (3) we get $R_F = R'_x + R_T$. Usually, the Fresnel reflection value is in the order of -14 dB, whereas R_T (dB) is more like -35 dB. Hence, little error is incurred if one assumes $R_F = R'_x$.

2.3 OTDR: Description

The OTDR transmits narrow pulses into a fiber and displays the reflected signal versus time or, equivalently, distance. If the pulse width is narrow enough, the reflections from the components-under-test are separated from each other as well as from the coupler. Thus the calculations involved for the OCWR method are eliminated.

The use and specification of OTDR testing has been well documented for almost every application[11] except for reflection testing so we will briefly summarize its use here. Since all OTDRs display the reflected signal on a relative scale, one must first calibrate with a known reference reflection. The most readily available reference is the Rayleigh backscatter from the fiber itself which is:

$$R_{bs} = \frac{v_g}{2} PW \alpha_s S$$

where v_g is the group velocity; PW is the temporal pulse width of the equivalent rectangular pulse; α_s is the fiber attenuation due to Rayleigh scattering; S is the proportion of backscatter that is captured by the fiber (which is a function of the fiber's spot size). The uncertainty in calculating R_{bs} is typically a few tenths of a dB due to fiber parameter uncertainties.

For wide pulse widths, R_{bs} may approach the reflectance value of the component-under-test and the OTDR will display the power sum of the two. R_{bs} must be subtracted to obtain the correct reading.[12] If very narrow pulse widths are used, R_{bs} becomes too small to measure. In this case one can also calibrate with a glass-to-air Fresnel reference (which can also be used to check the R_{bs} value). Caution is advised in that many commercial OTDRs were designed to measure only small reflections, and may be saturated or nonlinear for large ones.

3. Reflectance Comparison Experiment: (Round-robin)

Twelve test connections were made from pairs of 35-foot single-mode jumper cables which had ST connectors on either ends. The test connections, numbered from 1 through 12, were not disturbed until all the reflectance measurements were complete. These were then measured on two different OCWRs and three different OTDRs. Since the OCWR method usually requires making and breaking the test connection, the five measurement techniques were performed in the following sequence:

3.1 Whippany: OCWR

The procedure of Sec. 2.2 was followed to measure the reflectance of the 12 test connections. Correction factors were ignored since R_T was small (<-35 dB).

3.2 Whippany: Millimeter OTDR

The OTDR used here consisted of an assembly of components manufactured by Optoelectronics, Inc. The laser is modulated by a 0.5 ns pulse, yielding a resolution distance of 5 cm in the fiber. The repeatability of this system is $\approx$ 0.3 dB. Since it could not measure Rayleigh backscatter, a rotary splice ferrule polished with chromium oxide was used as the reference Fresnel reflection; its reflection was determined as -14.7 dB using

the procedure described in Sec. 2.2.1.

3.3 Crawford Hill: 50-cm OTDR

This reflectometer has a received pulse length of 5 ns resulting in a resolution of 50 cm. It was calibrated with a Fresnel reflection. Since the jumpers being tested were longer than 50 cm, it was not necessary to correct the data for other reflections. However, a correction was needed for the loss of C_i (Fig. 1 (b)). This loss was determined by comparing the power out of coupler port 3 before connection of the jumper assembly with the power out of T1 after the connection and subtracting the loss in the test connection C_x. (The loss value of C_x was taken from Sec. 3.1.)

3.4 Atlanta: 200-m OTDR

This technique uses a 1.3-μm Anritsu MW98A OTDR with a 2-μs pulse. Normally the test connection, C_x, is positioned at the end of a long length of fiber and the OTDR simultaneously displays the fiber backscatter and the reflection from C_x. The difference between the two is measured, then by knowledge of the amount of fiber backscatter, C_x's reflectance is found.

Since the 2-μs pulse has a spatial width of over 400 meters, this method requires that any two reflections be at least 200 meters apart if they are to be independently visible on the OTDR. An even greater separation is required to view the fiber backscatter. So several hundred meters of fiber must precede and follow C_x for accurate measurements.

In the experiment reported herein C_x was the junction of two ST connectors, each on the end of a 35-foot jumper cable. This resulted in three reflections, (C_1, C_x, and C_2 as in Fig. 4) which could not be distinguished from each other. Consequently the following 7 step procedure was used to measure the reflectance of C_x instead of the usual method:

1. The power, P_2, from C_2 is measured with a power meter. This is for the later determination of the insertion loss of the first two ST connections. Fig. 4(a)
2. An approximately 1/8" diameter loop is tied in the fiber that follows C_x. This attenuates the reflection from C_2 to well below C_x's value. The combined reflection from C_x and connector C_1 is measured on the OTDR. This is designated as $R_m = R_1 + \eta_1^2 R_x$. Fig. 4(b)
3. An approximately 1/8" diameter loop is tied in the fiber that precedes C_x. This attenuates the reflection from C_x and C_2. The reflectance R_1 is measured on the OTDR. Fig. 4(c)
4. Connection C_1 is disassembled and the power, P_1, from the 1-km test lead is measured. Fig. 4(d)
5. The insertion loss of the two STs is calculated as:

$$\eta_1 \eta_x = \frac{P_2}{P_1} \tag{7}$$

6. Normally C_x would be disassembled and the power measured to determine η_x as in the preceding two steps. However disassembling the connectors would have precluded further measurements so instead the value from Sec. 3.1 was used.
7. R_x is calculated to be:

$$R_x = \frac{R_m - R_1}{\eta_1^2} \tag{8}$$

where all the parameters on the right hand side are known, η_1 being determined from steps 5 and 6.

3.5 Atlanta: OCWR

The measurements followed the procedure outlined in Sec. 2.2. Correction factors were not accounted for since the end reflectance was either comparable to, or lower than, the measured values of ST reflectance. However, instead of measuring η_i every time a new jumper connection is made to port 3 of the coupler, the Atlanta method uses a standard value of L_i=-10 log η_i=0.5 dB, to facilitate rapid reflectance measurements. This 0.5 dB value for L_i has been substantiated from loss experiment with a large sample size of STs.

4. Results and Discussion

In Table 1 are listed technique-to-technique reflectance variations

$$v_i = R_{x_i} - \overline{R_x} \ \ (dB)$$

where i=1 to 5 and $\overline{R_x}$ denotes the mean reflectance of a ST connection over the 5 measurement techniques. Based on the small values of standard deviation σ (σ < 1 dB for 9 out of 12 STs), it is clear that both the OCWR and the OTDR methods yield accurate results. The sum of the five v_is across some rows do not add to zero due to rounding errors.

When compared to the OTDR data, the OCWR results were slightly more optimistic due to the neglect of correction factors which account for unwanted reflection from index-matched terminations. In such cases, fiber loops are shown to offer a simple and effective alternative to index-matching, since the (unwanted) returned power can be suppressed to the desired level by increasing the number of loops and/or by decreasing the fiber bend radius within safe limits.

To summarize, the various methods compare well but each has advantages in certain applications. For instance if one is measuring closely spaced components and wants to avoid the inconvenience of fiber-looping/index- matching, a properly calibrated, high resolution OTDR is superior to some of the other techniques described in this paper. If on the other hand one wants to measure the total power reflected from numerous components (including fiber backscatter), the OCWR is the best. Or if one wants to measure the reflections from widely spaced splices on a long installed fiber route, a wide pulse-width OTDR would be optimum. Finally, while not evaluated here, OFDRs may be advantageous for measuring the effects of multiple reflections on the analog transmission systems.

References

1. O. Hirota and Y. Suematsu, IEEE J. of Quantum Electronics, QE-15, p.142, March 1979
2. R. W. Tkach and A. R. Chraplyvy, J. Lightwave Tech., Vol. LT-4, p.1655, Nov. 1986
3. W. I. Way and M. M. Choy, J. Lightwave Tech., Vol. 6, No.1 p.100, Jan. 1988
4. A. R. Chraplyvy, D. Marcuse and R. W. Tkach, J. Lightwave Tech., Vol. LT- 4, No.5, p. 555, May 1986
5. J. L. Gimlett et.al., OFC 88, paper WG4
6. P. P. Bohn and S. K. Das, J. Lightwave Tech. Vol. LT-5, No.2, p.243, Feb 1987
7. K. Fujito, et.al., OFC 88, paper THO
8. M. Nazarathy, D. W. Dolfi and S. A. Newton, OFS 88, paper WDD7-1
9. Electronic Industries Association, "Return Loss", FOTP-107 (proposed)
10. Bell Communications Research, TR-TSY-00326, Issue 1, August 1987
11. B. L. Danielson, Applied Optics, Vol. 24, N0.15, p.2313, Aug.1,1985
12. A.F. Judy and H.E.S. Neysmith, in Proc. SPIE, 574, Fiber Optic Couplers, Connectors and Splice Technology II, p. 146 (1985)

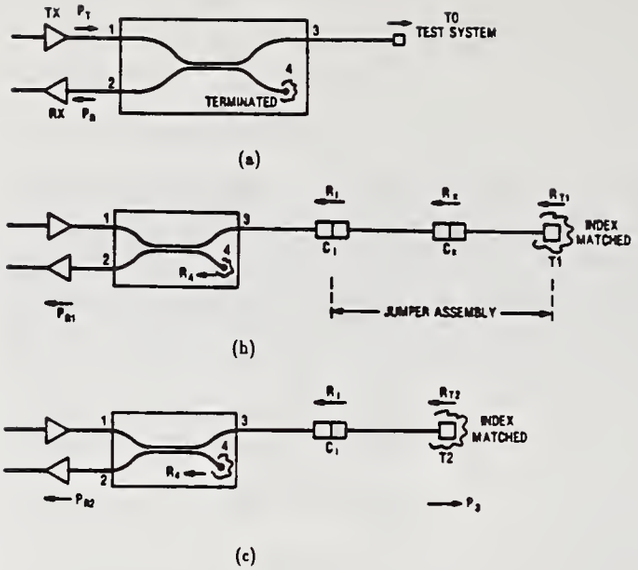

Fig. 1. (a) Coupler connections in a typical reflectance measurement set-up. (b) Test connector/splice C_x connected to port 3 of the coupler via intermediate connection C_i. (c) C_x is opened and the leading connector/splice terminated.

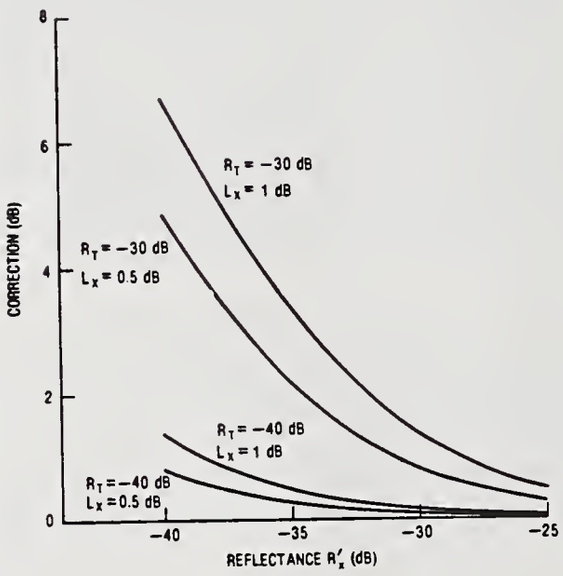

Fig. 2. Correction ΔR_x in dB, as a function of the raw reflectance R'_x (dB), to account for the non-zero end reflection from ST ferrule termination T1.

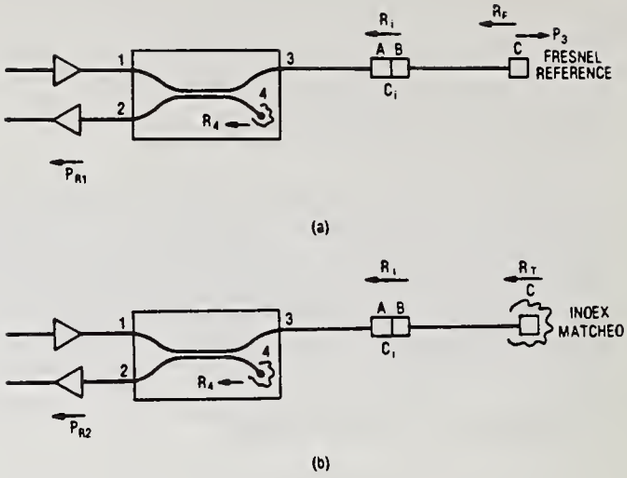

Fig. 3. (a) Set-up to measure reflectance of the Fresnel reference. Jumper BC has the Fresnel reference at end C. (b) End C is index-matched.

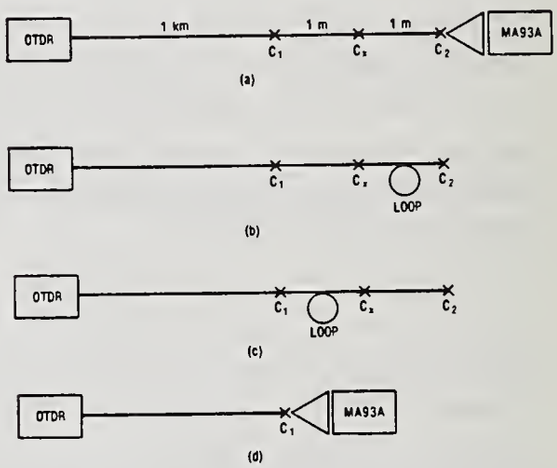

Fig. 4. Set-up to measure reflectance of C_x with a 200-m OTDR.

Table 1
Technique-to-technique Reflectance Variation (dB)

Connection #	Whippany OCWR	Whippany OTDR	Crawford Hill OTDR	Atlanta OTDR	Atlanta OCWR	σ
1	0.3	-0.4	-0.4	-0.2	0.5	0.4
2	1.9	0.3	-0.8	1.8	-3.0	2.0
3	-0.2	-0.5	-0.2	0.5	0.3	0.4
4	0.6	0.4	0	-0.2	-0.9	0.6
5	0	0.4	0.2	0.1	-0.5	0.3
6	-3.3	0.4	1.2	1.6	0.3	1.9
7	-0.1	-1.2	0.5	0.5	0.3	0.7
8	-0.4	1.1	1.0	0.3	-2.2	1.4
9	-0.4	-1.1	0.7	1.0	-0.2	0.9
10	-0.4	-0.2	0.3	0.1	0	0.3
11	-0.2	0	-0.1	-0.4	0.9	0.5
12	0.1	0.9	-0.3	0.1	-0.8	0.6

Calibration and Use of an Optical Time Domain Reflectometer For Measurements of Reflectance (Return Loss) of Optical Fiber Components

Paul R. Reitz
AMP, Incorporated
Harrisburg, PA.

Introduction

The typical measurement of return loss (optical source, coupler, and power meter) has several limitations which can be addressed with the OTDR. Use of the OTDR is not new [1], but has not become widespread, partly due to questions about accuracy. In a manner implied by Judy and Neysmith [2], we report a straightforward calibration method for the OTDR based on the use of known index oils with a cleaved-end fiber.

Description of the Method

Most workers approached measurement of reflectance with the OTDR by calculating the backscatter level to enable determination of the relative power produced by a reflectance. Our method is to calibrate the instrument together with an optical fiber by measuring the reflection spike amplitude, A_r, from a length of optical fiber as a function of the index of a medium into which the output end of the fiber is placed. This data is then used to determine the effective fiber index, n_1, from which a scale factor K for the OTDR can be determined. Return loss can then be readily calculated. Once the effective fiber index at the measurement wavelength is known, a much simpler procedure is sufficient to calibrate other instruments.

Theory

Referring to Figure 1, the displayed signal amplitude, P_1, on an OTDR trace at point 1 just prior to the output end of the fiber can be generalized as

$$P_1 = c_1 \cdot c_2 \cdot P_{inc} \cdot k \qquad (1)$$

where c_1 is an instrumentation factor (including return-trip fiber loss), P_{inc} is the incident power propagating at point 1, and k is the backscatter fraction for the fiber that includes both scattering loss and backscatter capture. C_2 includes the effects of pulse duration, which affects backscatter without affecting the peak magnitude of the reflected signal. The displayed signal amplitude at the peak of the reflection spike, P_2, is modeled as

$$P_2 = P_1 + c_1 \cdot c_3 \cdot P_{inc} \cdot R \qquad (2)$$

where c_3 is a detection system pulse response factor. R is the reflectance of the fiber / medium interface, given by the reflection equation for normal incidence:

$$R = \{[n_1 - n_2]/[n_1 + n_2]\}^2 \qquad (3)$$

where n_1 is an effective fiber material index at the measurement wavelength, and n_2 is the index of the medium into which the fiber is terminated.

The reflection spike amplitude, A_r, read from the OTDR display from the base to the peak of the reflection spike in decibels (10 log vs. 5 log), is given by

$$A_r = 10 \log [P_2 / P_1]$$
$$= 10 \log [1 + K \cdot R] \quad (4)$$

where $K = c_3 / c_2 \cdot k$.

The return loss, L_r, (ignoring connection loss), is calculated as

$$L_r = 10 \{ - \log K + \log [10^{(A_r / 10)} - 1]\} \quad (5)$$

Experiment

K was determined by measuring A_r for specific values of R calculated by determining appropriate values for n_1 and n_2, using a typical single-mode fiber with a cleaved output end. Previous work has shown that polished ends should not be used. Since an exact value of n_1 was not known, A_r was measured for a series of 20 oils covering the range of n from ≈ 1.39 to ≈ 1.51, with the fiber sequentially terminated in each oil. Oil indices were translated to the OTDR wavelength using Cauchy's equation.

A value of n_1 was iterated until the computed K values were nearly equal for both high and low n's. The resultant value of K was used to calculate theoretical A_r values using equation 4, which are compared with the measured ones in Figure 2. Figure 3 shows the error as a function of the computed return loss. The agreement is excellent for all but the largest and smallest values of A_r. The error at large A_r is amplitude nonlinearity while the error at small A_r is both amplitude uncertainty (related to a periodic undulation in the backscatter level, a characteristic of this OTDR), residual n_1 uncertainty, and limitations of the simple model..

The relationship between measured A_r and return loss is shown in Figure 4 for three different pulse duration settings of the same OTDR; this instrument could measure return loss on single-mode fiber from -25 dB to at least -60 dB. This range is ideal for the specification requirements likely to be placed on passive components, as values above -30 dB would typically constitute failure for low-reflection components. Table 1 summarizes the results for various fibers and instrument settings. The single-mode data suggest that only small errors would be introduced with a fiber other than the calibration fiber.

Primary sources of uncertainty with this method include (1) linearity and noise of the OTDR amplitude scale, (2) errors in the value and stability of K, (3) end angle on the calibration fiber, and (4) connection loss to the component to be measured.

The OTDR is readily characterized in terms of the maximum usable A_r value, based on the departure of the theoretical curves from the measured data, and A_r uncertainty. Care must be taken to operate the instrument in this region. Typical reproducibility of A_r is on the order of 0.2 dB (3 sigma) for 5 dB < A_r < 22 dB.

While only two A_r and index data are sufficient, in principle, such a procedure would not be robust against either calculation or contamination error in an index value. By performing the calibration with many index oils, the determination of K is quite independent of a single oil index

error. The fact that measured and calculated A_r's fit with so little apparent fluctuation in n suggests that the extrapolation error is more systematic than random. A systematic error of 0.5% in n causes < 0.1 dB error in A_r.

Figure 5 shows that the reduction of reflectance caused by fiber end angle follows accepted theory sufficiently well to be correctable for small end angles. The error reduction that can be achieved depends on error in the measurement of end angle; in many cases the end is flatter near the center of the fiber.

The loss of the connection with which the component to be measured is attached to the calibration fiber can be measured with the OTDR, given sufficient fiber length. Higher optical resolution OTDRs would be helpful, but an optical power meter can also be used.

Comparison with the Coupler Method

Results obtained with the OTDR have been compared to the coupler method on sixteen multimode components exhibiting return losses ranging from -26 to -32 dB. A mean difference of 0.61 dB was observed, with the OTDR indicating higher return loss. Return losses have been measured on mechanical splices in excess of -60 dB.

Conclusions

The OTDR is a viable method for the quantitative measurement of reflectance from optical components, and will become more attractive as further advances are made in OTDR optical resolution. Measurement of return loss over the range of ≈ -25 to -60 dB with an estimated accuracy of ≈ 1 dB is feasible. The calibration method can also be used in the coupler method to eliminate the need for a known-reflectance "golden" lead.

Acknowledgements

The author would like to thank the following individuals for their contribution: S. J. Harms, oil index calculations and 100 / 140 data; R.H.Rebuck, procedure and single-mode data; and W. K. Long, comparison data.

References

1. Methods for Reducing Optical Fiber Connector Reflection Through Use of Index Matching Materials.
   I. Sankawa, T. Satake, and N. Kashima, Review of the Electrical Communications Laboratories (NTT), Vol. 34, No. 6, 1986.
2. Reflections from Polished Single-mode Fiber Ends. A. F. Judy and H. E. S. Neysmith, Proceeedings of SPIE, Vol. 574, 1985.

Fiber Size / Type	K	Pulse Width	n_1
10/125 matched-clad single-mode	780000 342000 94500	160 ns 640 ns 2.56 us	1.4520
9.5/125 matched-clad single-mode	700000	160 ns	1.4517
62.5/0.275 multimode, 850nm.	6500	160 ns	1.4795
100/140 multimode, 850 nm.	20000 6000	20 ns 160 ns	1.4850

TABLE 1. Summary of Results for Various Fibers

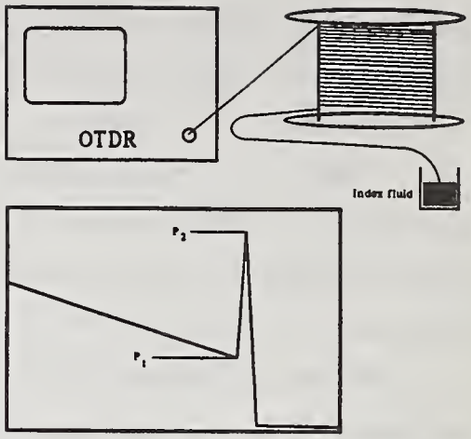

Figure 1. Calibration Set-up and OTDR Trace

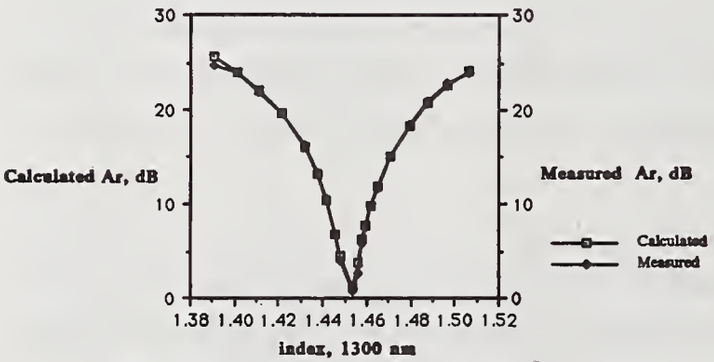

Figure 2. Calculated and Measured Ar

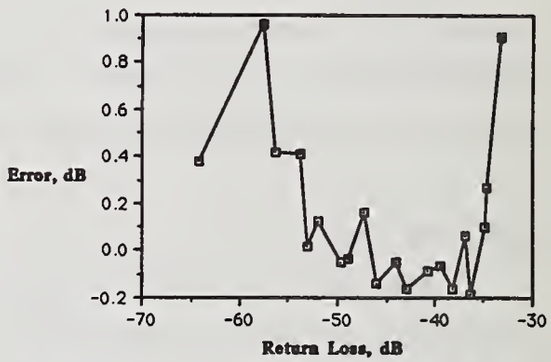

Figure 3. Error in Ar vs. Measured Return Loss

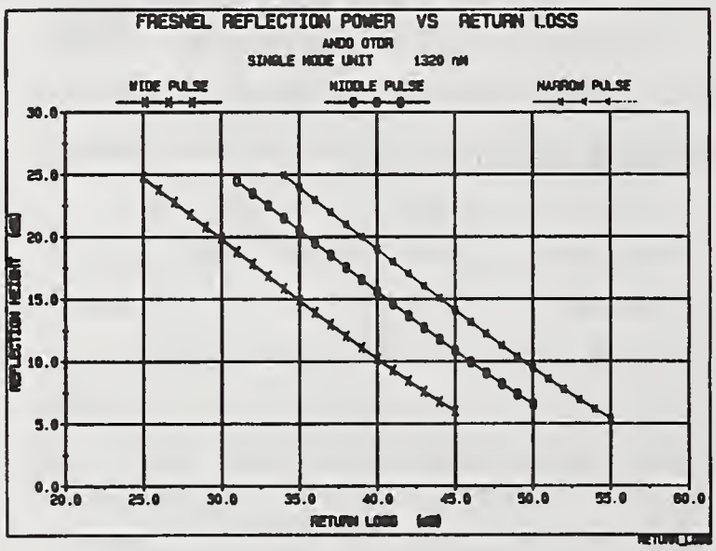

Figure 4. A_r vs. Pulse Width and Return Loss

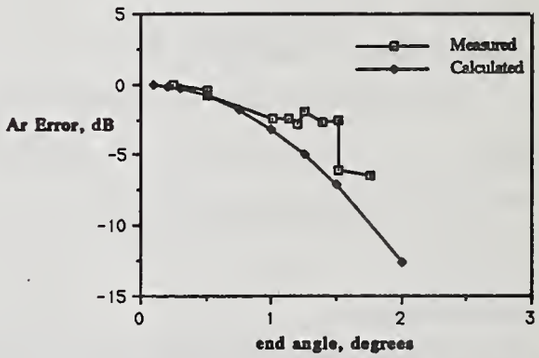

Figure 5. Effect of End Angle on Ar

OTDR MEASUREMENTS OF OPTICAL RETURN LOSS

Felix P. Kapron, Edward A. Thomas, and John W. Peters

Bellcore
445 South St.
Morristown, NJ 07960-1910

Abstract

Precautions are given for using an optical time-domain reflectometer to measure the return losses of discrete reflections. We present a new method for determining the backscatter level of the fiber type under test, and show its importance in optical return loss measurements. Some improvements for OTDR manufacturers are offered for consideration. A new EIA FOTP on optical return loss via OTDR is warranted for both component and link characterization.

Introduction

Reflections from discrete points along a fiber optic link can degrade transmitter or receiver performance in high-speed systems [1,2]. To avoid an excessive link power penalty, the minimum allowed optical return loss (ORL) for elements such as splices and connectors is sometimes specified [3]. In terms of reflectance (captured reflected power P_{rfl} over incident power P_{inc}) of the element, and in positive dBs

$$ORL = 10 \log_{10} \frac{P_{inc}}{P_{rfl}} \quad . \tag{1}$$

The usual method for measuring ORL utilizes a 2x2 coupler [3,4] and is somewhat tedious. In contrast, the optical time-domain reflectometer is uniquely qualified to efficiently measure both the magnitude [5] and location [6] of a sequence of reflections that may require corrective action in the field. However, since OTDRs are not yet commonly used for this purpose, current instruments are optimized for attenuation (rather than ORL) measurements.

In this paper we show that the accuracy of the OTDR method is sensitive to the correct values of pulse duration, pulse height, and fiber backscatter level. We obtain these values by a combination of coupler and OTDR techniques. Finally, we suggest improvements for future instruments.

Return Loss Using a Coupler

As shown in Figure 1, a source is connected to coupler port a, and a fiber reel is fusion-spliced to port c. For a partially reflecting far-end under test we measure powers P_{inc} out of the fiber far-end (which is actually slightly smaller than the true incident power); P_R out of port b, when the far-end is reflecting; P_0 out of port b, when the far-end is non-reflecting.

The reflected power (P_R - P_0) has suffered a loss in travelling from the far-end to c to b. This loss is measured by first splicing the source to the far-end, and measuring P_{out} at port b. Then the fiber reel and coupler (but not the splice) are removed by cutback, and P_{in} is measured. The optical return loss is calculated from

$$ORL = 10 \log_{10} \frac{P_{out}\, P_{inc}}{P_{in}\, (P_R - P_0)} \quad . \tag{2}$$

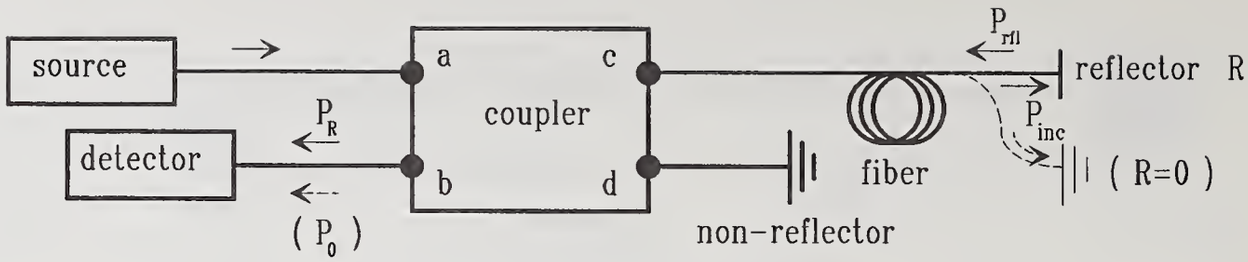

Figure 1 - ORL using a coupler

Return Loss Using an OTDR

A reflection from a fiber discontinuity is displayed on an OTDR as a logarithmic replica of the incident optical pulse, modified by the receiver response and any fiber attenuation and dispersion. It is superimposed to a height P (in dB) above the fiber backscatter level (Figure 2). Under the assumptions of a "rectangular" optical input pulse of time duration D (in ns) and negligible pulse broadening, the optical return loss is [7]

$$ORL = B - 10 \log_{10} [(10^{P/5} - 1)\, D] \quad . \tag{3}$$

B is the fiber backscatter level in dBs below the power P_{inc} of a pulse having a 1-ns duration incident upon the reflective discontinuity. A quantity related to B can be determined [8], but we measure B by a new method as shown later below.

Pulse Duration

Pulse duration D of both a wide and a narrow pulse was measured. Figure 2 shows typical OTDR traces from a high reflection (low ORL) fiber far-end. For low reflections, the backscattering background (which increases for wider pulses) will distort and broaden the reflected pulse, giving a less reliable value of pulse duration.

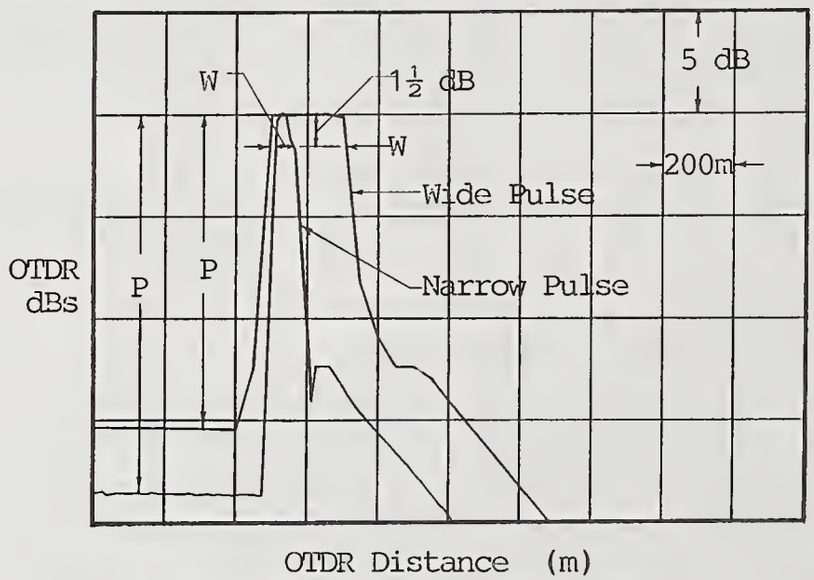

$D(\text{ns}) = N\ W(\text{m})/0.1499$
N = group index
W = OTDR pulse width

Figure 2 - Wide and narrow OTDR pulses from a high reflection (low ORL)

Note that the pulses are not rectangular, and that there are few resolvable distance points within a pulse. Therefore, the precise value of D is somewhat ambiguous. We measured pulse duration at the usual [9] 1½ dB below peak power, corresponding to the FDHM of linear optical power. In addition, since the backscatter power is proportional to pulse energy [8], we measured D as the pulse energy (area) divided by the peak linear power. Results are given in Table 1.

	Wide	Narrow
1½ dB duration (FDHM)	2,127	377
energy/power duration	2,499	489

Table 1 - Pulse durations D (in ns) for two definitions and pulse types

Pulse Height

A fiber reel with a reflecting far-end was fused to the OTDR pigtail, and the height P of the far-end reflection peak above the backscatter level there was measured. For a highly reflecting far-end, receiver clipping masked the true pulse height. Our solution to this was to introduce a non-reflective bending attenuation into the fiber as shown by the signature in Figure 3. This should not affect the true (unclipped) height P.

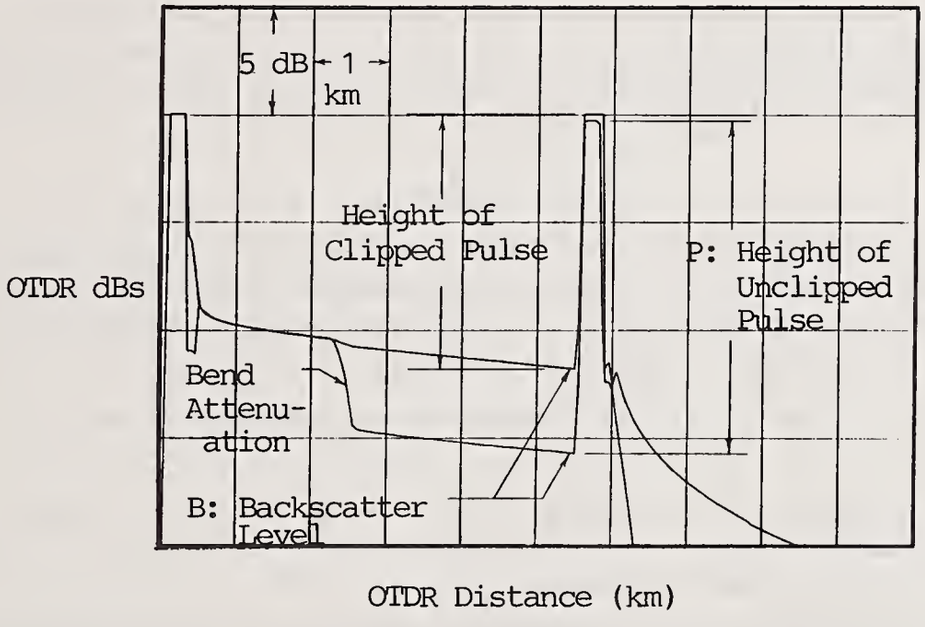

Figure 3 - A full-length OTDR trace, showing clipping and bending attenuation

However, for excessive attenuation, P decreased by up to 2 dB and 0.4 dB for 3½ km and 5½ km fiber lengths, respectively. This is because the receiver's recovery tail due to the near-end reflection [9] adds substantially (on the logarithmic scale) to the backscatter level, but adds little to the end-reflection pulse peak. (The near-end recovery tail is not influenced by the attenuation.) For the minimum (but still large) induced attenuation sufficient to prevent clipping, height P was not noticably affected when the 5½ km fiber was used.

Fiber Backscatter

Three single-mode fiber types were investigated: depressed-clad, matched-clad, and one having a large mode-field diameter (not typical of commercial production). Various reflectors (i.e. cleaves) were characterised for each fiber by both coupler and OTDR methods. Then the fiber backscattering level B was determined by adding the ORL from coupler Equation (2) to the logarithmic term of OTDR Equation (3). Table 2 shows the B values for each fiber type.

Fiber Type	ORL (dB) by coupler	Backscatter B (dB)				
		Wide Pulse		Narrow Pulse		
		FDHM	energy/power	FDHM	energy/power	
matched-clad	14.4	79.3	80.0	78.9	80.0	*
	25.7	80.2	80.9	79.7	80.9	
	35.1	80.5	81.2	79.6	80.7	
depressed-clad	14.3	78.0	78.7	77.7	78.8	*
	23.3	79.0	79.7	78.6	79.7	
large mode diameter	14.7	80.0	80.7	79.5	80.6	
	21.9	80.6	81.3	80.2	81.3	#

* average of 3 similar cleaves, # average of 2 similar cleaves

Table 2 - ORL and backcsatter values for several types of fiber and cleave

Note that for a particular fiber, the wide and narrow pulses give similar B values if the duration is defined by pulse energy over pulse peak power. Values obtained with high reflections (low ORLs) are slightly higher for reasons not fully understood. Note also that B values can differ by up to 2 dB between fiber types.

Conclusions

We have shown that the OTDR can reliably measure return loss if care is taken in obtaining reflected pulse parameters. Moreover, just as fiber group index needs to be known for accurate distance measurements, it has been demonstrated that fiber backscatter level needs to be known for accurate return loss measurements.

For purposes of ORL determination, we offer these suggestions for consideration by OTDR manufacturers:

- Specify the pulse duration by the ratio of pulse energy to pulse peak power, rather than by only the FDHM.
- Minimize the recovery tails of reflection pulses.
- Introduce an anti-clipping capability (e.g. variable attenuation) for reflected pulses.

Acknowledgements

The authors wish to express appreciation for valuable discussions with William W. Wood, G. Shinn, and William C. Young.

References

[1] S.Wang, D.Burpee, & L.Jou, submitted to Electron. Lett.
[2] M.Choy, J.Gimlett, R.Welter, L.Kazovsky, & N.Cheung, Electron. Lett., v. 23, p. 1151 (1987)
[3] Bellcore Technical Reference TR-TSY-000326 (1987)
[4] EIA FOTP-107
[5] A.Judy & H.Neysmith, Fib. & Int. Opt., v. 7, p. 17 (1988)
[6] V.So, J.Lamont, & P.Vella, IEEE J. Sel. Area Comm., v. SAC-4, p. 737 (1986)
[7] This improves upon a result in [5].
[8] A.Hartog & M.Gold, J. Lightwave Tech., v. LT-2, p. 76 (1984)
[9] G.Shinn, Proc. EFOC/LAN 87, p. 151 (1987)

RETURN LOSS STUDIES OF A SINGLE-ENDED SINGLE-MODE FIBER: EFFECT OF THE NONFLAT FIBER ENDFACE

V. Shah, W. C. Young, and L. Curtis
Bellcore
331 Newman Springs Road
Red Bank, NJ 07701-7020
(201)-758-3156

INTRODUCTION :

In optical fiber systems, optical feedback from reflections caused by index discontinuities such as connectors and splices can generate intensity noise in lasers,[1] or interferometrically convert the intrinsic phase noise of lasers into high levels of intensity noise.[2] Both of these effects can adversely affect the performance of direct detection and/or coherent lightwave systems.

When an index matching oil is used, improvement in the return loss value is limited due to the presence of the polishing induced high-index region at the fiber endface.[3] However, it is theoretically known[4] that by tilting the fiber endface at an angle α with respect to a plane perpendicular to the fiber axis, the amount of reflected power coupled to the fundamental mode of the single-mode fiber can be reduced by several orders of magnitude (for α as low as five degrees). This results in very high return loss and improves the system performance. Such a technique was recently used[5] in multiple single-mode fiber splices to achieve high return losses without adversely affecting the insertion loss performance. During the course of that investigation it was observed that return losses of a single-ended single-mode fiber, measured as a function of the tilt angle α, increased much less rapidly than predicted by the theory,[4] particularly for values of $\alpha > 5$ degrees. In this range of α, it was occasionally observed that, instead of increasing, return loss values either did not change or in fact decreased when a larger tilt angle was polished. These observations indicate that even though the return loss performance improves by increasing α above 5 degrees, the improvement is not as significantly large as predicted.[4]

The theoretical values in the previous work were obtained by treating the return loss in terms of the coupling loss between two angularly misaligned gaussian beams assuming flat fiber endfaces. In this paper, we show that experimental results discussed above can be explained by extending the theoretical model to account for the polishing-induced departure from flatness of the fiber endface. The results show that even a small departure from flatness can have a large impact on the return loss performance. In addition, it shows the importance of optimum polishing and of proper wetting of the endface with index matching oil in obtaining good return loss performance.

EXPERIMENT :

Return loss measurements were made with a 1540 nm wavelength laser and a fused biconical coupler. A short ($\approx$ 1 m) length of fiber was fusion spliced at one output end of the coupler while the other output end was terminated by polishing a 14 degree tilt angle on the endface and immersing it in an index

matching oil. Because of the presence of the polishing induced high-index region at the fiber endface,[3] an oil with n = 1.6 was used. Fig. 1 shows the measured values (o) of the return loss plotted as a function of the tilt angle on the endface of the 1 m length of fiber. The solid curve represents the theoretical values computed using Gaussian theory.[4] It can be seen from Fig. 1 that the measured values differ considerably from the theoretical values both for small and large tilt angles. We note that the solid curve was obtained by assuming a perfectly smooth and flat endface. However, due to the differences between the hardness of the core and the cladding material, polishing of the endface usually results in a depression in the core region as shown in Fig. 2a. The high-index region present at the endface is modeled as shown by the dashed line in Fig. 2a which represents the interface between the bulk material and high index region. The refractive index of this region is assumed to be uniform. When index matching oil is used to match the high index region, only the interface between the bulk material and high index layer remains as shown in Fig. 2b.

THEORY :

In deriving the expression for power coupled in the fundamental mode due to reflections, we have used the model in Fig. 2b. In addition to assumptions made above, we assume that : (1) The fundamental mode has a Gaussian distribution with mode field diameter 2w, (2) That α is assumed to be small and, therefore, simple Fresnel formula for normal incidence is used. Thus, with n_c and n_g denoting refractive indices of the core and the oil, respectively, the power reflection coefficient $R_0 = [(n_g - n_c)/(n_g + n_c)]^2$, (3) The depth of depression d_0 is small compared to the core diameter 2a, (4) The depression is assumed to be spherical. The radius R of the sphere depends on d_0 and is given by: $R = (a^2+d_0^2)/(2d_0)$, and (5) The cladding portion of the endface is assumed to be flat. With these assumptions, the field coupling coefficient C_0 for the fundamental mode is given by:

$$C_0 = 4\frac{\sqrt{R_0}}{w^2}\left(e^{-i2kn_c g(a)}\int_0^a f(r)e^{i2kn_c g(r)}\,dr - \int_0^a f(r)\,dr + \frac{w^2}{4}\exp(-\{kn_c w\tan\alpha\}^2/2)\right) \qquad (1)$$

where $f(r) = r\exp(-2r^2/w^2)\,J_0(2kn_c r\alpha)$, and $g(x) = (R^2 - x^2)^{1/2}$. The return loss RL (in dB) is obtained as

$$RL = -10\log\left(\left|C_0\right|^2\right) \qquad (2)$$

Fig. 3 shows the plot of RL as a function of α, with the solid curve from Fig. 1 repeated as curve A. Curves B and C corresponding to d_0 = 0.05 and 0.1 micron, respectively, show the effect of the very small departure from the flatness of the fiber endface and were obtained by using Eqs. (1) and (2). The crosses (x) represent the experimental values. Even though the simple model of Fig. 2b does not correspond to the measurement conditions in all details because of the various assumptions discussed above, good agreement between the measured values and our model is obtained when one notes that d_0 may have different values each time the endface is polished. The essential features of the experimental observations are also closely predicted by our model which is therefore expected to play an important role

in providing valuable insights in optimizing high performance joints.

CONCLUSION:

In conclusion, even a very small polishing-induced departure from the flatness of the fiber endface results in a much less rapid increase in return loss with increasing endface tilt angle compared to that obtained with the flat fiber endface. The values of return losses as a function of endface tilt angle are in good agreement with a nonflat endface model, thus indicating that the polishing-induced nonflatness of the fiber endface plays a significant role in obtaining optimum return loss performance by tilting the fiber endface.

REFERENCES:

[1] O. Hirota, Y. Suematsu, and K. S. Kwok, IEEE J. Quanttum Electron., QE-17, 1014 (1980).

[2] M. M. Choy, J. L. Gimlett, R. Welter, L. G. Kazovsky, and N. K. Cheung, Electron. Lett. 23, 1151 (1987).

[3] V. Shah, W. C. Young, and L. Curtis, OFC/IOOC'87, TUF4, (1987)

[4] D. Marcuse, Bell Syst. Tech. J. Vol. 56, 703 (1977)

[5] W. C. Young, V. S. Shah, L. Curtis, submitted to Electon. Lett.

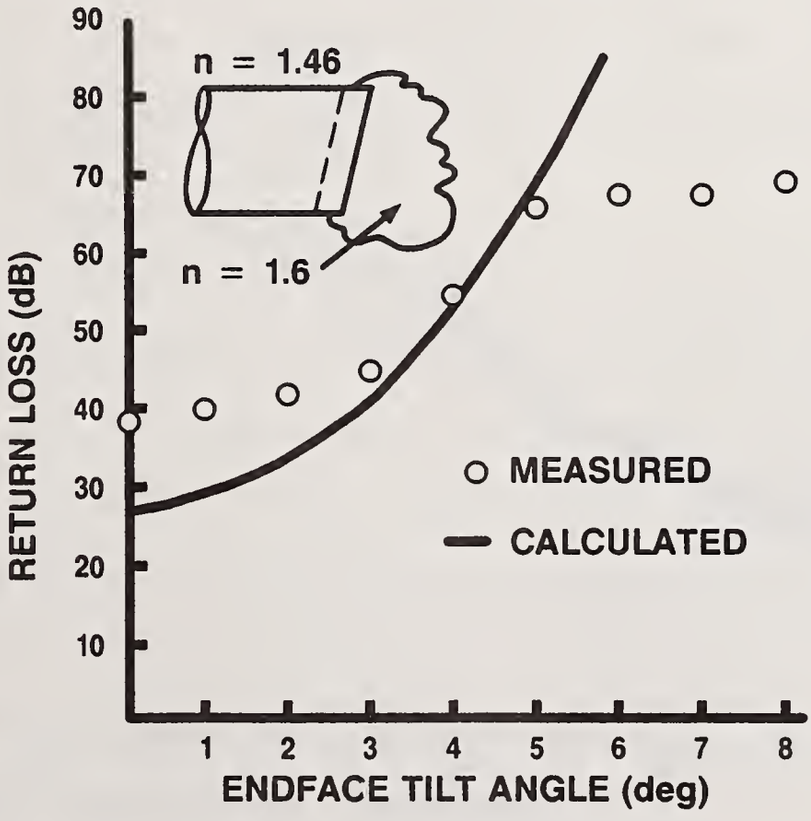

Fig. 1 Return loss for a single-ended single-mode fiber plotted as a function of the tilt angle. The endface is immersed in an oil with n = 1.6. Calculated values are obtained by assuming the endface to be flat.

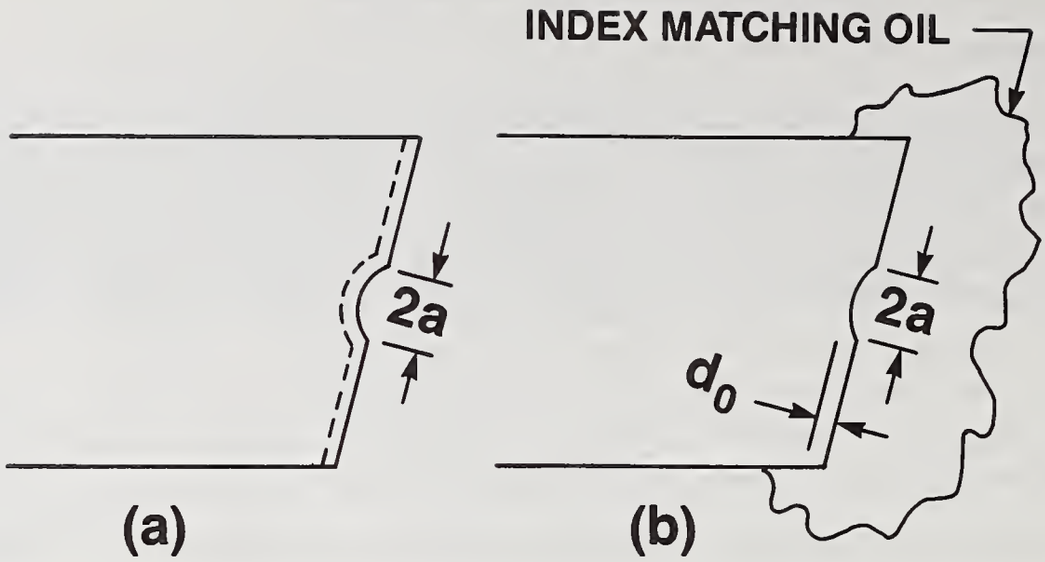

Fig. 2 (a) Fiber endface model with the high-index region at the endface. (b) Fiber endface model with an index matching oil used to match the high-index region.

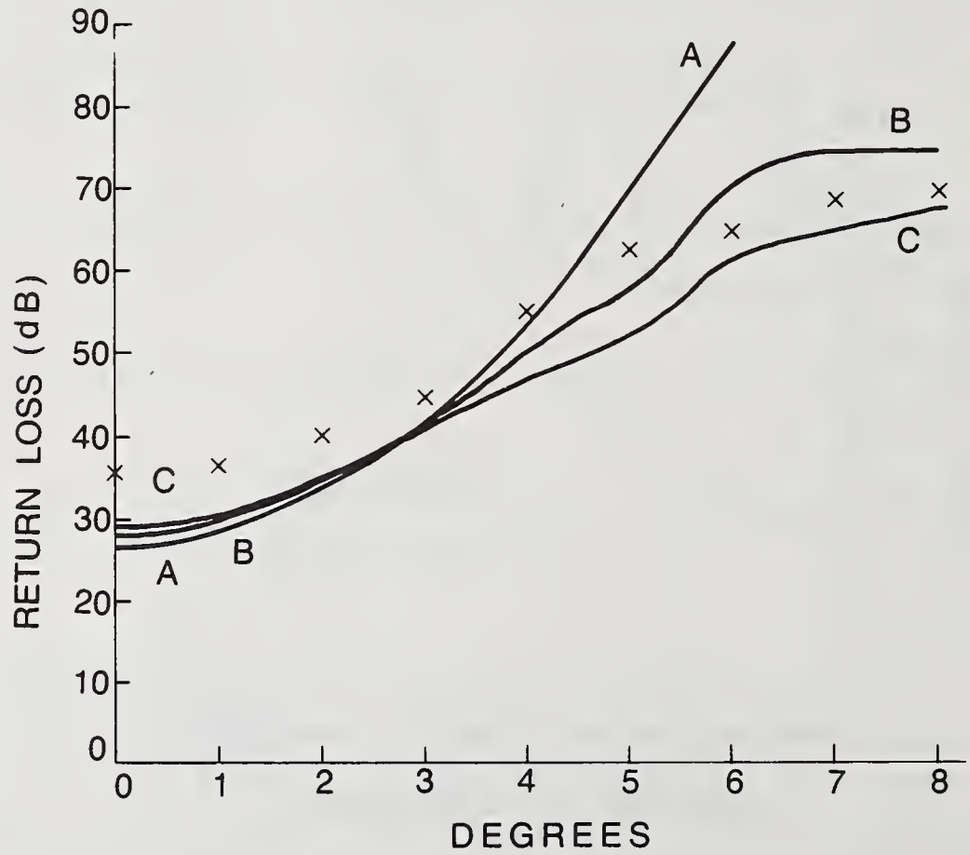

Fig. 3 Return loss plotted as a function of the tilt angle. Curve A is the solid curve of Fig. 1. Curves B and C correspond to d_0 = 0.05 and 0.1 micron, respectively, and are obtained by using Eqs. (1) and (2) in the text.

Optical Fiber Up-Taper Backreflector for Laser Transmitter Evaluation

Alan F. Benner, Daniel A. Fishman*, Herman M. Presby
AT&T Bell Laboratories
Crawford Hill Laboratory
Holmdel, New Jersey 07733

*AT&T Bell Laboratories
Holmdel, New Jersey 07733

INTRODUCTION

As optical communications systems progress to higher data rates, reflection effects become increasingly detrimental to system performance. Reflections cause two types of system degradation. First, optical feedback into the laser cavity causes amplitude and phase fluctuations, introducing errors in the transmitted bit stream. Second, when more than one reflection point exists in a system, doubly reflected light interferes at the receiver with unreflected light, causing interference between different time slots in the bit stream. Thus multi-path interference (MPI) has been shown to cause data-dependent error bursts and bit-error-rate floors and is unaffected by laser isolation.

In order to directly evaluate laser feedback effects, we have constructed a variable back-reflector capable of producing uni-directional optical feedback in the range -16.9 to -50 dB, without introducing observable MPI effects. The device utilizes optical fiber up-tapers (Fig. 1) to reduce reflection levels in the apparatus to below -50 dB, and an in-line optical isolator to eliminate spurious system reflections. We have made measurements using this apparatus on optical feedback effects for various multi-longitudinal-mode laser chips operating at 1.7 Gb/s.

EXPERIMENTAL ARRANGEMENT

The experimental apparatus is shown in Fig. 2. Elimination of secondary reflections was made possible by the use of an in-line optical isolator and optical fiber

up-tapers with beveled end-faces[2].

Optical fiber up-tapers (Fig. 1) achieve single-mode beam expansion by a gradual increase in the fiber cross-section, allowing adiabatic conversion of the single-mode fiber power into the (larger) fundamental mode of the expanded cylindrical section. Up-tapers can expand the standard fiber mode diameter of 9 μm up to 50 or 100 μm. The up-tapers used in this experiment had 55 μm mode diameters. Beam expansion results in greater collimation of the emitted beam, relative to SM fiber, and allows insertion of components between the tapers with minimal additional insertion loss ($<$3 dB in this case). In addition, the common technique of beveling a fiber termination to increase the return loss has a much greater effect for up-tapers than for SM fibers, due to the expanded mode size[3], and the 3° bevel angle used here yielded a return loss $>$50 dB.

The laser chip is coupled to the input up-taper using a microlens on the fiber pigtail. A variable beamsplitter and variable attenuator produce the optical feedback into the laser chip in the range -16.8 to -50 dB relative to the laser facet power level. The mirror is mounted on a piezoelectric translator allowing 30 μm travel, to adjust reflected phase. A multi-mode fiber at the fourth port of the beamsplitter leads to a PIN photodiode, allowing real-time measurement of the relative feedback power and RF spectrum. Light collected at the receiving up-taper is passed through the isolator and then through either a 6m length of 5D fiber jumper or through 3.1 km of dispersion-shifted fiber before reaching a PIN diode direct-detection receiver. A microcomputer interfaced with a BER test set is used to measure laser transmitter performance under various reflection levels.

RESULTS

A sample BER measurement, made for a 1.3 micron multi-mode laser is shown in Fig. 3. BER curves with and without 3.1 km of dispersion-shifted fiber, with and without -16.8 dB feedback are shown. Intentional misalignment of up-tapers showed no modal noise effects. With feedback and no dispersion, the laser transmitter shows $\sim$1.5 dB power penalty, with little excess curvature. With dispersion added, the BER curve is drastically degraded, showing an error floor at 10^{-8} BER. Varying the reflected phase had no effect on BER results.

CONCLUSION

We have constructed a variable back-reflector which allows measurements of the effects of optical feedback on a semiconductor laser, without introducing multi-path interference effects. Optical fiber up-tapers greatly simplify alignment of the apparatus, and allow very low reflection levels to be achieved more easily than with standard SM fiber. This apparatus is the first use of up-tapers in transmission experiments, and demonstrates the capability of up-tapers for reducing reflections in optical fiber systems.

REFERENCES

1. J. L. Gimblett, J. Young, R. E. Spicer, N. K. Cheung, "Degradations in Gbit/s DFB Laser Transmission Systems Due to Phase-to-Intensity Noise Conversion by Multiple Reflection Points", Electron. Lett., 1988, *24*, pp. 406-408.
2. H. M. Presby, N. Amitay, A. Benner "Straight-Tip Optical Fiber Up-Tapers for Single-Mode Hardware Applications", Electron. Lett., 1988, *24*, pp. 34-35.
3. A. Benner, H. M. Presby, N. Amitay, "Low-Reflectivity In-Line Variable Attenuator Utilizing Optical Fiber Up-Tapers", submitted to J. Lightwave Technology.

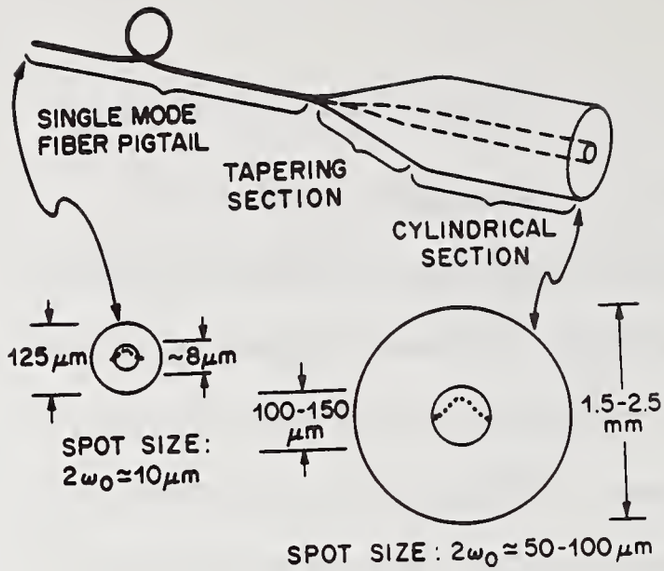

FIGURE 1 OPTICAL FIBER TAPERS

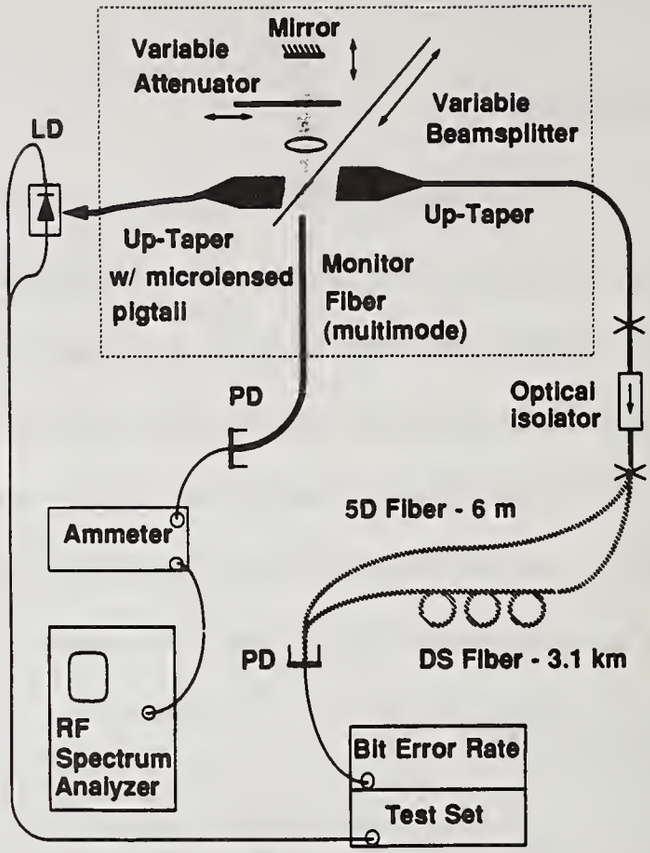

Fig. 2 Experimental Arrangement

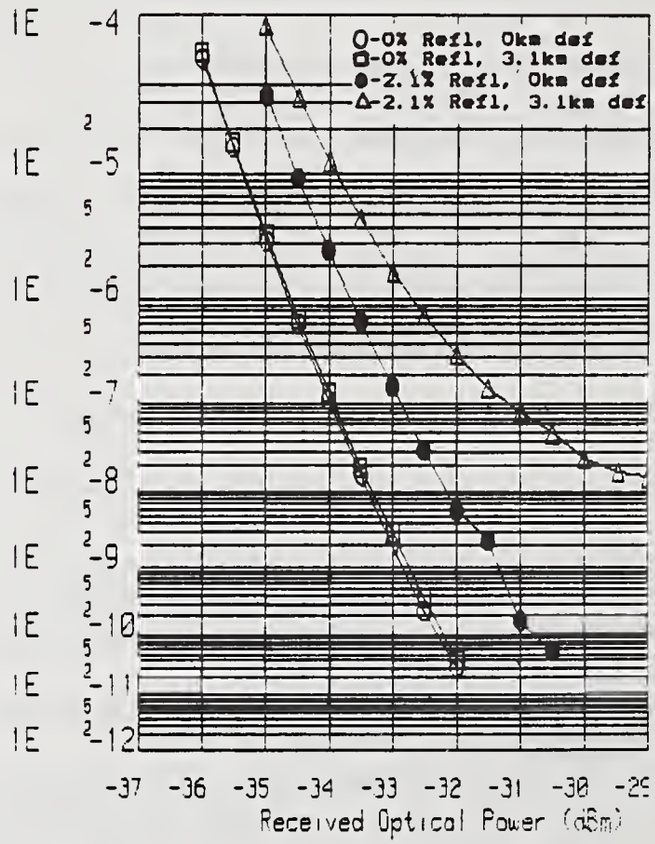

Fig. 3 Multi-mode 1.3 μm laser, with and without dispersion and reflection

Measurements of Polarization Mode Dispersion in Optical Fibers

Craig D. Poole

AT&T Bell Laboratories
Crawford Hill Laboratory
Holmdel, New Jersey 07733

The need for accurate measurements of polarization mode dispersion (PMD) in single-mode fibers has been enhanced in recent years by the emergence of ultra-high bit rate lightwave systems. To date, the vast majority of PMD measurements have been made in short fibers. While such measurements have provided important information on intrinsic fiber properties, it has been known for some time that in long fibers (i.e. > 100 meters) extrinsic factors, such as external perturbations created in spooling or cabling, can have a profound impact on the dispersion through random mode coupling [1]. Until recently, the scarcity of data in long fibers could be largely attributed to the lack of a practical model. The purpose of this paper is to review recent measurements of PMD in long fibers using a recently developed phenomenological model. With this model the effects of PMD, both in the frequency domain and in the time domain, can be characterized in fibers of arbitrary length.

Historically, modal dispersion in multimode waveguides with random perturbations has been treated using the coupled-power model in which the temporal response in optical power of a waveguide is determined by considering the average distribution of power among modes. For PMD this approach is impractical because source coherence times are often comparable to or larger than the differential propagation delay times involved. Under these conditions the transmission properties of a fiber become very sensitive to the source frequency and to environmental conditions (e.g. ambient temperature) through coherent

interference in the mode coupling process. Thus the coupled-power model, which neglects the phase of the mode fields, can only predict the average behavior of an ensemble of fibers (or equivalently, the behavior of an individual fiber averaged over source wavelength and environmental conditions).

Recently, a model of PMD for highly coherent sources was proposed in which the dispersion in a fiber is described in terms of a differential delay time $\Delta\tau$ associated with two orthogonal input principal states of polarization [2],[3]. This description comes about as the first order term in a frequency expansion of the transmission matrix of a fiber about the source center frequency and, in the case of significant mode coupling, is restricted to the regime of source spectral width $\delta\nu$ given by $|\Delta\tau|\delta\nu << 1$. In the absence of mode coupling, the principal states are aligned with the polarization modes of the fiber and the differential delay time is simply the differential group delay time for the modes. In the presence of random mode coupling, however, the principal states and differential delay time are no longer correlated with local fiber properties and can not be known *a priori* since they depend on the details of the mode coupling. Furthermore, both become sensitive to the source wavelength and to the fiber environment.

Since the principal states model can be viewed as a generalization of the eigenmode picture in short fibers, many of the same measurement techniques that have been used to measure modal group delay times in short fibers can be applied to the measurement of $\Delta\tau$ in long fibers. One approach that has been used in several recent experiments is to make measurements in the frequency domain [4]-[7]. In the frequency domain, PMD manifests itself as a frequency or wavelength dependence in the state of polarization at the output of a fiber. This takes the form of a frequency dependent rotation of the output polarization on the Poincare sphere, where the angular rate of rotation is exactly equal to the differential delay time $\Delta\tau$. Figure 1 shows the rotation of the polarization at the output of a 147 km undersea

cable for three different launch conditions [7]. Note that the direction and magnitude of the rotation is independent of the input polarization. The data is obtained by temperature tuning the output of a DFB laser over an 18 GHz interval. While the frequency is being swept, the state of polarization at the output of the cable is measured in real time using an electro-optic polarimeter. Figure 2 shows the differential delay time between the principal states as a function of wavelength for the four fibers in the cable. The curves are generated by determining the rate of rotation of the polarization at each wavelength. Significant variation of the delay time over the 10 Å interval can be seen in the upper curves. The estimated accuracy in this particular experiment is limited by the DFB laser temperature monitor to $\sim \pm$ 10%.

The most obvious and direct approach to measuring PMD is to make time domain measurements. Figure 3 shows the results of recent measurements of pulse propagation in 10 km of dispersion-shifted fiber [3]. Three output pulses are shown corresponding to the input pulses having polarizations aligned with the two principal states (solid curves labeled $\hat{e}_{\pm}$) and with the input split equally between these states (dashed curve). A time shift of $\sim$ 40 psec between the the principal states is clearly seen. The intermediate waveform shows the expected broadening of $\sim$ 4% (indicated by a slightly lower peak). In this experiment, there is clear evidence that mode coupling plays a significant role in the dispersion. This is indicated by a slow drift in both the principal states and the differential delay time. Figure 4 shows the change in the differential delay time over a twenty-four hour period. More than a factor of two change is observed and can be attributed to small changes in ambient temperature.

As the data in Figure 4 illustrates, PMD in the case of highly coherent sources ultimately requires a statistical treatment. For example, for a population of statistically equivalent fiber, the rms value of the differential delay time is given by [8] $\sigma_{\Delta\tau} = \sqrt{\langle \Delta\tau^2 \rangle} = \frac{\Delta\beta'}{\sqrt{2}\,h}(e^{-2hL} - 1 + 2hL)^{1/2}$ where $\Delta\beta' = \frac{d}{d\omega}(\beta_x - \beta_y)$ is the differential

group delay time between polarization modes, L is the fiber length, and h is the well known h-parameter that characterizes the coupling between modes due to random perturbations. The symbols < > indicate an average over the ensemble of fibers. At short lengths the dispersion reduces to the differential group delay time between the modes, $\lim_{hL \to 0} \sigma_{\Delta\tau} = \Delta\beta' L$, and at long lengths exhibits the expected square root of length dependence, $\lim_{hL \to \infty} \sigma_{\Delta\tau} = \Delta\beta' \sqrt{L/h}$. Random mode coupling therefore has the effect in long fibers of reducing the dispersion by a factor of $\sqrt{hL}$ relative to the no mode coupling case. It has also been shown that the probability density function for $\Delta\tau$ approaches a Gaussian shape at long lengths [8].

Under the usual assumption of ergodicity, measurement of $\sigma_{\Delta\tau}$ or alternatively $<|\Delta\tau|>$ can be accomplished by averaging measurements over some physical parameter such as temperature or source wavelength. In other words one assumes that $<|\Delta\tau|>_{ensemble} = <|\Delta\tau|>_T = <|\Delta\tau|>_\lambda$. Figure 5 shows the apparatus used recently to measure the length dependence of $<|\Delta\tau|>$ in conventional single-mode fiber [9]. Measurements are made by scanning the wavelength of the source between 1.2 and 1.6 μm while monitoring the power transmitted through an analyzer positioned at the output of the test fiber. The oscillations in the transmitted power reflect the rotation of the polarization and are used to determine the dispersion over a broad wavelength interval. Figure 6 shows the results of cut-back measurements made on two pieces of fiber taken from a single spool. To determine the effect of external perturbations, one of the pieces is wound on a conventional 15 cm diameter spool (open circles) while the other is wound at low tension in a single layer on a 28 cm diameter drum (solid points). Each data point represents the average of $|\Delta\tau|$ over the wavelength interval 1.2 -1.6 μm. A theoretical fit is performed for each set of data using the values of h-parameter shown and the measured modal group delay time of 2.8 psec/km. The importance of external perturbations is demonstrated by the more than order of magnitude difference between the data on the drum and that on the spool (two orders of magnitude in

the h parameter). The transition from linear to square root dependence in the length is clearly seen in the drum data while the spool data exhibits a square root dependence down to the shortest length due to the much greater mode coupling.

In conclusion, PMD in long fibers is sensitive to such variables as source spectrum, mechanical perturbations on the fiber, and environmental conditions (e.g. ambient temperature). All of these factors need to be considered when making measurements. A statistical treatment of the dispersion based on the ensemble average of the differential delay time between principal states is one approach to obtaining a meaningful characterization of the dispersion that is both measurable and relevant to lightwave system penalties.

REFERENCES

[1] K. Mochizuki, Y. Namihira, and H. Wakabayashi, Electron. Lett. 17, 153 (1981)

[2] C. D. Poole and R. E. Wagner, Electron. Lett., 22, 1029 (1986).

[3] C. D. Poole and C. R. Giles, Opt. Lett. 13, 155 (1988)

[4] N. S. Bergano, C. D. Poole, R. E. Wagner, IEEE J. Lightwave Technol. LT-5, 1618 (1987).

[5] D. Andresciani, F. Curti, F. Matera, and B. Daino, Opt. Lett. 12, 844 (1987)

[6] M. Tsubokawa and Y. Sasaki, Electron. Lett. 24, 350 (1988)

[7] C. D. Poole, N. S. Bergano, R. E. Wagner, and H. J. Schulte, IEEE J. Lightwave Technol. LT-6, 1184 (1988)

[8] C. D. Poole, Optics Lett. 13, August Issue (1988)

[9] C. D. Poole, Submitted to Optics Lett.

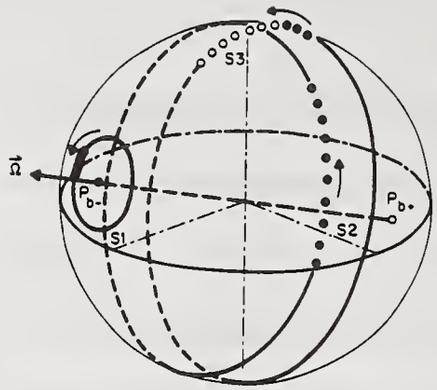

Fig. 1. Frequency dependent polarization out of 147 km cable.

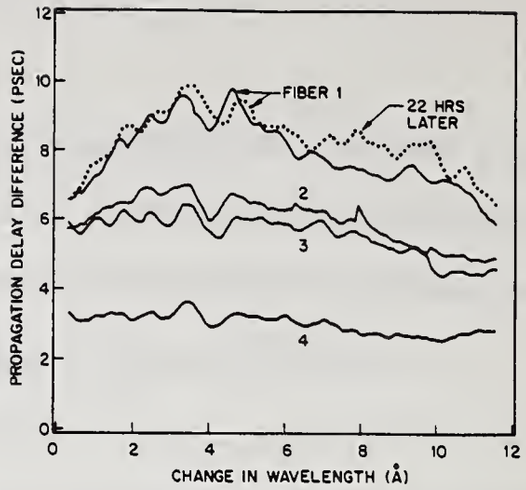

Fig. 2. Differential delay time for four fibers in 147 km cable.

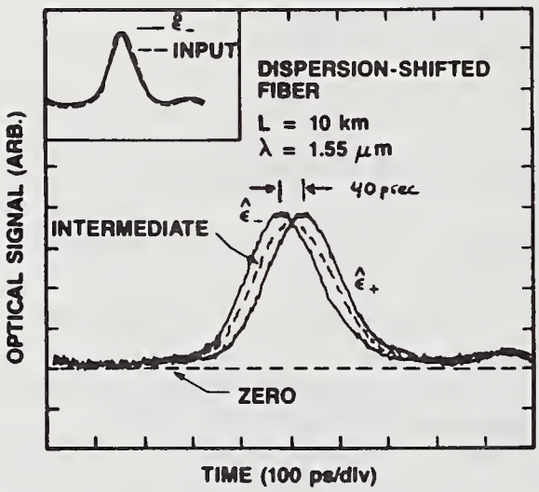

Fig. 3. Pulses transmitted through 10 km of dispersion-shifted fiber.

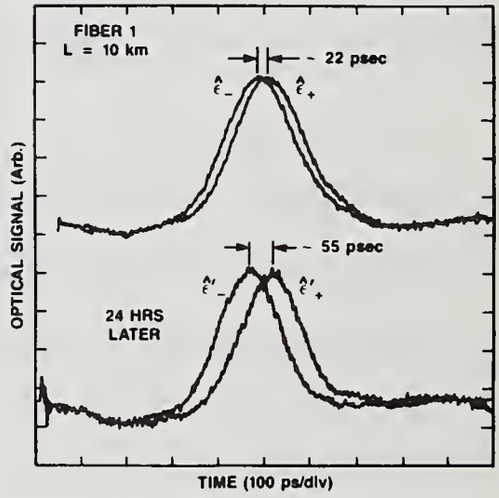

Fig. 4. Drift of differential delay time over 24 hours.

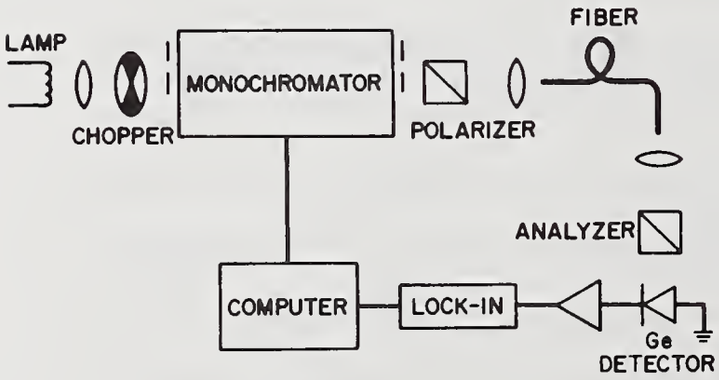

Fig. 5. Set-up for measuring polarization dispersion.

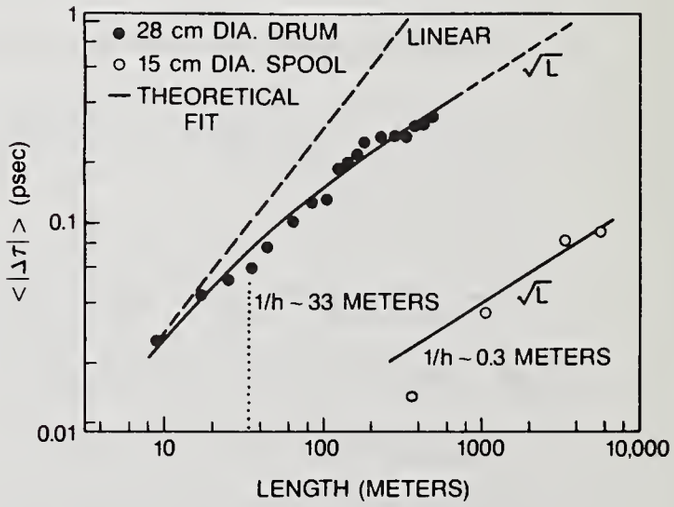

Fig. 6. Length dependence of dispersion.

HETERODYNE FIBER POLARIMETRY WITH STOKES PARAMETER DETECTION

R. Calvani, R. Caponi, F. Cisternino

CSELT - Via Reiss Romoli 274 - 10148 Torino - Italy

Abstract

A novel heterodyne polarimeter for Stokes parameter measurement is demonstrated. A two parameter output, tested with a known polarization phase input, gives expected results. A precise beat-length measurement on a high birefringence fiber is performed.

Introduction

Heterodyne polarimetry is a recent measurement method particularly suitable for a fast detection of the state of polarization (SOP) of the light at the output of an optical fiber [1]. The inherent principle is the same as in coherent transmissions, where the optical information carrier is scaled into the radio-frequency (RF) range through a beating with a radiation at a slightly different frequency (local oscillator). This techique, applied to both components E_x, E_y of an optical coherent field, provides two electrical RF signals which reproduce phase ϕ and amplitude ratio R of the SOP to be measured. In a more general case, when depolarization phenomena occur (for example in polarization crosstalk measurements on long fiber spans), E_x and E_y are no more sufficient to identify the SOP, which requires the four independent Stokes parameters s_0, s_1, s_2, s_3.

To this end, the proposed heterodyne polarimeter has been developed to provide directly at the output (with analog electrical processing) the aforesaid parameters. In the present paper, first experimental results of this novel instrument version concerning s_2, s_3 are discussed. A test with an external stress apparatus on a polarization maintaining fibre has given highly precise measurements of the submillimeter beat-length.

The Stokes polarimeter, being a device suitable for a complete characterization

of the statical and dynamical polarization behaviour of single-mode fibers, can be usefully applied in advanced research areas, such as coherent communications and optical sensors [2].

Measurement principle and experimental implementation

In heterodyne polarimetry, two RF signals are obtained from the beating of a reference field (linearly polarized at 45°) with the two measurand E_x, E_y [1]

(1) $$S_x \propto E_{0x} \cos(\Omega t) \quad S_y \propto E_{0y} \cos(\Omega t - \phi)$$

where ϕ is the polarization phase. In the present system, the reference beam is derived from the same source, in a conventional interferometric setup (Mach-Zehender configuration), where an acousto-optic device introduces the frequency shift Ω (Fig. 1).

At this point, simply by mixing the electrical signals S_x, S_y (and filtering the 2Ω component), one obtains a quantity proportional to s_2 parameter; s_3 can be derived the same way, delaying either of the two RF's by 90°

(2) $$s_2 = 2 E_{0x} E_{0y} \cos\phi \quad s_3 = 2 E_{0x} E_{0y} \sin\phi$$

For the s parameter a different processing of S_x, S_y is required; the two RF's are separately square low detected and finally subtracted

(3) $$s_1 = E_{0x}^2 - E_{0y}^2$$

This kind of signal treatement has already found interesting applications in the coherent communication systems which use polarization modulation as information coding [3,4].

On the other hand, the s energy parameter has to be obtained by a radiometric measurement. The polarized energy $(s_1^2+s_2^2+s_3^2)$ is given by the sum of the two square law detected outputs $(S_x^2+S_y^2)$ and its ratio with respect to the total energy provides the polarization degree.

To test the effectiveness of the proposed method, the scheme of Fig. 1 has been chosen. The source is a single frequency He-Ne laser; the fiber is polarization maintaining (bow tie), with 513 nm cutoff wavelength, fabricated

by York Technologies. A stress applying device for fiber measurement is also added.

Results and discussion

A first test on this heterodyne polarimeter has been performed by using the two output signals S_x, S_y in a conventional way, i.e. by sending the two RF beatings to an x-y oscilloscope, in order to visualize directly a known SOP ellipse (Fig. 2). This way is also possible to calibrate the instrument, compensating for spurious birefringences of optical components [1].

The new electrical processing scheme, in terms of s_2, s_3 parameters, has been checked using a known SOP phase modulation (180° depth), provided by a Pockels cell placed on the measurement arm. The resulting curve on s_2, s_3 plane has been visualized on the x-y oscilloscope (in this case the output signals oscillate at the SOP modulation frequency, because the RF's are subtracted at the mixers). Because of the 180° phase modulation, the resulting curve is an half circumference, as espected (Fig. 3).

The fiber measurement (beat-length L_B) has been performed by scanning a short fiber span with the movable stress device, which heavily modifies the local SOP. The output signal periodicity on either of s_2, s_3 parameters gives the L_B value [1]. From the measured data (Fig. 4), the averaged L_B is 0.94 mm in excellent agreement (1%) with the value measured at the factory. The possibility of choosing between different Stokes parameters, provided by this instrument, makes this measurement independent of the SOP at the fiber input (so avoiding the search of the eigenaxes).

References

[1] R. Calvani, R. Caponi, F. Cisternino, G. Coppa, JLT, LT-5, 1176 (1987).

[2] B. Culshaw, Optical Fiber Sensing and Signal Processing, London, 1984.

[3] R. Calvani, R. Caponi, F. Cisternino, El. Lett., to be published.

[4] E. Dietrich, B. Enning, R. Gross, H. Knupke, El. Lett., 23, 421 (1987).

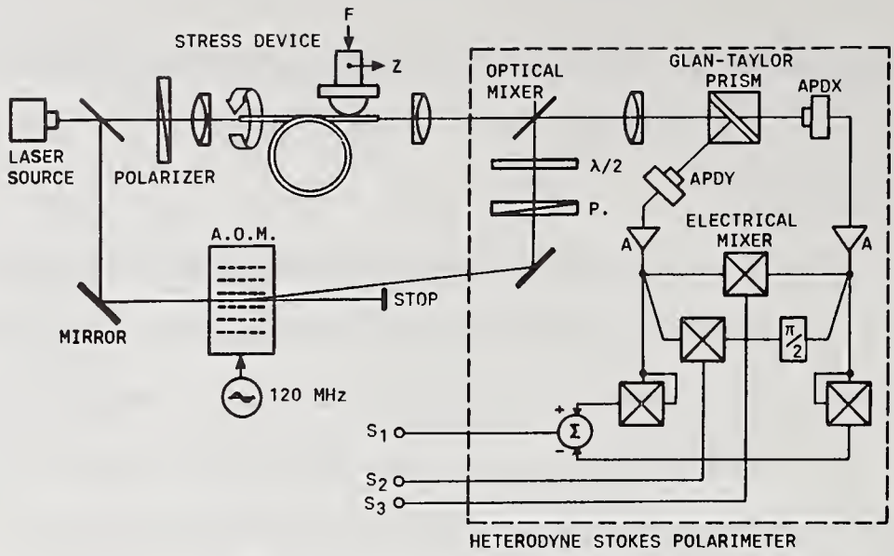

Fig. 1 - Experimental setup for the Stokes polarimeter

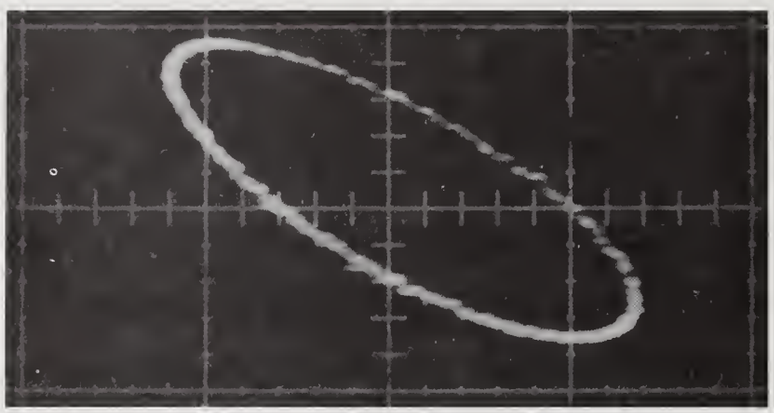

Fig. 2 - x-y visualization of an output SOP ellipse

Fig. 3 - Display on s_2, s_3 Stokes parameter plane with a 180° polarization phase modulation

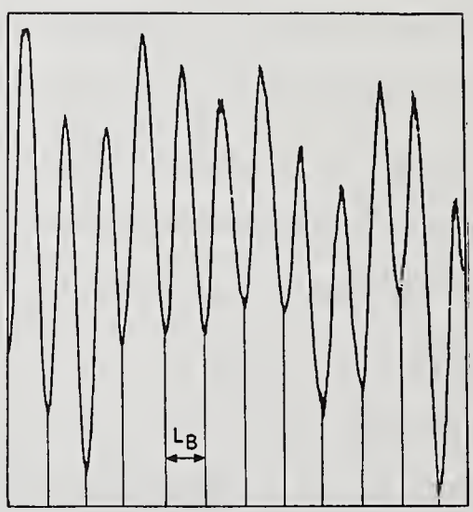

Fig. 4 - Experimental data of s_2 Stokes parameter versus axial scanning

COMPLETE BIREFRINGENCE CHARACTERISATION OF LITHIUM NIOBATE INTEGRATED OPTIC POLARISATION CONTROLLERS

G R Walker, N G Walker

British Telecom Research Laboratories

Martlesham Heath, Ipswich IP5 7RE, United Kingdom

Abstract: A computer-controlled system for the measurement of birefringence is described. Results are presented from a study of a novel lithium niobate polarisation controller.

Introduction: Many optical devices are polarisation dependent, and a means of readily characterising their birefringence is needed. A specific example is polarisation controllers, which are important components for coherent optical transmission systems and certain optical fibre sensors. Various lithium niobate waveguide polarisation controllers have been proposed and fabricated, but assessment of their performance has typically been limited to measurement of conversion efficiency by power measurements along specific axes [1,2,3]. This may be sufficient for simple structures and applications, but more detailed characterisation of device performance is clearly desirable. This paper describes a novel approach which gives a complete birefringence characterisation, and which has been successfully applied to two lithium niobate device structures [4,5].

Experimental Arrangement: The system for measuring birefringence is shown in figure 1. Linearly polarised light passes through a half-wave plate, which rotates to allow any linear state of polarisation (SOP) to be launched into the device being characterised. The resulting output SOP is measured using a rotating quarter-wave plate polarimeter [6]. Represented on the Poincaré sphere, the device birefringence corresponds to a rotation about the birefringence axis through an angle given by the magnitude of birefringence [6]. Measurement of the output SOPs for at least two different known input SOPs enables this birefringence to be calculated, although four launch states are used in practice to give some averaging. Since any rotation of magnitude 2π radians leaves all SOPs on the Poincaré sphere unchanged, the magnitude of the birefringence can only be measured modulo 2π. However, by assuming that the birefringence is a continuous function of the device control voltages, this $\pm 2\pi$ ambiguity can be resolved, and the device birefringence is then completely characterised.

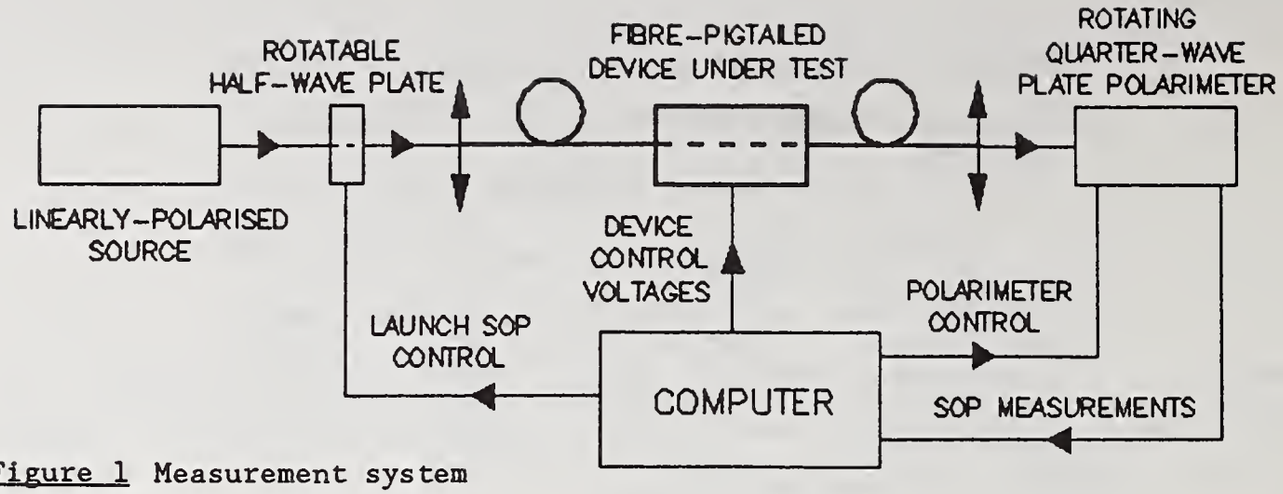

Figure 1 Measurement system

The technique can also be used if there is a fixed birefringence between the generated launch states and the device to be characterised, and/or between the device and the polarimeter, as would be the case for a fibre pigtailed device, or an electrooptic device with sections of waveguide extending beyond the electrode pattern. It is possible to compensate for these unwanted rotations by referencing the measured output states to the output SOPs observed for the condition of zero birefringence of the device under test. When using this approach, any error in determining the zero of the birefringence of the device will cause large errors in the calculated birefringence axis orientation for birefringence angles close to 2π, 4π and so on. This problem is avoided by presenting the data as birefringence vectors with length equal to the sine of half the birefringence angle, an approach which may also be significant in assessing the control capabilities of the device.

Results: A novel lithium niobate integrated optic polarisation controller has been thoroughly characterised using the arrangement described above. The operation of the device has been reported in detail elsewhere [4]. In outline it is expected to give a birefringence vector of variable magnitude which can be rotated in the equatorial plane of the Poincaré sphere. A scan of 1,600 birefringence measurements takes about an hour, and the results obtained for a typical waveguide are shown in figure 2(a). The four surfaces are the three components of the birefringence vectors with length equal to the sine of half the birefringence angle, and the cosine of half the birefringence angle, plotted as functions of the two electrode control voltages. Figure 2(b) shows the corresponding results from a computer simulation of an "ideal" device. There is remarkable agreement

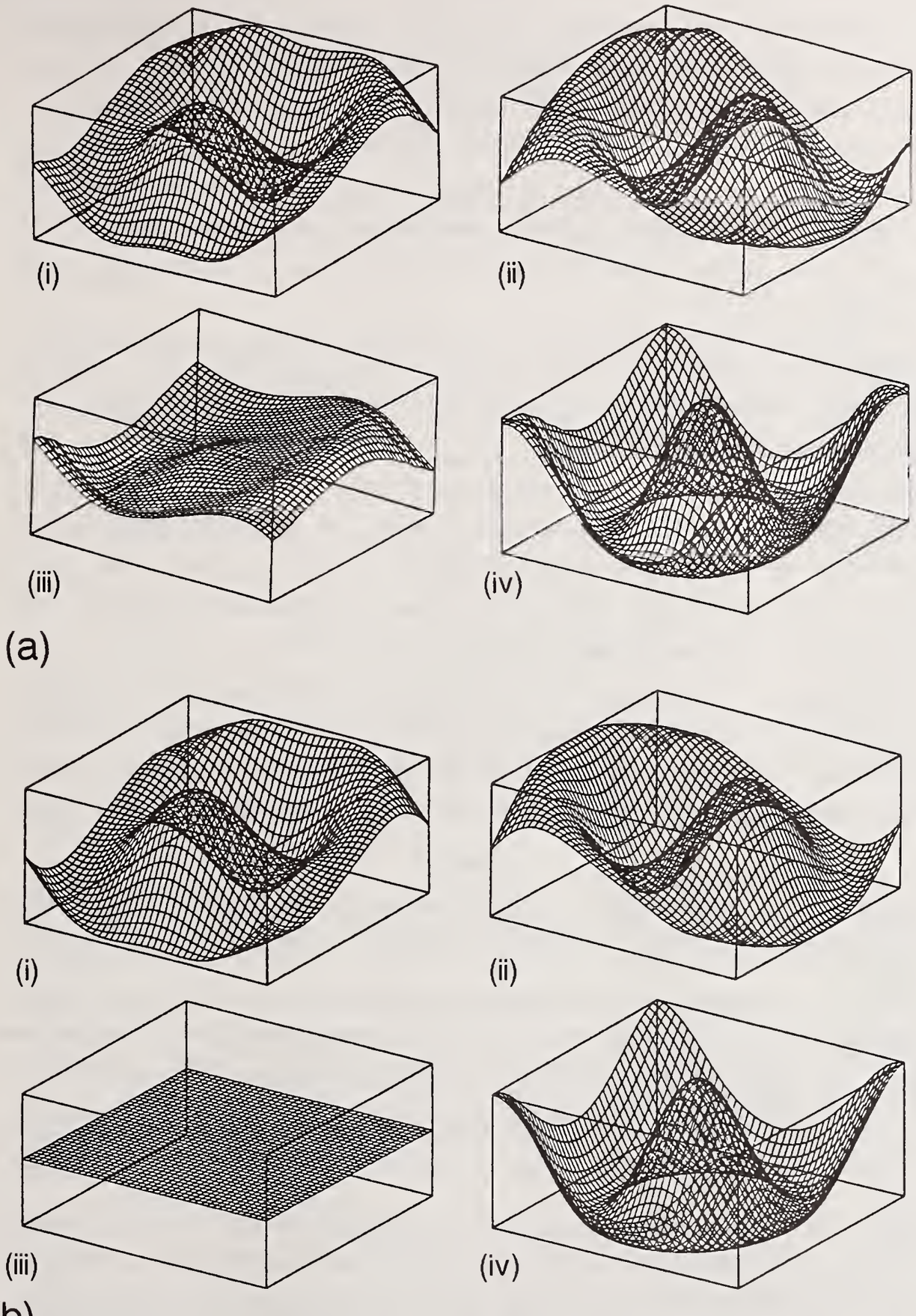

Figure 2 Birefringence characterisation of a lithium niobate polarisation controller: (a) experimental, and (b) computer simulation of an "ideal" device. Plots (i), (ii) and (iii) are the components of the birefringence vector with length equal to the sine of half the birefringence angle, and plot (iv) is the cosine of half the birefringence angle.

over the full birefringence range of over 3π. As an example of the detail which can be revealed by this technique, the deviation of the Z-component from zero was identified by further computer simulations to be caused by a slow variation in the intrinsic waveguide birefringence along the length of the device. It is interesting to note that the bulk-optic fractional wave-plates in the measurement system could potentially be replaced by this lithium niobate device, greatly increasing the speed of operation of the birefringence analyser.

Conclusions: A novel technique has been described for complete birefringence characterisation of optical devices, and its application to a waveguide polarisation controller has been demonstrated. It has been applied to two different electrode patterns on lithium niobate, and has produced results in excellent agreement with the predicted performance. Such detailed assessments of device performance can be obtained for a wide range of optical devices, and will become increasingly important for complex polarisation controller and filter structures.

Acknowledgements: The authors thank Jonathan Davidson and other colleagues in the Lithium Niobate Device Development Group for fabricating the devices characterised. The Director of Research and Technology, British Telecom Research Laboratories is acknowledged for permission to publish this paper.

References

1 Alferness R C: 'Electrooptic Guided-Wave Device for General Polarization Transformations', *IEEE J. Quantum Electron*, QE-17, No 6, pp965-969, (1981).

2 Heidrich H, Helmholt C H, Hoffman D and Ahlers H: 'Integrated optical compensator on Ti:$LiNbO_3$ for continuous and reset-free polarization control', *Proc. ECOC*, Finlandia Hall, Finland, Tech. Digest 1, pp257-260, September 13-17, (1987).

3 Donaldson A and Wong K K: 'Phase-matched mode convertor in $LiNbO_3$ using near-z-axis propagation', *Electron Lett.*, 23, No 25, pp1378-1379, (1987).

4 Walker N G, Walker G R, Davidson J, Cunningham D C, Beaumont A R and Booth R C: 'Lithium Niobate Waveguide Polarisation Convertor', *ibid*, 24, No 2, pp103-105 (1988).

5 Walker N G, Walker G R and Booth R C: 'Performance of lithium niobate polarisation convertor/tunable filter', *ibid*, 24, No 5, pp268-270, (1988).

6 Walker N G and Walker G R: 'Polarisation Control for coherent optical fibre systems', *Br. Telecom Technol. J.*, 5, No 2, pp63-76, (1987).

TECHNIQUES FOR REFRACTIVE INDEX MEASUREMENTS ON SEMICONDUCTOR WAVEGUIDES: PRISM COUPLING AND MODAL CUT-OFF SPECTROSCOPY

C. De Bernardi, M. Meliga, S. Morasca, B. Sordo
CSELT S.p.A. - Via G. Reiss Romoli 274 - 10148 Torino, Italy

Introduction

Integrated optical waveguides on semiconductor materials are in rapid development, for the great potential offerd by integrated optoelectronics, both in optical communications and in optical data processing. Waveguide attenuation, in both GaAs and InP based materials, has dropped well below 1 dB/cm, and is practically equal to the values exhibited by lithium niobate and other waveguide materials: this makes it practical to consider integration of several components and devices, requiring relatively long paths, on a single chip, without incurring in intolerable losses or requiring on-chip amplification.

The design of sophisticated components needs accurate knowledge of the refractive indices both of the substrate and of the layers involved in the propagation of radiation (waveguide, cladding and cover layers etc.), which depend not only on the composition of the material, but also on the doping levels; unfortunately, so far the available data on this aspect are not as rich as needed, from the point of view both of quantity and precision, and device design relies more on estimates from theoretical models than on precise experimental determinations of these physical parameters.

In this paper we present results based on two techniques developed to improve the knowledge of these refractive indices: the first one is an extension of the well-known prism coupling technique to high index materials, and uses a silicon prism to determine the refractive index of substrate material or of epitaxial layers, with an accuracy to the fourth decimal place. The second method, modal cut-off spectroscopy (MCS), yields the refractive index of waveguides at the wavelengths where cut-off of a guided mode is detected, if the substrate refractive index is known; the accuracy reaches the third decimal place.

Prism coupling measurements

The use of a prism to couple radiation into waveguides is well known [1], and is widely applied to the measurement of modal indices in planar guides. However, so far this technique has not been used, to our knowledge, in the case of semiconductors, probably due to their high refractive index and brittleness. We have used a silicon prism, suitable for InP and a range of InGaAlAs and InGaAsP compositions, due to its high index of refraction; in our case the prism data are: refracting angle $\alpha=64.25^{o}$, refractive index at 1.31 μm $n=3.5039$, calculated from a Herzberger interpolation formula [2] (direct measurement of this value by

minimum deviation is in progress); presently a diode laser source at 1.31 μm is used, but extension to other wavelengths with a color center laser is planned.

To characterize InP substrates the critical angle between prism and wafer is measured, observing from the cleaved edge the beam refracted into the wafer; data for samples with different doping are reported in Table 1: the accuracy reached in our case on thin wafers is similar to that provided by minimum deviation measurements on bulk material [3], without requiring special fabrication, or sample preparation, or waste of costly material.

For planar waveguides, coupling angles were measured for InGaAlAs on InP: results are listed in Table 2 for a guide 2.7 μm thick, grown by molecular beam epitaxy. In this case the synchronous angles appear rather broadly defined in comparison to glass or $LiNbO_3$ guides, up to about 0.1^o instead of the usual value of a few 0.001^o: this aspect is being investigated.

Table 1. Refractive index (n) of InP wafers at 1.31 μm

Sample	Doping	n
#1	S	3.1634 ± 0.0003
#2	Fe	3.2055 ± 0.0003
#3	Sn	3.2009 ± 0.0002
#4	undoped	3.2063 ± 0.0002
#5	Sn	3.2008 ± 0.0003

Table 2. Effective modal indices for an InGaAlAs/InP waveguide

Mode	n_{eff}
TE_0	3.3274 ± 0.0002
TE_1	3.3083 ± 0.001
TE_2	3.2714 ± 0.001
TE_3	3.223 ± 0.002

Modal cut-off spectroscopy measurements

The spectrum of modal cut-offs in planar waveguides is function of the refractive index difference between substrate and guiding layer and of its thickness, for step-index guides as in the present case; for graded-index ones, also on the profile shape. Since the substrate index can be obtained by the previous prism technique and the guiding layer thickness can be accurately measured, the determination of the cut-off spectrum in combination with theoretical dispersion curves yields values of the refractive index of the guide layer. An extension of the theoretical model to laterally confined waveguides can be used to obtain the same optical parameters for stripe guides [4,5]. This method has the advantage of operating directly on stripe guides, providing results accurate to the third decimal figure, at each wavelength of detected cut-off, which appears as a peak in the insertion loss spectrum of the guide. Measurements have been performed on InGaAsP and InGaAlAs ridge guides grown by liquid phase epitaxy (LPE) and molecular beam epitaxy (MBE) respectively. A schematic of the experimental set-up is shown in Fig. 1: a stabilized tungsten-halogen lamp is filtered by a scanning monochromator, and the monochromatic light is coupled to a single-mode fibre, which in turn is butt-coupled to the guide under measurement; the output from the guide is focused onto a photodetector, whose current is measured by a lock-in amplifier. An example of spectral scan is shown in Fig. 2, while numerical results are listed in Table 3.

Table 3. Refractive indices of epitaxial layers obtained by MCS

Material	Thickness	λ gap μm	cut-off λ TE	Δn^2	cut-off λ TM	Δn^2	n
MBE InGaAlAs	3.2 μ m	1.04	1.14 μm	0.872	1.12 μm	0. 883	3.395
"	"	"	1.44 μm	0.838	1.40 μm	0. 817	3.314
LPE InGaAsP	3.6 μm	1.10	1.31 μm	0.970	1.30 μm	0. 976	3.351
"	"	"	1.61 μm	0.965	1.58 μm	0. 967	3.310

In this table Δn^2 is the difference between the refractive indices squared of the epitaxial layer and of the substrate, and is directly obtained from the measurement, as illustrated in Fig. 3; the refractive index n is derived from the relevant InP value calculated by an interpolation formula forced through the value at 1.31 μm. The uncertainty in n provided by this method depends on the uncertainty of the epilayer thickness and of the cut-off wavelength; typical values of 50 nm and 10 nm respectively lead to an accuracy of $\pm$ 0.002 .

Discussion

The two techniques described here are complementary; the accuracy of their results, besides allowing more sophisticated design, is also helpful to determine the composition of compound materials, e.g. by using a modified single oscillator model, which connects refractive index to material composition [6]. Prism coupling requires monochromatic, high intensity sources and offers very high precision, comparable to bulk techniques, on standard wafers, while MCS can yield results at any desired wavelength, by a proper choice of guide thickness, which affects the cut-off wavelengths. Both techniques are insensitive, in comparison to ellipsometry and reflectometry, to surface oxide films.

Conclusions

Results are presented for two refractive index determination techniques applied to semiconductors, namely silicon prism coupling and modal cut-off spectroscopy; acccuracy to the fourth decimal place is demonstrated, as well as operation directly on stripe waveguides. This allows more accurate design of elaborate integrated optoelectronic devices.

Acknowledgments

The authors thank G. Fornuto, C. Rigo and A. Stano for providing the semiconductor samples. This work has been partially supported by EEC under Esprit Project 263.

References

[1] T. Tamir, "Integrated Optics", (Springer Verlag, Berlin, 1975), p. 22.

[2] L. Levi, "Applied Optics", (J. Wiley & Sons, New York, 1980), Vol. 2, p. 911.

[3] E. D. Palik, "Handbook of optical constants of solids", (Academic Press, Orlando, 1985), p. 504.

[4]M. Meliga, S. Morasca, B. Sordo, C. De Bernardi, "Spectral cut-off behaviour of Ti:$LiNbO_3$ and semiconductor waveguides: analysis and experiment", SPIE Proc. 835, p. 251-256, 1987.

[5] S. Morasca, B. Sordo, C. De Bernardi, M. Meliga, "Refractive indices of semiconductor films measured by waveguide cut-off spectroscopy",Appl. Phys. Lett. 52, 1593-1595 (1988).

[6] B. Broberg, S. Lindgren, "Refractive index of $In_{1-x}Ga_xAs_yP_{1-y}$ layers and InP in the transparent wavelength region", J.Appl.Phys. 55, 3376-3381 (1984).

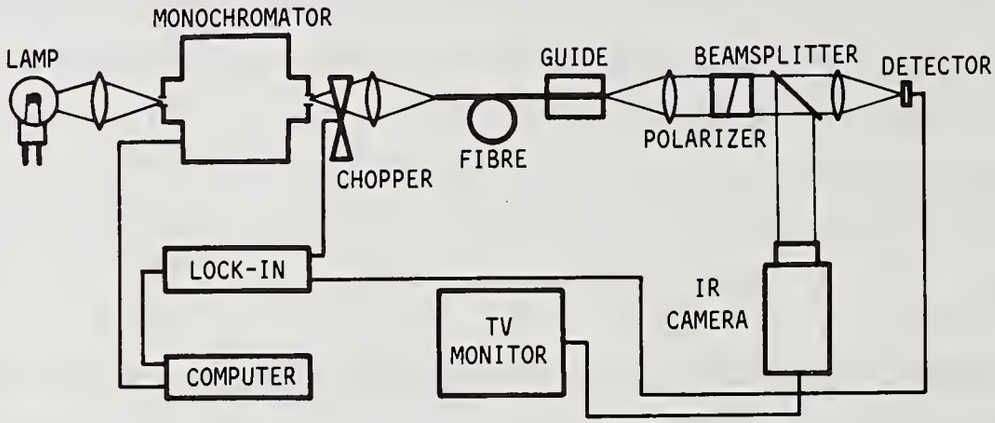

FIG. 1. Schematic of the optical setup for modal cut-off sprctroscopy

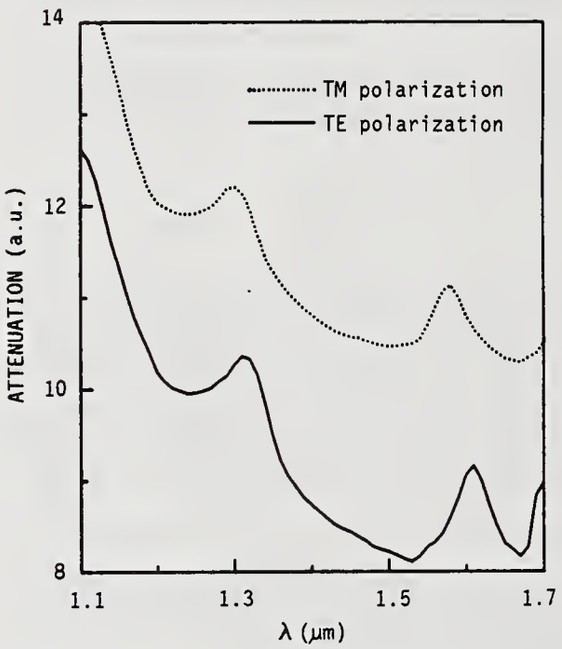

Fig. 2. Measured cut-off spectra on a InGaAsP ridge guide 10 μm wide, 3.6 μm thick.

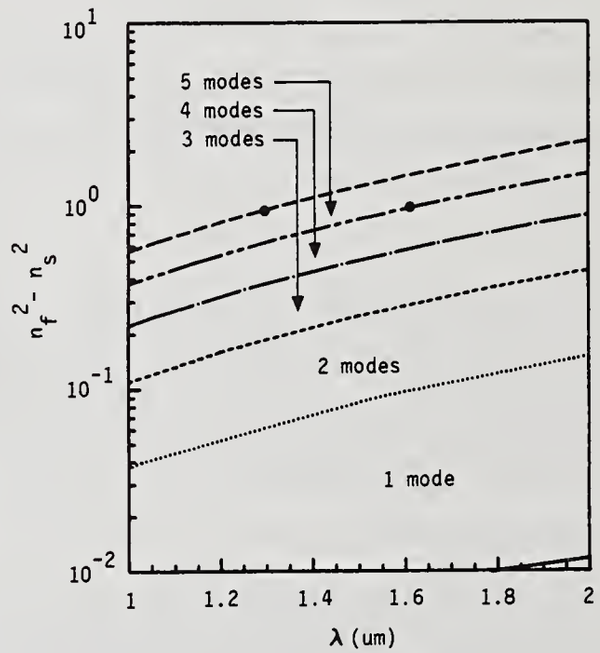

Fig. 3. Cut-off curves calculated for the guide of Fig. 2 for TM polarization.

ELECTRICALLY CALIBRATED PHOTOTHERMAL DEFLECTION MEASUREMENT FOR SEPARATING CHANNEL WAVEGUIDE LOSS MECHANISMS*

Robert K. Hickernell, Donald R. Larson and Robert J. Phelan, Jr.
National Bureau of Standards, Electromagnetic Technology Division
Boulder, CO 80303

Introduction

Absorption and scattering are the two primary sources of attenuation in optical waveguides. Their respective contributions to loss may differ widely, depending on the wavelength, substrate material, fabrication method and processing parameters. While the understanding of propagation loss is important to the further reduction of insertion loss in waveguide devices, it appears that little experimental research has been directed toward the separation of loss mechanisms.

Some studies have analyzed the relative angular distribution of out-of-plane scattered light or the total waveguide attenuation using surface and volume scattering theory [1,2]. However, the absolute measurement of power scattered from a waveguide, both in-plane and out-of-plane, is very difficult. Absorptive loss in Ti:$LiNbO_3$ waveguides has been measured using calorimetry [3] and the pyroelectric effect [4], but published values of the relative contributions of absorption and scattering disagree significantly.

Recently we applied the photothermal deflection (PTD) effect [5] to the measurement of total propagation loss in channel waveguides [6]. The method is noncontact and applicable to a wide range of channel waveguide geometries and materials, including buried guides. Since it is based on the absorbed power as a relative indicator of the guided power, it has an advantage over methods based on scattered light in that scattering centers and unguided background light do not affect the PTD measurement directly. With an absolute calibration of absorbed power, it is possible to use the PTD method to measure absorptive loss in waveguides. In this paper we present a technique for distinguishing absorptive from scattering contributions to channel waveguide loss by electrically calibrating the PTD effect. The technique is illustrated by experimental results with ion-exchanged glass waveguides.

Measurement Apparatus and Techniques

The experimental apparatus used to make loss measurements in waveguides is shown in Fig. 1, the details of which are described in Ref. 6. In summary, the pump laser light is chopped and coupled into a waveguide, and its absorption induces a modulated temperature and index gradient near the guide. The gradient refracts a probe beam, at 633 nm wavelength, by an amount measured by a bicell detector and lock-in amplifier. We present data in the form $\Delta V/V$, the ratio of the ac and dc signals of the bicell. Measurements were performed on straight, potassium ion-exchanged, channel waveguides in soda-lime glass substrates. The substrates were masked with 10-μm channel widths, and the resulting guides were multimode at a wavelength of 633 nm.

Calibration of the PTD signal was accomplished by mimicking the absorbed waveguide power with a thin film heater. We deposited NiCr stripes 160 nm thick, 5 μm wide and 10 mm long on the glass waveguide substrates and connected them to a square-wave signal generator, as shown in Fig. 2. The resistance of a stripe was 63 kΩ. The probe-beam optics were the same as those used to measure the PTD signal originating from absorbed, guided light. When a known voltage was applied to the measured resistance, a calibrated amount of heat was generated in a profile which approximated the generation of heat by guided light.

Experimental Results and Discussion

For a probe spot diameter of 25 μm and 633 nm guided light chopped at 500 Hz, the normalized PTD magnitude is plotted in Fig. 3 as a function of the probe position transverse to a typical waveguide. The PTD signal was zero at the center of the guide, where there was no thermal gradient. It peaked at a magnitude of 3.8×10^{-5} at a position approximately 15 μm from the center of the guide. We monitored the peak PTD signal as a function of position down the length of the guide and plotted the results in Fig. 4. Linear regression indicates a total propagation loss of 1.2 ± 0.2 dB/cm. The uncertainty is caused not by measurement error but by local absorption inhomogeneities in the waveguide [6].

We measured the throughput power of the waveguide, accounted for reflection losses, and calculated the guided power at the location along the waveguide where the measurements of Fig. 3 were taken. The peak of the

chopped power was 2.9 mW; therefore, a peak of 0.81 mW/cm of light was lost at that location due to both absorption and scattering.

In the electrical calibration procedure the voltage across the wire was a positive square wave with a 4.0 V amplitude and a frequency of 500 Hz, which generated a peak 0.26 mW/cm of heat. A transverse scan of the normalized PTD signal due to the wire heater is shown in Fig. 3 for comparison with the absorption-induced signal. The shapes of the two scans are very nearly the same, indicating that the wire heater approximately models the waveguide absorption. The PTD signal from the thin-film heater was identical for different positions along the stripe and peaked at 6.4×10^{-5}. Waveguide absorption loss as a fraction of total loss is calculated as the ratio of the PTD signals for the waveguide and the resistive heater, normalized to their respective powers lost per length. The absorption fraction measured here was 0.19 ± 0.05. This value is comparable to the bulk propagation loss measured in the substrate, which was 0.12 times the waveguide propagation loss. The ion-exchange process adds to the bulk loss both scattering and absorptive contributions.

Uncertainty in the absolute calibration of absorption loss is due to uncertainty in the measurement of total loss. As mentioned above, for the waveguides used here the uncertainty is caused by the random distribution of inhomogeneities in the waveguide material. Waveguides in higher quality substrates are expected to exhibit a lower uncertainty. Studies of other waveguides and at near-infrared wavelengths are currently being performed.

References

[1] M. Gottlieb, G.B. Brandt and J.J. Conroy, IEEE Trans. Circuits Syst. CAS-26, 1029 (1979).

[2] G.H. Ames and D.G. Hall, IEEE J. Quantum Electron. QE-19, 845 (1983).

[3] S.D. Allen, E. Garmire, M. Bass and B. Packer, Appl. Phys. Lett. 34, 435 (1979).

[4] A.M. Glass, I.P. Kaminow, A.A. Ballman and D.H. Olson, Appl. Opt. 19, 276 (1980).

[5] W.B. Jackson, N.M. Amer, A.C. Boccara, and D. Fournier, Appl. Opt. 20, 1333 (1981).

[6] R.K. Hickernell, D.R. Larson, R.J. Phelan, Jr. and L.E. Larson, Appl. Opt., July 1988 (to be published).

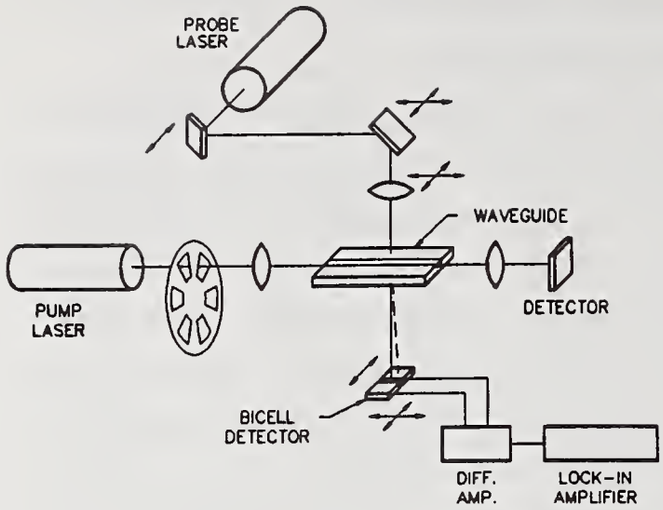

Fig. 1. Crossed-beam configuration for photothermal deflection measurement of a waveguide.

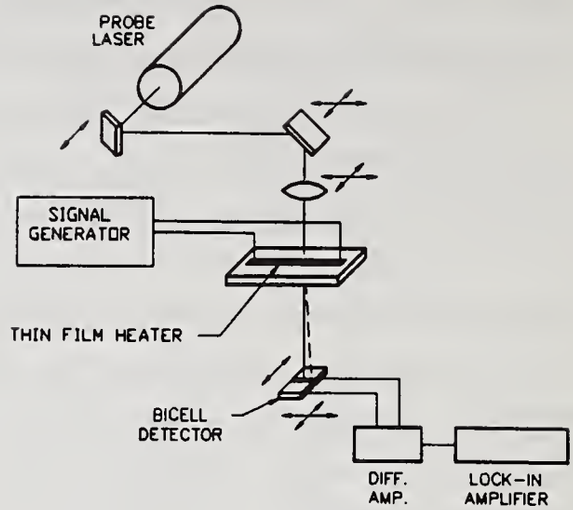

Fig. 2. Apparatus for electrical calibration of photothermal deflection.

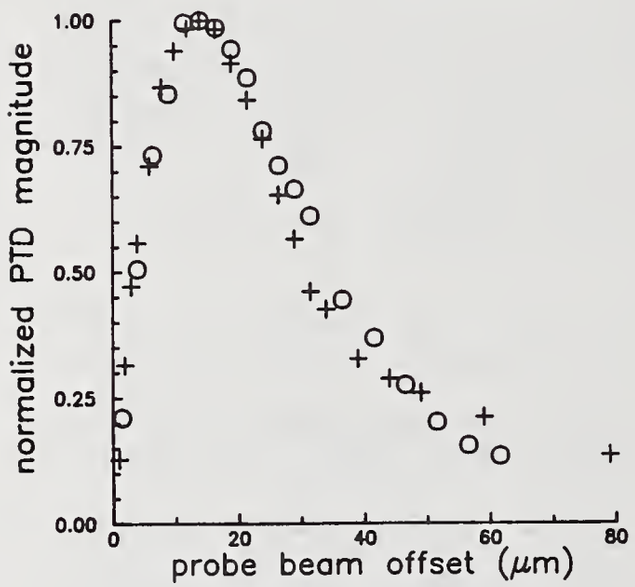

Fig. 3. Normalized PTD signal magnitude as a function of probe beam offset from waveguide or wire center: waveguide (+); wire heater (o).

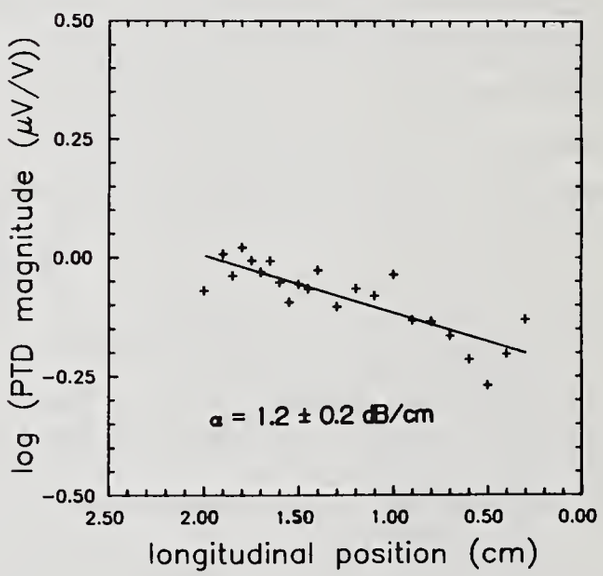

Fig. 4. Logarithm of the peak PTD magnitude as a function of distance along the waveguide. Best-fit line yields a propagation loss of 1.2 ± 0.2 dB/cm.

Fiber Measurements for Long Term Reliability: Strength, Hydrogen, and Radiation

F. V. DiMarcello, P. J. Lemaire and J. R. Simpson

AT&T Bell Laboratories
Murray Hill, New Jersey 07974

INTRODUCTION

The long-term reliability of glass fiber lightguides acquires increased importance as system requirements become more stringent. In addition, lightguides are finding applications in adverse environments which tend to accelerate many degradation mechanisms. Three important reliability issues[1] have emerged: the degradation of fiber strength with time, optical loss increases due to the permeation of H_2 into the fiber, and optical effects resulting from the interaction of various types of radiation with the fiber. The design of meaningful experimental methods as well as the development of accurate measurement techniques play important roles in predicting long-term reliability.

STRENGTH

At liquid nitrogen temperatures, where moisture is eliminated from the testing environment, silica fiber strengths of approximately 2×10^6 psi (13.8 GPa) have been measured.[2] At ambient temperature and moisture conditions, however, this intrinsic value is reduced to approximately 800 ksi (5.5GPa) in short gauge lengths as a result of the fatigue which takes place during the measurement. Furthermore, it is found that as longer lengths of fiber are tested, the strength distribution is basically bimodal with a narrow high strength mode at approximately 800 ksi (5.5 GPa) and a broad low strength tail. This low strength mode is clearly extrinsic and is explained by the classic Griffith model[3] of brittle fracture and its fracture mechanics extensions[4,5] in which the presence of mechanically or chemically induced flaws or cracks act as stress concentrators and cause localized failure. Since the failure stress is inversely proportional to the flaw size, the variability of the strength of optical fibers is a reflection of the flaw size distribution. For any tested length of fiber, fracture will occur at the position of the largest flaw. Thus, as the length of the fiber increases, the strength will decrease because of the greater probability of encountering increasingly larger flaws. Extrinsic flaws can result from contaminants in the preform or fiber, airborne particles in the processing environment, particle contamination in the polymer coating, or surface abrasion during processing. There has been much effort to improve the fiber materials and processing techniques to minimize the number of large flaws in today's high performance fibers.[6,7]

Once the fiber is made, the larger remaining flaws can be eliminated by stressing (proof testing) the entire length to a level determined by a fatigue design analysis for the particular application. This provides a guaranteed minimum initial strength or a corresponding minimum lifetime for a particular length of fiber. However, when proof testing at high levels, one must be concerned about damage or fatigue which may occur during the testing. In order to insure a guaranteed minimum strength it is necessary to implement environmental controls during prooftesting along with rapid unloading of the proof test load.[8,9] Fig. 1 shows a proof tester design which has been used successfully up to levels of 500 ksi (3.5 GPa).[10,11] During proof testing, the fiber passes between the belts and wheels with 2 turns around the lower floating pulley on which the load is hung. Proof testing is normally conducted at relative humidities of 40 - 50% with the stress being applied for 1 sec and unloaded in < 0.1sec.

In addition to the initial strength degradation due to flaws in the silica fibers, a time dependent phenomenon known as delayed failure or fatigue can also occur. In this case, a stress lower than that which causes immediate failure allows the flaws to grow slowly in an active environment until they reach the critical size for fast fracture. It is generally agreed that a stress corrosion mechanism is responsible in which the stress enhancement of the reaction $SiOSi + H_2O \rightarrow 2SiOH$ causes the cracks or flaws to lengthen. This subcritical crack growth is usually described by the power law model of Charles[12] and the application of fracture mechanics principles[13] which leads to the relationship between the time to failure, t, and the applied stress, σ,

$$\log t = -n \log \sigma + \log (B\sigma_i^{n-2})$$

where σ_i is the fracture strength in an inert environment and B and n are parameters related to the material and environment.

The logarithm of the applied stress is usually plotted as a function of the logarithm of the time to failure typically resulting in a linear plot with a reciprocal slope, n, the stress corrosion susceptibility parameter, and an intercept at $\log\sigma = 0$ of $\log (B\sigma_i^{n-2})$. This plot is normally extrapolated to make long-term predictions of static fatigue.[14,15] The value of n is typically 20 for silica fibers in non-aggressive environments but can vary widely due in part to the large scatter in failure times resulting from the statistical distribution of maximum flaw sizes in repeated tests. Further difficulties arise in predicting fatigue behavior because of the complex interactions of environmental conditions such as temperature, humidity, pH, and polymer coating chemistry.

There are two types of tests for time dependent failure of silica fibers which are differentiated by the manner in which the stress is applied. The static fatigue test is conducted in an active environment by applying a constant stress below that required for fast fracture, measuring the time to failure, and plotting $\log \sigma$ vs $\log t$ to obtain the stress corrosion susceptibility factor, n. The dynamic fatigue test measures the breaking strength of the fiber at a constant strain rate in an active environment. By plotting log failure stress vs log strain rate or log time to failure the n value is also obtained.

There are three techniques, shown on Figs. 2 & 3, commonly used for measuring static and dynamic fatigue: tension, mandrel bending, and 2-point bending. In the tensile technique,[16] a length of fiber is gripped at each end and either placed in tension using weights or pulled to failure in a tensile tester. The coated or uncoated center section of fiber can be threaded through an environmental chamber. However, the coating must remain intact where the fiber passes through the rubber seal and at the grips to prevent mechanical damage.

In the mandrel bending technique[17] a coated fiber is wrapped around a rod of known radius which defines a tensile strain on the outside surface. The entire mandrel may be placed in the environment to be studied. The major advantage of this technique is the ease of preparing many test specimens using rods of different radii. However, there is a serious problem with gripping the fiber ends. Stress concentrations can be introduced at these points causing premature failure. A modification of this technique[18] has been described, however, which apparently avoids this problem.

The third technique, two-point bending,[19–22] can be used for either dynamic or static fatigue measurements, as shown in Fig. 3. The dynamic fatigue test involves constraining a bent loop of fiber between two polished face plates which are then brought together in a controlled manner until the fiber breaks. The static fatigue test is conducted by bending a number of fibers and inserting them into a precision bore glass tube or other suitable fixture as shown in Fig. 3. The stress, in this case, is determined by the inside tube diameter and failure of the fibers is monitored acoustically. The advantages of these techniques include the elimination of gripping problems, the ability to easily test coated and uncoated fibers in various environments, and in the case of static fatigue, the convenience of being able to test many specimens at the same time.

Fig. 4 shows a summary of some static fatigue data obtained from tensile tests and gives an indication of its sensitivity to temperature, pH, humidity, and polymer coating. It has been found that, under certain environmental conditions, $\log t$ is not linearly dependent on $\log \sigma$ with an n value of ~20, but shows a transition in slope resulting in more rapid degradation. This transition was first observed by Wang and Zupko[23] at 32°C and 90% relative humidity for a fiber coated with an epoxy acrylate. Under these conditions, the value of n abruptly decreased to ~7 after approximately 20 days. Krause's experiments[16,24] showed that the time for the transition changed to 1 day and 1 hour for coated and uncoated fibers, respectively, tested in water at 90°C. However, neither the presence of a coating or the increase in temperature changed the post-transition n-value of ~7. Chandan and Kalish[25] later examined the static fatigue of a polyurethane acrylate coated fiber in 40°C - 90°C water and also found enhanced fatigue at low stress levels, with n-values varying from 1-8 depending on temperature. Although Chandan and Kalish extrapolated the temperature dependence of n and concluded that there was no enhanced fatigue at temperatures of 3°C, it has been suggested [15,26] that their temperature dependence was a result of coating effects, and that enhanced fatigue should not be neglected in lifetime estimates. The coating influence on static fatigue is underscored in Fig. 4 by the absence of a static fatigue transition for fibers with a two-layer silicone[27] and a fluorinated acrylate[28] coating tested in 80°C and 100°C water, respectively.

Fig. 4 also describes the dramatic pH dependence of static fatigue failure times for uncoated fiber at 90°C[15]. The data before the transition shows a dependence of n on pH with n varying from 31 at pH 1, to 13 at pH 14. The post-transition n values, however, are independent of pH, with $n \approx 6$. Mathewson and Kurkjian[26] show a generally similar dependence of static fatigue on pH from two-point bending experiments. They also show a

crossover in fatigue behavior between coated and bare fibers. At low applied stress coated fiber has the shorter lifetime while the converse is true at higher stresses. Thus the effect of environment and polymer coating chemistry on static fatigue is very complex and must be carefully considered when making fatigue measurements and lifetime predictions.

Because of the permeability of the polymer coatings to moisture and their complex surface interactions which affect static fatigue, thin metallic[29] or ceramic-like[30–32] hermetic coatings have been deposited on the fiber surface to improve long-term reliability. Measurements using both tension and bending have shown dramatically improved static fatigue resistance for some of these hermetically coated fibers. For example, a design analysis for a 25 year service life of a carbon coated fiber shows that the service stress can be ~80% of the prooftest stress, as compared to ~30% normally estimated for conventional fiber.[33]

HYDROGEN

Optical fibers are known to experience detrimental loss increases if they are exposed to sources of hydrogen. H_2 can readily diffuse into a fiber's core, causing loss increases by one of two basic mechanisms: (1) H_2 becomes IR active when dissolved in a silica glass matrix, giving rise to absorption peaks between 1.08 and 1.26μm, and a rising loss edge beyond about 1.4μm[34,35], (Fig. 5) and (2) H_2 reacts with structural defects in the glass, causing, for instance, the formation of OH at nonbridging oxygen sites in the fiber core.[36,37] The physical dissolution of H_2 molecules in SiO_2 is a reversible process. Therefore these loss increases will gradually disappear if the H_2 atmosphere is removed. Losses due to this dissolved H_2 are substantially the same for all fibers, regardless of the glass composition. On the other hand, the chemical reaction of H_2 with defects generally results in permanent loss increases, the magnitudes of which depend sensitively on the glass composition.[38,39]

The issue of hydrogen reliability is of concern because there is always some finite level of H_2 present in a cable, due both to H_2 outgassing of polymers and to possible galvanic corrosion of cable materials. One strategy is to avoid hydrogen problems by means of suitable cable design, or by the use of non-reactive or hermetic fibers.[31,32,39] However, it is frequently necessary to characterize a given fiber type so as to allow the accurate prediction of long term loss increases, and to permit the specification of a "tolerable" hydrogen level within a cable. The remainder of this section will discuss the identification of hydrogen induced losses and the prediction of fiber loss increases in hydrogen-containing environments.

Determining that hydrogen induced losses have indeed occurred is best done by use of spectral loss measurements, preferably taken before and after the occurrence of the loss increases. Molecular hydrogen has a distinct spectral signature, as shown in Fig. 5. The magnitudes of these losses are proportional to the concentration of H_2 in the fiber core. The rate of loss increase is determined by the diffusion rate of H_2 in SiO_2[40] and is readily predicted using classical diffusion theory.[41] The hydrogen level in the core of a single mode fiber will equilibrate with an applied atmosphere in about 2 weeks at 21°C. Thereafter the losses due to this effect will be constant, as long as the external hydrogen level does not change. A fiber exposed to 1 atm of H_2 at 21°C will show loss increases of about 0.21 and 0.55 dB/km at 1.31 and 1.55μm respectively, and a 9.5 dB/km loss increase at the 1.24μm H_2 overtone peak.

The formation of OH at defect sites causes readily measured increases in the OH overtone in the 1.4μm region. If sufficient spectral resolution is used, it will frequently be noted that the peak has two components, centered on 1.39 and on 1.42μm, indicative of SiOH and GeOH, respectively.[42] In the case of fibers co-doped with Ge and P the growth of the GeOH component can be quite pronounced, and is accompanied by a rising long wavelength loss edge.[36,39,43] Qualitatively similar behavior has been noted in single mode fibers contaminated with unusually high levels of alkali impurities.[44,45] In Ge-doped single mode fibers the OH overtone growth occurs primarily at 1.39μm, but can have a detectable 1.42μm shoulder.[46]

Reaction of H_2 with other types of defects in Ge-doped fibers causes a short wavelength loss edge that can significantly influence losses at 1.31 and 1.55 μm, but which is most readily noted in the wavelength region below 1μm. (Fig. 5)[47,48] The absorption cross section of the defect responsible for this edge is temperature dependent, and thus the magnitude of the excess loss depends on the measurement temperature.[49] This loss edge is often the dominant hydrogen loss mechanism for Ge-doped single mode fibers at typical operating conditions.

Predicting losses due to molecular H_2 is quite straightforward if the hydrogen pressure is known, as previously discussed. However, in many cases the pressure of H_2 around a fiber is rather low, typically below 10^{-3} atm. Molecular H_2 peaks will not be observable under these conditions, and reactive types of loss increases will occur very slowly. The concern in these cases is that small but "significant" loss increases might occur over prolonged periods, due to reactions at defects. In order to predict the loss increases it is necessary to accelerate the reactions by raising the temperature and/or the hydrogen pressure, and then to extrapolate back to anticipated temperatures and pressures. To make valid predictions it is necessary to separately characterize the temperature and pressure dependences of each type of hydrogen induced loss. In practice, one type of loss will often be dominant in a given fiber type, (e.g. the short wavelength edge in Ge-doped single mode fibers), and it is this mechanism that must be carefully characterized. The results obtained for one type of fiber (e.g. a Ge-doped single mode fiber) will usually not be applicable to other fiber types (e.g. Ge-P doped multi-mode fibers).

The use of in-situ spectral loss measurements is invaluable in characterizing the reactions that occur in these accelerated tests.[47] Monitoring the loss changes of a fiber while it is exposed to H_2 at an elevated temperature will show an initial rapid rate of increase due to molecular hydrogen, followed by more gradual increases due to reaction of H_2 at defects. (Fig. 6) The reactive component of the loss increase itself has an initially rapid rate of increase, followed by a slow approach to a saturation level as reactive defects are depleted.[47] As long as only a small fraction of the defects have been depleted by reaction it is fair to approximate the rate of loss increase to be a constant, resulting in loss changes that are proportional to the exposure time. It is therefore, the initial rate of loss increase that is generally characterized, usually at several temperatures and hydrogen pressures for a given fiber type. Ideally, an Arrhenius relation should be followed for experiments run at different temperatures and a given hydrogen pressure. Fig. 7 shows such behavior for Ge-doped single mode fibers.[47,49] The straight line fit indicates that a single mechanism is dominant over the temperature range studied. Extrapolation to lower temperatures necessarily assumes that a lower slope portion will not occur on the Arrhenius plot at lower temperatures. For this reason it is best to perform experiments at temperatures as close as possible to actual operating temperatures, although this will entail experiments of longer duration.

Similarly it is necessary to determine the dependence of the initial reaction rate on the hydrogen pressure. Results to date for several fiber types have shown that the rate of loss increase is usually proportional to the square root of the hydrogen pressure at relatively high pressures ($P_{H_2} > 0.1$ atm).[39,50] However, experiments on Ge-doped single mode fibers have shown that the dependence on the hydrogen pressure changes to a linear dependence at low hydrogen pressures ($P_{H_2} < 0.04$ atm).[47,49] Using this data for the temperature and pressure dependences it is possible to determine tolerable hydrogen levels for given values of allowable loss increases, as shown in Fig. 8.[47] At low temperatures, reactions are slow and the losses due to molecular H_2 are the primary effect. At higher temperatures the hydrogen reactions are faster and the loss increases are primarily due to the growth of a short wavelength loss edge. The loss increases due to OH, while noticeable near 1.4μm, have little effect at 1.31 and 1.55μm.

Comparison of two different types of fiber, A and B, using a "standard" accelerated test at some selected temperature and hydrogen level requires some caution. A meaningful comparison experiment requires knowledge of both the temperature and the pressure dependences for each fiber. For instance, assume that rates of loss increase in fiber A have a stronger temperature dependence than those for fiber B. At high temperatures, loss increases will be larger for fiber A than for B, while at low temperatures the converse will be true. (That is, the lines for A and B will cross on an Arrhenius plot.) A relative ranking of the two fibers would therefore depend on the temperature chosen for the experiment. A similar argument can be made regarding the importance of choosing a meaningful hydrogen pressure for a comparison experiment.

Recent advances have made it possible to apply hermetic carbon coatings to optical fibers.[31,32] These coatings dramatically reduce the levels of H_2 seen by the lightguiding portion of a fiber, and allow the fibers to be used in applications where the external hydrogen pressure is quite high. Because so little H_2 penetrates these coatings at normal conditions it has been necessary to use both elevated temperatures and high P_{H_2}'s to get measurable loss changes in accelerated tests. Pressures of 2000 psi and temperatures from 120 to 200°C lead to detectable H_2 permeation, making it possible to estimate the permeation time constants for real operating conditions.[51]

RADIATION

The loss added to an optical fiber by interactions with ionizing radiation is of interest in both low dose terrestrial and undersea environments as well as the high dose surroundings of a nuclear blast, nuclear reactor or spacecraft.[52–56] Prediction of the fiber response in these surroundings is complicated by the substantial variations in total dose, dose rate, temperature and radiation type, as evident from Table I. Correspondingly, the measurement and prediction of fiber responses must take these variables into consideration. Nuclear blast studies frequently consider transient components which require specific methods not discussed here.[57,58] Fiber radiation sensitivities are further complicated by dependence on wavelength, mode excitation, launched optical power and ambient light. Attempts to establish a standard testing procedure have recently been made by the NATO Panel IV, Research Study group 12 and by the Electronics Industries Association.[59–61]

Steady state radiation induced loss measurements, typically used to qualify fiber, are divided into two ranges, low dose (<3000 rads at a dose rate of 5 to 18000 rads/hr) and high dose (3000 to 1,000,000 rads at a dose rate of 5 to 200 rads/sec) with low dose measurements made using a before-and-after cutback method. In high dose measurements the loss is monitored throughout the exposure and for several minutes following the exposure.[59–61]

Common to all radiation measurements is the need for accurate dosimetry. The radiation dose is typically expressed in rad (Si) where one rad equals an absorbed energy of one erg per gram of silicon. Standard methods to measure the absorbed dose employ thermal luminescent detectors (TLD's), radiochromic dyes (used by NBS), and Fricke dosimetry.[62] The TLD method is perhaps the most convienient in that the detectors may be purchased as chips, a few millimeters square, which are reusable after annealing and may easily be placed on the fiber reel. The TLD material is chosen depending on the dose range of interest, with lithium fluoride suggested for the range of 1 mrad to 300,000 rads and lithium borate manganese for the range of 50 mrad to 1,000,000 rads, to name a few.[63] Reading the TLD is readily accomplished using commercial equipment which integrates the light output of the material as it is subjected to a well controlled temperature cycle. This output reading serves only as a relative indication of the absorbed dose and requires comparison with the integrated light output from a known dose and verification of linear response with dose for calibration. The TLD materials respond independent of dose rate (up to 10^{12} rad/sec.) and energy (from less than 10 kev to several Mev) and fade less than 5% per year at room temperature. A reproducibility of approximately 20% in the measured dose can be expected with this technique. Mixed gamma/neutron doses may be measured with combinations of TLD's. The Fricke dosimetry method is based on the change in optical absorbance at 304 nm by ferric ions created during the radiation of a ferrous ammonium sulfate aqueous solution. This has been a widely accepted chemical dosimeter, as have the dyes, with claimed accuracy of ±5%. However, the Fricke dosimeter is limited to a relatively small dose range of 4 to 200 krad by the oxygen content of the solution.

Control of dose uniformity over the area of the fiber reel is an additional concern given that radiation sources are typically contained in single or multiple point source configurations. Dose field uniformity may be achieved by placing the fiber reel sufficiently far from the source. However, this also decreases the dose rate. One manufacturer of a Co^{60} source achieves a flat dose field by providing a variable thickness lead shield to compensate for differences in dose rate over the sample area.[65] Dose non-uniformity over a reel of fiber may also arise from shielding by overwound fiber, a potential problem in the low dose, several kilometer length sample configurations.

Equipment and procedures for measuring the radiation induced losses in fibers are typically adaptations of standard loss test sets as shown in Figure 9, with measurement procedures dependent upon the total dose and dose rates of the exposure.

Evaluation of the low dose (<3,000 rad)/low dose rate (5 to 50 rad/hr) sensitivities is performed using the standard cutback technique, before and after the irradiation. Care must be taken to ensure that the ambient light is not contributing to photobleaching both during exposure and during measurement. Fiber lengths of a few kilometers are required to observe a few tenths of a dB added loss in state of the art radiation resistant fiber.

Low dose (< 3,000 rad)/high dose rate (50 to 20,000 rad/hr.) and higher dose measurements are usually performed in-situ, monitoring the added loss both during and after exposure. Measurements of this type for three generic fiber compositions are shown in Fig. 10, demonstrating the diversity in responses.[64] As a further complication, these responses have a temperature dependence as shown in Fig. 11.[65] In these tests, less than 100

meters of fiber are used and control of an equilbrium mode distribution becomes more important to insure repeatability. A stable source and launch are also required in that the exposure may last an hour, with recovery typically monitored for nearly 3 hours.

In general, the optical power present during the measurement has been shown to affect the induced losses, with the higher power causing lower induced losses. This photobleaching effect is especially noticable in undoped silica core fibers. However, the average optical power during in-situ measurements of any fiber type is suggested to be 1μW or less to minimize the effect.[59,60,61] The photobleaching effect may be further minimized by sampling the transmission only a few times during the measurement.[61]

In summary, the measurement of the radiation response of an optical fiber must be designed for the specific environment of interest, and is established primarily by total dose, dose rate, temperature and radiation type. The fiber response to this environment is, in turn, a complex sum of effects mainly determined by its composition, the wavelength, and the optical power of the probe signal.

CONCLUSIONS

The three relibility issues discussed here are associated with degradation mechanisms affected by complex interactions of materials and environment. Inherent difficulties of extrapolation for predicting long-term reliability necessitate a thorough understanding of the degradation processes in order to allow the design of meaningful test methods.

REFERENCES

1. S. R. Nagel, SPIE Proceedings, **717**, 8-20, Sept. 1986.
2. B. A. Proctor, I. Whitney, and J. W. Johnson, Proc. R. Soc. London, Ser. A. **297A**, 534-557, 1967.
3. A. A. Griffith, Phil. Trans. Roy. Soc., London, A **221**, 163, 1920.
4. G. R. Irwin, Encycl. Phys. **6**, 55, 1958.
5. S. M. Wiederhorn, J. Am. Ceram. Soc. **52**, 99, 1969.
6. F. V. DiMarcello, A. C. Hart, J. C. Williams, and C. R. Kurkjian, Physics of Fiber Optics: Advances in Research and Development, ed. B. Bendow and S. S. Mitra, Plenum, N. Y. 125-135, 1979.
7. A. L. Harmer, Top Meet. Opt. Fiber Commun., Tech. Dig WF5, 70-73, 1979. 82-85, 1979.
8. A. G. Evans and E. R. Fuller, Mater. Sci. Eng. **19**, 69-77, 1975.
9. B. K. Tariyal and D. Kalish, In "Fracture Mechanics of Ceramics", Vol 3, R. C. Brandt, D. P. H. Hasselman, and F. F. Lange, eds. Plenum, N. Y. 161-195, 1978.
10. Private Communication, J. G. Wright and D. L. Myers, AT&T Technologies, Norcross, GA.
11. F. V. DiMarcello, D. L. Brownlow, R. G. Huff, A. C. Hart, Proceedings OFC '85, PDO6, San Diego, 1985.
12. R. J. Charles, J. Appl. Phys. **29**, 1554-60, 1958.
13. A. G. Evans, Int. J. Fract. **10**, 251, 1974.
14. J. T. Krause, D. A. Meade, S. Shapiro, Proc. Suboptic Int. Conf. on Opt. Fib. Subm. Telecomm. Sys., Paris, 117-22, 1986.
15. J. T. Krause and C. J. Shute, Adv. Ceram. Mat. **3**, 118-121, 1988.
16. J. T. Krause, J. Non-Cryst. solids, **38-39**, 497-502, 1980.
17. M. Nishimura, K. Yoshida, M. Oda, Y. Ishida, Proceedings of 6th ECOC, York, 133-136, 1980.
18. P. C. P. Bouten and H. H. M. Wagemans, Electron Lett. **20**, 280-81, 1984.
19. P. W. France, M. J. Paradine, M. H. Reeve, & G. R. Newns, J. Mater. Sci. **15**, 825-30, 1980.
20. S. F. Cowap and S. D. Brown, Am. Ceram. Soc. Bull. **63**, 495, 1984.
21. M. J. Mathewson, C. R. Kurkjian, S. T. Gulati, J. Am. Ceram. Soc., **69**, 815-21, 1986.
22. M. J. Mathewson, C. R. Kurkjian, J. Am. Ceram. Soc., **70**, 662-68, 1987.
23. T. T. Wang and H. M. Zupko, J. Mat. Sci. **13**, 2241-48, 1978.
24. J. T. Krause, Proceedings of 5th ECOC, postdeadline paper, 19.11-19.4, Amsterdam, 1979.
25. H. C. Chandon and D. Kalish, J. Am. Ceram. Soc. **63**, 171-73, 1982.
26. M. J. Mathewson and C. R. Kurkjian, J. Am. Ceram. Soc. **71**, 177-83, 1988.
27. D. Roberts, E. Cuellar, L. Middleman, and J. Kucker, SPIE Proceedings, Paper 721-14, 1986.

28. B. J. Skutnik, B. D. Munsey, and C. T. Brucker, Mat. Res. Soc. Sym. Proc. 88, ed. S. R. Nagel, J. W. Fleming, G.H. Sigel, and D. A. Thompson, MRS, Pittsburgh, 1987.
29. D. A. Pinnow, G. D. Robertson, G. R. Bair, and J. A. Wysocki, Top. Meet. Opt. Fiber Commun. Tech. Dig. TUCS, 16-17, 1979.
30. E. G. Hanson, et al, U.S. Patent 4, 512,629, April 23, 1985.
31. R. G. Huff, F. V. DiMarcello, and A. C. Hart, OFC '88 TUG2, New Orleans, 1988.
32. K. E. Lu, G. S. Glaesemann, R. V. Vandewoestine, and G. Kar, Journ. Lightwave Tech **6**, 240-43, 1988.
33. J. T. Krause, C. R. Kurkjian, F. V. DiMarcello, and R. G. Huff, 6th EFOC/LAN Conf., Paper 2.8 Amsterdam, June 29 - July 1, 1988.
34. J. Stone, A. R. Chraplyvy, C. A. Burrus, Optics Letts., **7**, 297, 1982.
35. K. Mochizuki, Y. Namihira, Electron. Lett., **19**, 743, 1983.
36. N. Uesugi, T. Kuwabara, Y. Koyamada, Y. Ishida, N. Uchida, Appl. Phys. Lett., **43**, 327, 1983.
37. P. J. Lemaire, M. D. deCoteau, Optical Fiber Materials and Properties, Materials Res. Soc. Symp. Proc., **88**, 225, MRS, 1987.
38. K. Noguchi, N. Shibata, N. Uesugi, Y. Negishi, J. Lightwave Tech., **LT-3**, 236, 1985.
39. J. D. Rush, K. J. Beales, D. M. Cooper, W. J. Duncan, N. H. Rabone, British Telecom Technol. J., **2**, 84, 1984.
40. R. W. Lee, R. C. Frank, D. E. Swets, J. Chem. Phys., **36**, 1062, 1962.
41. J. Crank, The Mathematics of Diffusion, Oxford Univ. Press, London, 1975.
42. J. Stone, G. E. Walrafen, J. Chem. Phys., **76**, 1712, 1982.
43. S. Tanaka, M. Kyoto, M. Watanabe, H. Yokota, Electron. Lett., **20**, 283, 1984.
44. A. Iino, J. Tamura, K. Orimo, K. Okubo, Conf. on Optical Fiber Comm, Atlanta, 1986. Paper TU13.
45. H. Itoh, H. Hanafusa, Y. Hibino, Trans. IECE Japan, **E69**, 782, 1986.
46. P. J. Lemaire, A. Tomita, European Conf. Optical Comm., Stuttgart, 1984. Paper 15A1.
47. A. Tomita, P. J. Lemaire, Electron. Lett., **21**, 71, 1985.
48. N. J. Pitt, A. Marshall, Electron. Lett., **20**, 513, 1984.
49. A. Tomita, P. J. Lemaire, European Conf. Optical Comm., Stuttgart, 1984. Postdeadline paper PD-1.
50. K. Noguchi, N. Shibata, N. Uesugi, K. Ishihara, Y. Negishi, Electronics and Commun. in Japan, **69**, 1, 1986. (Translation from Denshi Tsushin Ronbunshi, **68B**, 795, 1985.)
51. P. J. Lemaire, K. S. Kranz, K. L. Walker, R. G. Huff and F. V. DiMarcello, Proc. of 14th Europ. Conf. on Optical Comm., Brighton, UK, 1988.
52. J. B. Haber, E. Mies, J. R. Simpson, and S. Wong, J. Lightwave Tech. **6**, 150-154, 1988.
53. H. J. Schulte, Proceedings of OFC, paper TUQ2, San Diego, 1985
54. R. E. Warren and A. Beilis, Report prepared for the Defense Nuclear Agency under contract No. DAEA-18-75-A-0059-8Z01AC by AT&T Technologies, 1985.
55. J. K. Partin, Proceedings of SPIE Fiber Optics in Adverse Environments, **506**, 42-49, 1984.
56. E. J. Friebele, Proceedings of OFC, paper WA7, Reno, 1987.
57. L. D. Looney, G. Turquet de Beauregard, P. B. Lyons and R. E. Kelly, Proceedings of SPIE Fiber Optics in Adverse Environments, **296**, 17-25, 1981.
58. E. J. Friebele, J. Lightwave Tech., to be published.
59. Electronics Industries Association (EIA), Wash. D.C., "Proposed Procedure for Measuring Gamma Irradiation Effects in Optical Fibers", FOTP-49, 1987.
60. R. A. Greenwell, Fiber and Integ. Optics, **6**, 179-80, 1987.
61. E. J. Friebele, E. W. Taylor, G. Turguet de Beauregard, J. A. Wall, and C. E. Barnes, J. Lightwave Tech. **6**, 165-71, 1988.
62. J. H. O'Donnell and D. F. Sangster, "Principals of Radiation Chemistry", Amer. Elsevier Publishing Co. Inc., New York, 39- 41, 1970.
63. Harshaw/Filtrol, TLD systems & materials performance specifications
64. J. R. Simpson, Proceedings of OFC'88, Paper TU-G3, New Orleans, 1988.
65. J. R. Simpton, T. Mensah, S. Wong, A. J. Ritger, E. Mies, A. Klein and P. Glodis, Proceedings of ECOC, Helsinki, 1987.

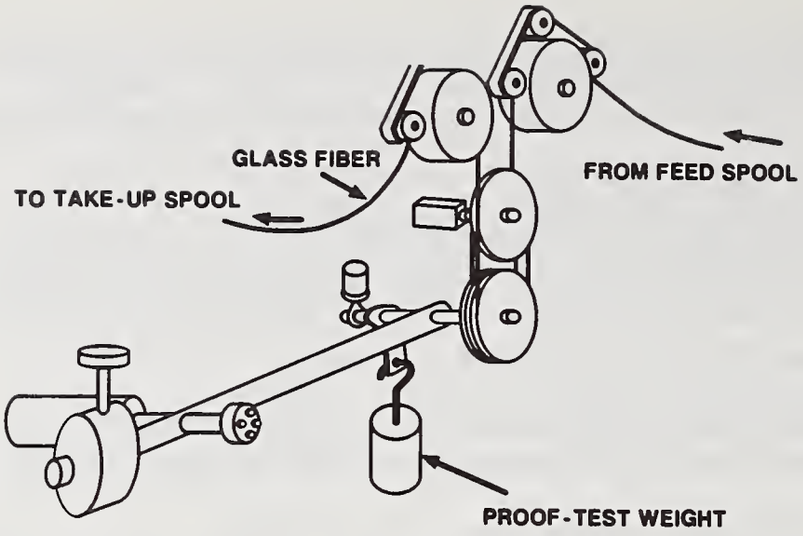

Fig 1. Constant load prooftester.

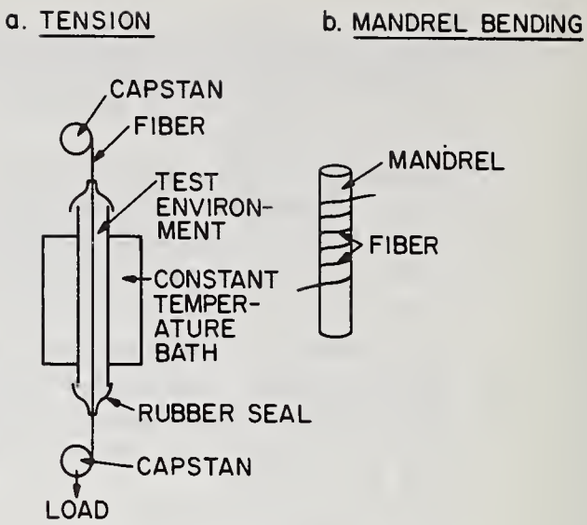

Fig 2. Fatigue test methods.

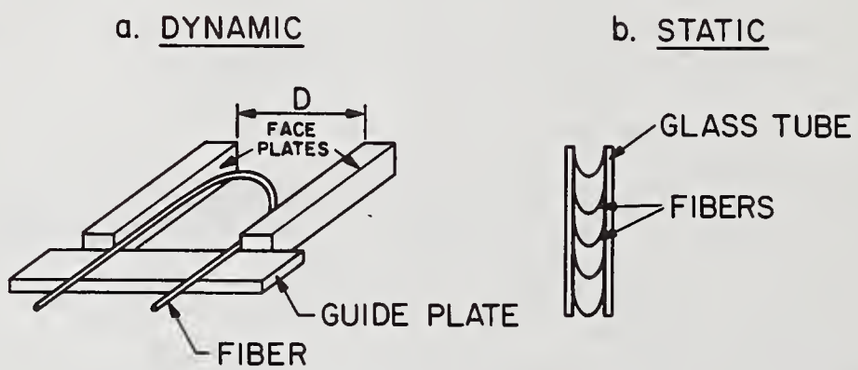

Fig 3. Two-point bend techniques.

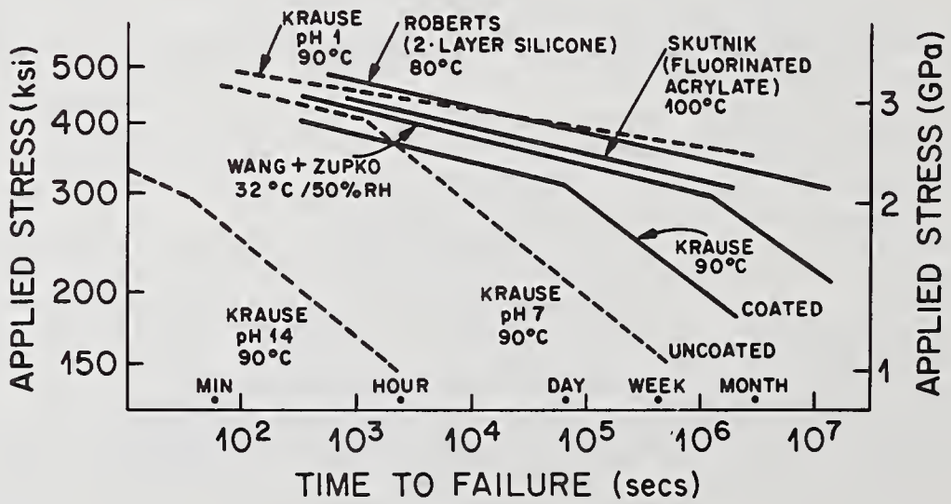

Fig 4. Static fatigue of silica fiber.

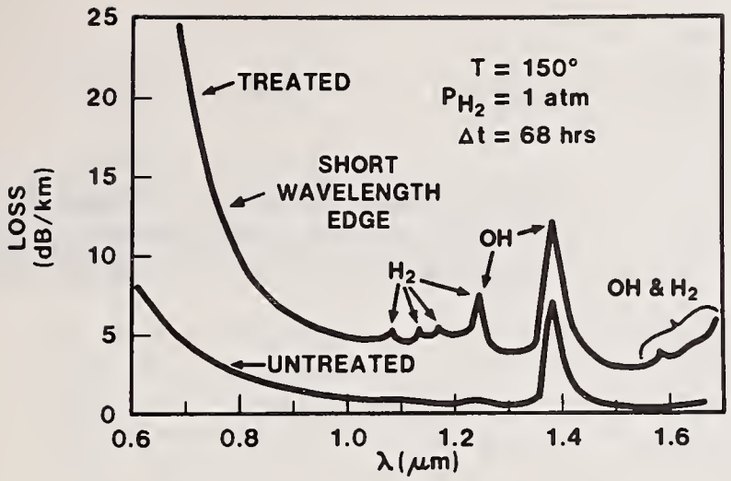

Fig 5. Loss spectra for untreated and for hydrogen treated fibers, showing basic hydrogen induced losses.

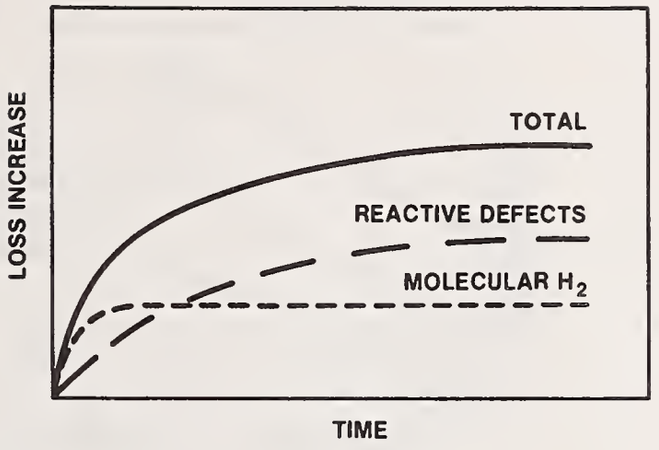

Fig 6. Loss increases versus time for fiber exposed to hydrogen, showing components due to molecular H_2 and due to reactions at defects.

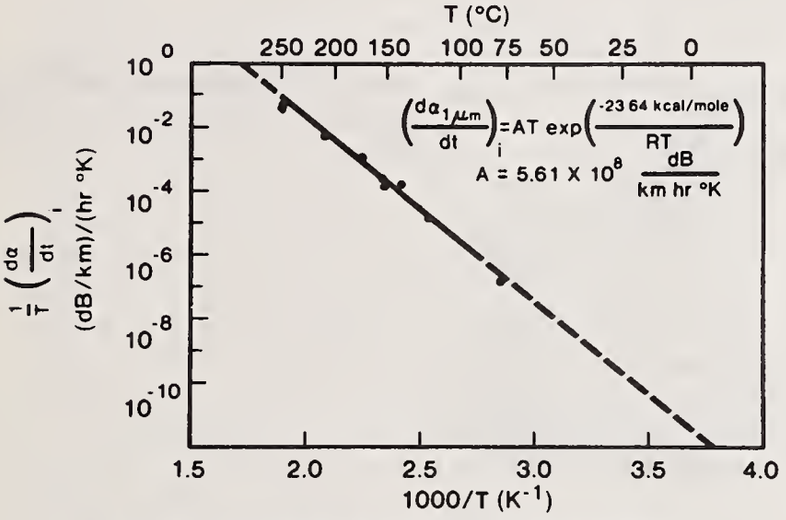

Fig 7. Temperature dependence for initial rate of loss increase in Ge-doped single mode fibers. Short wavelength loss edge component measured at 1.0μm. Hydrogen pressure is 1.0 atm.

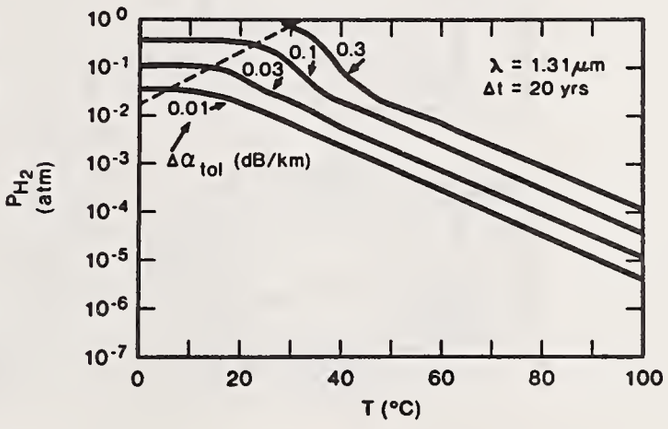

Fig 8. Tolerable hydrogen pressures for Ge-doped single mode fibers. Curves are for different values of allowable loss increases at 20 years.

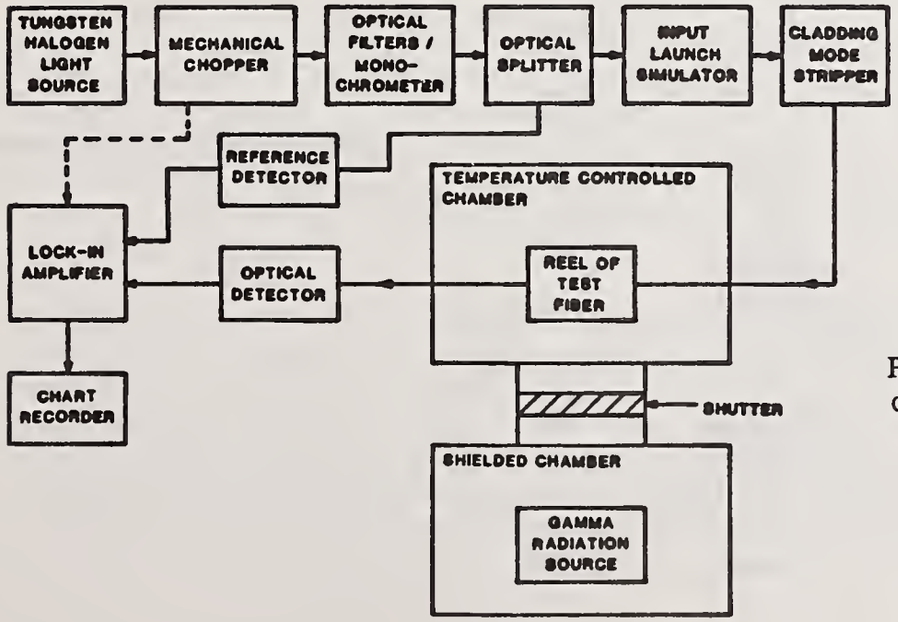

Fig 9. Instrumentation for testing the effects of adverse nuclear environments.

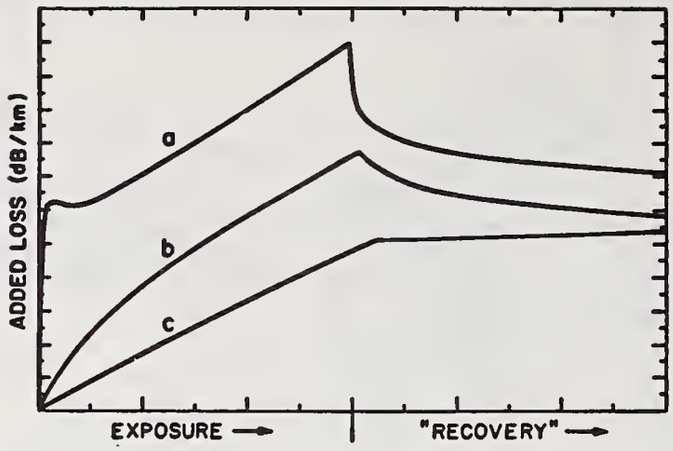

Fig 10. Radiation induced loss responses for three common optical fiber core compositions: a, silica; b, germanium doped silica; c, phosphorus doped silica.

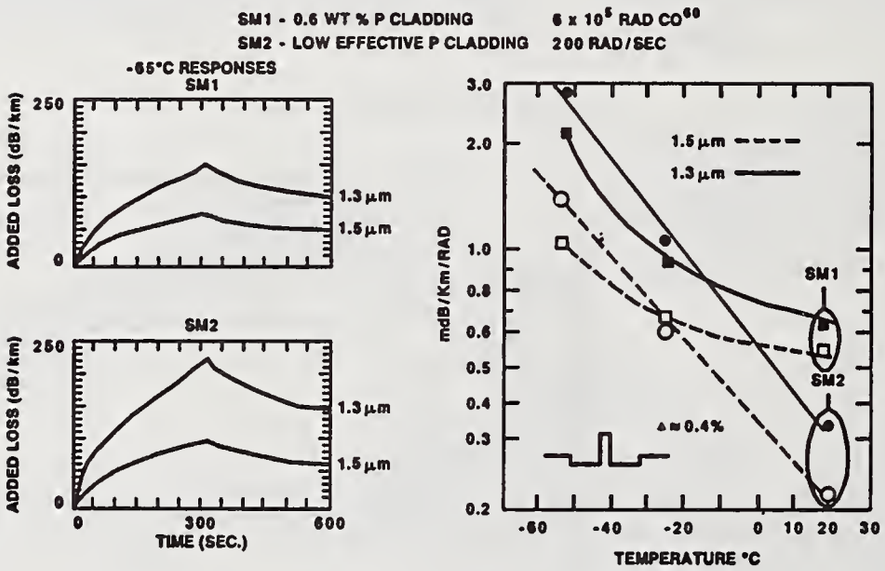

Fig 11. Temperature dependence of the radiation induced loss for two single mode fibers.

RADIATION ENVIRONMENTS

Environment	Radiation Type	Dose Rate	Temperature
Terrestrial	Gamma from U_{238}, K_{40}, Th_{232}	100-500 mrad/yr	-50-150°C
Undersea	Gamma from U_{238}, K_{40}, Th_{232}	100 mrad/yr	3°C
Nuclear Blast	Mixed gamma, neutrons and charged particles	worst case free field at 2 psi. overpressure 35,000 rads at 16 rads/sec	-50-200°C
Nuclear Reactor	Mixed gamma, thermal and fast neutrons	gamma $10\text{-}10^6$ rad/hr/MW neutron $10^{-5}\text{-}10^{12}$ n/cm^2-sec/MW	-150-120°C
Spacecraft	Mixed gamma and charged particles	1-46 rad/day	-150-120°C

Table 1 Radiation Environments

FLUORIDE OPTICAL FIBER MEASUREMENTS: TECHNIQUES AND STATUS

Lynda E. Busse
Naval Research Laboratory
Optical Sciences Division
Washington, D.C. 20375

From the time when the first fluoride glasses were made in 1974 and it was determined soon thereafter that these glasses had the potential for losses lower than silica in the infrared, there has been a strong research effort at laboratories throughout the world to produce optical fibers from these materials [1-3]. Calculations and extrapolations based on experimental data of the intrinsic Rayleigh scattering level and the contribution from the multiphonon edge gave a determination of a minimum loss "window" to be near 2.5 microns with a loss of 0.01 dB/km [2]. The interest is in obtaining long lengths of low loss fluoride fibers for optical communications applications.

The nature of fluoride glasses causes their fiberization to be difficult due to the intricate and interwoven problems which must be overcome. The glass compositions typically contain five or six heavy metal fluoride components, for example ZrF4-BaF2-LaF3-AlF3-NaF. Each of these components must be purified of transition metal and rare earth elements which absorb in the infrared. In addition dry preparation conditions must be maintained to reduce the OH absorption loss at 2.9 microns. While silica is inherently stable to crystallization during melting, fluoride glasses are very unstable upon cooling or reheating. Thus process control must be stringent to prevent the presence of defects such as crystals or bubbles in the fibers [1-3].

Control of waveguide parameters is also essential. The fibers have a step index profile which must be accurate, and core diameter control and core/cladding concentricity must be maintained. To date fluoride fibers have been mostly multimode, with core diameters of 50-100 microns and numerical apertures from 0.1 to 0.2. Some recent fibers which are single mode will be discussed.

In this paper fluoride optical fiber measurement techniques will be discussed, including those which are typical of conventional silica measurements (e.g. cutback and scattering) as well as some other types which have been developed recently to give insight into the sources of defects and absorption loss. The experimental techniques and current loss levels will be discussed.

TOTAL LOSS To measure the total loss in a given length of fluoride fiber, the cutback method, similar to that used for silica fibers, has been used. There are some differences in the experimental setup, however. At NRL, a high intensity infrared zirconia source is used; the light is directed through a set of order-sorting filters and into a monochromator which has a computer-driven stepper motor. Two gratings are used for

scans from 1-4 microns, with step size of 0.01 micron. The light exiting the monochromator is chopped and then collimated and focussed by two spherical mirrors, mounted slightly off-axis. The light is focussed to match the fiber numerical aperture, and the spot size at the focus is either equal to or greater than the core diameter. The fiber output end is mode stripped by immersing it in index matching fluid. The light exiting the fiber is collected by an indium antimonide infrared detector which is connected to a lock-in analyzer interfaced to the computer. Care is taken to do the measurement at zero tension.

Figure 1 is a summary plot [2] of the best losses achieved to date at British Telecom Research Laboratories, Nippon Telephone and Telegraph (Japan), and NRL. NRL and NTT have achieved 1 dB/km [4] and 0.7 dB/km [5], respectively, over 30 m. lengths. BTRL has achieved 3.9 dB/km over 100 m. as shown and 9.5 dB/km over 400 m. [6]. Due to the inhomogeneous number of scattering defects in the fibers, longer lengths often show higher loss. The consistency of total loss results among the different laboratories has not been fully tested, but will be essential as losses get even lower. Several kilometers of fiber will be needed to accurately determine losses as they approach the theoretical limits.

Some single mode fluoride fiber results have been reported [7,8]. The lowest loss achieved was 3 dB/km at 2.5 microns [8]. The core diameter was 11 microns, $\Delta n=0.47\%$, and the cutoff wavelength was 2.1 microns.

SCATTERING LOSS Since the total loss is composed of scattering and absorption, it is necessary to determine each to evaluate a fiber's quality. There are many sources of extrinsic scattering loss in fluoride fibers, including crystals, bubbles, sub-micron scattering centers, and interface defects. Tighter process control has substantially lowered the number of crystals and sub-micron particles, but defects still exist. Thus an accurate determination of the scattering loss in fluoride fibers is essential for process improvement.

The measurement is done with a scattering sphere detector, similar to work done on silica fibers over ten years ago. The loss is calculated by: $\alpha(\text{dB/km}) = 4.34 \times 10^5 \, [P_{sc} / (P_o \times L)]$, where P_{sc} = Scattering intensity; P_o = Intensity of light exiting the fiber; and L = Diameter of the scattering sphere. Several measurements have been made in the visible with a krypton laser [9], for example, using a scattering sphere which has an inner white reflective surface. A plot was made to determine whether the scattering follows a Rayleigh scattering law (i.e. varies as λ^{-4}) or Mie scattering (i.e. varies as λ^{-2}). The scattering value at 2.5 microns is then inferred from an extrapolation.

At NRL scattering measurements can be done directly at 2.5 microns with a color center laser. The scattering sphere is gold coated to be reflective in the infrared, and an indium antimonide detector is used. Although only 5 cm. lengths are measured at a given time, many such measurements can be made to

give a general level of scattering in the fiber.

Although present fibers are of good quality such that the losses obey a Rayleigh scattering behavior, there is a non-trivial contribution to the scattering due to a wavelength independent offset. Early fluoride fibers had wavelength independent offset values of several dB/km [10] but more recent fibers show an offset of less than 1 dB/km [9,11]. Figure 2 shows such an offset for fluoride fibers measured in the past at NRL. The source of this offset has not been determined, but is suspected to be due to particles of size greater than the probe wavelength, or core diameter fluctuations.

Recently NRL has reported scattering measurements on a fluoride fiber which approach the theoretical limit of Rayleigh scattering [11]. The results are listed in Table I; this fiber had a core diameter of 30 microns and numerical aperture of 0.13. Note that the measured fiber scattering value at 2.55 microns was 0.025 dB/km, which is almost equivalent to what is obtained from a Rayleigh scattering extrapolation of the value (7.5 dB/km) measured at 0.63 microns. Thus there is no observed wavelength independent loss in this fiber.

There have been other measurements done to probe the causes of scattering in fluoride fibers. At NTT a three-dimensional scattering experiment was devised to give a full angular scattering plot of a small segment of fiber [12]. A comparison of a silica fiber and two fluoride fibers of different composition was made; it was found that the silica fiber and one of the fluoride compositions gave a Rayleigh scattering polar plot, while one of the fluoride compositions showed some backscattering which was attributed to phase separation.

Determining what the scattering defect is poses a difficult problem, as optical microscopy cannot resolve particles of micron size or smaller. At British Telecom Laboratories, theoretical calculations were made to determine the effect on the scattering of various types and sizes of particles suspected to be in their fibers [13]. NTT has developed a direct technique of analyzing particles in fibers by micro-Raman scattering [14]. They found that particles in their fibers gave Raman spectra which matched that of zirconium oxide crystals. At NRL various sources of scattering have been found by isolation of the particles and subsequent electron microscopy and diffraction measurements. Fluoride crystals nucleated by platinum, phosphide impurities, and phase separation are some of the defects found by such analyses [15].

ABSORPTION LOSS It is also important to measure absorption loss in fluoride fibers, since there are many infrared absorbing impurities in the raw materials which make the glass; these include the transition metal ions of iron, cobalt, copper, and nickel. Purification of the raw materials is a challenging task, as levels must ultimately reach parts per trillion for the fiber to be ultra low loss [1]. To measure the absorption loss, the technique of laser calorimetry as developed by White and Midwinter [16] for silica glass and fiber has been used

for fluoride fibers at various wavelengths using a krypton laser [17]. The technique involves measuring both the rise time and temperature increase in a fiber after the laser light is launched into it. Using known thermal properties of the glass and fiber parameters, and after calibration with a source of known heat loss, the absorption coefficient at that wavelength can be determined. As shown in Figure 4, with enough measured absorption (as well as scattering) values at given wavelengths, the total loss can be deconvoluted to give the various impurity levels.

Another critical source of absorption loss is neodynium, a major contaminant in lanthanum; its absorption peak is at 2.51 microns, which is near the fiber's minimum loss wavelength. A technique for measuring this absorption using photoluminescence has been developed at both NRL and GTE Laboratories [18,19]. By using a proper excitation wavelength (e.g. 514 nm.), the luminescence spectrum may be obtained. Using standards of known impurity content, the quantity of neodynium in a fiber can be determined [20].

SUMMARY The types of optical measurements made on fluoride fibers have been discussed. As losses become lower and approach theoretical limits, there is need for longer lengths of fiber and comparison of results among laboratories to insure accuracy of total loss measurements. Scattering measurements are necessary to improve fiber preparation techniques. For the first time, NRL has reported scattering values approaching the theoretical Rayleigh scattering limits. Techniques for measuring absorption in fluoride fibers have been described, including laser calorimetry and photoluminescence. Both scattering and absorption techniques will need to be improved in order to measure the ultra low transmission losses possible with these new fluoride fibers.

ACKNOWLEDGEMENT The work of George H. McCabe in obtaining the NRL scattering data reported herein is gratefully acknowledged.

REFERENCES

1. D.C. Tran et al., J. Lightwave Tech., V. LT-2, p. 566 (1984); see also Materials Science Forum, V. 5-6 (1985) and V. 19-20 (1987).

2. P.W. France et al., Br. Telecom Technol. J., V. 5 (1987).

3. Proc. of the 5th Intl. Symp. on Halide Glasses, Japan, June 1988, to be publ. in Mat. Sci. Forum.

4. D.C. Tran et al., SPIE V. 618, Infrared Opt. Mater. and Fibers IV, p. 48 (1986).

5. T. Kanamori and S. Sakaguchi, Jap. J. Appl. Phys., V. 6, p. L468 (1986).

6. P.W. France et al., Halide Glasses for Infrared Fiber-optics, ed. by R. M. Almeida, Martinus Nijhoff Publ., p. 253 (1987).

7. Y. Mimura, Mat. Sci. Forum, V. 19-20 (1987).

8. Y. Ohishi et al., J. Lightwave Tech., V. LT-2, p. 593 (1984), and Y. Ohishi et al., Electron. Lett., V. 22, p. 1034 (1986).

9. P.W. France et al., Mat. Sci. Forum, V. 19-20, p. 381 (1987).

10. D.C. Tran et al., Electron. Lett., V. 19, p. 165 (1983).

11. I. Aggarwal et al., "Scattering Losses in Fluoride Optical Fibers", Ref. 3.

12. H. Hattori et al., Appl. Optics, V. 25, p. 3549 (1986); H. Hattori et al., ibid., V. 26, p. 650 (1987).

13. M.W. Moore, "Scattering Losses in Fluoride Glass Fibre", Ref. 3.

14. T. Kanamori, Mat. Sci. Forum, V. 19-20, p. 363 (1987).

15. G. Lu and J. Bradley, ibid., V. 6, p. 551 (1985); V. 19-20 (1987); and "Phase Separation and Crystallization in a Lead-Containing Fluorozirconate Glass", Ref. 3.

16. K.I. White and J.E. Midwinter, Opto-Electronics, V. 5, p. 323 (1973).

17. M.W. Moore et al., Proc. 12ECOC, Barcelona, p. 299 (1986).

18. J.A. Freitas et al., Mat. Sci. Forum, V. 19-20 (1987).

19. W.J. Miniscalco et al., ibid.

20. J.A. Freitas et al., Ref. 3.

TABLE I

Scattering losses in bulk glass and short lengths of fiber

λ (microns)	LAUNCH N.A.	SCATTERING LOSS (dB/km) MEASURED	EXTRAPOLATED
0.63 (Bulk)	---	3.9	0.015
0.63 (Fiber)	0.10	7.5	0.028
2.55 (Fiber)	0.10	0.025	---

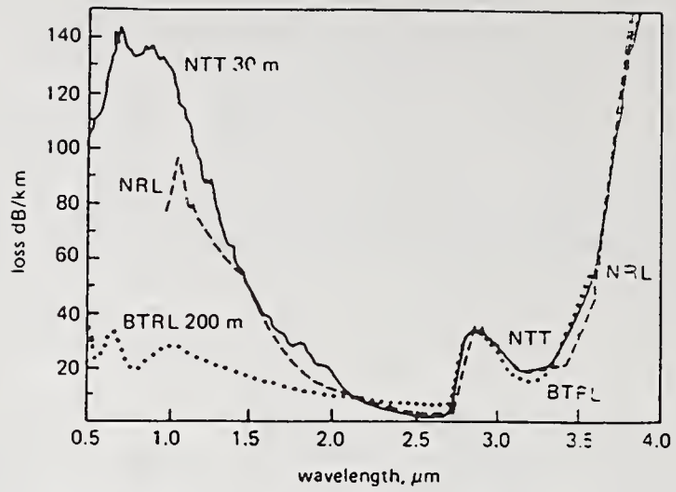

FIGURE 1 : Comparison of total loss results on fibers made at BTRL, NTT, and NRL [2].

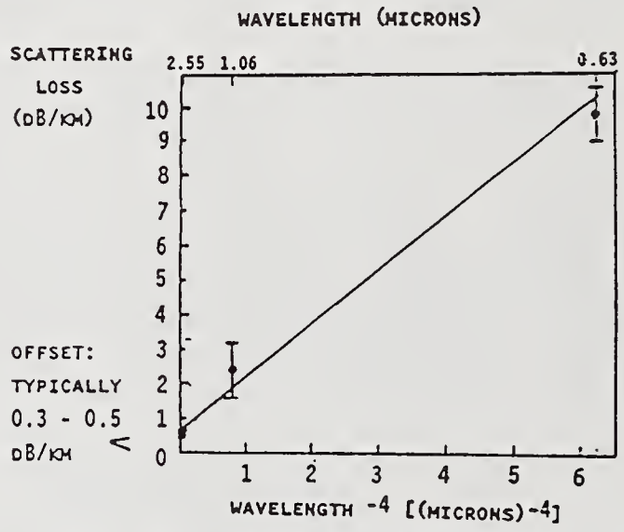

FIGURE 2 : Past NRL fiber scattering results, showing the wavelength independent offset [11].

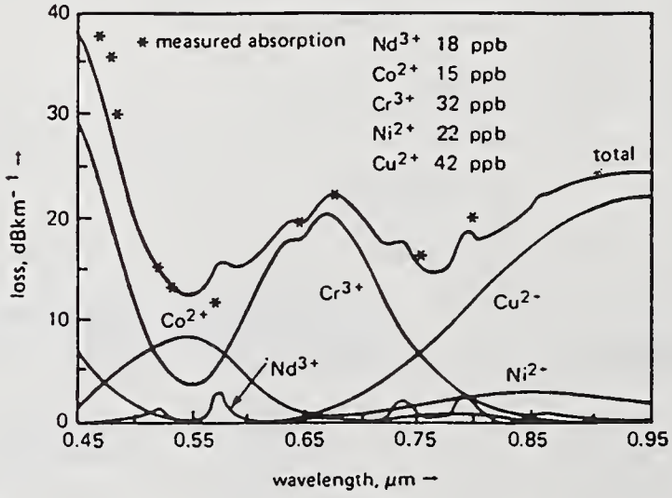

FIGURE 3 : Deconvolution of loss to obtain impurity levels [17].

BEND LOSS MEASUREMENTS ON SINGLE MODE FIBERS

A. Hordvik, M. Eriksrud, S. Lauritzen
Optoplan, P.O.Box 1963 N-7002 Trondheim, Norway

Introduction

The bend loss sensitivity of a fiber is of considerable practical importance. There often is a need to wind short lengths of fibers in a small coil f.inst. in splice boxes, and in cables where fiberbending is an important loss mechanism [1,2].

This paper presents the results of bend loss measurements on a number of single mode fibers. It is shown that to properly characterize a fiber's bend loss performance, measurements must be made over a range of bend radii. Further, that when making measurements at lower bend losses, great care must be taken to avoid microbend losses. We do not observe the discrepancy seen by others [2,3], between theoretically predicted behaviour and the experimental results.

Experiment

Bend losses were measured at 1300nm, 1550nm, 1600nm and 1640nm by winding the fiber on cylinders of varying diameters. The spectral bandwidth was 4nm. The fiber was laid in a single layer. To avoid microbend losses it was important to use cylinders with good circularity and smooth surfaces and to wind the fibers loosely. Experiments were done with fiber lengths as long as 300 m and more than 1000 turns.

Seven different commercial fibers were investigated. Three were matched clad (MC) fibers which will be designated A, B and C. Fiber D was by the manufacturer called an MC fiber, but it actually has a slightly depressed cladding. Fibers E and F were depressed cladding (DC) fibers, and fiber G was a dispersion shifted (DS) fiber.

Results

In Fig. 1 is shown bend losses versus bend diameter at 1550nm for the MC fibers and the DS fiber. For fibertype A curves for two fibers (A1 and A2) are shown. In addition there is drawn a theoretical loss curve for fiber A based on Marcuse's theory [4] and where the nominal fiber parameters have been used in

the calculations. The losses are given in dB/km, and several tests were done to confirm that the loss per unit length was independent of the number of turns.

Some of the curves show variations in slope. This is believed caused by whispering gallery modes [5]. The true MC fibers (A, B and C) show on an average no deviation from the expected theoretical slope as has been observed by others [2, 3]. Fiber D shows a less steep slope. This is probably due to the slightly depressed cladding [6].

To achieve good agreement with theory it was necessary to take great care to prevent loss contributions from microbends. This was especially the case at larger bend radii where the bend loss was small and the number of turns large. By using cylinders with round and smooth surfaces and winding the fiber loosely and evenly spaced, microbend losses could be avoided.

The curve for fiber A2 follows on an average the theoretical curve. Fiber A1 shows a lower loss. Larger variations in loss were seen for other fibers of type A, but the variations were within the expected limits considering the specified tolerances on the fiber parameters.

In Fig. 2 is shown bend loss curves at 1550nm for the two depressed clad fibers. For comparison the bend loss curve for a MC fiber (A2) is also included. The DC fibers show a marked change in slope with increasing bend radius. This behaviour is in quantitative agreement with Andreasen's theory for bend losses in DC fibers [6]. In some regions there is an increase in loss with decreasing bend radius. Measurements at longer wavelengths indicate that this effect is caused by whispering gallery modes.

The DC fibers generally show a smaller bend loss than the MC fibers at small bend radii. At larger bend radii the MC fibers have the lower losses, (Fig. 2).

Discussion

For some applications it is the bend sensitivity at small radii which are of interest as f.inst. in splice boxes, transmitters and receivers. For cabling purposes one is concerned with long fiber lengths where bend losses (in the range of) 0.01 dB/km can be harmfull. In this case it is the bend performance at larger radii which is of importance [1, 2].

The experiments show that for DC fibers the results from small radii cannot be extrapolated to larger radii. To establish the sensitivity of the DC fibers to cabling induced losses, measurements must be made at larger bend radii where great care must be excercised to avoid microbending losses.

For MC fibers it was found that the slope of the loss curves on the average agreed with the predicted behaviour. But even for these fibers it is necessary to make measurements over a range of radii to ensure that whispering gallery modes do not interfere with the results.

It should also be noted that to properly characterize a specific fiber type, measurements must be made on a number of fibers to establish the spread in bend sensitivity. Our measurements indicated that the spread varies considerably from fiber type to fiber type.

Acknowledgement

Optoplan gratefully acknowledges the support of STK - Alcatel, Oslo, Norway for this work.

References

1. A. Hordvik, M. Eriksrud, "Loss Mechanisms in Single-Mode Fibers Jacketed with a Loose Jelly-Filled Tube", J. Lightwave Technol. vol LT-4, pp 1178-1182 (1988)
2. P. Geittner, H. Lydtin, F. Weling, D.U. Wiechert, "Bend loss characteristics of single mode fibers", 13th Europ. Conf. on Optical Comm. (ECOC), Helsinki, Finland 13-17 Sept. 1987, Technical Digest, Volume II pp 97-108 (1987)
3. P.K. Bachmann, D. Leers, D.U. Wiechert, "The bending performance of matched cladding, depressed cladding and dispersion flattened single mode fibres", OFC/IOOC 87, Reno, Nevada, 19-22 Jan. 1987, Technical Digest, Postdeadline paper PDP1 (1987)
4. D. Marcuse, "Curvature loss formula for optical fibers" J. Optical Soc. Am. 66, pp 216-220 (1976)
5. A.J. Harris, P.F. Castle, "Bend loss measurements on high numerical aperture single-mode fibers as a function of wavelength and bend radius", J. of Lightw. Techn. LT-4, pp 34-40 (1986)
6. S.B. Andreasen, "New bending loss formula explaining bends on loss curve", Electronics Lett. 23, pp 1138-1139 (1987)

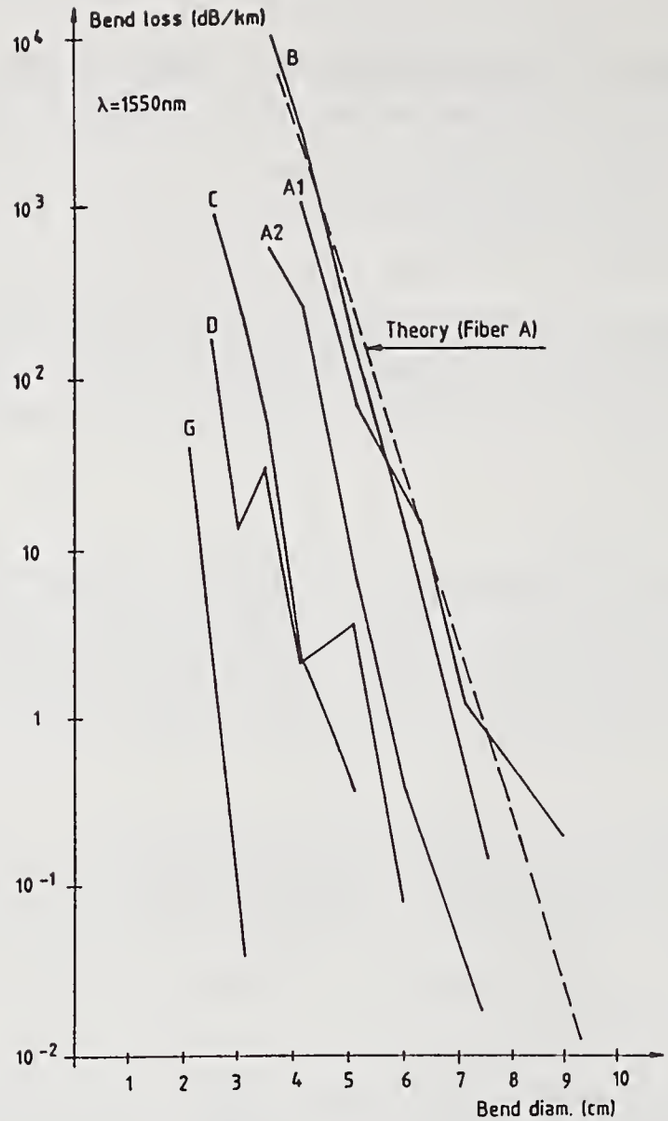

Fig.1

Bend loss vs. bend diameter for five MC fibers (A1, A2, B, C and D) and one DS fiber (G). The broken line shows the calculated bend loss for a fiber of type A using nominal fiber parameters.

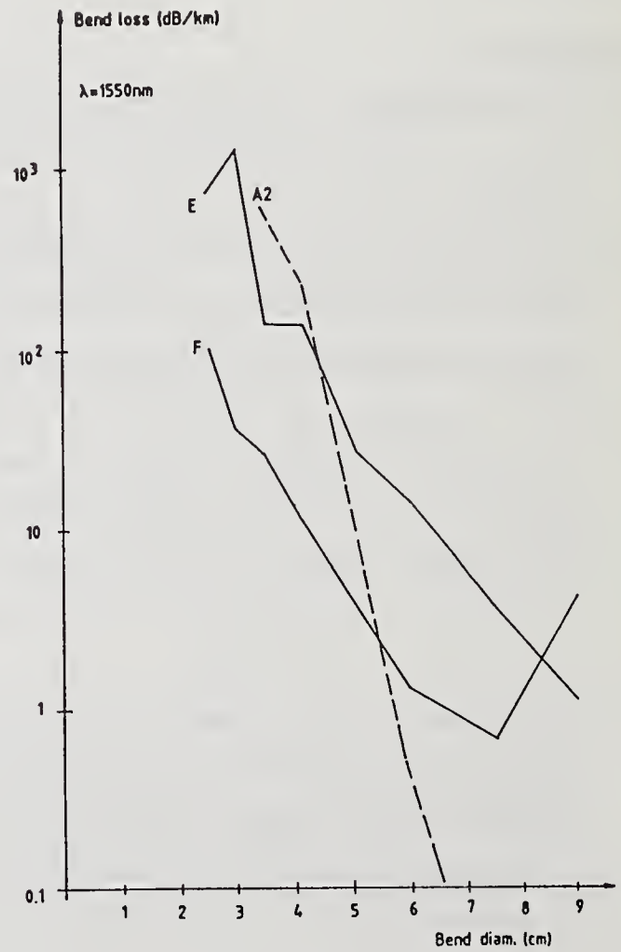

Fig. 2

Bend loss vs. bend diameter for two different DC fibers (E and F). The broken line shows the bend loss for a MC fiber (A2).

INDUCED LOSSES IN STRAINED LOOSE TUBE FIBER CABLES

L. Bjerkan, E. Nesset and O. Alm

EB Cables, P.O. Box 419, N-1371 Asker, NORWAY

INTRODUCTION

In optical fiber cables designed for outdoor use (aerial, burial or sea cables) the most common designs are fibers immersed in a loose tube or slotted core structure. When such cables are subjected to high tension or high temperatures, the fibers may be pressed against the inner wall of the surrounding medium and microbend attenuation occurs. So far microbend experiments have been limited to lateral load tests where a short length of fiber is compressed between plates covered with sandpaper[1,2], or compressed against a wire mesh[3], by introducing a short length of fibers in a vessel filled with small metallic spheres and applying pressure[4], or by introducing microbends by a helical winding arrangement of the fibers where fiber layers cross each other[5]. These experiments have provided interesting data for microbend attenuation vs. wavelength and fits to existing theoretical expressions have been achieved[4].

However,whether these experiments adequately describes the situation in an actual cable is questionable. Therefore new experiments where the fiber is pressed directly against the wall of actual tube materials for loose tube cables will be described. Several fiber types spanning large ranges of production tolerances of basic fiber parameters have been subjected to these experiments.

EXPERIMENTS

About 140 m of tube was wound in one layer on a large 33 cm diameter drum. During laying the tube was split in the length direction using a splitting tool designed for that purpose. This experimental arrangement allowed for well-controlled and repeatable fiber insertion under controlled tension. Two tube materials, polycarbonate (PC) and polybutylene terephthalate (PBT), which both have been commonly used in loose tube cable designs have been investigated. The PC tube had inner and outer diameters of 1.6 and 2.2 mm respectively while the corresponding figures for the PBT tube were 1.4 and 2.2 mm. Both tubes were filled with jelly during extrusion, and part of the jelly remained after splitting and winding the tube. During repetitive winding an unwinding of fibers, however, the amount of jelly gradually diminished.

The fibers were wound on the drum one at a time under controlled tension as shown in figure 1. During winding the fibers followed smoothly the bottom of the splitted tube and was in this way pressed against the tube wall with the tangential tension (cf. fig. 1) $T=mg/2\cos\alpha$. The relative fiber elongation is then:

$$\varepsilon = T/EA = mg / 2EA\cos\alpha \qquad (1)$$

where EA is the effective elastic stiffness of the primary coated

fiber which is ≈ 880 N.

The attenuation vs. wavelength was measured using a conventional spectral attenuation (cut-back) measurement setup. The attenuation of the fiber configuration on the drum was corrected for intrinsic fiber attenuation, and the pure strain-induced losses were found. Three classes of fibers of current single-mode design were subjected to this treatment: The first was conventional match clad fibers (MC1) designed for 1.3 μm operation. The second class was match clad fibers (MC2) designed for less bending and microbending sensitivity at longer wavelengths while the third class was depressed inner cladding (DIC) fibers. All fibers were primary coated with acrylate, but the coating on the match clad and DIC fibers were of different types. Fibers have been selected from the available supplies such that basic fiber parameters mode field diameter (MFD), 2w, and cut-off wavelength λ_c span wide regions within their specified limits. Table I shows first the fiber manufacturers tolerances of these parameters and secondly the actual parameter ranges of the fibers used in this investigation. Some of the fibers were wound repetitively on the drums in order to check the reproducibility of the experiments and also the influence of the diminishing amount of jelly in the splitted tube.

Table I

General production tolerances and actual range of parameters for three classes of fibers used in this study.

Class of fiber	MFD and cut-off range (producers specs.)	MFD and cut-off range (fibers studied)
MC1	2w=9-11 μm λ_c=1130-1270 nm	2w=9.82-10.52 μm λ_c=1153-1260 nm
MC2	2w=9-10 μm λ_c=1190-1330 nm	2w=9.13-9.80 μm λ_c=1219-1320 nm
DIC	2w=8.1-9.9 μm λ_c=1200-1280 nm	2w=8.2-9.2 μm λ_c=1205-1275 nm

RESULTS AND DISCUSSION

A. Tube materials. The inner walls of the two tube materials were photographed using a scanning electron microscope. Figure 2 shows pictures of the two tube materials with the magnification indicated. The microscopic structure of these materials are clearly different. Using an image analyzer the maximum amplitude of the irregularities are ≈3 μm for the PC tube and ≈0.5 μm for the PBT tube.

B. Microbend loss results. Figures 3 and 4 show the range of induced losses experienced for the three fiber types at ε=0.22 % tensile strain calculated from (1) for the PC and PBT tube materials respectively. Figure 5 shows an example of induced losses vs. wavelength with different strains. The results revealed that the induced losses depend strongly on mode field diameter and also on the cut-off wavelength of the fibers. Fibers

with high values of the MFD and low cut-off were most sensitive while the opposite condition with low MFD and high cut-off exhibited the smallest induced losses. This behavior was common to all three classes of fibers studied. The MC1 class exhibited the largest sensitivity while the two other fiber designs showed comparable results. As indicated in fig. 3 the most sensitive fiber of the MC1 class exhibited considerable losses even at 1.3 μm for ε=0.22 % on the PC tube.

The induced losses seem to have a much stronger dependence on wavelength compared to conventional sandpaper press tests[2]; results also confirmed in our own laboratory. Not surprisingly the wavelength dependence in our results agrees better with results from a conventional tension-wind test[2]. However, experiments with the PBT tube showed less induced losses, about 40 - 60 % at 1.55 μm, than exhibited by the PC tube under otherwise equal experimental conditions. This behavior was present for all the fibers and is a clear indication that the microstructure of the tube material contributes to the induced losses (cf. fig. 2).

By winding the same fiber repeatedly with the same tension at various stages of the experiments it was observed that the induced losses gradually became less. This may be explained from the diminishing amount of jelly in the split tube and that the jelly itself may possess some kind of microstructure which contributes to the induced losses. At present this has not been further analyzed.

CONCLUDING REMARKS

Experiments with strained fibers in a realistic cable structure have been carried out and induced loss tolerances for current single-mode fiber designs have been obtained for fibers embedded in actual tube materials. Efforts are underway to interpret the results in terms on existing theoretical expressions and to compare the obtained results with experiments on a strained complete cable.

ACKNOWLEDGEMENT

The authors thanks the Norwegian Telecommunications Administration (NTA) for partial financial support, and S. Hopland, NTA and S. Stueflotten, EB Cables for encouraging discussions. We also thank Corning and Philips for kindly supplying relevant fibers .

REFERENCES

[1] J. A. Dixon, M.S. Giroux, A. R. Isser and R. V. Vandewoestine Tech. Dig. OFC/IOOC' 87 Reno, NV (1987) paper TuA2.
[2] P. F. Glodis, C. H. Gartside, J. S. Nobles: Tech. Dig. OFC/IOOC' 87 Reno, NV (1987) paper TuA3.
[3] A. O. Garg, C. K. Eoll: Tech. Dig. Symp. on Opt. Fiber. Measurements, Boulder CO. (1986) p.125.
[4] M. Artiglia, G. Coppa, P. diVita H. J. Kalinowski and M. Potenza: Proc. ECOC 87, Helsinki (1987) p.125.
[5] N. Kamikawa, C.-T. Chang: Tech. Dig. Symp. on Opt. Fiber Measurements, Boulder CO. (1986) p.129.

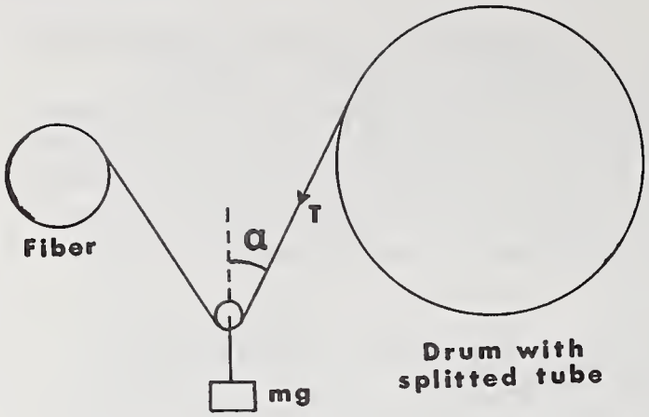

Figure 1

Spooling of fiber
in splitted tube

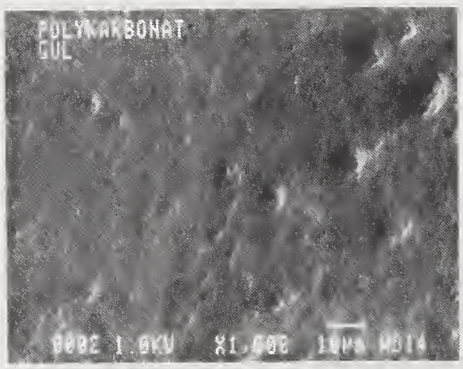

a.

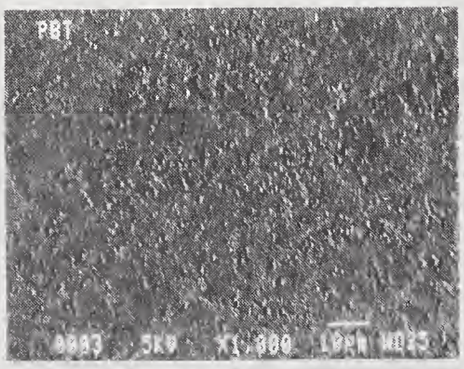

b.

Figure 2

Photograph of inner
tube wall, a: PC,
b: PBT

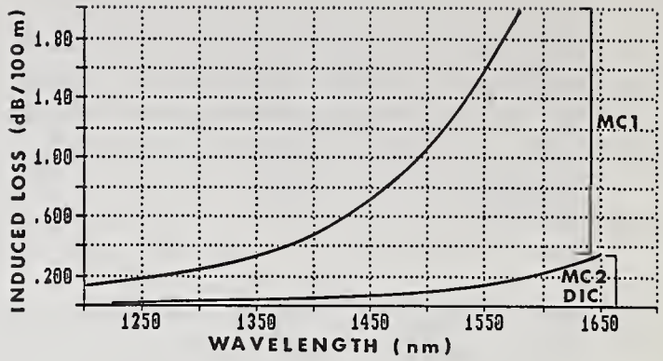

Figure 3

Ranges of induced losses
on PC tube, ε=0.22 %,
three fiber classes

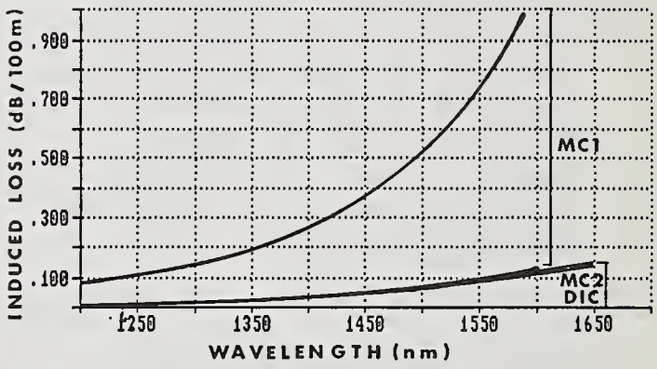

Figure 4

Ranges of induced losses
on PBT tube, ε=0.22 %,
three fiber classes

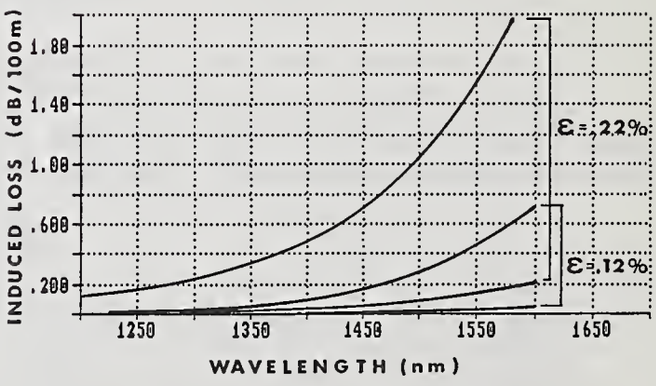

Figure 5

Ranges of induced losses
at different strains.
Class MC1 fibers, PC tube

MEASUREMENTS OF SINGLE MODE FIBER ATTENUATION OVER AN EXTENDED SPECTRAL RANGE

Z. Pasturczyk, C. Saravanos, R.S. Lowe,
Northern Telecom Canada Ltd.
Optical Cable Division
Saskatoon, Saskatchewan, Canada

ABSTRACT

A simple modification of the standard cutback method is proposed to allow reliable measurements of attenuation of single mode fiber for wavelengths shorter than the cutoff wavelength. Limitations of the standard cutback method were eliminated by optimization of the fiber layout conditions. Experimental work carried out on depressed cladding and matched cladding fiber samples demonstrated good repeatability for fiber attenuation measurements: $\pm$ 0.020 dB/km at 780 nm, and $\pm$ 0.010 dB/km at both 1310 nm and 1550 nm.

1.0 INTRODUCTION

Recently, low cost transmission systems for use in subscriber loop networks have been built[1] utilizing inexpensive 800 nm lasers and conventional Single Mode Fiber (SMF) optimized for 1300 nm operation. At this wavelength, transmission rates of 150 Mbits/sec over distances of 22.5 km have been achieved by applying special filtering techniques[2] both to strip higher order modes and to suppress intermodal dispersion and modal noise. In fact, it has been demonstrated that when such a system is set up using lasers operating in a single longitudinal mode, it is attenuation, and not dispersion, limited. Under these conditions, it is imperative to know precisely and accurately the attenuation of SMF when operating below the cutoff wavelength of the second, and, even the third, order modes.

Unfortunately, the ordinary cutback measurement technique cannot be used below the factory measured cutoff wavelength due to the presence of the so-called "mode hump". A mode hump corresponding to each higher order mode shows up on the traces of attenuation versus wavelength (see Figure 1a) if the effective cutoff wavelength of that mode in the "long" test fiber is considerably different than the corresponding cutoff wavelength in the "short" reference fiber. In these cases, attenuation measurements within a mode hump are not valid because the modal content in the "long" fiber is different from that in the "short" fiber.

This paper describes a method for accurate measurements of SMF attenuation parameters over a wide range of wavelengths by completely eliminating the mode hump effect. This has been accomplished by modifying the fiber layout conditions such that the fiber cutoff wavelengths for higher order modes become independent of length.

2.0 FIBER LAYOUT OPTIMIZATION

Optimization of the fiber layout involved measurements of cutoff wavelength as a function of the fiber length and fiber bend conditions (i.e. bend diameter and number of bends). It was found that the cutoff wavelength dependence on the fiber length can be changed under certain bend conditions. Reducing the fiber bend diameter attenuates the LP_{11} mode and shifts the effective cutoff wavelength towards shorter wavelengths. At these shorter wavelengths, the attenuation of the LP_{11} mode in a straight piece of fiber becomes negligible in relation to its value at the factory measured cutoff wavelength. Under these circumstances, attenuation due to fiber bending dominates overall attenuation of the LP_{11} mode and the effective cutoff wavelength becomes independent of fiber length. Therefore, by taking advantage of this inverse correlation between the length and bend dependence of cutoff wavelength, the right combination of bend diameter and number of bends will result in the same cutoff wavelengths in the "long" and "short" fiber. Once this is accomplished, the mode hump will disappear from traces of attenuation versus wavelength as shown in Figure 1b.

A number of experiments were conducted to characterize the cutoff wavelength dependence on the fiber bend diameter, number of bends and fiber length. The objective was to determine the maximum bend diameter and minimum number of bends required to reduce significantly the length dependence of the fiber cutoff wavelength for two types of single mode fiber; depressed cladding and matched cladding. Each fiber was approximately 2 km in length.

Cutoff wavelength measurements were done using the multimode fiber reference technique.[3] The results are shown in Figures 2, 3 and 4. Figure 2 shows the dependence of cutoff wavelength (λ_c) on the bend diameter. It is seen that λ_c is a linear function of the reciprocal of the bend diameter. The slope of each line represents the sensitivity of λ_c to bending.[4] Figure 3 shows how the cutoff wavelength (λ_c) changes with the number of bends (N) for a fixed bend diameter. Note that increasing the number of bends (N) has a similar effect on λ_c to decreasing the bend diameter but since λ_c is inversely proportional to log (N), the dependence is weak and changing N is not a replacement for changing the bend diameter. It is more like fine tuning of the optimum fiber layout. Figure 4 shows the cutoff wavelength dependence on the fiber length for different bend diameres. It is seen that reducing the bend diameter changes the slope of each line and for bend diameters of 2 - 3 cm, the cutoff wavelength is almost independent of the fiber length.

It should be pointed out that bending the fiber more than absolutely necessary will attenuate the LP_{01} mode at long wavelengths and adversely affect the attenuation measurement accuracy and repeatability in that region. The optimum fiber layouts selected for fibers used in this work is shown in Table 1. Fiber attenuation measurements using the layout conditions listed in Table 1 are discussed in the following section.

3.0 FIBER ATTENUATION MEASUREMENTS

Fiber attenuation measurements were performed using the standard cutback measurement technique for single mode fiber. The spectral range of interest was from 750 nm to 1600 nm. The fiber under test was deployed using the layout conditions shown in Table 1. Both, matched cladding and depressed cladding SMF samples were measured. Each fiber was measured five times to check the repeatability of the proposed test method. As Table 1 indicates the achieved measurement repeatability is $\pm$ 0.02 dB/km at 780 nm and $\pm$ 0.01 dB/km at both 1310 nm and 1550 nm.

4.0 CONCLUSIONS

It has been shown in this paper that accurate and precise measurements of SMF attenuation within the extended spectral range of 750 nm to 1600 nm can be performed using the standard cutback method if the fiber layout condition is optimized. In addition, it has been observed that the cutoff wavelength dependence of fiber length $\lambda_c(L)$ is a function of bend diameter. The tighter the bend the weaker the dependence $\lambda_c(L)$. It has also been demonstrated that the cutoff wavelength is inversely proportional to the logarithm of number of bends of fiber for all bend diameters down to 1.0 cm.

A final word of caution. The optimum fiber layout introduces a delicate balance between the attenuation of the LP_{11} mode and the attenuation of LP_{01} mode. Different fiber types require different layout conditions. Depressed cladding fiber needs tighter bends than matched cladding fiber.

5.0 REFERENCES

[1] M. Stern, W. Way, V. Shah, M. Romeiser, W.C. Young and J.W. Krupsky, in Technical Digest, Conference on Optical Fibers Communication (Optical Society of America, Washington, D.C., 1987) paper MD2.

[2] V. Shah, P. Morris, L. Curtis, M. Stern, M.A. Saibi, W.C. Young, in Technical Digest, Conference on Optical Fibers Communication (Optical Society of America, Washington, D.C., 1988) paper WQ13.

[3] EIA FOTP-80

[4] L. Wei, R.S. Lowe, C. Saravanos, "Practical Upper Limits to Cutoff Wavelength for Different Single Mode Fiber Designs". J. Lightwave Technology, Vol. LT-5, No. 9, p. 1147, 1987.

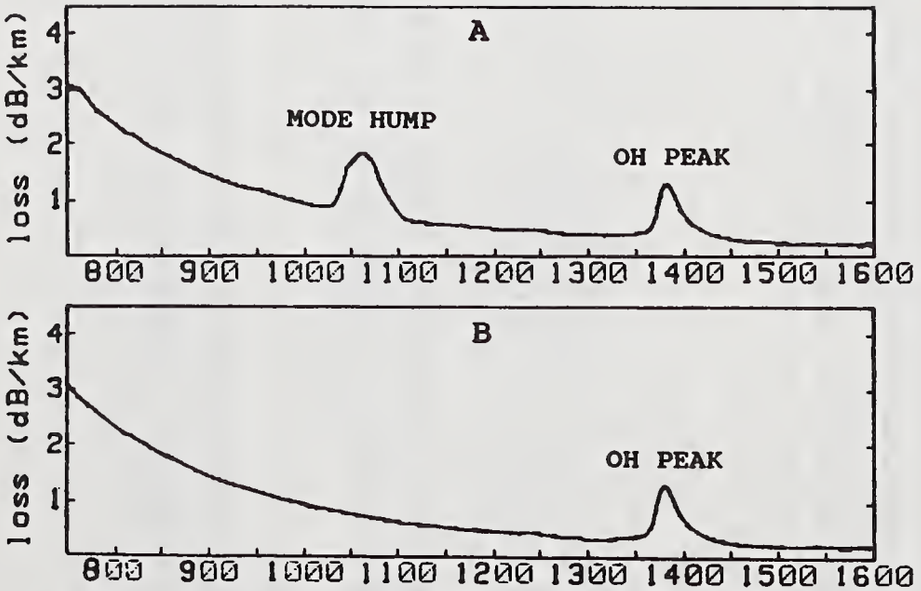

FIGURE 1. Attenuation versus wavelength.
a) Fiber layout **not** optimized.
b) Fiber layout optimized.

TABLE 2. SMF Optimum Layout and Corresponding Attenuation Measurements in [dB/km] for Selected Wavelengths in [nm].

Fiber Type	Optimum Layout	780 nm	890 nm	1310 nm	1550 nm
Depr. Clad.	2 bends 2cm dia	2.646 ±.020	1.526 ±.015	0.348 ±.006	0.217 ±.008
Match Clad.	3 bends 3cm dia	2.520 ±.007	1.472 ±.005	0.321 ±.003	0.182 ±.011

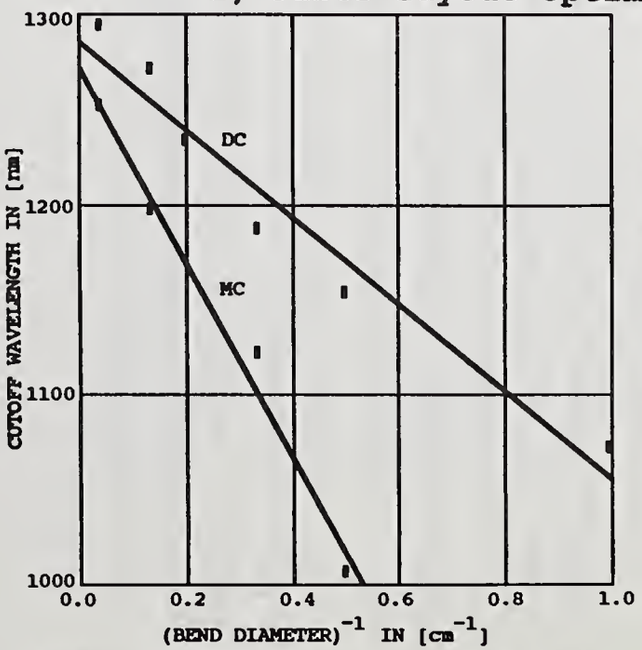

FIGURE 2. Cutoff wavelength dependence on bend diameter for single loop of fiber.

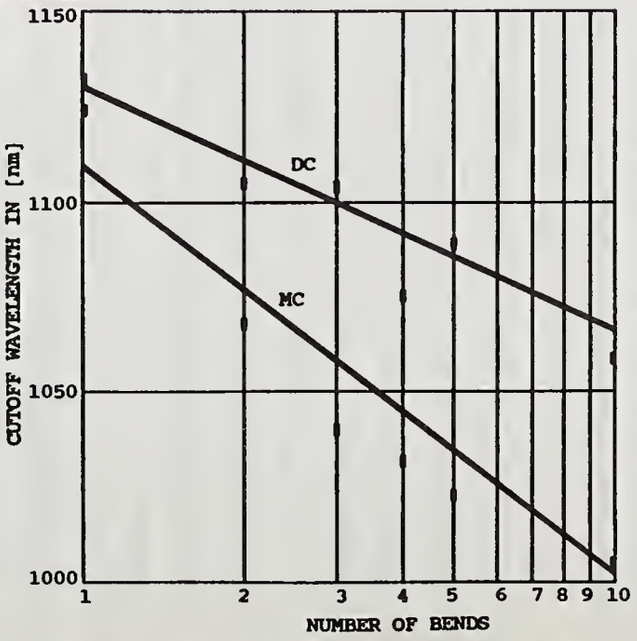

FIGURE 3. Cutoff wavelength dependence on number of bends for 3.0 cm bend diameter.

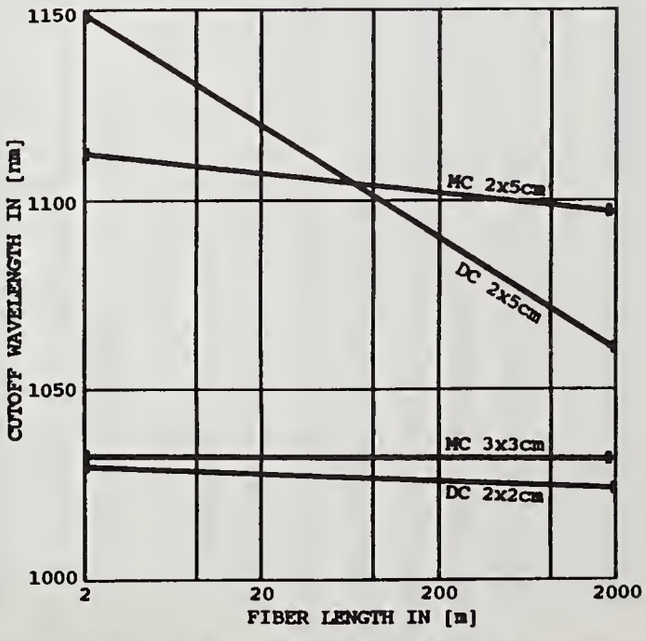

FIGURE 4. Cutoff wavelength dependence on fiber length for various bend diameters.

MODE TRANSITION MATRIX TECHNIQUES FOR MULTIMODE FIBER–OPTIC COMPONENTS

Udo B. Unrau

Institut für Hochfrequenztechnik der Technischen Universität

P.O.Box 3329, D–3300 Braunschweig, Germany (FRG)

Abstract

The work on mode transition matrices done by several groups is reviewed and compared. Applications and practicability of the method are discussed.

1. Introduction

Differential mode attenuation (DMA) and differential mode delay (DMD) cause usually no trouble in two point fiber links, but DMA becomes important in networks where mode–selective components are concatenated and may cause problems. Since it is impossible to keep track of a few hundred guided modes Holmes reported in 1981 on the use of a 2×2 mode power matrix [1]. The matrix was measured for two pieces of fiber, and a splice matrix was assumed. He demonstrated that multiplication of the individual matrices of the fibers and that of a splice predicted quite well the measured response of the concatenated fibers. Subsequently, this method was elaborated to my knowledge by three groups A–C around A: R.L. Gallawa (U.S.A.) and J.M. Maisonneuve (U.S.A. and France), B: A.R. Mickelson (Norway and U.S.A.) and, C: our group. All groups used different approaches to measure the matrix which will be reviewed in the following. Several names have been coined for the matrix itself; neither 'transmission matrix' or 'power matrix' should be used since the first is known in microwaves as a matrix containing full phase information, and the latter is used to describe simple power transfer between several ports. We prefer 'mode transition matrix' (MTM) since it is a crude approach to the 'state transition matrix' (STM) known in electric network theory [1].

2. Mode transition matrix measurements

2.1 The mode transition matrix

Holmes [1] has shown that the solution of the coupled power flow equations in a fiber carrying M mode groups can be expressed in matrix form as $[P_m(z)] = [H_{mn}(z)] \cdot [P_n(0)]$ with $m,n = 1...M$, where $P_\nu(z)$ is the power in the ν–th mode group at position z and $[H_{mn}(z)]$ is the STM. It is quite impossible to excite a single mode group selectively, therefore, the above matrix equation has for practical reasons to be simplified to

$$[P_i] = [T_{ij}] \cdot [P_j] \qquad (1)$$

where $[P_i]$ and $[P_j]$ are the output and input power vectors, respectively, and $[T_{ij}]$ is the MTM. Most groups used 2×2 matrices, only ours explored indices i,j up to 3. Note that the length dependence has been omitted in eq. (1) since the MTM concept was soon extended to characterize fiber components as well [2], and it was pointed out that the real length dependence in fibers would be extremely difficult to measure due to mode coupling [3]. With $i,j = 1...3$ the MTM is only a very crude approximation to $[H_{mn}]$ where m,n may span a few decades.

For use in short–haul networks step–, quasi–step– and graded–index fibers are equally well suited. Table 1 shows the kind of fiber or fiber components the different groups worked with to obtain MTM's, and their relevant publications.

Group	SI	QSI	GI
A	[4,5]	——	——
B	——	——	[3,6]
C	——	[7–11,13]	[2,9–13]

Table 1: Publications on work with step–index (SI), quasi–step–index (QSI) and graded–index (GI) fibers and components, done by groups A, B, C

2.2 Mode–selective excitation

For measuring a MTM one needs a differential launch – differential detection scheme to resolve the mode blocks in eq. (1). It is generally accepted that in order to allow easy and definite mode selective detection, a mode continuum should be excited in a fiber with numerical aperture A_N by a source of minimum linewidth $\Delta\lambda \approx \lambda^2 \cdot A_N / (2\pi \cdot a \cdot n_1{}^2)$ as shown in [14]. For $\lambda \approx 820$nm and $A_N \approx .2$ this reads $\Delta\lambda \approx .5$nm. We recommend however to launch a flat mode continuum by a much larger $\Delta\lambda$ [10].

Mode selective excitation is simplest in **step–index fibers** and can be done by a plane wave impinging with polar angle θ_0 on the fiber front face. It excites modes with the phase coefficient $\beta \approx n_1 \cdot k \cdot \cos(\theta_0 / n_1)$ where n_1 is the core refractive index and k the wavenumber. A spread $\Delta\theta_0$ is directly related to a mode block extending over $\Delta\beta$. This technique was used by group A [4,5] to obtain 2×2 matrices of pieces of high NA fibers and components. Since for **quasi–step–index fibers** (which may have quite odd index profiles) no general optimal selective excitation exists, the plane wave technique is a good compromise here, too [7].

Several methods have been developed for **graded–index fibers**. (All groups restricted the work to parabolic profiles). We preferred gaussian beam excitation through a single–mode fiber which was transversely offset in front of the GI fiber. A thorough discussion of it together with theoretical and measured selectivity curves can be found in [10]. Group B used a lens arrangement where the beam can been restricted in its NA and its spot size and was also transversely moved across a GI fiber endface [3]. A detailed treatment of this excitation method is given in [15]. Unfortunately, the theory used to compute the launch selectivity curves shown in [15] has only been compared to measured near–fields which is quite uncritical, and since no λ–information is given, a comparison with the curves in [10] is difficult. We noted near–field pattern deformations in the test fiber with the offset method and discussed it in [10], they were not mentioned by group B.

A simple but effective excitation method by plane waves combined with mandrel wrap filters was reported in [16] with theoretical and measured selectivity curves. In retrospect we regret that we did not develop it further. Evers found [13] that even without the filter good selectivity for 2×2 matrices in GI fibers can be achieved.

2.3 Mode selective detection

For **step–index fibers**, the mode analysis is again very simple and can be directly derived from the radial far–field, measured either by a detector on a hinging device [4] or by a vidicon camera. As far as the profile function *f(r/a)* is monotone, the mode content of all **graded–index fibers** can be analyzed with a vidicon camera by differentiation of the radial near–field–intensity function *I(r)* with respect to *f(r/a)* as shown in [17]. Slight corrections to non–monotone profiles are tolerable as demonstrated on **quasi–step–index fibers** [10]. It is mandatory that *I(r)* is not a function of the azimuthal angle φ and shows no speckle. Ways to circumvent these difficulties are outlined in [10]. Groups B and C used the near–field technique for **parabolic–index fibers**; it proved to be very reliable. Different far–field techniques exist for graded–index fibers. Rittich derived a useful formula for power–law profiles [18] and applied it with good success in practical comparison to the proven near–field technique. We tried a ring aperture technique to resolve the mode block power in short pulses [12] but found the problems with high precision mechanics nearly unsurmountable. We ran a computer simulation of this modified far–field technique [19] and compared it with the near–field technique. The latter was superior with less tolerance requirements and higher stability. The measured field distributions are generally smoothed either by FFT filtering and curve fitting [6] or by sliding window averaging [10]. A method to reduce errors in the resulting matrix by checks against other physical requirements and measured data is found in [13], where also the case of a butt joint between fibers of different radii is discussed.

3. Results, applications, practicability

All groups applied MTM's to DMA– and DMD–concatenation problems, always with good results, regardless whether 2×2 or 3×3 matrices were used. Matrices were measured for fiber pieces, couplers, connectors, splices and simple networks built thereof [4–13]. The main application of the MTM method is aimed at the design of local network structures. In [20] we tried to assess modal effects in L.A.N.'s with measured matrices as reference. Because of their high mode selectivity cheap biconically fused couplers are the most critical components in such networks. Provided that otherwise low tolerance components (e.g. fibers with high centricity, low–loss connectors) are used, we found that no MTM technique is required if up to four couplers are concatenated and if the couplers are characterized by a restricted launch technique. For predicting power level margins in larger networks concatenating such couplers, the MTM method can be very helpful under the same provisions. The expected power levels and their tolerances at different points of the network should be quite well predictable. At least, the MTM method is the only known procedure to allow such predictions. If high tolerance fibers and connectors are used, the MTM method will fail certainly, too. Comparing the work done so far, 2×2 matrices should be sufficient and much easier to measure than 3×3 matrices. For all types of fibers the tilted plane wave excitation, possibly combined with mandrel wrap filters, appears most attractive and inexpensive. At the detection side near–field analysis and Rittich's far–field technique seem equally well suited. Using the new GaAlAs–Lasers with collimation optics enough power might be available to allow scanning the far–field with a detector on a simple hinging device. $[P_j]$ in eq. (1) could be measured as the output from a short reference fiber which could subsequently be butt–jointed to the test object on one of the newly available optimising coupling units. A round robin test on a typical L.A.N. structure would show if the MTM method is practicable and would help to formulate a standardized test procedure.

References

[1] *Holmes, G.T.:* Estimation of concatenated system response based on measured transfer functions for low and high order modes. Proc. 7th Europ. Conf. on Opt. Commun., Copenhagen 1981, paper 3.4

[2] *Agarwal, A.K.; Unrau, U.:* Characterization of optical components for multimode fiber networks. Proc. All India Symp. on Fibre Optic Sensors, Bangalore (1983), 39 — 44

[3] *Vayshenker, I.P.; Hjelme, D.R.; Mickelson, A.R.:* Multimode Fiber Systems Characterization. Tech. Digest Symp. on Optical Fiber Measurements, Boulder, Co. (1986), NBS special publ. **720**, 85 — 88

[4] *Maisonneuve, J.M.; Gallawa, R.L.:* The use of power transfer matrices in predicting system loss: theory and experiment. Fiber and Integr.Opt. **6** (1987), 11 — 26 [based on: Maisonneuve, J.M; Gallawa, R.L.: Proc. SPIE 500 (1984), 88 — 93]

[5] *Maisonneuve, J.M.; Churoux, P.; Gallawa, R.L.:* Use of mode transfer matrices in L.A.N. loss evaluation. Proc. SPIE 559 (1985), 182 — 185

[6] *Mickelson, A.R.; Eriksrud, M.; Aamlid, S.; Ryen, N.:* Role of the fusion splice in the concatenation problem. J. Lightw. Technol. **LT—2** (1984), 126 — 138

[7] *Evers, G.; Kober, A.; Unrau, U.:* Measurement of mode transition matrices of quasi—step—index optical fiber components. Proc. SPIE 500 (1984), 94 — 99

[8] *Evers, G.:* Mode transition matrices for fibre—optic connectors. Electr. Lett. **21** (1985), 401 — 402

[9] *Unrau, U.:* Mode transition matrices as a means for the design of local—area networks with optical fibers (In German). mikrowellen magazin (Germany) **10** (1984), 644 — 648

[10] *Agarwal, A.K.; Evers, G.; Unrau, U.:* A measurement set—up for differential mode analysis of fiber—optic components. ntzArchiv (Germany) **8** (1986), 229 — 238

[11] *Evers, G.; Unrau, U.:* Assessment of modal effects in local area networks. Electron. Lett. **22** (1986), 859 — 861

[12] *Evers, G.:* Calculation and measurement of mode transition matrices for DMA and DMD characterization of optical fibers. Opt. Eng. **27** (1988), no. 2, 179 — 186 [based on: Evers,G.; Henze, F.; Unrau, U.: Proc. SPIE 559 (1985), 176 — 181]

[13] *Evers, G.:* Mode transition matrices for fiber—optic components (In German). Dr.—Ing. thesis, Techn. Univ. Braunschweig, Faculty of mechanical and electrical engineering, 1987

[14] *Mickelson, A.R.; Eriksrud, M.:* Mode continuum approximation in optical fibers. Opt. Lett. **7** (1982), no. 11, 572 — 574

[15] *Mickelson, A.R.; Eriksrud, M.:* Mode—dependent attenuation in optical fibers. J. Opt. Soc. Am. **73** (1983), no. 10, 1282 — 1290

[16] *Agarwal, A.K.; Evers, G.; Unrau, U.:* New and simple method for selective mode group excitation in graded—index optical fibres. Electron. Lett. 19 (1983), 694 — 695

[17] *Leminger, O.G.; Grau, G.K.:* Near—field intensity and modal power distribution in multimode graded—index fibres. Electron. Lett. **16** (1980), no. 17, 678 — 679

[18] *Rittich, D.:* Practicability of determining the modal power distribution by measured near and far fields. J. Lightw. Technol. **LT—3** (1985), no. 3, 652 — 661

[19] *Kitayama, K.–I.; Tateda, M.; Seikai, S.; Uchida, N.:* Determination of mode power distribution in a parabolic—index fiber: theory and application. IEEE J. Quant. Electron. **QE—15** (1979), no. 10, 1161 — 1165

[20] *Evers, G.; Unrau, U.:* Assessment of modal effects in local area networks. Electron. Lett. **22** (1986), 859 — 860

A SINGLE LAUNCH TECHNIQUE FOR DETERMINATION OF MODE TRANSFER MATRICES

by S. Yang, D. R. Hjelme, I. P. Januar, I. P. Vayshenker, and A. R. Mickelson

Department of Electrical & Computer Engineering
University of Colorado
Boulder, Colorado 80309

Introduction:

Component intensive multimode fiber systems such as those presently finding application in fiber optic local area nets and premise wiring require more characterization than simply loss statistics. This fact is due to the mode dependency of the fiber compatible components and the fact that the propagation distances of a component intensive system preclude the achievement of any steady-state modal distribution. Mode transfer matrices, as were first introduced by Holmes [1] are powerful tools for multimode system characterization. Unfortunately, as is shown in a recent work [2], mode transition matrices are launch dependent and, as measurement of a mode transfer matrix requires various different launches, the mode transfer matrix of a given component cannot be unique. This lack of uniqueness could be alleviated by standardizing the measurement procedure. However, a lack of uniqueness tends to put into question the repeatability of a measurement technique.

In the present work, we take a slightly different approach to the standard one. The mode transfer matrix is actually just a representation of mode transmission function [2], which is an object which should truly represent the transmission characteristics of a fiber or component. Determination of the transfer function therefore allows one to determine any of its representations and, therefore, all the possible non-unique forms of the mode transfer matrices. A simple model of the mode transfer function for low loss ($\leq$ 0.5 dB) components is derived and determined experimentally, and the results of the use of the mode transmission function to derive mode transfer matrices is compared with direct measurements of mode transfer matrices.

Theory:

The mode transfer function $T(R, R')$ for a component can be defined by the relation [2]

$$p^0(R)m(R) = \int dR' T(R, R') p^i(R') m(R') \tag{1}$$

where $p^0(R)$ is the modal power distribution exiting the component, $m(R)$ is the mode density, $p^i(R')$ is the modal power distribution incident on the component, and R is the mode parameter as

defined in any of various works [3]. $T(R, R')$ is a function of two continuous variables R and R' and is therefore not generally to be found directly from (1). However, one can make a parameterized model for $T(R, R')$ and use (1) as a fitting equation to determine the parameters. In essence, this procedure does not differ too greatly from fitting procedures used to determine matrix elements [4]. To derive a parameterized model, one can assume that the mode-continuum approximation holds but that coupling only occurs between modes at the same frequency, as was assumed in the experimentally verified model in reference [5]. The resulting transfer function is

$$T(R, R') = \delta(R - R') - \int dR'' m(R'')\alpha(R'', R)\delta(R - R') + m(R)\alpha(R, R') \tag{2}$$

where the coupling function is a characteristic of the component under test. Assuming the component causes (low) loss and symmetric coupling, one can assume the coupling function to be

$$\alpha(R, R') = \frac{1}{2}\alpha_0 e^{-|R^2 - R'^2|/2\tau} \tag{3}$$

where α_0 and τ are the fitting parameters.

A Single Launch Measurement Technique:

Once the α_0 and τ of the $\alpha(R, R')$ function are determined, matrices of any order can be determined from the transfer function. A standard measurement made on components is that of overfilled loss. The overfilled loss L can be related to α_0 and τ by the relation

$$L = \alpha_0 V^2 \tau\, 2\tau(1 + 2\tau)\left[1 - 2\tau(1 - e^{-1/2\tau})\right] \tag{4}$$

where V is the fiber V number. Equation (4) can be derived from (1) together with (2) and (3) where $p^i(R)$ is taken to be unity. Clearly, α_0 can be eliminated from (3) using (4), and the resultant $T(R, R')$ is a function of only τ. If, when one measures L, however, one were also to record the $p^0(R)$ that results from an overfilled launch, one could use τ to fit the relation (1). The resultant best fitted τ could then be used to determine $T(R, R')$. As this $T(R, R')$ is a complete representation of the component under test, any size matrix can be generated from it, and therefore the transfer matrix of the component can be generated from data taken for a single launch.

Experimental Verification:

To truly verify that the measurement technique outlined above is a viable one, one needs to both verify the ansatz of (3) and to compare matrices generated by the above technique with matrices generated directly. In order to do this, a fiber concatenation experiment was carried out

in which four 1 meter pieces of fiber were spliced together using input and output fibers with five fusion splices. Comparison of the measured near-fields and those computed using mode transfer functions are given in Figure 1. Typical comparison of mode transfer matrices calculated from the mode transfer function are given in Table 1. Agreement in all cases was good.

Conclusion:

By overfilling an input fiber and recording the total loss and near-field output of a test component, it is possible to find a transfer function for the component. From this transfer function, it is possible to generate any of the non-unique transfer matrices for this component. This technique is preferable to presently applied techniques for two reasons. One is simply that only a single launch is necessary, and therefore intricate submicron scanning techniques of questionable repeatibility are not necessary. Second, the transfer function contains more information about a component than do any of its associated transfer matrices. It is safe to conclude that the transfer function approach to the multimode fiber characterization problem is a most desirable one to follow.

References:

[1] G. T. Holmes, "Estimation of Concatenated System Response Based on Measured Transfer Functions for Low and High Order Modes," *Proc Seventh European Conf on Opt Comm*, Copenhagen, 3.4-1–3.4-4 (September 1981).

[2] S. Yang, I. P. Vayshenker, D. R. Hjelme, and A. R. Mickelson, "A Transfer Function Analysis of Measured Transfer Matrices," manuscript in preparation.

[3] A. R. Mickelson and M. Eriksrud, "Mode-Continuum Approximation in Optical Fibers," *Opt Lett* **7**, pp. 572–574 (1982).

[4] See, for example, the technique described in A. R. Mickelson, M. Eriksrud, S. Aamlid, and N. Ryen, "Role of the Fusion Splice in the Concatenation Problem," *Journ Lightwave Tech* **LT-2**, pp. 126–138 (1984).

[5] A. R. Mickelson, Ø. Klevhus, and M. Eriksrud, "Backscatter Readout from Serial Microbending Sensors," *Journ Lightwave Tech* **LT-2**, pp. 700–709 (1984).

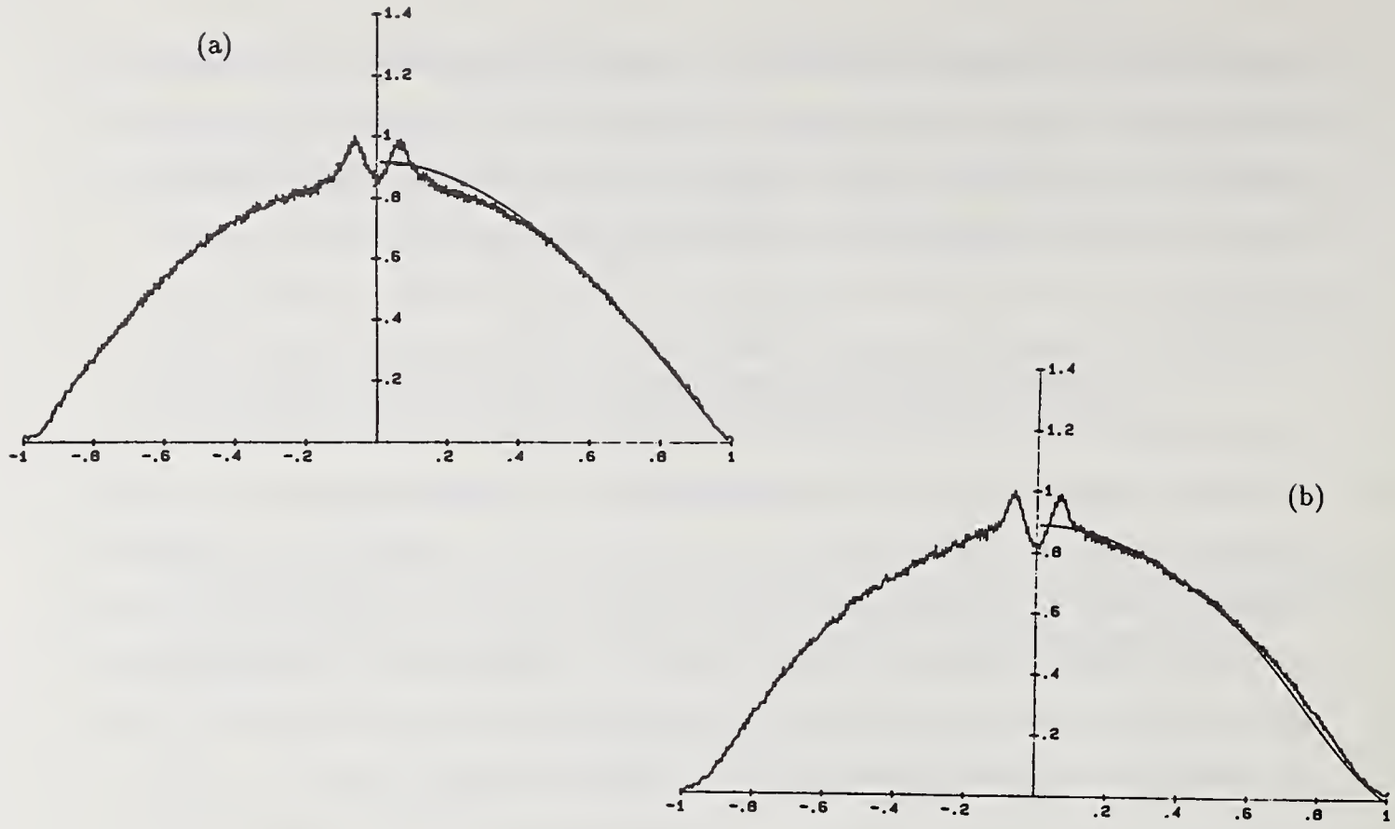

Figure 1: *(a) Measured (noisy) and theoretical (smooth) input near-field distribution for overfilled launch. (b) Output near-field distributions measured (noisy) and calculated from the transfer function (smooth).*

L	τ		T_{11}	T_{12}	T_{21}	T_{22}
.09	.08	Tc	.9963	.0066	.003	.9573
		Tm	.983	0	.001	.978
.16	.085	Tc	.9932	.0064	.0052	.9229
		Tm	.992	.006	.007	.924
.28	.1	Tc	.9835	.0115	.0116	.8599
		Tm	.941	.002	.001	.930

Table 1: *Comparison of measured matrices (Tm) and matrices calculated from the transfer function (Tc) for three splices. The transfer functions are determined from the same experimental data for the corresponding transfer matrices. L is the overfilled loss and τ is the coupling coefficient.*

SENSITIVITY OF THE MODE TRANSITION MATRICIES TO VARIATIONS OF THE INPUT POWER VECTORS

T. J. GRYK, G.E. HOLMBERG, H.M. BLOUNT
NAVAL UNDERWATER SYSTEMS CENTER
NEW LONDON LABORATORY
NEW LONDON, CONNECTICUT 06320

INTRODUCTION:

A matrix method for characterizing the modally dependent losses of fiber optic components was first reported by Holmes.[1] The method has been successfully applied to quasi-step-index components,[2] multimode fiber transmission,[3] and graded-index fusion splices.[4] The method uses the near field pattern generated by some type of selective mode excitation to determine independent power vectors which can be related to the elements of a square transition matrix. In these reports, however, little is said about the exact nature of the independent power vectors, and to our knowledge, there exists no report on the sensitivity of the matrix elements to variations of the independent power vectors. It is the purpose of the present work to establish a relationship between the repeatability of the matrix elements and the independence of the mode block excitations.

EXPERIMENTAL DETAILS:

The mode transition matrix (MTM) in the present work is a 2x2 matrix requiring two independent input power vectors to uniquely determine the four matrix elements. The through and coupled port MTMs of a 3dB, 100/140μm fiber optic coupler were measured for two different sets of excitation parameters. The measurement set-up is shown in Figure 1. Variable mode block excitation is accomplished using a set of apertures which are imaged onto the fiber endface. Figure 2 illustrates the two excitation states. They are: center/offcenter circular spot and spot/anulus. Only spatial variations in the launch are made; the numerical aperture of the beam remaining fixed. It was found that generation of the selective mode blocks yielded a large group of excited leaky modes. These leaky modes were removed by a mode filter with minimal mixing of guided modes. The near field pattern for one excitation both before and after mode filtering is shown in Figure 3. The leaky modes are easily visualized as the "ears" in the near field. The modal power distribution is calculated from the first derivative of the near field pattern as described by Daido,[5] and then integrated into two independent power vectors. The division of the mode blocks is arbitrary, and in the present work the division is made at a relative mode number $\delta/\Delta=0.5$. Four independent power vectors must be measured in order to determine the four matrix elements. They are the input and output power vectors for two independent excitation states. In order to determine the input power vectors the fiber lead containing the mode filter was cut back leaving a length of input fiber approximately one meter long.

EXPERIMENTAL RESULTS AND DISCUSSION:

It is the purpose of this report to discuss the uncertainties involved in a calculation of the MTM elements. The largest errors introduced into the MTM calculation can be traced to an inability to accurately and precisely measure the power emitted from the optical fiber (3% error is assumed). This uncertainty, however, is mostly random, and therefore the propagation of these

uncertainties can be found statistically. The elements of the MTM are determined using Kramer's Rule:

$$MTM = \begin{pmatrix} T_{ll} & T_{hl} \\ T_{lh} & T_{hh} \end{pmatrix}$$

where

$$T_{ll} = \frac{\begin{vmatrix} P_{ol1} & P_{ih1} \\ P_{ol2} & P_{ih2} \end{vmatrix}}{\det P} \; ; \; T_{hl} = \frac{\begin{vmatrix} P_{il1} & P_{ol1} \\ P_{il2} & P_{ol2} \end{vmatrix}}{\det P} \; ; \; T_{lh} = \frac{\begin{vmatrix} P_{oh1} & P_{ih1} \\ P_{oh2} & P_{ih2} \end{vmatrix}}{\det P} \; ; \; T_{hh} = \frac{\begin{vmatrix} P_{il1} & P_{oh1} \\ P_{il2} & P_{oh2} \end{vmatrix}}{\det P}$$

and $$P = \begin{pmatrix} P_{il1} & P_{ih1} \\ P_{il2} & P_{ih2} \end{pmatrix}$$

The notation, although somewhat cumbersome, is required for clarity and is as follows: the T-values are the matrix elements whose subscripts denote transitions between low(l) and high(h) order modes [i.e. T_{hh} denotes transitions from high-order to high-order modes]; the P-values are power levels whose three subscripts denote the exact mode group containing the power. The first subscript refers to the power as output(o) or input(i), the second as high-order(h) or low-order(l), and the third as excitation state 1 or 2 [i.e. P_{ih2} is the power contained in the input fiber's high-order mode block when excited by the second launch condition].

Because the matrix elements are described by the ratio of two determinants, the percent uncertainty of the elements is found to be a combination of the percent uncertainties of each determinant. It is convenient to define these as the Normalized Amplitude Factor (NAF) and the Normalized Independence Factor (NIF), these factors corresponding to the uncertainties of the determinants of the numerator and the denominator respectively. The percent uncertainty of the matrix element is then given by:

$$\frac{\delta T_{ij}}{T_{ij}} = 2 \cdot \left[NIF^{-2} + NAF_{ij}^{-2} \right]^{1/2} \cdot \text{PERCENT UNCERTAINTY IN POWER MEASUREMENT}$$

where i,j can have the values of l or h.

and $$NIF = \frac{P_{il1}P_{ih2} - P_{il2}P_{ih1}}{P_{il1}P_{ih2} + P_{il2}P_{ih1}} \qquad NAF_{ll} = \frac{P_{ol1}P_{ih2} - P_{ol2}P_{ih1}}{P_{ol1}P_{ih2} + P_{ol2}P_{ih1}}$$

$$NAF_{hl} = \frac{P_{il1}P_{ol2} - P_{il2}P_{ol1}}{P_{il1}P_{ol2} + P_{il2}P_{ol1}} \qquad NAF_{lh} = \frac{P_{oh1}P_{ih2} - P_{oh2}P_{ih1}}{P_{oh1}P_{ih2} + P_{oh2}P_{ih1}} \qquad NAF_{hh} = \frac{P_{il1}P_{oh2} - P_{il2}P_{oh1}}{P_{il1}P_{oh2} + P_{il2}P_{oh1}}$$

The normalized factors defined above have physical significance. The NAF is a measure of the relative size of the matrix element, while the NIF is a measure of the independence of the input

power vectors. The percent uncertainty increases inversely with the magnitude of either the NAF or NIF. The NAF is a characteristic of the fiber optic component itself. For a component which weakly couples modes, the off-diagonal matrix terms are small by definition; and therefore, the percent uncertainty in the measured cross elements will be large. This is seen in Table I which shows the values of the matrix elements of a 3dB coupler for a given set of input conditions (fixed NIF). The uncertainty due to the NAF is independent of the measurement technique, and can only be reduced by increasing the precision of the power measurement. The NIF is a characteristic of the input power vectors. The NIF becomes small (uncertainty increases) as the input power vectors become linearly dependent. Therefore, this uncertainty can be reduced by carefully exciting linearly independent input power vectors. Since the spot/anulus input power vectors are more independent than the center/offcenter input power vectors, one would expect the uncertainty to be smaller for the spot/anulus condition. Table I shows this not to be true, however, the uncertainty of the spot/anulus launch being larger than predicted. [It should be noted, however, that the uncertainty presented with the measured matrix values is the standard deviation and, as such, only yields a value for the repeatability of the measurement, not the actual uncertainty.] Therefore, another source of error (possibly due to leaky mode excitation or near field irregularities) limits the precision of our measurement and is currently under investigation. As the NIF becomes very small, this other source of error becomes insignificant, and the theoretical uncertainty matches the measured uncertainty as shown by a comparison of the measured and expected uncertainties for the center/offcenter excitation found in Table I. Another key feature of the matrix elements is their invariance to the specific set of independent input vectors. The discrepancy between the mean values of the matrix elements calculated with the above input excitations is insignificant. Only the uncertainty is a function of the vectors, and therefore any set can be used to determine the matrix elements. It should be noted, however, that if strongly dependent input conditions are used, the precision of the measurement will become vanishingly small.

In conclusion, we have measured the repeatability of the matrix elements as a function of the independence of the input power vectors, and compared them to the uncertainty predicted from statistics. We have found that the values of the matrix elements are independent of the variations of the input power vectors, however, the uncertainty of the measurement varies inversely with the magnitude of the Normalized Independence Factor.

REFERENCES:

[1]Holmes, G.T., "Estimation of Concatenated System Response Based on Measured Transfer Functions for Low and High Order Modes," Proc. 7th European Conference on Optical Communication, Copenhagen, 1981.
[2]Evers, G., Kober, A., and Unrau, U., "Measurement of Mode Transition Matrices of Quasi-Step-Index Optical Fiber Components," SPIE Vol. 500 Fiber Optics: Short-Haul and Long-Haul Measurements and Applications II, 1984.
[3]Vayshenker, I.P., Hjelme, D.R., and Mickelson, A.R., "Multimode Fiber Systems Characterization," Technical Digest: Symp. Opt. Fiber Measurement, NBS Special Publication 720, 1986.
[4]Eriksud, M., Mickelson, A.R., Aamlid, S., and Espe, B., "Mode Dependence of Splice Loss in Graded-Index Optical Fibers," IEEE Jour. Quant. Elec., Vol. QE-19, No. 5, 1983
[5]Daido, Y., Miyauchi, E., Iwama, T., and Otsuka, T., "Determination of Modal Power Distribution in Graded-Index Optical Waveguides From Near-Field Patterns and its Application to Differential Mode Attenuation Measurement," Applied Optics, Vol. 18, No. 13, 1979, p.2207.

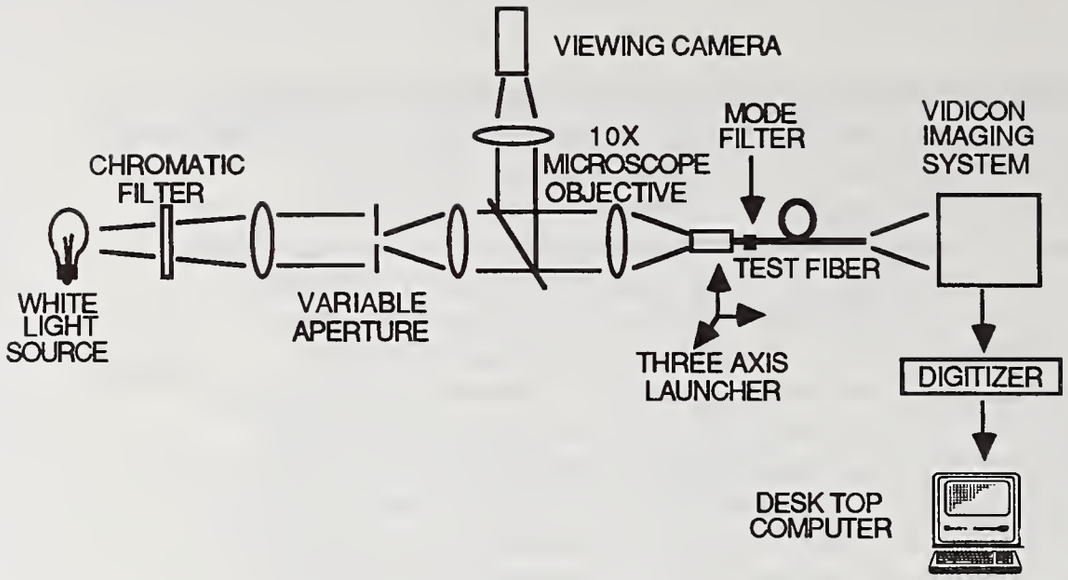

FIGURE 1. APPARATUS USED TO DETERMINE THE NEAR FIELD OF A 100/140 μm GRADED-INDEX FIBER

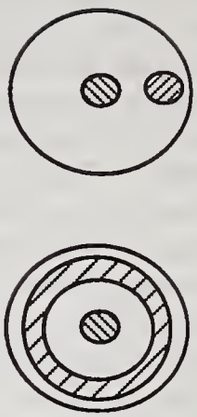

FIGURE 2. SELECTIVE MODE EXCITATION

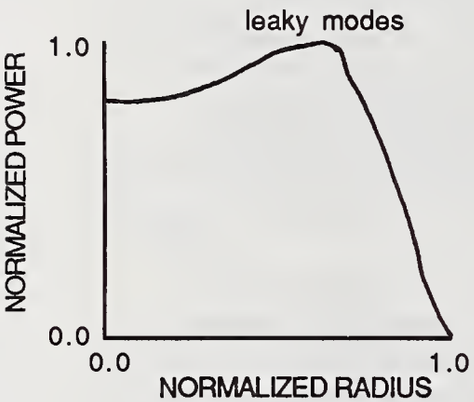

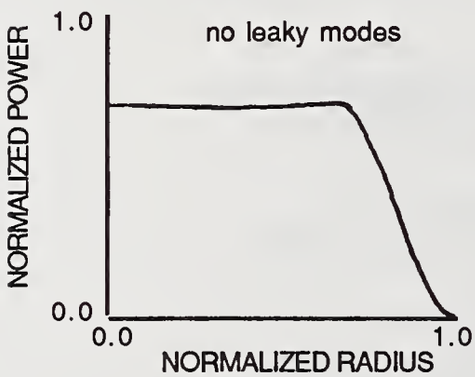

FIGURE 3. NEAR FIELD PATTERN BEFORE AND AFTER MODE FILTER

CORE/ANULUS EXCITATION

	THROUGH PORT			COUPLED PORT	
measured (7 trials)	.59 ± .08	.01 ± .06		.36 ± .03	.07 ± .04
	.00 ± .02	.43 ± .07		.05 ± .01	.36 ± .02
calculated uncertainty	.05	.11		.04	.01
	.05	.04		.05	.03

CENTER/OFFCENTER EXCITATION

	THROUGH PORT			COUPLED PORT	
measured (7 trials)	.58 ± .08	.04 ± .06		.31 ± .01	.24 ± .09
	.00 ± .03	.39 ± .06		.06 ± .02	.35 ± .06
calculated uncertainty	.08	.08		.07	.04
	.01	.05		.06	.05

TABLE I. MATRIX VALUES WITH MEASURED AND CACLULATED UNCERTAINTIES FOR VARIOUS INPUT CONDITIONS

EVOLUTION OF POWER DISTRIBUTIONS IN FIBER OPTIC SYSTEMS - DEVELOPMENT OF A MEASUREMENT STRATEGY

M. J. Hackert
Corning Glass Works
Corning, N. Y. 14831

Introduction

System power budgeting using multimode fiber is made more complex by the dependence of the actual loss experienced in the system on the power distribution carried by the components. Also, each component comprising the system has the potential to alter the mode power distribution (MPD)[1] carried by the fiber[2]. Thus, the actual loss introduced by each component is controlled by the components which precede it in the system, as well as the power distribution launched by the source. This paper presents a basic description of MPD evolution through components and some experimental results of component characterizations which illustrate these behaviors.

Equilibrium mode distribution (EMD) and steady state MPD are commonly used interchangeably. However, they have very distinct definitions[3]. An equilibrium MPD has the property that irrespective of the input power distribution, the output distribution is consistently the same as some MPD which is characteristic for the device under test. In a steady state MPD, on the other hand, the input and output MPD are the same. Thus, a steady state MPD is not necessarily defined by the system element, but rather is dictated by the launch condition.

Fiber Characterization

The propagation of power through a fiber is relatively easy to understand and characterize since high quality fibers generally carry steady states - the output MPD is equivalent to the input MPD. However, if the launched distribution puts power into the higher order modes of the fiber, which are loosely bound or do not propagate to the end, the fiber will act as a mode filter. Using a uniformly overfilling source, MPDs at the end of a length of fiber clearly show this filtering as a reduction in higher order mode relative power. Also, the mode filtering occurs gradually over some distance which is evident when the transient loss is plotted versus length.[3]

A number of steady states can exist for fiber. As long as power is not launched into the transient modes, the fiber will carry the steady state. Examples of common power distributions (OFL, LPS, and an ultra-restrictive launch) are given in Figure 1. The existance of a steady state is confirmed by noting that the 2 m power distribution is equivalent to the 2.2 km MPD within the measurement reproducibility except for the OFL case, where mode filtering would occur.

Component Characterization

In general, components are much more difficult to characterize because they can produce an equilibrium MPD as opposed to a steady state. An equilibrium producing component will filter the MPD in a similar fashion to a steady state producing component if the launch power distribution exceeds the equilibrium MPD. If, on the other hand, the launch MPD is more restrictive than the equilibrium MPD, the component will mix power into some higher order modes to produce the equilibrium MPD.

An important similarity between fiber and components is that it generally takes a few hundred meters of fiber or a couple of components to develop a steady state or equilibrium, respectively. Therefore, in order to study the cumulative effect of a particular type of a component in a system, a number of the components (6 to 10) need to be joined in series with low-loss fusion splices.

As an example, 6 wavelength division multiplexers / demultiplexers fabricated by ion exchange technology[4,5,6] were concatenated. The end-to-end loss for three different launch conditions - OFL, LPS, and an ultra-restricted launch (15 μm / 0.1 launch NA) - was measured as each component was removed from the concatenation, and the results plotted in Figure 2. The sum of the individual component measurements for each launch condition is also included. For the OFL and ultra-restricted launches, end-to-end and sum loss measurements diverge rapidly for increasing component count. Thus, OFL overestimates the actual loss experienced (by as much as 6 dB), and the ultra-restricted launch underestimates it. It can then be concluded that, because the error increases with increasing component count, neither of these launch conditions are adequate for prediction of actual system loss.

It can be noted in Figure 2 that the slopes of the concatenation losses tend toward the same value for increasing component count in the case of the LPS measurement condition. This suggests that, just like with fiber, there is a steady state attenuation (approximated in this case by LPS) combined with a transient as equilibrium is achieved. To clarify this point, the loss added to the concatenation for each launch condition as each component was added was calculated. The difference in loss between this added loss and the LPS loss measured on the component is given in Figure 3. Because this difference in added loss when an LPS launch is used most closely approximates zero, the LPS power distribution most closely approximates the equilibrium power distribution. This result is convenient. However, it is not necessarily true that other types of components will have the same ability to use LPS to approximate their equilibrium loss.

There are two ways to verify from our data that equilibrium was indeed developed in these particular components. First, equilibrium is implied by the ultra-restricted launch loss. In Figure 3, the difference in ultra-restricted launch loss shows a transient for the first few components (similar to OFL but with a different sign), but goes to zero. This implies that the low order mode power of the ultra-restricted launch loss is being mixed up to higher order modes. The resultant power distribution produces a higher loss and is characteristic of the equilibrium.

The second way to confirm that equilibrium is actually being developed is to measure the MPD for an overfilling and ultra-restricted launch. If the exiting MPD is the same at the end of the concatenation, the power distribution is that of an equilibrium by definition. The MPDs in Figure 4 show this to be the case.

Conclusions

From the results presented here, fibers and fiber-optic components can be classified as either steady state producing filters or equilibrium producing mixers - typically fiber or components, respectively. By assuming that the system will be comprised of filters and/or mixers, accurate system design rules can be greatly simplified. The work to date suggests that the steady state loss combined with a one time transient due to mode mixing and filtering can optimally characterize a component. By doing so, the double book-keeping of the transient when a non-steady state loss is used in the prediction of a system (a concatenation of components) should be eliminated. However, further work in the form of experimentation and model system testing is necessary to develop a simple set of design rules.

References

(1) M. Calzavara, P. DiVita, and U. Rossi, "Mode Power Distribution Measurements in Optical Fibers", CSELT Rapporti Tecnici, Vol. XI, no. 5, p. 447-451, October 1981.

(2) P. Reitz, M. Hackert, J. Matthews, K. Murphy, D. Hanson, M. Hartmann, T. Huegerich, K. Kevern, T. Odderstol, "A Comparison of Loss Measurement Methods with Observed System Loss in Optical LAN Links", presented at the SPIE Fiber Optics Technical Symposium - 559-24, San Diego, California, August 21-22, 1985.

(3) M. Hackert, "Development of Equilibrium Mode Distribution (EMD) in a Fiber", presented at the Second International SPIE Technical Symposium - 584-28, Cannes, France, November 25-29, 1985.

(4) G. Chartier, P. Callier, A. Guex, P. Faussaucl, and Y. Won, "Graded-Index Surface or Buried Waveguides by Ion Exchange in Glass," Applied Optics, Vol. 19, pp. 1092-1095, April/June 1980.

(5) A. Beguin, T. Dumas, M. Hackert, R. Jansen, C. Nissim, "Fabrication and Performance of Low Loss Optical Components Made by Ion Exchange in Glass," presented at Optical Fiber Conference '88, New Orleans, Louisiana, January 25-28, 1988.

(6) K. Murphy, "Integrated Optics on Glass," Photonics Spectra, November, 1987.

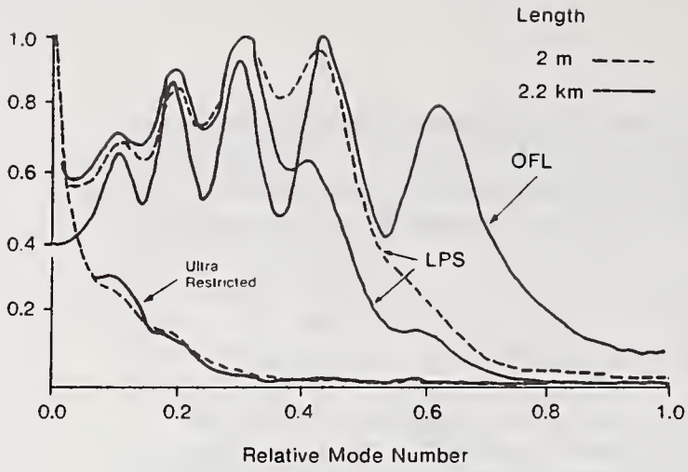

50/125/0.2 Fiber

Mode Power Distributions

Figure 1

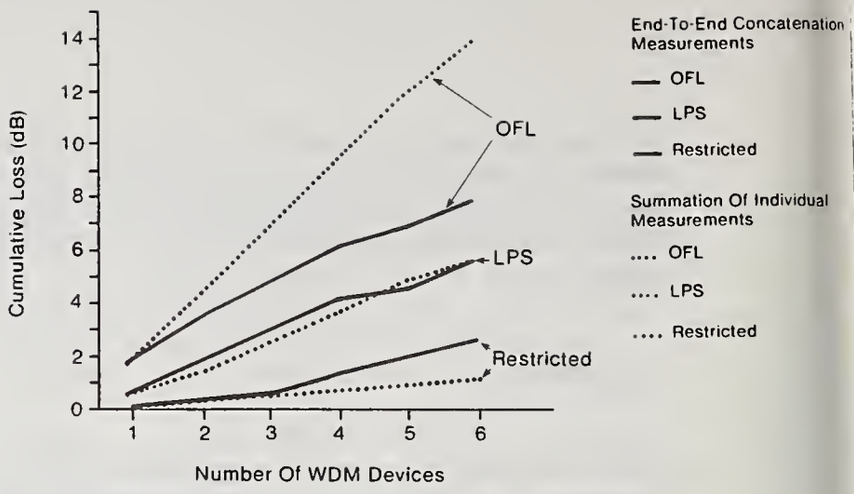

Cumulative Loss Performance

WDM Concatenation

Figure 2

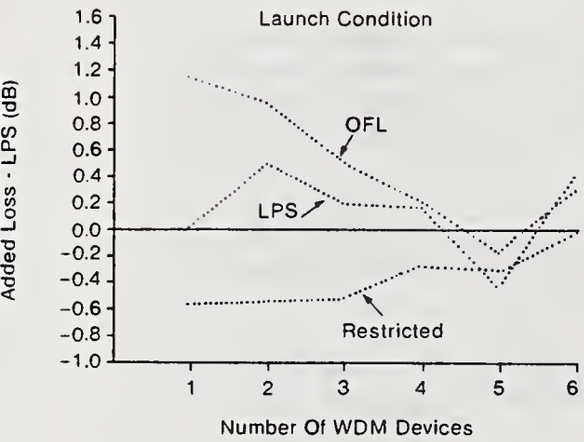

Equilibrium Loss Development In A WDM Concatenation

Figure 3

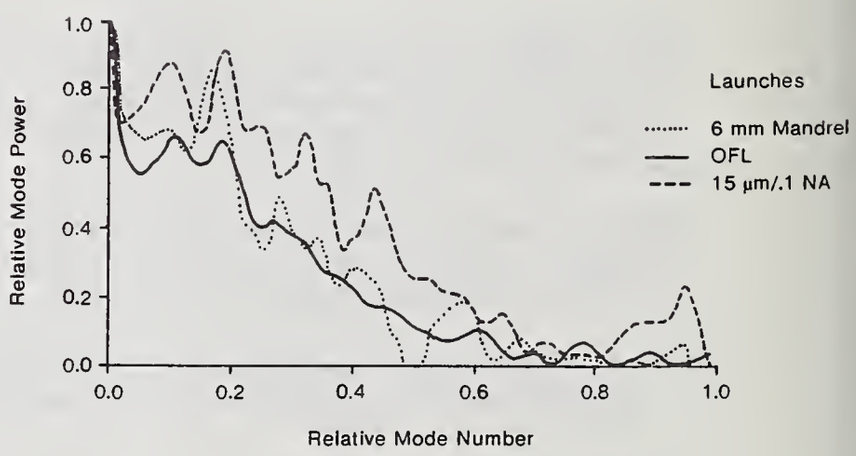

Mode Power Distributions Of A Component Concatenation

Figure 4

Accurate Measurement of Optical Power in Fibre Optic Systems

D H Nettleton

National Physical Laboratory Teddington, Middlesex TW11 OLW, UK

INTRODUCTION

Optical power is measured in fibre optic systems with commercially produced fibre optic power meters fitted with an appropriate connector. If power measurements are to be made accurately these meters must be calibrated against national spectral responsivity scales. Traditional calibration facilities are not suitable to carry out these calibrations because of the difficulty in coupling radiation into the meters except with an optical fibre and so special facilities and transfer standards have to be developed.

ABSOLUTE RESPONSIVITY

Absolute responsivity calibrations of fibre optic power meters are carried out at NPL against a specially developed transfer standard detector. This is shown in Figure 1. It is constructed with a 5 mm diameter germanium photodiode mounted on the exit port of a 50 mm diameter integrating sphere. An FC-type connector is mounted on the input port. The response of this detector is measured against calibrated thermopile radiometers using laser diode sources at 850 nm, 1300 nm and 1550 nm. Radiation is imaged from the sources into the integrating sphere or onto the calibrated thermopile radiometer in an automated calibration rig. The integrating sphere removes the sensitivity of the response of the detector to image size and position. This eliminates uncertainties caused by non-uniformities in the response across the surface of the germanium photodiode. It also makes it possible to change the connector type at the input port without altering the response of the detector. Finally reflections from the germanium photodiode have a negligible affect on the system to be measured. The only disadvantage of this transfer standard is the reduction of the signal by three orders of magnitude. However, if calibrations are carried out at a power level of 100 μW (- 10 dBm), uncertainties can be kept very low. Calibration using single mode fibre has been achieved with an uncertainty of ± 0.25% (± 0.01 dB) and with multimode fibre ± 0.5% (± 0.02 dB). Replacing the

germanium photodiodes with silicon photodiodes for measurements at 850 nm and InGaAs photodiodes for measurements at 1300 nm and 1550 nm will reduce the noise level and make possible measurements at lower power levels.

LINEARITY

The response of fibre optic power meters at other power levels can be measured using a cooled 5 mm diameter germanium photodiode fitted with a suitable connector cap. If all measurements are made relative to the 100 μW (- 10 dBm) absolute response calibration, the long term stability of the cooled detector is not important; nor is the patch size and position as long as it is maintained throughout one set of measurements.

RELATIVE SPECTRAL RESPONSE

The change in response of fibre optic power meters away from the spot wavelength calibration of the laser diodes is carried out by reference to 5 mm diameter germanium photodiodes which hold the relative spectral response scale at NPL. This scale has been established with pyroelectric detectors which have a platinum black surface behind a silica window. The relative spectral reflectance is calculate from the measured reflectance of the black and the transmission of the window. The uncertainty of the scale is shown in Figure 2.

Fibre optic power meters are calibrated by recording the response to monochromatic radiation from a spectrally dispersed incandescent source imaged either onto the sensing element with the connector cap removed or into a fibre connected to the meter. Measurements are carried out at 20 nm intervals and the relative spectral power falling on the power meter measured by reference to the germanium photodiode standards.

ERRORS DUE TO INTER-REFLECTIONS

Solid state photodiode detectors can have high reflectivities even when anti-reflection coated. Typical reflectances are between 20% and 40%. Care must be taken, therefore, when connector caps are fitted as they may significantly increase the response of a power meter by inter-reflections. Increases as large as 16% (0.64 dB) have been measured. Of course if the meter is calibrated with the cap in place the

correct response will be recorded. However the calibration may not hold if different caps for different detector types are used. Because anti-reflection coatings are wavelength dependent, the increase in response due to inter-reflections may also be wavelength dependent.

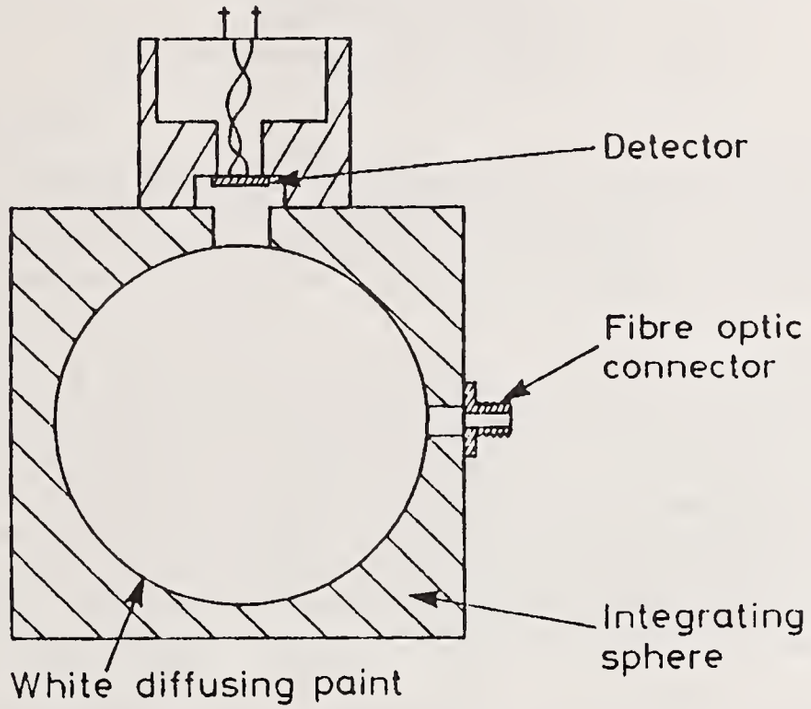

Figure 1. Transfer standard for the calibration of fibre optic power meters

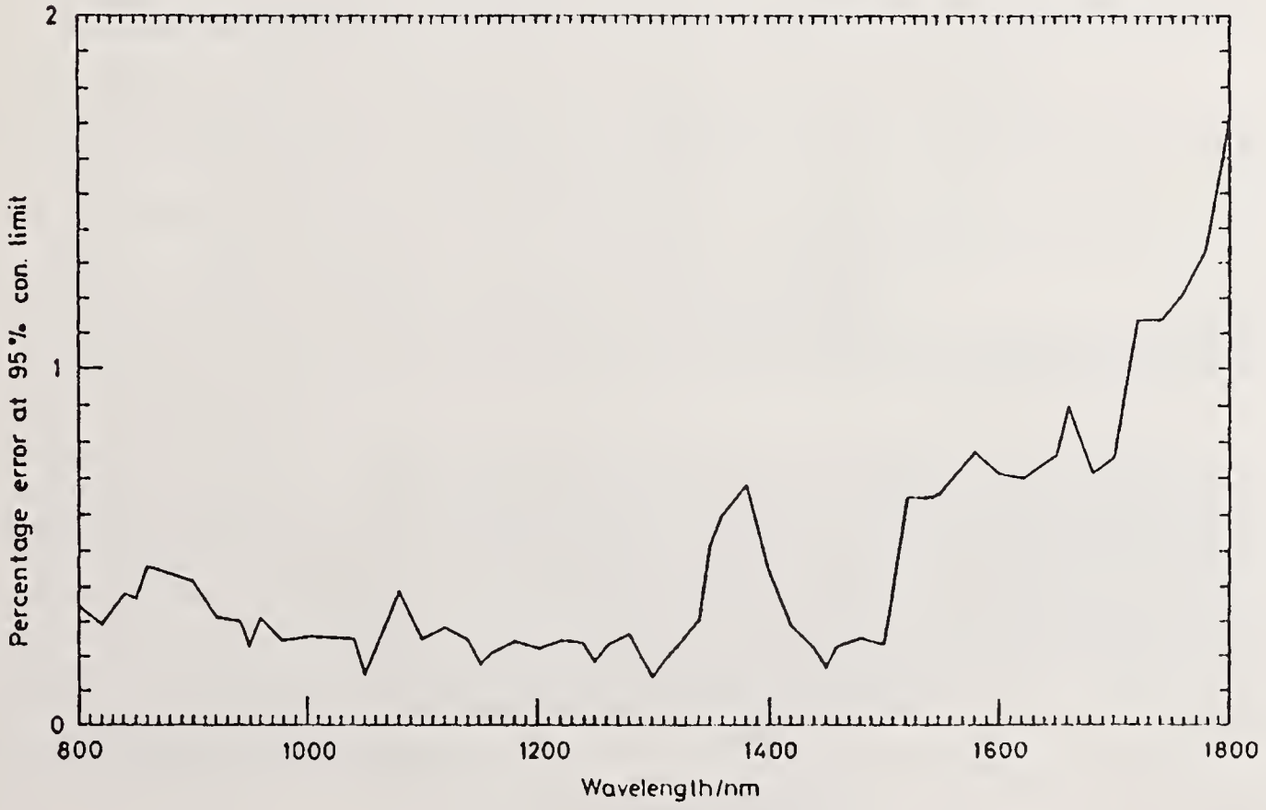

Figure 2. Uncertainty in NPL relative spectral responsivity scale

An Accurate Method of Determining Single-Mode Fiber Cutoff Wavelength

C. N. Okafor
D. W. Peckham

AT&T Bell Laboratories
2000 Northeast Expressway, Norcross, GA. 30071

1. INTRODUCTION

An important parameter for a single-mode optical fiber is the effective cutoff wavelength, because it indicates the minimum wavelength at which a system can operate efficiently. The term effective cutoff wavelength is defined as the wavelength where the first higher order mode (LP_{11}) starts to propagate and increases the total power transmitted through a fiber (of a given length and configuration) by 0.1 dB.

The mode suppression technique is the most common technique used to measure the effective fiber cutoff wavelength (EIA-455-80). The power through a short length of fiber (usually 2m) is measured at selected wavelengths (typically every 10 nm) both with and without a small diameter mode suppression loop. The cutoff wavelength is the wavelength at which the "loop loss" is 0.1 dB. When the 0.1 dB loss value falls between measured data points, linear interpolation is used to determine the fiber cutoff wavelength. This estimated cutoff wavelength tends to be higher than the actual fiber cutoff wavelength because the power vs. wavelength curve near λ_c is concave rather than linear (Figures 1 and 2). The measurement accuracy can be improved, at the expense of increase of measurement time, by decreasing the spacing between measured wavelengths.

In this paper, a more accurate method of determining the fiber cutoff wavelength by fitting an emperical model to the loss data is introduced. The advantages of this method over linear interpolation are:

1. Fewer data points, spaced 20 - 40 nm apart, can be used in the curve fit to achieve a given measurement resolution.
2. Fewer data points mean shorter measurement time, and a resulting savings in cost.
3. The determined cutoff wavelength is more accurate because it accounts for the actual shape of the "loop loss" vs. wavelength curve.
4. The precision is increased because a least-squares curve fitting procedure is used.

2. DERIVING AND LINEARIZING THE LOOP LOSS EQUATIONS.

An expression for the cutoff wavelength measurement "loop loss" is derived that more accurately describes the LP_{11} mode behavior near its cutoff than the straight line interpolation used in the EIA procedure.

We assume that a) the first higher order mode (LP_{11}) is so weakly guided near cutoff that it is completely attenuated by the loop inserted during the fiber cutoff wavelength measurement, and b) the attenuation of the fundamental mode (LP_{01}) caused by the loop and short length of fiber is negligible. Both of these conditions are generally met near λ_c if the diameter of the loop is properly chosen (typically 25-50 mm). Therefore, only the LP_{01} mode power P_{01} exits the fiber when the loop is present, and $P_{01} + P_{11}10^{-\alpha_{11}L/10}$ when the loop is removed. P_{01} and P_{11} are the initial launched powers guided by the LP_{01} and LP_{11} modes, respectively, α_{11} is the LP_{11} mode attenuation in dB/m, and L is the fiber length in meters.

Thus, the loss of the loop is written as:

$$\text{Loss} = 10\log\frac{(P_{01} + P_{11}10^{-\alpha_{11}L/10})}{P_{01}} \qquad (1)$$

Now assume that the power launched into the LP_{11} mode is a multiple factor of the LP_{01} modal power represented by ρ, ($\rho \approx 2$), so that $P_{11} = \rho P_{01}$.

The wavelength dependent attenuation of the LP_{11} mode, α_{11}, can be written as [1,2]

$$\alpha_{11} = \frac{A\chi^{(\lambda - \lambda_c)/10}}{L} \tag{2}$$

where $A = 10\log \frac{\rho}{10^{0.01} - 1}$ (A=19.3 for ρ=2), χ is a constant related to the fiber index profile† ($\chi \approx 1.4$ for AT&T depressed cladding fibers), λ is the wavelength where α_{11} is evaluated, λ_c is the cutoff wavelength to be determined, and L is the length of fiber at which λ_c is defined (generally 2m).

Substituting Eq. 2 into 1, with $P_{11} = \rho P_{01}$ gives

$$\text{Loss} = 10\log\left[1 + \rho 10^{\left(\frac{-A\chi^{(\lambda - \lambda_c)/10}}{10}\right)}\right] \tag{3}$$

We can simplify Eq. 3, the "loop loss" equation, to the form of a linear equation in λ by rearranging and letting $Y = 10\log\left\{\frac{-10}{A}\log\left(\frac{10^{\text{Loss}/10} - 1}{\rho}\right)\right\}$. Eq. 3 becomes:

$$Y = (\lambda - \lambda_c)\log\chi \tag{4}$$

This is a straight line equation in the λ and Y plane, i.e, $Y = a + b\lambda$ where $a = -\lambda_c\log\chi$ is the Y-intercept and $b = \log\chi$ is the slope.

Eq. 4 has two unknown parameters λ_c and χ which can be uniquely determined by using the same two data points as in the EIA linear interpolation procedure. (With additional data points, a more robust regression analysis can be performed as discussed in section 3.)

To compare the cutoff wavelengths determined by the two methods, a fiber was measured every 2 nm in the region around the cutoff wavelength. The loop loss model (Eq. 4) was fit to this data to accurately determine the wavelength where the "loop loss" is 0.1 dB, i.e, λ_c. Next, the cutoff wavelength using the EIA linear interpolation procedure, λ_c^{EIA}, was determined using data points spaced 10 nm apart. Using the same two data points that were used to determine λ_c^{EIA}, the loop loss model was used to determine λ_c^{2pts}. Figure 2 shows the plots of the results of these 3 calculations. The data points in the square boxes are the ones used to determine λ_c^{EIA} and λ_c^{2pts}. Figure 2 shows that λ_c^{2pts} is very close to λ_c because the model accurately represents the loss curve, however, the EIA method using linear interpolation, results in an overestimate of λ_c.

3. DISCUSSIONS OF THE ROBUST CUTOFF WAVELENGTH

The loop loss model can also be used for a more robust estimate of cutoff wavelength by using a linear least-squares regression analysis in the λ and Y plane to fit the model to more than two data points. The linear regression analysis gives the slope b and the intercept a of the linear equation of which $\lambda_c = -a/b$ and $\chi = 10^b$.

---

† It can be shown χ is related to the length scaling of the cutoff wavelength. For a straight fiber, the cutoff wavelength of a fiber of length L is $\lambda_c(L) = \lambda_c(2) - \frac{10}{\log\chi}\log(\frac{L}{2})$, where $\lambda_c(2)$ is the 2-meter cutoff wavelength.

When two data points are used, the model yields a cutoff wavelength, λ_c^{2pts}, that is more accurate than the linear interpolation method used in the EIA procedure. However, both methods force their respective interpolating functions through two particular data points, and the results are sensitive to any error in the measurements. Performing a linear least-squares regression analysis with more than two data points, spaced by 20 nm or more, has the advantage of:

1. Averaging the measurement uncertainties and yielding a more precise value of λ_c.
2. Including additional data points below the cutoff wavelength where potential modal noise generation is a concern.

In a fiber system, some fibers may be operated below their cutoff wavelength, and this causes concern about modal noise generation. Including two or more points within this region in determining the λ_c of the fiber yields a better representation of the LP_{11} mode attenuation in this region of interest. Therefore, the determined cutoff wavelength will be a more accurate estimate (considering modal noise) when specifying fibers.

Figure 3 shows the linear regression analysis on λ and Y, and a plot of λ and loop loss (dB) for a depressed-cladding single-mode fiber. The data points are spaced 20 nm apart and those in the square boxes are the ones used in the regression analysis.‡ Also plotted are three vertical lines showing the cutoff wavelengths determined by using 1) linear interpolation, λ_c^{LIT}, 2) the model with the same two data points used in the linear interpolation λ_c^{2pts}, and 3) the model with 3 or more data points, λ_c^{cfit}. The cutoff wavelengths estimated by the three methods are 1267.4, 1263.6 and 1264.3 nm, respectively.

Table 1 shows tabulations of the calculated cutoff wavelengths using three different methods (λ_c^{EIA}, λ_c^{2pts}, λ_c^{cfit}) compared to the "actual" cutoff wavelength, λ_c, determined by measuring additional data points spaced 2 nm apart in the cutoff wavelength region and fitting the model through the points. The data points used in determining λ_c^{cfit} and λ_c^{2pts} are spaced 20 nm apart while the ones used in determining λ_c^{EIA} are spaced 10 nm apart. The average error of the EIA method is higher than the other two methods where the model is used, even though the data points are spaced 20 nm apart.

4. CONCLUSIONS

The model described in this paper determines cutoff wavelength more accurately and with fewer measurements (and hence, lower cost) than by using the standard EIA-455-80 procedure. Fitting two data points with the model gives a more accurate estimate of the "traditional" fiber cutoff wavelength (even if the data points are spaced 20 nm apart) when compared with the EIA method. Including 3 or more loss values in the 3.0 - 0.03 dB range gives a robust value of cutoff wavelength that incorporates the concern of potential modal noise generation. Using the model, 20 to 40 nm spaced data points can be used with excellent accuracy. This new model works well with both depressed and matched cladding fiber designs.

REFERENCES

[1] D. G. Duff, F. T. Stone, and J. Wu, "Measurements of Modal Noise in Single-Mode Lightwave System," *Technical Digest*, 8th Conference on Optical Fiber Communication, San Diego, California, (Feb. 11-13, 1985), paper TU01.

[2] F. T. Stone, "Modal Noise in Single-Mode Fiber Communications System," Proceedings of the SPIE, San Diego California, vol. 500, pp. 17-22, (1984).

‡ "Loop loss" values in the 3.0 - 0.03 dB range are used in the regression analysis. At higher loss values some of the assumptions of the model are no longer valid, and below 0.03 dB small measurement uncertainties can dominate.

Table 1. Comparism of the cutoff wavelength determined by the three different methods with the actual cutoff wavelength.

Fiber Cutoff Wavelengths				
Fiber ID #	Errors			
	Actual λ_c	$\lambda_c^{EIA} - \lambda_c$	$\lambda_c^{2pts} - \lambda_c$	$\lambda_c^{cfit} - \lambda_c$
Fiber #1	1294.2 nm	+1.6 nm	-0.2 nm	+1.0 nm
Fiber #2	1309.3 nm	+0.6 nm	+0.5 nm	+0.3 nm
Fiber #3	1335.7 nm	+0.8 nm	-0.1 nm	-1.0 nm
Fiber #4	1331.6 nm	+1.6 nm	+1.2 nm	+0.2 nm
Average Error		+1.15 nm	+0.35 nm	+0.12 nm

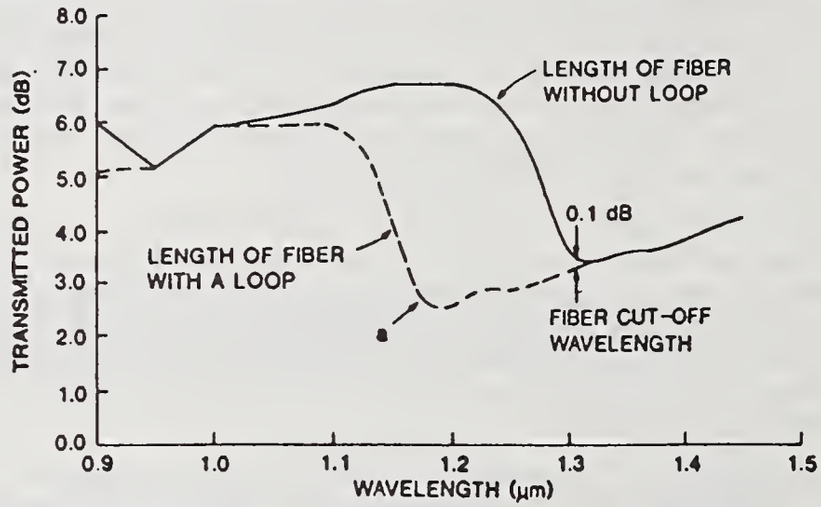

FIG. 1. Normalized Plot of Transmitted Power With and Without a Mode Suppression Loop

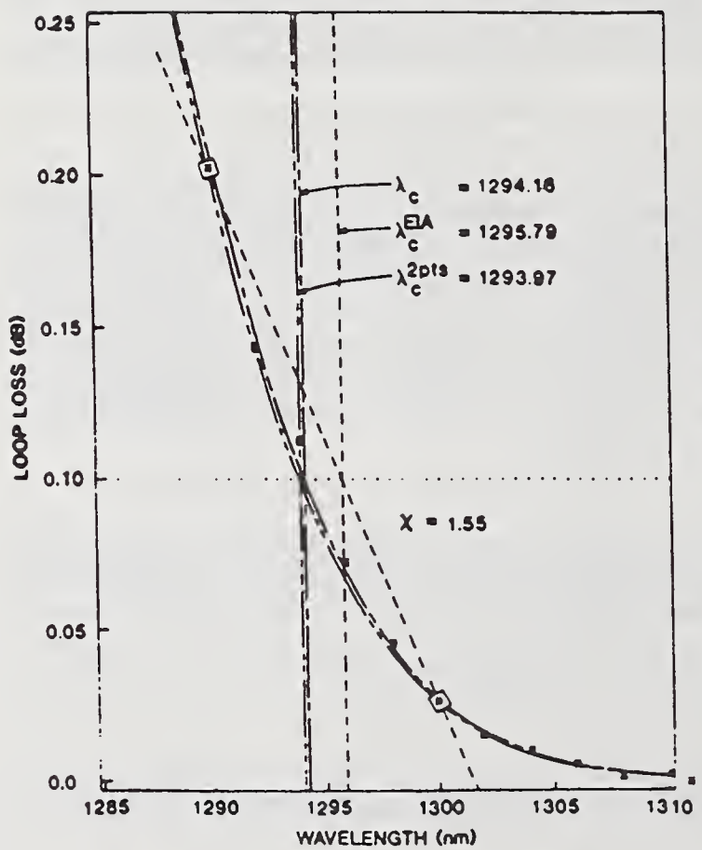

FIG. 2. Plots of λ_c, estimated by three different methods.

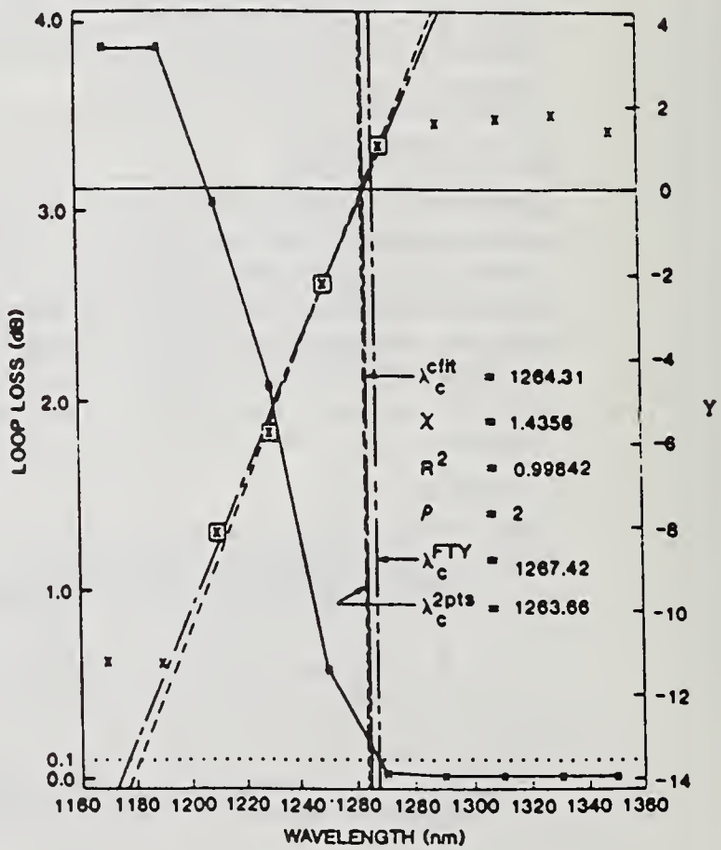

FIG. 3. Plots of λ and Y, λ and Loop Loss (dB), and the estimated λ_c.

A Technique to Estimate the Cutoff Wavelength Profile in Single Mode Fibers Using a Switchable Dual Wavelength OTDR

by
K.W. Kowaliuk and J. Ferner

Northern Telecom Canada Limited
Optical Cable Division
Saskatoon, Saskatchewan, Canada

ABSTRACT

A technique is presented which provides a measurement of the cutoff wavelength profile in single mode fibers using a dual wavelength OTDR. The theory of this technique is based on the dependance of the backscatter capture fraction on the mode field diameter and on the dependance of the mode field diameter on wavelength and cutoff wavelength. Accuracies of ± 20 nm in the measurement of the relative deviation of λ_c are reported for typical single mode fibers. However, in certain circumstances caution must be exercised when interpreting results.

BACKGROUND

The backscatter signal obtained from the OTDR measurement of an optical fiber is the result of the combination of three key mechanisms; power decay or attenuation, local scattering and the backward capture and transmission of the scattered light. In its simplest form, the backscatter power P received from a given point z in a fiber can be represented as the product of these effects.

$$P(z) \propto P_o \ \alpha_s(z) \ B(z) \exp\left[-2 \int_o^z \gamma(x)dx \right] \qquad (1)$$

where P_o is the power launched into the fiber, $\alpha_s(z)$ is the local scattering coefficient, $B(z)$ is the backscatter capture fraction, and $\gamma(z)$ is the local attenuation coefficient.

A technique developed by DiVita and Rossi [1] provides a highly reliable means of separating the decay and waveguide imperfection effects from an OTDR signature. For OTDR signatures $S_1(z)$ and $S_2(z)$ (which include the processing performed in the OTDR) launched from opposite ends of the same fiber of length L, the imperfection contribution I(z) becomes:

$$I(z) = S_1(z) + S_2(L-z) = 10 \log_{10} [\alpha_s(z) \ B(z)] + A_1 \qquad (2)$$

while the attenuation (decay) contribution D(z) is:

$$D(z) = \frac{S_1(z) - S_2(L-z)}{2} = A_2 - A_3 \int_o^z \gamma(x)dx \qquad (3)$$

where A_1, A_2 and A_3 are constants. The above expressions are derived assuming a pulse of negligible width. For practical applications, the finite width of the laser pulse must be accounted for by shifting the signatures relative to each other before the separation process.

Correct interpretation of the imperfection line requires an understanding of the mechanisms involved. For a typical single mode fiber with a Gaussian field distribution, it has been shown [2] that the backscatter capture fraction B(z) is proportional to $(\lambda/w)^2$ where λ is the wavelength of incident light and w is the LP_{01} mode field diameter. It can also be shown that the influence of the local scattering coefficient $\alpha_s(z)$ on the imperfection line can be neglected compared to the MFD contribution.

An empirical expression was developed by Marcuse [3] which relates the mode field diameter of a step index fiber at a given wavelength to the fiber V number and core diameter. The expression can be rewritten to be a function of wavelength, LP_{11} cutoff wavelength and core diameter. To eliminate the core diameter dependance, the expression is evaluated at two wavelengths λ_1 and λ_2 and the two expressions divided. The ratio of mode field diameters, R, can be written as:

$$R = \frac{w(\lambda_1)}{w(\lambda_2)} = \frac{0.65 + 0.434\left(\frac{\lambda_1}{\lambda_c}\right)^{3/2} + 0.0149\left(\frac{\lambda_1}{\lambda_c}\right)^{6}}{0.65 + 0.434\left(\frac{\lambda_2}{\lambda_c}\right)^{3/2} + 0.0149\left(\frac{\lambda_2}{\lambda_c}\right)^{6}} \quad (4)$$

For simplicity of processing, equation (4) was converted to a more solvable form. For test wavelengths in each of the 1310 nm and 1550 nm regions, equation (4) can be approximated (over the cutoff wavelength range of 1100 nm to 1400 nm) by a second order polynomial of the form:

$$\lambda_c = c_1R^2 + c_2R + c_3 \quad (5)$$

where c_1, c_2 and c_3 are constants.

ANALYSIS ALGORITHM

After obtaining and separating the signatures according to equations (2) and (3), the imperfection lines at each wavelength are referenced to the arbitrary reference point $z = z_o$. The modified imperfection line I'(z) can then be represented as follows:

$$I'(z) = I(z) - I(z_o) = 20 \log_{10}\left[\frac{w(z_o)}{w(z)}\right] \quad (6)$$

By taking the difference between the modified imperfection lines at both wavelengths, the expression becomes:

$$\Delta I(z) = I'(\lambda_2, z) - I'(\lambda_1, z) = 20 \log_{10}\left[\frac{w(\lambda_2, z_o)}{w(\lambda_1, z_o)} \cdot \frac{w(\lambda_1, z)}{w(\lambda_2, z)}\right] \quad (7)$$

Expressing equation (7) in terms of the MFD ratio R gives:

$$R(z) = R(z_o) \cdot 10^{(\Delta I(z)/20)} \quad (8)$$

$R(z_o)$ can be determined either by estimating or physically measuring the cutoff wavelength $\lambda_c(z_o)$ and substituting this into equation (4). R(z) is then calculated from equation (8) which is then used in equation (5) to determine $\lambda_c(z)$. Although this calculation will produce an absolute profile of $\lambda_c(z)$ based on the estimated value of $\lambda_c(z_o)$, it is preferable to present the result of this technique as a profile of the deviation in cutoff wavelength rather than an absolute cutoff wavelength profile. Figure 1 illustrates the various stages of this analysis technique.

EXPERIMENTAL

To verify the reliability of this technique, a number of fibers were produced with severe variations in cutoff wavelength along their length. All the fibers produced for this study were dispersion-unshifted-depressed-clad single mode fibers. OTDR signatures were obtained from each fiber and were separated and analyzed using the technique described above. Each fiber was then cut at regular length intervals and a sample of fiber was taken from each position. The samples were then measured for cutoff wavelength according to EIA-455-80.

Test results from one of these fibers (labelled fiber A) is shown in Figure 1(e). From the test results produced, the technique has proven capable of predicting relative cutoff wavelength variations with an accuracy of ± 20 nm, provided the appropriate pulse width is used.

LIMITATIONS OF TECHNIQUE

There are several key assumptions made in the development of the analysis algorithm which must be taken into account when interpreting the results of this technique. Some of these assumptions include step index behavior of the fibers and the Gaussian form of the mode field diameter. In addition, the effects of the digital filtering performed internally to the OTDR equipment have been neglected. Indeed, it would be possible to develop a more detailed theory to take these factors into account. However, based on the results achieved to date, this technique is limited more by the resolution and signal-to-noise of the reflectometer than by the theory itself.

Nevertheless, one key limitation to this technique is that the theory used assumes that the cutoff behavior of the LP_{11} mode can be predicted based on the behavior of the LP_{01} mode. Provided the shape of the refractive index profile is known, the relationship between these modes can be predicted. However, in order for the prediction to be effective, the general shape of the refractive index profile must remain relatively consistent throughout the fiber length so as not to affect the behavior of one mode relative to the other. This can become particularly important when analyzing fibers with refractive index profiles which deviate substantially from a step index form.

CONCLUSION

The work presented here provides a further interpretation of OTDR signatures for single mode fibers. The technique provides a relatively accurate, non-destructive method to determine the cutoff wavelength profile in most typical single mode fibers. Accuracies of ± 20 nm in this prediction have been routinely achieved. Due to the relative speed and simplicity of the test, the technique has a number of potential applications in such areas as manufacturing process research and production process monitoring.

The theory behind this analytical approach assumes that the fiber tested exhibits ideal step index behavior. Although a more detailed theory could be developed to include more realistic fiber behavior, the step index model has shown good results. There are circumstances where significant errors in the prediction may result. Therefore, care must be taken when attempting to interpret the results of the technique.

REFERENCES

[1] P. Divita, V. Rossi; Backscattering Measurements in Optical Fibers: Separation of Power Decay from Imperfection Contribution, Electronic Letters 15, p. 467, (1979).

[2] M.S. O'Sullivan, R.S. Lowe; Interpretation of SM Fiber OTDR Signatures Proceeding SPIE '86 Optical Testing and Metrology (1986).

[3] D. Marcuse; Loss Analysis of Single Mode Fiber Splices Bell System Technical Journal, May-June (1977).

[4] L.B. Jeunhomme; Single Mode Fiber Optics: Principles and Applications Marcel Dekker, Inc.); V. 4 p. 151 (1983).

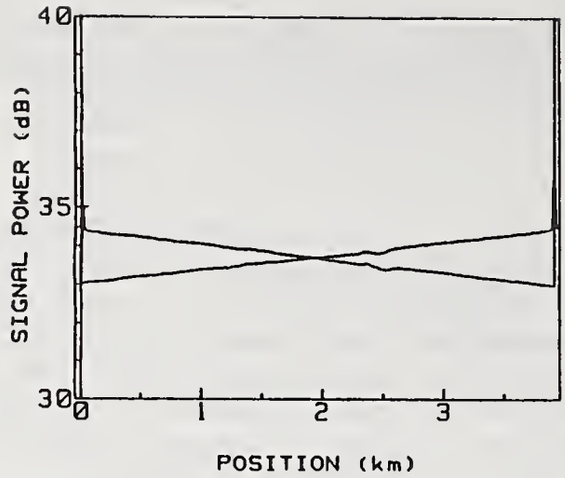

Figure 1(a)

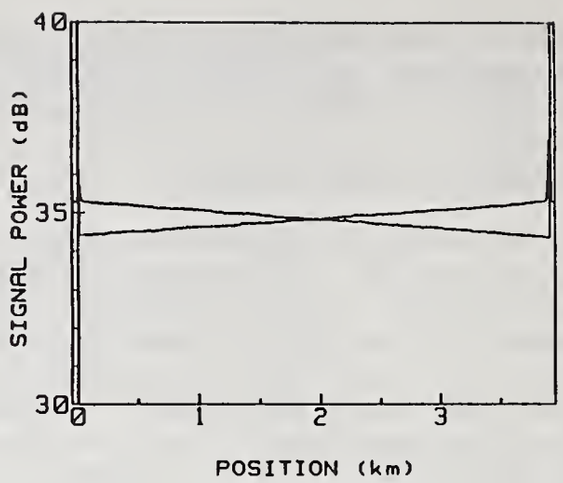

Figure 1(b)

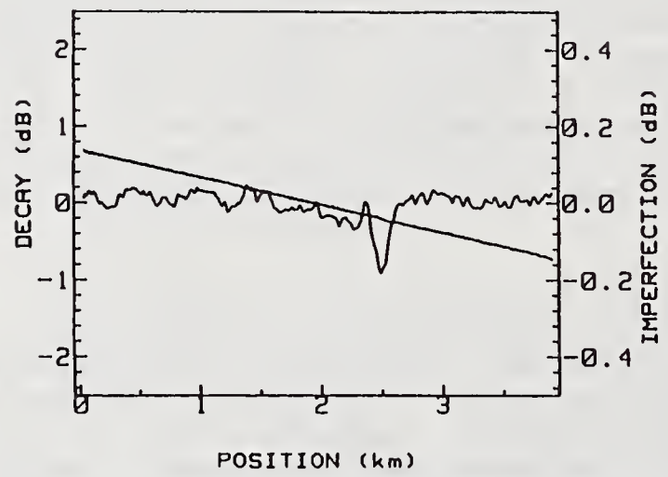

Figure 1(c)

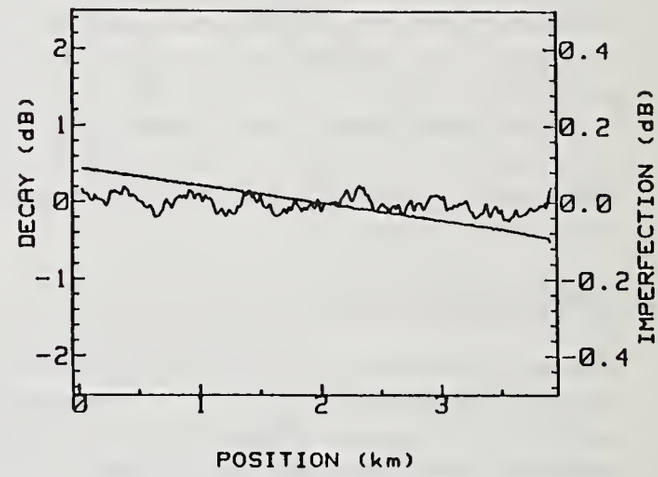

Figure 1(d)

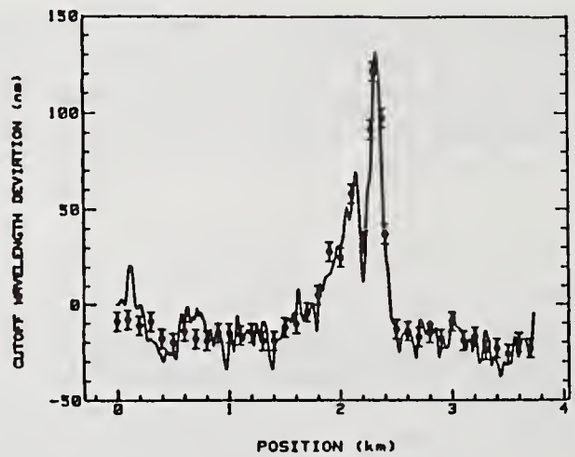

Figure 1(e)

Figure 1 Illustration of OTDR Analysis Technique (Fiber A)
1(a) (b) Original OTDR signatures at 1308 nm and 1545 nm
1(c) (d) Separated OTDR traces at 1308 nm and 1545 nm
1(e) Predicted cutoff wavelength profile correlated with actual measurement performed using EIA-455-80.

Predicting The Cutoff Wavelength of Cabled Single Mode Fibers From Cable Structure

W. H. Hatton and M. Nishimura
Sumitomo Electric Fiber Optic Corporation
Research Triangle Park, NC 27709

Introduction

Accurately predicting the cutoff wavelength of cabled single mode fiber is desired by both fiber and cable manufacturers because fibers which exhibit improved bend performance (longer uncabled cutoff) can be utilized. The Electronic Industries Association (EIA) has adopted a test procedure (FOTP-170) where cutoff is determined by measuring a 22 meter section of cable. This method produces results which simulate worst case field conditions, however, routine measurements would be uneconomical from a cablers point of view, and impossible for a fiber supplier.

It has been suggested that a linear function which maps uncabled fiber cutoff into cabled fiber cutoff be experimentally determined [1]. This is a beneficial procedure, but without a complete understanding of how cable structure effects cutoff, a different mapping would be required for each cable design (a very time consuming process). In addition, it has been proposed that cabling effects could be simulated by replacing the 22 meters of cable by 22 meters of uncabled fiber looped at a minimum bend diameter of 280mm [2]. This technique may be adequate for certain cable designs, but in most cases, the results would be extremely pessimistic due to an over exaggeration of fiber curvature (i.e. effective cabled fiber bend diameters of 100 mm to 200 mm are common). In this paper, a method for predicting cutoff shift (uncabled-cabled) from cable design (effective bend diameter) will be presented.

Experiment

To accurately determine cabled fiber cutoff both length and curvature effects must be considered [3,4]. Changes in cable design primarily effect curvature, and thus, the fiber deployment shown in Figure 1 was developed to offer a variable scheme for simulating cable effects on cutoff. With the addition of a variable mandrel, the fiber can be looped at a bend diameter equivalent to that occurring inside the cable. The effective bend diameter can be calculated from design parameters such as tube pitch, tube diameter, and central tension member diameter (for loose tube designs). By adjusting the mandrel size, the relationship between cable structure and cutoff could be determined.

A collection of both matched clad and depressed clad single mode fibers (22 meter length) were prepared. Each fiber was subjected to various bend diameters and cutoff was determined by comparing the spectral power transmitted through the above deployment to that when an additional smaller diameter bend was introduced. For each diameter, a linear least squares routine was used to map uncabled cutoff into predicted cable cutoff. Figures 2A & 2B illustrates the relationship between cutoff shift (uncabled - predicted) and effective bend diameter.

It is well known that effective cutoff of depressed clad fiber is less sensitive to curvature effects [3], and to some extent this was reflected in the measured results. There was, however, a critical diameter of 150 mm where bending effects could not be neglected. Conversely, matched clad fiber, being more bend sensitive [3], demonstrated a much stronger bend dependence. For typical effective bend diameters of 100 mm to 200 mm, a cutoff shift of 40 nm existed. A model which neglects, or over exaggerate curvature effects, would be inadequate for this fiber type.

Table 1 compares predicted cutoff shift to measured (FOTP-170) for various loose tube cable designs and both fiber types. Figures 3A and 3B shows fitted curves (predicted and measured) comparing uncabled and cabled fiber cutoff.

Conclusions

Cabled fiber cutoff wavelength can be simulated accurately if both length and curvature effects are considered. It has been shown that by developing the relationship between effective bend radius and cutoff shift (uncabled-simulated cabled) cabled fiber cutoff can be accurately and easily predicted. This eliminates the need for developing separate mapping functions for each cable design. A more detailed comparison between predicted and measured cabled fiber cutoff will be presented at the conference.

References

[1] J. P. Kilmer, IWCS Symposium Proceedings, pp. 49-56, 1987

[2] D. W. Peckham, Technical Digest, OFC 88, paper WE5, 1988.

[3] L. Wei, IEEE JLT Vol. LT-5, No. 9, p. 1147, 1987.

[4] W. T. Anderson, IEEE JLT, Vol. LT-2, No. 3, P. 238, 1984.

Table 1 Measured and predicted cabled fiber cutoff for various loose tube cable structures

Fiber Type	Effective Bend (mm) Diameter	Cutoff Wavelength (nm) Shift	
		Measured	Predicted
Depressed	160	83	80
Depressed	146	89	87
Depressed	160	77	80
Matched	120	121	124

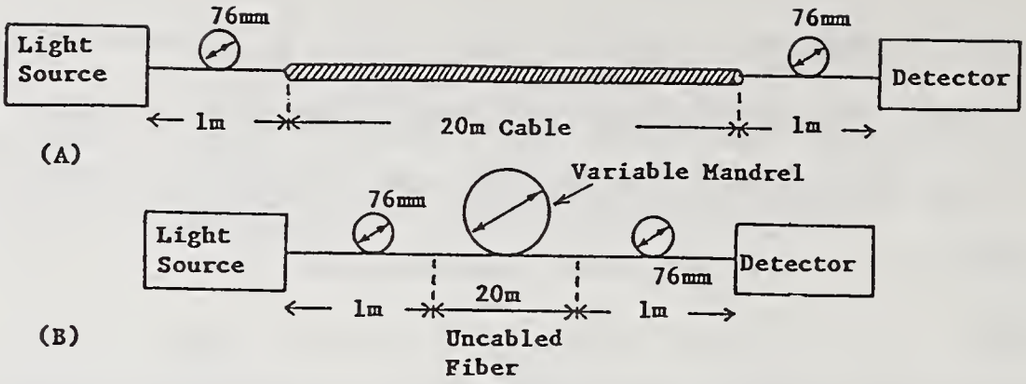

Figure 1 Schematic Diagram of A) deployment for cable cutoff (FOTP-170), and B) simulated cable cutoff.

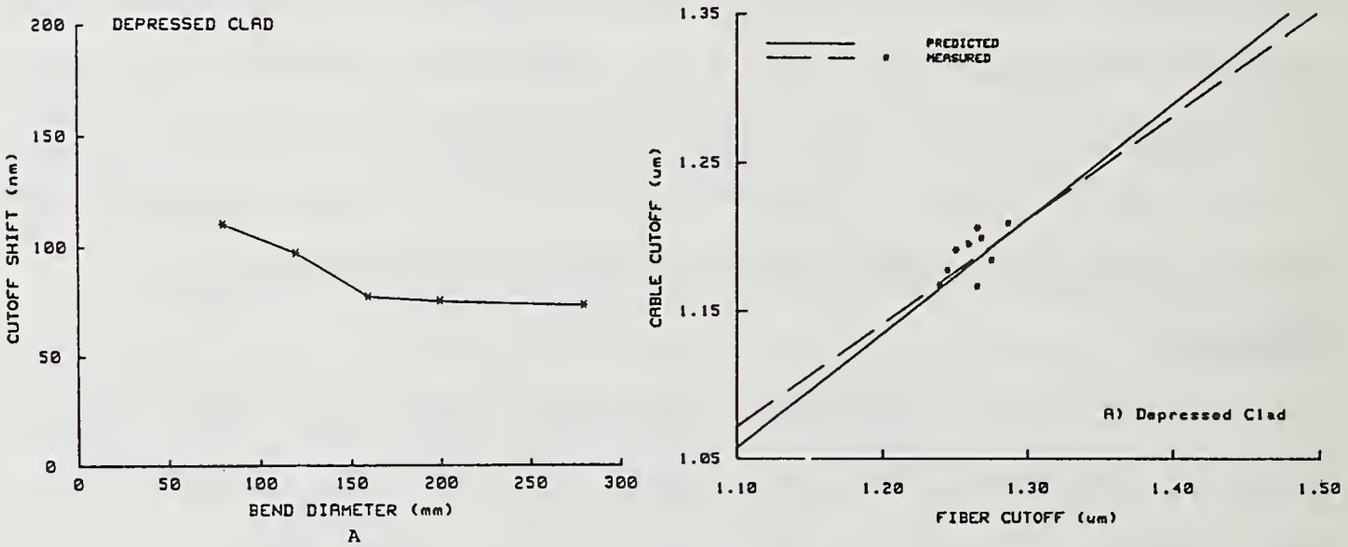

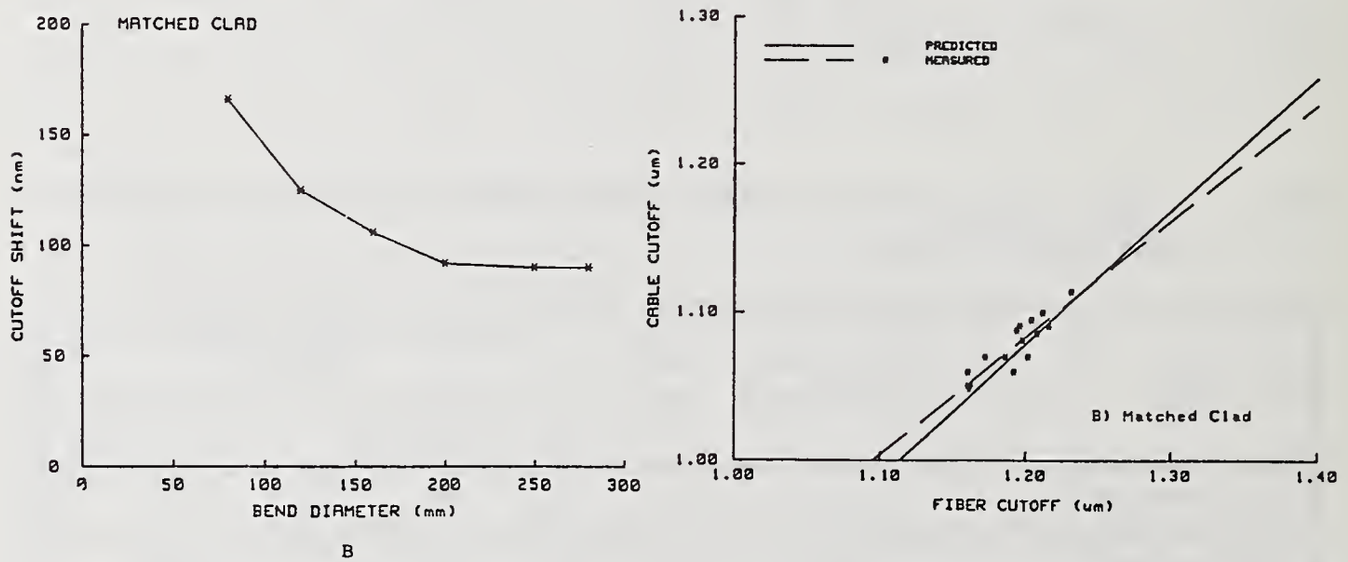

Figure 2 Relationship between effective bend diameter and cutoff shift (uncabled-predicted) for A) depressed clad fiber, and B) matched clad fiber

Figure 3 Comparison between predicted and measured cabled fiber cutoff for A) depressed clad fiber, and B) matched clad fiber

SIMULATED CABLE DEPLOYMENT FOR CABLE CUTOFF WAVELENGTH MEASUREMENTS

J. P. Kilmer, R. M. Kanen, and W. T. Anderson

Bell Communications Research
Morristown, New Jersey

1. Abstract

The simulation of the cable cutoff wavelength deployment configuration with 22 meters of coiled uncabled fiber is experimentally studied. The results show the simulation gives equivalent λ_{cc} results for depressed-clad fibers and more conservative λ_{cc} results for matched-clad fibers.

2. Introduction

Cutoff wavelength refers to the wavelength below which a single-mode fiber is capable of supporting more than one mode and is the primary limitation on the lower edge of the single-mode fiber's 1300 nm operating window. The future use of multiple high bit-rate WDM systems around 1300 nm may make the neglected 1250 to 1300 nm region more attractive than the 1550 nm region where there is greater chromatic dispersion. Cutoff wavelength must be controlled in order to prevent single-mode system operation in the fiber's multimode region [1-3]. The Electronic Industries Association (EIA) has two definitions for cutoff wavelength. The first definition, fiber cutoff wavelength (λ_{cf}), is a convenient parameter for a manufacturer to monitor for process control but provides the user with information which is not directly applicable to system design. λ_{cf} is measured on a 2 m fiber sample deployed in a fashion which is never found in the field, as described in the test procedure FOTP-80 [4] (see Figure 1). The second definition, cable cutoff wavelength (λ_{cc}), provides the user with a functional value of cutoff wavelength which can be used in system design. FOTP-170 [5] describes the test procedure to measures λ_{cc}. CCITT Recommendation G.652 also contains similar definitions and procedures for cutoff wavelength.

While the cabled fiber sample's deployment conditions can be specified in the detail specification, FOTP-170 contains two possible default deployment configurations. The first default deployment configuration is a 20 meter (65.6 ft.) cable length with one meter of exposed fiber at each cable end. One 76 mm (3 in.) loop is inserted in each exposed fiber end (see Figure 2). 20 meters is considered a worst-case minimum cable length likely to be deployed in the field (typically repair sections or stubs), and splice organizers contain trays with space to coil slack fiber typically into 3 in. loops. Since this deployment configuration requires 20 meters of cable, cable cutoff wavelength is by nature more difficult to measure on a routine basis than fiber cutoff wavelength. Therefore, a variation on this cable deployment configuration has been proposed in order to facilitate routine measurement. This second default configuration consists of an uncabled fiber length totaling 22 m coiled in a loop of 28 cm diameter or greater with the two 76 mm loops at the fiber ends (see Figure 3). The coiling of the fiber length in a loop of 28 cm diameter or greater simulates the cabling effect. Cabling a fiber, if it affects the fiber at all, may introduce some periodic bends which serve to reduce cutoff wavelength. Therefore, uncabled fiber should give a slightly higher (or more conservative) λ_{cc} value. Since the 3 in. loops are expected to dominate cutoff wavelength reduction [6], coiling the uncabled fiber in a loop of 28 cm or larger should not affect the measured λ_{cc}.

3. Experiment

To verify that the 22 m of coiled uncabled fiber is an adequate simulation of the 20 meter cable length with one meter of exposed fiber at each cable end, two cable samples were measured for λ_{cc}'s according to the first default configuration (Figure 2). One cable sample consisted of depressed clad fibers (DCF)

manufactured by the inside vapor deposition process (IVD) bundled together inside a crossply cable sheath. The other cable sample consisted of matched clad fiber (MCF) manufactured by the outside vapor deposition process (OVD) in a loose tube cable construction employing a reversing oscillating lay. After measuring λ_{cc} in cable form, the fibers were carefully removed from the cable and deployed in the coiled uncabled fiber deployment configuration (Figure 3). A comparison of the cabled and simulated-cable measurements appears in the following tables:

Coiled Fiber and Cable Cutoff Wavelength Comparisons (in nm)
DCF IVD Fiber in Fiber Bundle Cable

Fiber	Coiled	Cabled	Difference
Blue/Blue	1173	1161	12
Blue/Brown	1215	1212	3
Blue/Slate	1186	1189	-3
Blue/White	1197	1207	-10
Blue/Red	1192	1197	-5
Blue/Yellow	1180	1178	2
Blue/Dash Orange	1194	1207	-13
Orange/Blue	1235	1218	17
Orange/Orange	1178	1168	10
Orange/Green	1177	1187	-10
Orange/Brown	1186	1199	-13
Orange/Slate	1176	1179	-3
Orange/White	1209	1212	-3
Orange/Red	1189	1189	0
Orange/Yellow	1187	1198	-11
Orange/Violet	1201	1215	-14
Orange/Dash Blue	1162	1171	-9
Orange/Dash Orange	1208	1196	12
Green/Blue	1204	1214	-10
Green/White	1213	1218	-5

Coiled Fiber and Cable Cutoff Wavelength Comparisons (in nm)
MCF OVD Fiber in Loose Tube Cable

Fiber	Coiled	Cabled	Difference
Blue/Blue	1149	1147	2
Blue/Orange	1093	1099	-6
Blue/Green	1118	1094	24
Blue/Brown	1154	1117	37
Blue/Slate	1126	1112	14
Blue/White	1120	1109	11
Orange/Blue	1136	1128	8
Orange/Orange	1139	1116	23
Orange/Green	1129	1115	14
Orange/Brown	1150	1119	31
Orange/Slate	1118	1115	3
Orange/White	1120	1116	4
Green/Blue	1116	1124	-8
Green/Orange	1116	1098	18
Green/Green	1119	1088	31
Green/Brown	1130	1117	13

On average, there is a -2.65 ± 9 nm (1 standard deviation) bias for the IVD DCF fiber and a 13.68 ± 13

nm bias for the OVD MCF fiber between the two deployment configurations. While there is no statistically significant difference between the two deployment configurations for the DCF fiber type, there is a small bias for the MCF fiber type. This bias is expected due to the increased cutoff wavelength bend sensitivity of the MCF fiber type [7]. Since the bias is positive in this case, the simulated cable configuration gives a conservative (i.e., higher) value for λ_{cc} than the cabled configuration.

4. Conclusion

The coiled uncabled fiber simulation gave equivalent λ_{cc} results to the cabled fiber deployment configuration for a depressed-clad type fiber and gave slightly more conservative λ_{cc} results for a matched-clad type fiber due to the increased cutoff wavelength bend sensitivity of the MCF type fiber. Consequently, the 22 m coiled uncabled fiber is an adequate simulation for cable cutoff wavelength measurements. Since the coiled-uncabled fiber simulation is conservative, manufacturers can use it prior to cabling to assure λ_{cc} requirements are met in the final cabled form.

REFERENCES

[1] F. T Stone, "Modal Noise in Single-Mode Fiber Communication Systems," *SPIE Proceedings 500-04*, San Diego, (1984).

[2] R. W. Tarwater, M. J. Maslaney, D. L. Philen, F. T. Stone and D. G. Duff, "Bandwidth and Cutoff Wavelength of Single-mode Lightguide System Considerations," *IWC Symposium Proceedings*, pp. 261-265, Reno, Nevada, (1984).

[3] N. K. Cheung and P. Kaiser, "Cutoff Wavelength and Modal Noise in Single- Mode Fiber Systems," *NBS Special Publication 683*, pp.15-18, (1984).

[4] EIA-455-80, "Cutoff Wavelength of Uncabled Single-Mode Fiber by Transmitted Power," Electronic Industries Association, Engineering Dept., 2001 Eye St., N.W., Washington, D.C.

[5] EIA-455-170, "Cutoff Wavelength of Single-Mode Fiber Cable by Transmitted Power," Electronic Industries Association, Engineering Dept., 2001 Eye St., N.W., Washington, D.C.

[6] J. P. Kilmer, W. T. Anderson, R. M. Kanen and C. M. Connor Davenport, "Cabling Dependence of Optical Fiber Cutoff Wavelengths," *IWC Symposium Proceedings*, pp. 49-56, Arlington, Virginia, (1987).

[7] V. Shah, "Effective Cutoff Wavelength for Single-Mode Fibers," Symposium on Optical Fiber Measurements, *NBS Special Publication 683*, pp. 7-9, (1984).

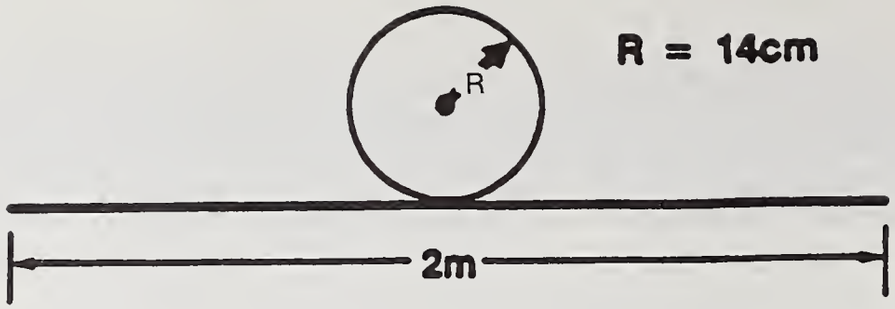

Figure 1. Fiber Cutoff Wavelength (FOTP-80) Deployment Configuration

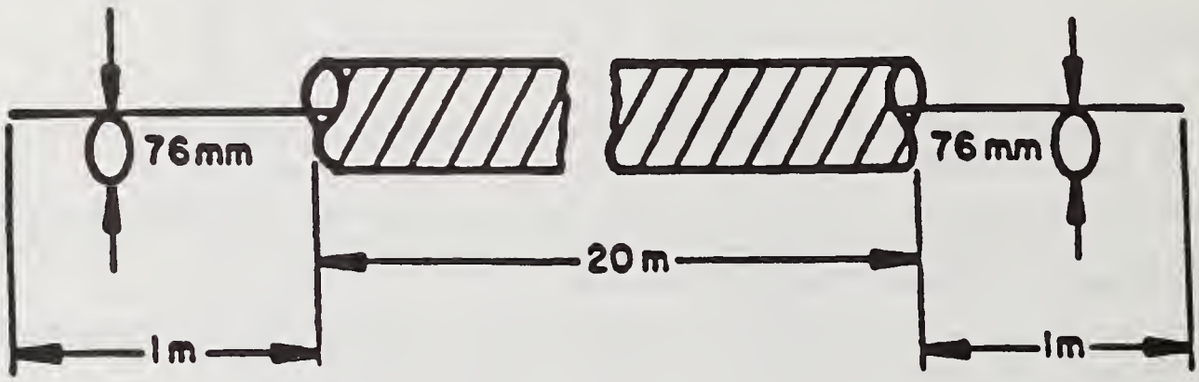

Figure 2. Cable Cutoff Wavelength (FOTP-170) Default Deployment Configuration 1

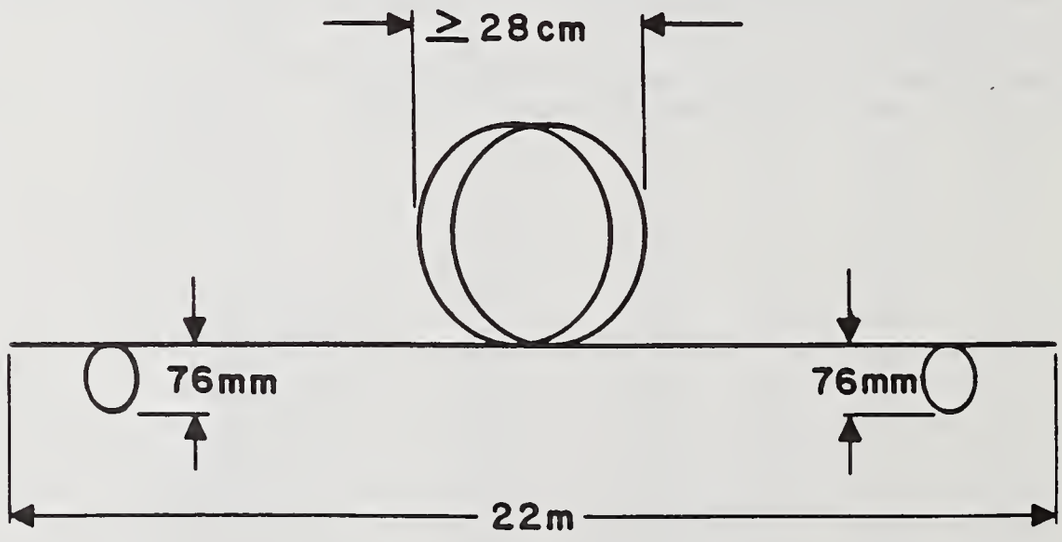

Figure 3. Cable Cutoff Wavelength (FOTP-170) Default Deployment Configuration 2

CUTOFF CHARACTERISTICS OF DISPERSION-SHIFTED AND DISPERSION-UNSHIFTED FIBERS

V. Shah, L. Curtis, and W. C. Young
Bellcore
331 Newman Springs Road
Red Bank, NJ 07701-7020
(201)-758-3156

INTRODUCTION:

Dispersion-shifted (DS) single-mode fibers, having the zero dispersion wavelength in the low attenuation 1550 nm wavelength region, may be required to realize high capacity long haul transmission systems. However, very little has been reported about the cutoff characteristics of such fibers. Recent work[1] on the cutoff characteristics of segmented core DS fibers reported the presence of a "hump" in the cutoff region of the fiber. In this paper, we report the presence of such a "hump" in dispersion-unshifted (1300 nm optimized) single-mode fibers of both the matched as well as depressed-cladding design. Based on the results of our study, a possible explanation of the presence of the "hump" in the cutoff region is presented and resulting systems implications discussed.

EXPERIMENTAL STUDY:

To measure the cutoff wavelength, the spectral powers, P_1 and P_0, transmitted through a 2-m long fiber arranged in large and small single loops of diameters D = 28 cm and d = 5 cm are measured, respectively. The normalized power (P_1/P_0) in dB is plotted as a function of the wavelength λ, and the cutoff wavelength is determined as the wavelength where the long wavelength edge of the curve increases by 0.1 dB over the baseline, as per CCITT Recommendation G.652 and EIA FOTP-80. Fig. 1 shows the normalized power-vs-wavelength curves for a segmented core DS fiber (curve A) as well as matched-cladding (curve B) and depressed-cladding (curve C) dispersion-unshifted fibers. As observed from Fig. 1, the "hump" appears in the cutoff region of each of these fibers. To investigate the nature of the hump, both P_1 (dashed curve) and P_0 (solid curve) are plotted as a function of the wavelength for the DS fiber in Fig. 2. The "hump" of Fig. 1 appears in $P_1(\lambda)$ of Fig. 2. This indicates that contrary to the expected

decrease in the transmitted power due to rapid attenuation of the higher-order modes, an increase in the transmitted power takes place in the wavelength region slightly below the cutoff wavelength. In the case of DS fiber, one may associate this phenomenon with the cutoff of two higher-order mode groups (LP_{02} and LP_{11}) having closely spaced propagation constants. However, in that case the cutoff curve is expected to show two different slopes (both having same sign) in the cutoff region rather than the "hump". In addition, the "hump" is observed in both depressed-clad and matched-clad dispersion unshifted fibers which, unlike the DS fiber, do not have closely spaced propagation constants for higher-order modes.

A possible explanation of the "hump" can be offered in terms of coupling between the whispering gallery mode[2] formed in the cladding region due to the high-index coating surrounding the fiber and the higher-order core mode. Power in the whispering gallery mode can couple to the higher-order core mode, resulting in the "hump(s)". To investigate this possibility, removal of this coupling mechanism is required. This can be achieved by removing the high index primary coating from the curved portion of the fiber and very closely matching the cladding index by immersing the fiber in an appropriate index matching oil. The whispering gallery mode is no longer supported under such conditions and therefore $P_1(\lambda)$ should show no "hump" in the cutoff region.

Fig. 3 shows the result of such an experiment carried out with the DS fiber. The figure shows P_1 plotted as a function of λ. The solid curve corresponds to the fiber with coating and has two "humps" in the cutoff region. The dashed curve corresponds to the fiber immersed in index matching oil and does not have any "hump" in the cutoff region. The results of these later measurements support the theory that the "hump" in the cutoff region may be the result of mode coupling between the whispering gallery mode and the higher order core mode.

CONCLUSION :

In conclusion, the fibers investigated (both DS and dispersion unshifted) exhibit a "hump" in the cutoff region. Experimental results are also presented which support the theory that these "hump(s)" occur as a result of coupling between the whispering gallery mode and the higher order modes.

REFERENCES:

[1] V. Shah, G. Kinshofer, L. Curtis, and W. C. Young, Tech. Dig. OFC'88, New Orleans, Paper WI5, (1988)

[2] A. J. Harris, and P. F. Castle, J.of Lightwave Tech., Vol. LT-4, No. 1, pp. 34, (1986)

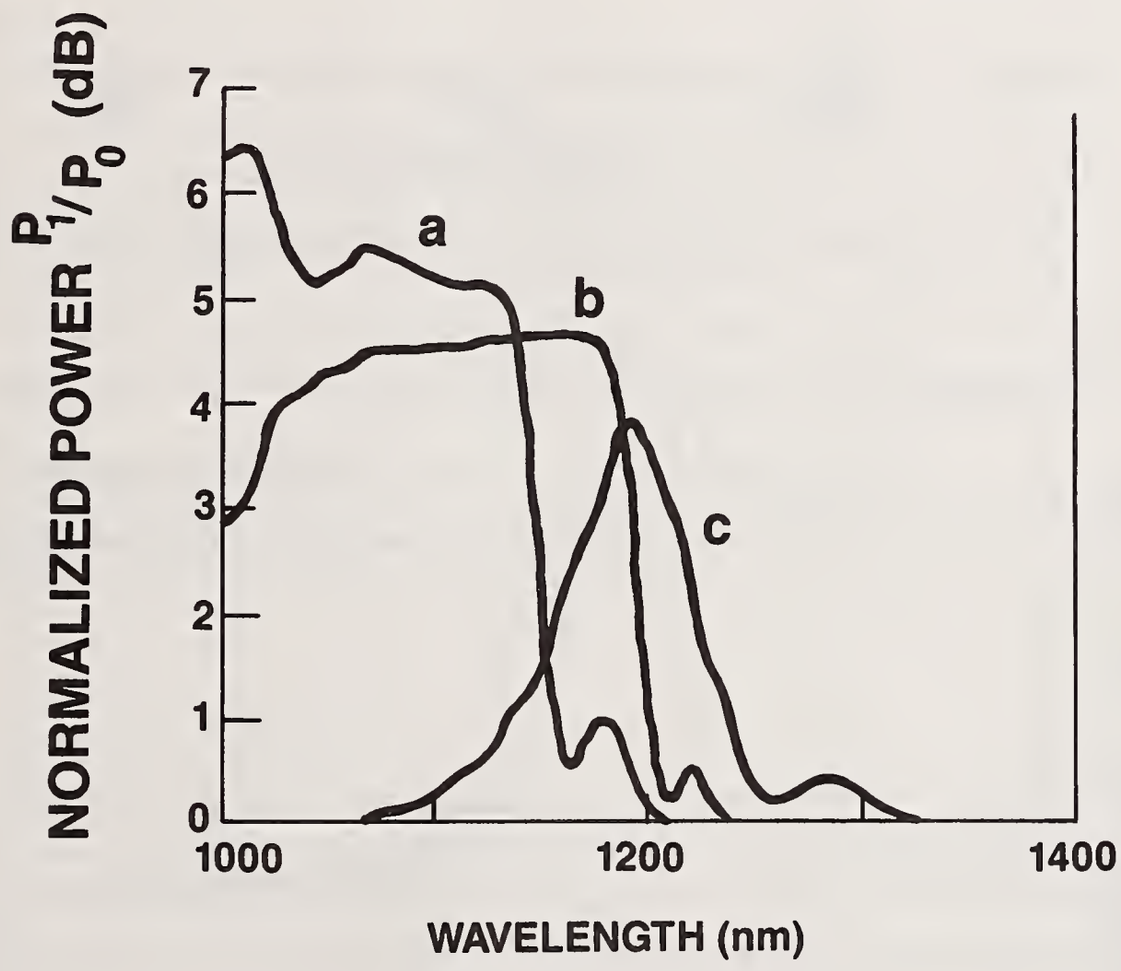

Fig. 1 Cutoff curves for a segmented core DS fiber (curve A), a matched-cladding fiber (curve B), and a depressed-cladding fiber (curve C).

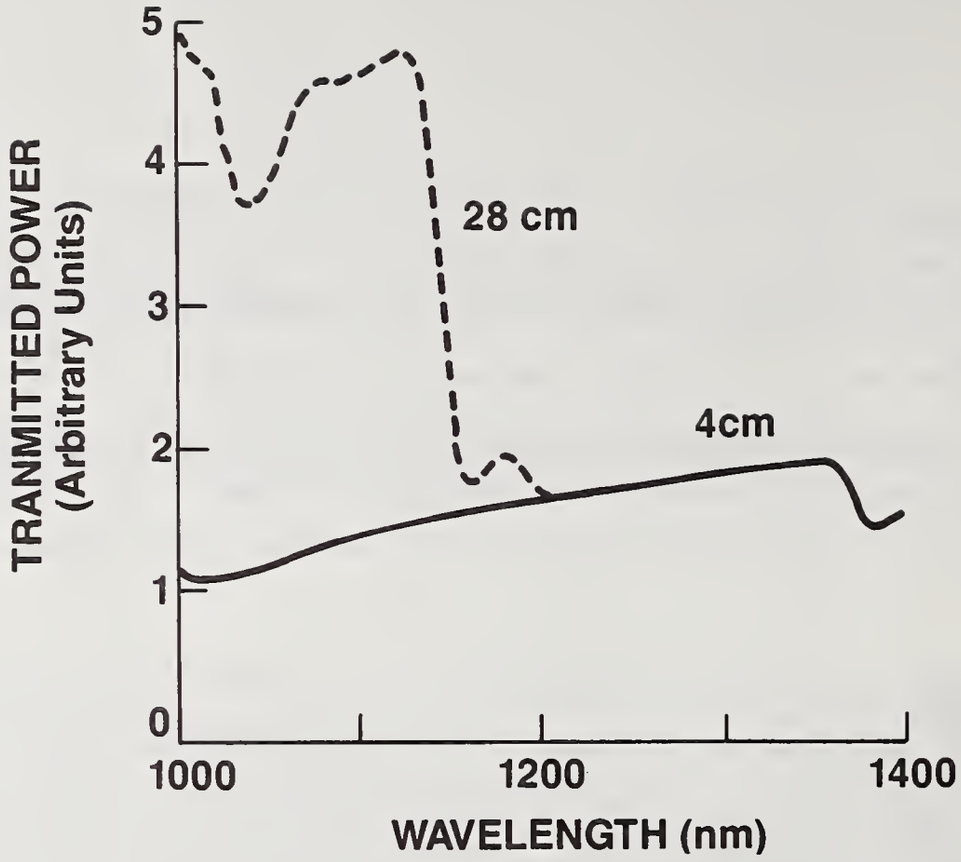

Fig. 2 $P_1(\lambda)$ (dashed curve) and $P_0(\lambda)$ (solid curve) plotted as a function of λ for a DS fiber.

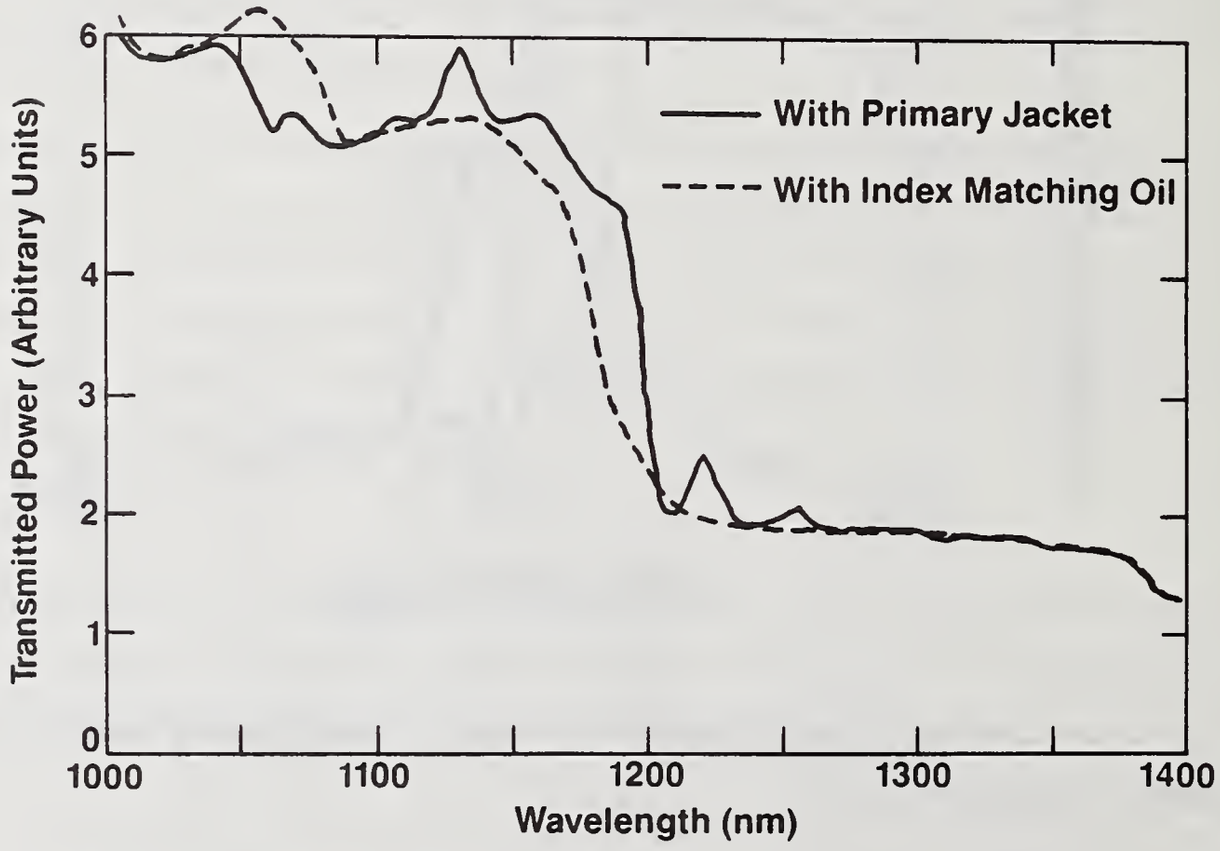

Fig. 3 $P_1(\lambda)$ plotted as a function of λ for a DS fiber.

1300 nm fiber characterization by LP_{01} and LP_{02} interferogram equalization wavelength measurement

François Gonthier, Suzanne Lacroix, Richard J. Black and Jacques Bures

Laboratoire d'optique guidée et d'opto-électronique, Ecole Polytechnique, Département de génie physique
C. P. 6079, Succ. A, Montréal, Québec, H3C 3A7, Canada

Abstract: When operated in the visible wavelength range with an on-axis launch, a standard telecommunications fiber supports the first two circularly symmetric modes LP_{01} and LP_{02}. The wavelength response of such a modal interferometer is observed and permits the measurement of the group velocity equalization wavelength, which is used to characterize the fiber parameters in the case of near-step-index. For more complex profiles, this measurement can provide valuable additional information regarding the form of the profile.

Introduction

Telecommunications fibers, which are single-mode at 1300 nm, are few-mode in the visible and very-near infrared. The interference of those modes can be used to characterize the basic parameters of the fiber. For instance, McMillan et al.[1] proposed to use the observation of the equalization wavelength the LP_{01} and LP_{11} modes to determine precisely the V-parameter of the guide as a way of replacing the often biased measurement of the second mode LP_{11} cutoff wavelength λ_c. Since it is a measurement of the phase between the modes rather than an intensity one, the determination is less sensitive to the bending and length of the fiber. However, due to the symmetry of the modes involved and the wavelength at which the LP_{01}-LP_{11} equalization occurs, this experiment is delicate to implement.

In this paper, we propose to use the LP_{01}-LP_{02} group velocity equalization wavelength in the characterization of telecommunications fibers in the visible domain, where they can be used in sensors applications [2,3]. The observations are made using an all-fiber modal interferometer. The step-index profile is examined and more complex profiles are discussed.

LP_{01}-LP_{02} modal interferometers

When operated in the visible wavelength range, single-mode telecommunications fibers (typically $V \approx 2.2$ at 1300 nm) become few-mode fibers ($V \approx 4.4$ at 650 nm). To realize a LP_{01}-LP_{02} modal interferometer - i.e. a fiber in which only LP_{01} and LP_{02} propagate and beat - one can splice strands of single-mode fiber ($V \approx 2.2$ at 650 nm) at each end of the telecommunications fiber under test. If the two splices are well centered, only the modes of circular symmetry LP_{01} and LP_{02} are excited and their interference is detected with an optimum contrast.

This structure is well described by a "coupling-beating-coupling" model [2,3]. The coupling is ensured by the splices where there is an overlap between the upstream guide modal fields and the downstream ones. In between, the excited LP_{01} and LP_{02} modes propagate without coupling and accumulate a phase difference ϕ due to their different

propagation constant β_{01} and β_{02}. Given L the few-mode fiber length, we have $\phi = \delta\beta\, L$, where $\delta\beta = \beta_{01} - \beta_{02}$ is a function of wavelength.

The total transmission T of such a modal interferometer takes the form:

$$T = P_1^2 + P_2^2 + 2\, P_1\, P_2 \cos\phi$$

where P_1 and P_2 are the fractions of initial power transmitted in the few-mode fiber through LP_{01} and LP_{02} respectively. Note that P_1 and P_2 vary slowly with wavelength compared to cos ϕ and depend on the fibers parameters.

Equalization wavelength: Theory and measurements

The equalization wavelength is, by definition, the wavelength at which the group velocities of two given modes, say LP_{01} and LP_{02}, are equal. Thus, at this particular wavelength, there is no intermodal dispersion. It can be shown that it corresponds to a maximum of the propagation constants difference $\delta\beta$ and thus of the phase ϕ. Consequently, the equalization phenomenon appears in the modal interferometer λ-transmission as an achromatic fringe, i.e. a fringe which shows a stationary dependence on the wavelength ($d\phi/d\lambda = 0$).

The experiment uses a white light source to input power in the fiber. The output end of the fiber illuminates a monochromator equiped with a photomultiplier. To normalize the signal, the system response is first recorded using only the 650 nm-single-mode fiber. Then, the fiber is cut into two halves and the few-mode fiber under study is spliced in between. The modal interferometer response is then recorded and normalized.

Figs. 1 and 2 show typical normalized responses for two different index profiles and fiber lengths $L \approx 1$m. In each case, the achromatic fringe position can be determined with a very good accuracy (± 0.5nm). As opposed to fiber cutoff wavelength measurement and as in the case of the LP_{01} and LP_{11} modes [4], the LP_{01}-LP_{02} equalization wavelength position does not depend on the fiber bends (Fig. 2 a) and b)) or length. Reproducibility is about ±1 nm.

Index profile dependence of the LP_{01}-LP_{02} equalization wavelength

The LP_{01}-LP_{02} equalization wavelength, as does the cutoff wavelength, depends on the fiber index profile. In the more simple case (matched-cladding step-index), the equalization takes place for a constant value of $V_e = 4.44$. The equalization wavelength λ_e can thus be easily related to the LP_{11} cutoff wavelength λ_c, knowing that the normalized frequency at cutoff is $V_c = 2.40$.

$$\lambda_c = (Ve / Vc)\, \lambda_e = 1.85\, \lambda_e$$

Furthermore, one can fit the response of a theoretical perfect step-index fiber on the experimental graph, as was done in Fig. 1. This gives an equivalent profile that has a radius of 4.92 ± 0.01 μm and a index step of 0.00312 ± 0.00001. The errors are due to the precision in the measurement of the interferometer length.

For graded-index profiles (i.e. clad power-law profile characterized by the q-parameter), V_e and V_c augment as the profile tends to a triangular one (q = 1). For a near-step-index profile (large q), the ratio V_c / V_e stays close to its

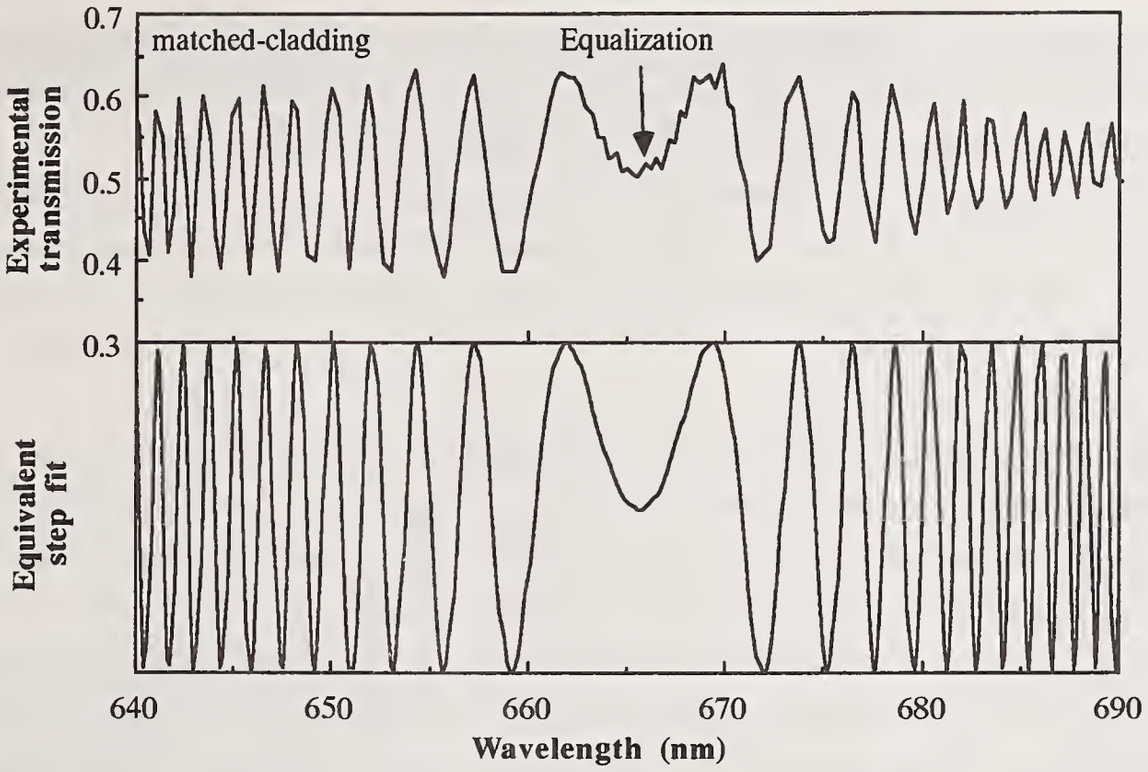

Fig. 1: Experimental wavelength response of an LP_{01}-LP_{02} modal interferometer made with a 1 m long step-index matched-cladding fiber and its theoretical fit with an equivalent step-index (radius = 4.92 μm, index step = 0.00312). The equalization can be seen to occur at 666 nm.

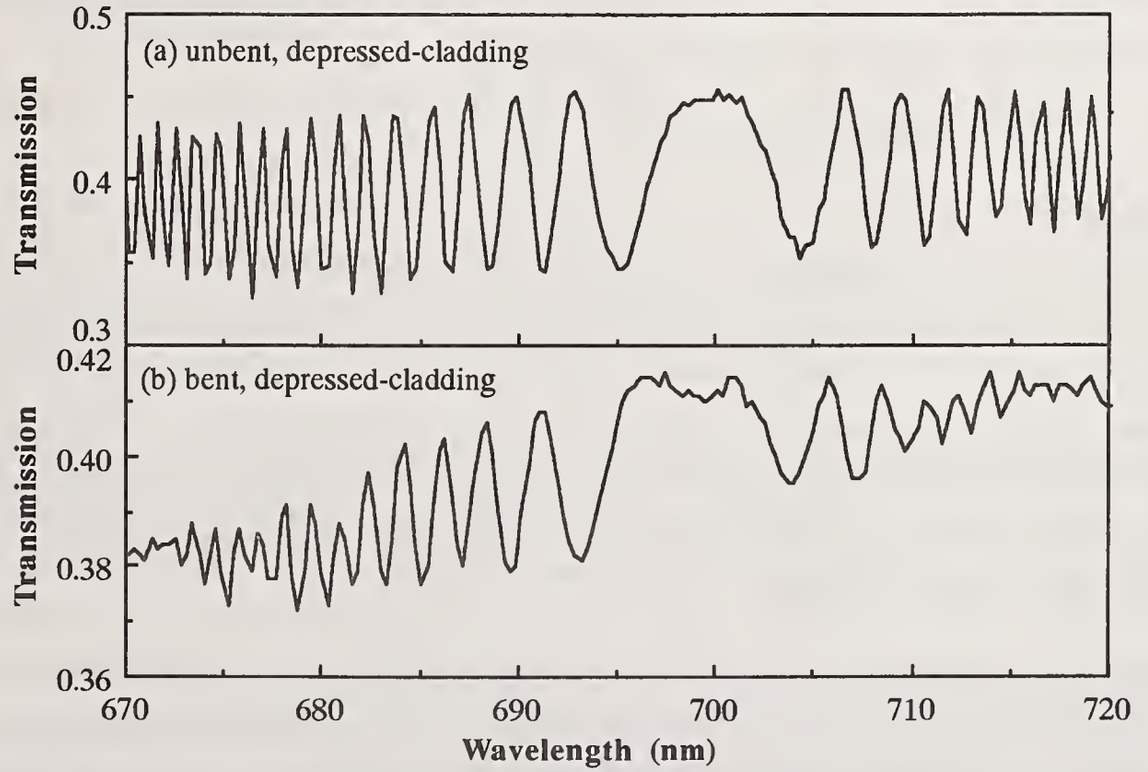

Fig.2: Experimental wavelength responses of an LP_{01}-LP_{02} modal interferometer made with a 1 m long depressed-cladding fiber . Although the fringe contrast decreases in going from (a) unbent fiber to (b) fiber bent with a radius of 1.7 cm, the equalization wavelength remains close to 699 nm.

1.85 asymptotic value. Fig. 3 shows how it varies for q>10, together with the theoretical LP_{11} wavelength cutoff for the Fig. 1 fiber. As a result, the cutoff wavelength λ_c = 1233 nm, deduced from the λ_e measurement (666 nm), assuming a perfect step-index, may be underevaluated (by 7 nm if q = 20, and 2 nm if q = 40).

More complex profiles have different effects on the equalization wavelength. While grading of the profile decreases λ_e away from λ_c, the effect of a cladding depression has the opposite. As an example, assuming perfect index steps, the Fig. 2 depressed-cladding fiber theoretical LP_{01}-LP_{02} equalization occurs at V_e = 4.8 and the LP_{11} cutoff at V_c = 3.0 (Ve / Vc = 1.6).

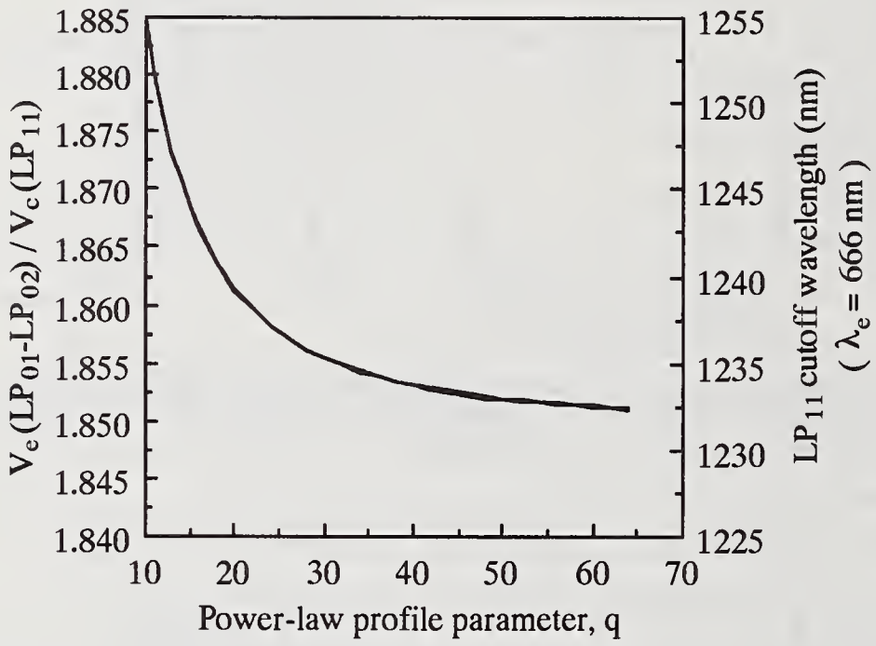

Fig. 3: Ratio of V values for LP_{01}-LP_{02} equalization and LP_{11} cutoff for the standard near-step-index power law profiles. Note that, for q>3, $V_e/V_c \approx 1.848 + 0.168 / q + 1.796 / q^2$. The right hand axis gives the LP_{11} cutoff wavelength deduced from the equalization wavelength measured for the near step-index fiber of Fig. 1.

Conclusion

The measurement of the equalization wavelength of the group velocities LP_{01} and LP_{02}, is simple, rapid and very precise. For a fiber which has a matched-cladding step-index profile, it permits an accurate measurement of the LP_{11} cutoff wavelength which is independent of fiber bends and length. For near step-index fibers, the error on the cutoff wavelength evaluation is small and is systematically negative. Furthermore, a theoretical fit of the wavelength response permits the determination of a precise step-index equivalent for the visible wavelength domain. For more complex profiles, combination of the equalization measurement with other standard measurements provides information about the form of the profile.

[1] J.L. McMillan and R.C. Robertson, "Cutoff wavelength determination in single-mode optical fibres by measurement of equalization wavelength", Electron. Lett. **20**, pp.698-699 (1984).

[2] F. Gonthier, S. Lacroix, F. Ladouceur, R.J. Black et J. Bures, "Interféromètres modaux à symétrie circulaire dans les fibres optiques", submitted to Annales des télécommunications.

[3] S. Lacroix, F. Gonthier, R. J. Black, and J. Bures, "Tapered-fiber interferometric wavelength response: the achromatic fringe", Optics Letters **13**, pp.395-397 (1988).

[4] A.C. Boucouvalas, S.C. Robertson, and J. Walker, "Optical fibre far field ESI determination using the equalisation wavelength", Technical digest, Symposium on Optical Fiber Measurements pp. 137-140 (1986).

FIBER GEOMETRY, A FIBER MANUFACTURER'S VIEWPOINT

by David A. Hall and Robert W. Smith

Corning Glass Works

Introduction:

The measurement of optical fiber in the manufacturing environment generally falls into one of three catagories: fiber loss measurements (attenuation and point defects), information capacity (bandwidth and dispersion) and fiber geometry (the measurement of physical dimensions of the fiber or its refractive index profile). Much has been written and discussed about loss and information capacity measurements, but much less is heard about the measurement of fiber geometry. In this paper the considerations for evaluating physical fiber geometry measurements and the experience we have had at Corning Glass Works in implementing fiber geometry measurements in manufacturing will be discussed. It will be shown that available fiber geometry measurement capability meets current manufacturing requirements, but that potential changes in fiber specifications will require substantial improvements in measurement technology.

Considerations for fiber geometry measurement:

There are many parameters which must be considered when selecting a fiber geometry measurement approach or implementing a system in the manufacturing environment. These considerations fall generally into three catagories: measurement performance, system industrialization, and commercial and support issues.

The performance of a measurement system is the most obvious issue in determining suitability, but it may be one of the most difficult issues to truly resolve. The parameters we consider as performance parameters are the system's accuracy, reproducibility, speed and conformance with standards. We consider accuracy to mean the degree to which the measurement represents true calibrated metrology, referenced to some acknowledged external standard. Reproducibility is similar to repeatability; but whereas repeatability is the ability to get the same measurement result with repeated measurements such as a short term cycle test, we use reproducibility to indicate the long-term stability of the measurement system as well as repeatability. That is, reproducibility is the ability to get the same measurement result with a complete new measurement set-up days or weeks later. Speed is a measure of the system's measurement time, both the actual cycle time (measurement

sequence only), and the likely total measurement time including operator set-up. Standards conformance is the degree to which the measurement algorithms and set-up meet the requirements of the national and international measurement standards recommendations.

The performance parameters must be evaluated against the true requirements of the system, since some parameters will probably trade off against others (measurement speed and accuracy, for instance). Also there may be a substantial difference between specified performance and demonstrated performance under factory use conditions. The way in which performance parameters are specified and the way tests are conducted and evaluated can have a significant bearing on the usefulness of the data. Demonstrated performance also should include consideration of the skill and training of the operator, particularly when targeting a system for use on the factory floor.

Industrialization parameters are fairly general in nature and therefore much more subjective in evaluation. These include the nature of the operator interface, reliability and maintainability, flexibility and integration.

In a large manufacturing facility the operator interface may be more important than in a small operation where one person may be operating the system. The operator interface includes the ease of use and accessibility of the hardware, the software interface and degree of automation, the sensitivity of the measurement performance to operator set-up and operation, and the level of training required. Operator actions and judgement should have very little influence over the accuracy of the measurement results in a factory environment.

Reliability and maintainability are difficult parameters to evaluate unless information is available from other users of a system. One can subjectively evaluate the system for anticipated maintenance problems, complexity and the use of proprietary parts and assemblies. In an automated system, the use of proprietary CPUs and system architectures is a concern. The availability of testing and calibration devices and maintenance training is also important.

Flexibility and the ability to integrate the measurement into the manufacturing system are both important considerations. Flexibility allows one to easily change the measurement parameters or sequence, and even the measurement algorithms, if a measurement standard or product parameter should change. In a highly integrated manufacturing environment, the ability to automatically transfer data to manufacturing systems and deal with ware flow management systems is also important.

The commercial issues deal with the supplier relationship, and include value, warranty, support and training, spares and maintenance agreements and upgrade policies. Having a good working relationship with the system supplier is very important, and can impact the total operating cost of the system.

Corning's Experience with Fiber Geometry Systems:

The following information describes Corning's experience in evaluating and implementing fiber geometry systems for factory floor operation. The opinions and decisions discussed are in the context of Corning's requirements and are not meant to speak to other requirements or operations. The background of our system choice, the general structure and operation of our system, and the measurement results we currently get with the system will be discussed.

When the project to develop a system for factory measurement of fiber geometry began, the only commercial system available was an image shearing microscope system. One of these was purchased and is still in use today, but it was not adaptable to our manufacturing operation. While it was found to be quite accurate and very flexible, it was very difficult to use well and was quite slow. At that time it had no automation capability, so it would not integrate with our manufacturing systems. Other imaging systems which have been evaluated are much closer to meeting our requirements, but most are based on proprietary architectures and hence are very inflexible. The refractive nearfield measurement system used in the plant for process analysis has proved to be very difficult to use as a production measurement.

With this background, it was decided to develop our own geometry measurement system in conjunction with an electro-optic measurement system company. The system is based on gray-scale image analysis technology, using a video camera and scan digitizer hardware, custom optics and illumination system, and a customized PC based computer system. The software provides machine sequence, data acquisition and analysis, operator interface and communication of measurement results to the manufacturing system. This measurement system provides a fast, fully automated measurement which meets the performance requirements. It is flexible at both the measurement parameter and programming level, and is fully integrated with our manufacturing system. An additional benefit of a custom system is that the operator interface can be made similar to other measurement systems, reducing training requirements significantly. The principal disadvantage of a system such as this is the cost of development.

The implementation of this system in our manufacturing operation, and the results which we obtain with the system will now be discussed. Reproducibility will be separated from accuracy, as we consider reproducibility to be controlled by the system and its operation on the factory floor, while accuracy is primarily a function of the quality architecture in place.

The operation of the fiber geometry systems begins with fiber end preparation. A commercial fiber cleaver and an interference type end inspection system are used. All fibers are required to be inspected, and to have < 2° end angle and a clean cleaved surface. Since the end quality directly affects the measurement results, careful management of end preparation is very important.

The operator interface of the measurement system is designed to help the operator mount and align the fiber and enter the required information. The system is automated so that it completes the measurement from final auto-focus through results reporting without further operator intervention. The measurement algorithms are designed to conform with CCITT and EIA requirements for data fits and computations. The system provides clad diameter, clad non-circularity and core-clad concentricity measurements on single-mode fiber; and all of the above plus core non-circularity on multimode fiber. The measurement time for this system is approximately 1 minute machine cycle time.

A significant development unique to this instrument is an illumination system designed to enhance the contrast of the image and to improve the consistency of data acquisition. The fiber end is illuminated in such a way that the fiber cladding is dark against the bright background and bright core, producing a gray-scale image with very steep edges. This technique sharpens the contrast, thereby improving the dimensioning precision on the edges. It also reduces the effect of the chips and hackle on the fiber surface, since the image is like a shadow of the fiber end.

The following results for clad diameter measurements show excellent system reproducibility. Ongoing certification results using multiple fibers in a production environment show system reproducibility to be 0.15 μm (1 sigma). This measure of variability includes operator interface and setup, fiber end preparation, and system variability over many days. The measurement system itself in a short term cycle test on a single fiber end exhibits a repeatability of 0.08 - 0.1 μm (1 sigma). The actual resolution of the detection system on an image edge is 0.05 μm.

The quality systems required to ensure accuracy were much more complicated and difficult to develop, since they involved requirements for traceability and standardization. These considerations involve definitions of sub-micron level measurements and edge and illumination effects. NBS studies have shown that the ability to relate different optical measurement techniques is

limited to around 1 μm, even on chrome-on-glass standards. Since our production measurement system is designed specifically to measure optical fiber, a fiber was chosen as the most useful calibration standard.

The image shearing microscope at our product engineering laboratory is used as our standardization system. This system was carefully calibrated using a recticle traceable to National Physical Laboratory, and several selected fibers were measured with the system many times. The same fibers were then measured with both a photographic recticle overlay technique and a full contact measurement performed by Eli Whitney Metrology Laboratory. Comparison of all three measurement techniques showed agreement to within 0.2 μm, indicating accurate calibration of the reference system to that level.

Calibration begins by selecting fibers for their dimensional consistency and targeting them by measuring them several times on the calibrated reference system. The production system is then calibrated by measuring the targeted fibers and setting a calibration parameter for agreement with the targets. A certification system is also used to ensure proper continued operation of our measurement systems. This system works by requiring the measurement of targeted fibers daily by operators and an ongoing computerized statistical analysis of the resulting data for bias and reproducibility. If a measurement system fails to conform to the certification requirements, it is shut down and troubleshooting is done until the problem is resolved. Using this calibration and certification system, our factory floor measurements are accurate to within 0.5 μm. This is based on a ± 0.2 μm reference accuracy and a 95% confidence interval (2 sigma) of ± 0.3 μm. This capability is adequate to support a product specification of ± 2.0 μm clad diameter tolerance, using product assurance statistics.

Future Directions and Requirements:

The directions we see currently for factory fiber geometry measurements are both good news and bad news. The good news is that measurement equipment manufacturers are developing and announcing new and upgraded fiber geometry measurement systems, some of which are aimed at the factory floor. Since it is usually more cost effective to buy than build equipment if it meets the requirements, this is a very positive sign. The bad news is that fiber geometry specifications and therefore requirements for measurement systems are getting tighter. Recent market requirements have driven diameter tolerances down from ± 3 μm to ± 2 μm and there is interest in even tighter specifications. Measurement systems and calibration capabilities will have to be substantially better if fiber specifications continue to tighten.

Several future needs for fiber geometry measurement systems follow from the forgoing information. First we need continued improvement in fiber end preparation and end inspection systems. The current end inspection systems work, but are tedious to use and difficult to interpret. A system which would evaluate an end automatically and would maintain statistics on a cleaving system would be very useful in insuring the quality of end preparation for fiber geometry and other measurement systems. A reduction in end preparation time is also quite important in the manufacturing environment.

Second, we need to continuously improve the capability of our measurement systems themselves. As was indicated above, the current measurement capability of available systems is not adequate for assuring conformance to sigficantly tighter fiber geometry specifications. These improvements need to be not only in measurement precision, but in automation and stability of the systems as well.

Finally, the standards and metrology community should develop and provide calibration and standardization systems as the basis for ensuring agreement within the optical fiber community on fiber geometry measurements. Standardized measurement procedures and techniques are only part of the solution. Transfer standards and calibration methodologies are also needed. As we move into the subscriber loop era where inexpensive mechanical splices and connectors are required, calibrated sub-micron measurements will be imperative in order to ensure the compatability of various components.

Summary:

The development of a fiber geometry measurement system and the required quality systems to support it at Corning has resulted in an excellent production measurement capability which meets the requirements of current fiber specifications. This was done as an internal development project to meet internal requirements for process control and product assurance. As more vendors of measurement equipment and more users of the measurements emerge, it is evident that the optical fiber business needs a mechanism for standardization and calibration of sub-micron level fiber measurements. As the business requirements change and require tightening of product specifications, this need will become even more acute.

Non-Contact, Interferometric Determination of the Outside Diameter of Optical Fibers

M. J. Saunders

AT&T Bell Laboratories
2000 Northeast Expressway
Norcross, Georgia 30071

To measure the outside diameters of optical fibers, AT&T Technologies uses a forward scattering method[1] [2] requiring a calibration fiber of known outside diameter. The diameter of this fiber was previously measured with an interferometer to determine the distance that two originally contacting plates are separated to just make contact with the fiber placed between the plates.[3] Therefore, it is subject to errors caused by the presence of small foreign particles, and to the uncertainty in determining when contact occurs. A new, accurate, (0.1-0.2 μm) non-contacting measuring technique to determine the outside diameter of the calibration fiber is the subject of this paper.

The fiber to be measured, A, is placed over a hole in plate B (Figure 1) that is supported by an uncoated optical flat, C. The interferometer, D, is a commercially available Michelson interferometer attached to the body tube, E, of a microscope that has a fine focus least count of 1 μm. This microscope is attached to a cross-slide that serves as a coarse focus control. The beamsplitter cube, F, together with other optical elements, form a 10X microscope objective. Therefore, the focussed object is crossed with interference fringes.

A white light source, G, is used to illuminate the interferometer that is adjusted until the optical path Y_0 between the center of the beam splitter, F, and the uppermost point on the fiber is equal to L_0, the invariable path between the center of F and H, the reference mirror of the interferometer (equal distance condition). Under this condition, a straight, uncolored interference fringe appears on the uppermost part of the fiber and, by adjusting the tilt of H, this fringe is oriented parallel to the fiber axis. (That only one fringe appears is due to the curvature of the fiber.) As the interferometer is moved to upset the equal distance condition, the uncolored fringe is replaced by one of color, whose brightness decreases with the deviation from the equal distance condition, and if this condition is upset by only 0.3 μm, the brightness decrease is discernible to the eye.

Bracket, J, attached to the microscope, supports a retroreflector, K, that is the movable mirror of another interferometer contained within the dashed circle on Figure 1 where M and L are mirrors, N is a laser and detector and O is a bidirectional fringe counter used to determine the motion of K and D. The least count of this interferometer is 0.16 μm.

After the equal distance condition has been obtained with the fringes on the top surface, the counter is zeroed and D lowered until another set of fringes, formed on the bottom surface of the fiber, is seen and the interferometer is adjusted so that the equal distance condition again holds. (Y_1 = the new distance between the center of the beamsplitter and the uppermost part of the fiber.) From Figure 2, equating the optical paths from the beamsplitter to the reference mirror and to the lower surface of the fiber,

$$2\left\{Y_1 + n_{CL}\,(D_0 - D) + n^-\,(D - D_{CO}) + n^+\,D_{CO}\right\} = 2\,Y_0\,, \tag{1}$$

where n_{CL}, n^- and n^+ and D_0, D and D_{CO} are the group indices and the diameters of the outer cladding (fused silica), depressed cladding and the core, respectively.

Solving for D_0,

$$D_0 = \frac{Y_0 - Y_1}{n_{CL}} - D\Delta^- + D_{CO}\,(\Delta^- - \Delta^+)\,, \text{ where } \Delta^- = \frac{n^- - n_{CL}}{n_{CL}} \text{ and } \Delta^+ = \frac{n^+ - n_{CL}}{n_{CL}}\,. \tag{2}$$

Using values characteristic of a depressed cladding design for single mode fibers, $D = 55\ \mu m$, $D_{CO} = 8.2\ \mu m$, $\Delta^- = -1.6 \times 10^{-3}$ and $\Delta^+ = 3.3 \times 10^{-3}$, the terms in eq. (2) other than $\frac{Y_0 - Y_1}{n_{CL}}$ are evaluated as 0.05 μm. Consequently, calculating D_0 from the following equation (2′) will give fiber diameters too small by the systematic error of 0.05 μm,

$$D_0 \approx \frac{Y_0 - Y_1}{n_{CL}}\,. \tag{2′}$$

As the interferometer is moved from the position for fringes on the uppermost surface of the fiber to that for fringes on the lowermost surface, monochromatic interference fringes counted by O, give $(Y_0 - Y_1)$ of equation (2′).

The group index, n_{CL}, is determined by the method of Figure 3. The fiber is replaced by two plane parallel, optically contacted, fused silica discs (A, B) of thickness T_A and T_B, respectively. The central white light fringe is obtained alternately along paths 2 and 3 by lowering and raising the interferometer. Y_2 and Y_3 are the distances between the center of the beamsplitter and the top of A and B when fringes are formed off the bottom of B along paths 2 and 3 respectively. The reading of the counter is equal to Δ.

The thickness, T_A, of disc A is equal to the interferometer motion required to obtain the equal distance condition for fringes formed on the top surface of disc A after having first obtained this condition for fringes on the top surface of disc B. Then, using the L_0 defined in Figure 2, and equating L_0 with the optical paths along paths 2 and 3, one obtains

$$n_{CL} = \frac{\Delta + T_A}{T_A} \quad . \tag{3}$$

Fifteen measurements of T_A and Δ give $\bar{n}_{CL}$ = (1.4810 ± 0.0003), in agreement with the group index calculated for fused silica at λ = 0.58 μm.[4] Ten measurements of the outside diameters of each of 12 fibers were determined (total error ~ 0.1 μm) and the average values compared with the forward scattering results. The average difference between the two methods is 0.2 μm, the largest positive and negative differences being + 0.6 μm and - 0.4 μm, respectively. These largest differences could be due to rotating the fiber about the fiber axis in one method (forward scattering) and keeping it constant in the other.

I thank W. B. Gardner, R. B. Kummer and D. W. Peckham for very helpful discussions, and C. Bice for making the forward scattering measurements.

REFERENCES

1. L. S. Watkins, *J. Opt. Soc. Am.* (**64**), 767 (1974).

2. D. H. Smithgall, L. S. Watkins and R. E. Frazee, Jr., *Applied Optics* (**16**), 2395 (1977).

3. D. H. Smithgall and C. M. Schroeder, *Symposium on Optical Fiber Measurements*, 1980, Boulder, Colorado, October 28-29, 1980.

4. F. L. Kapron, *Electronics Lett.* (**13**), 96 (1977).

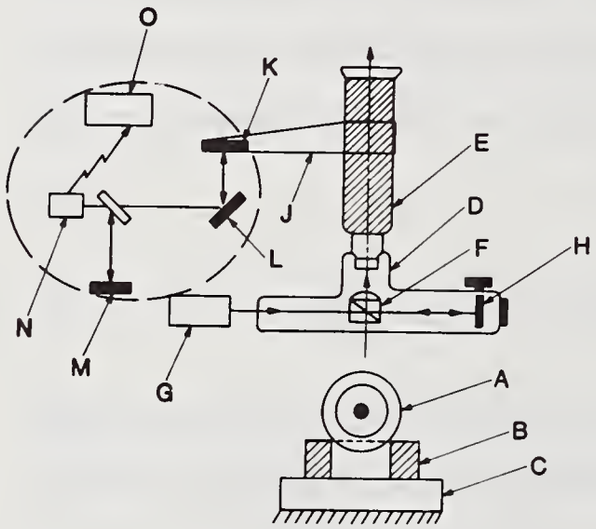

FIGURE 1

SCHEMATIC DIAGRAM OF APPARATUS

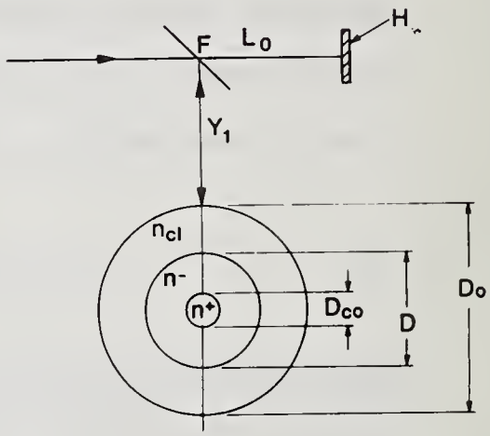

FIGURE 2

DIAGRAM TO DETERMINE OPTICAL PATH THROUGH FIBER

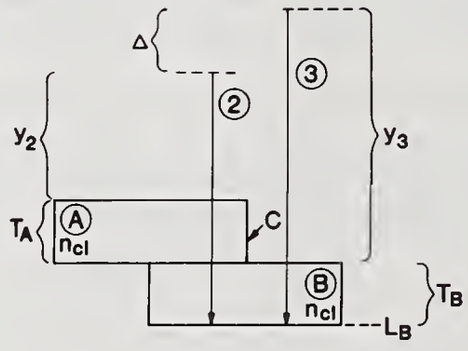

FIGURE 3

SCHEME FOR DETERMINING GROUP INDEX n_{cl}

ON THE DEVELOPMENT OF A CALIBRATION STANDARD FOR FIBRE GEOMETRY MEASUREMENT

J.G.N. Baines,[1] A.G.Hallam,[2] K.W.Raine[1]

1 - National Physical Laboratory, Teddington, Middlesex, UK
2 - York Technology, School Lane, Chandlers Ford, Hants, UK

Introduction.

The optical fibre industry is now sufficiently advanced as to require traceable and transferable calibration standards for both optical fibre manufacturers and system designers. Improvements in optical fibre fabrication techniques and the need for tighter tolerances in splice technology have generated a requirement for high accuracy measurement of fibre geometry.

This paper reports on investigations into the development of a chrome-on-glass mask suitable for geometrical calibration of refracted near-field (RNF) instruments. The mask takes the form of a clear circular aperture, 125um in diameter, surrounded by opaque chromium. Chrome-on-glass artefacts have been investigated because of their convenience of use, stability and longevity. In addition, dimensional measurements of such objects are well understood since they are frequently used in the microelectronics industry for calibration purposes, (1).

The use of RNF for Geometry Measurements.

Refracted near-field (RNF) instruments determine fibre geometry from the coordinates of points corresponding to 50% of the refractive index step at the oil/cladding or cladding/core boundary. In the case of graded-index cores some arbitrary level (eg 5%) is used. A computer program is used to calculate the geometrical properties such as average diameter, non-circularity and core concentricity error.

The normal mode of operation of the RNF instrument is analogous to the idea of a scanning spot phase-contrast microscope. However the transmission object considered in this work is unlike an optical fibre, which is a refractive object, and may introduce different systematic effects into the measurement. These effects have therefore been investigated.

Measurements.

The chrome aperture (nominally 125um in diameter) and the cladding diameter of a number of optical fibres were measured using an interferometrically calibrated image-shearing microscope with a numerical aperture (NA) of 0.45. The overall uncertainty was +/-0.3um. When these fibres were used to calibrate an RNF instrument (launch NA 0.85, blocking NA 0.47) it was consistently found that the chrome aperture was measured by the profiler to be about 0.5um smaller than when measured by image-shearing. Similarly, if the aperture was used to calibrate the RNF instrument this led to fibre diameters being measured about 0.5um too large.

However a similar mask used on a second RNF instrument having lower launch and collecting NA's (0.54 and 0.41 respectively) did not exhibit this effect,

although, as can be seen in the following section, this result was incidental and due to the particular operating conditions used.

Diffraction Effects.

The measurements show that the use of a chrome-on-glass mask for the geometrical calibration of RNF instruments can lead to a systematic error. This arises because as the opaque chromium film cuts across the focussed spot, the reduction in size of the unobscured light spot forces it to diffract through larger angles. Since the collecting NA is greater than the launch NA the amount of light collected when the focussed spot is initially intercepted will be proportionately larger than expected. This is because some of the light which would have been intercepted by the blocking disc is now diffracted past it. The magnitude of this effect will clearly depend on the difference between the launch and collecting NA's. As more of the spot becomes obscured the diffraction angle soon reaches 90 degrees and the collecting optics is no longer able to capture all of the light. The resultant reduction in the measured light power from that expected from geometrical arguments is dependent on the collecting NA and possible changes in the angular light distribution which could provide some compensation. Thus there are two opposing mechanisms which can distort the edge profile. The overall effect is not easy to calculate but is obviously determined by the launch NA, collecting NA and blocking NA. For example, if loss of light from the collecting optics is a dominant factor then an opaque chromium disc will appear too large whereas a clear aperture will be measured too small.

To demonstrate this, clear and opaque discs nominally 125um and 60um in diameter respectively were measured as a function of blocking NA. The results are shown in Fig 1. It can be seen that the smaller blocking NA leads to smaller diameters of the aperture (dashed curve), while the opaque disc shows the opposite effect (solid curve) . This is because in this RNF instrument the collecting NA is only slightly larger than the launch NA. Thus, when the blocking NA is small the amount of light gained through diffraction into the full collecting NA is a proportionately smaller fraction of the light collected than when there is no obscuration. The loss of light from the collecting optics therefore appears the dominant effect. Clearly the blocking NA can be increased to a point where this is no longer the case as can also be seen from the Figure when the blocking NA exceeds about 0.4.

Focus Effects.

A 125um clear aperture was mounted on a hollow hemispherical profiling cell and inserted in the first RNF instrument. The numerical apertures for the launch objective, blocking disc and collecting optics were 0.85, 0.47 and 0.83 respectively. A raster scan was performed over the region of the aperture with a scan increment of 2um, and a least-squares fit to the 50% intensity-level data points was applied to obtain the average diameter.

Fig 2 shows the effect on measured diameter of varying the focus position. The diameter scale was calibrated against a fibre measured on the microscope, discussed above. The optimum focus position was taken as the edge over which the approx 20%-80% risetime was minimum. A positive focus offset indicates the objective being withdrawn from the fibre end. The approximate sensitivity to focus is +0.12um diam/um focus.

A series of RNF scans across the edge of the aperture is shown in Fig 3, where increasing optical signal is in the downwards direction. A slight asymmetry with focus can be seen along with a discontinuity in the slope of the edge. Spherical

aberration effects appear to be evident since the in-focus position should correspond to a minimum or maximum if diffraction were the only difficulty.

The profiling cell was then filled with matching oil of index 1.47. This had the effect of reducing the exit NA from the cell, which thus increased the proportion of light that was blocked and reduced the sensitivity to diffraction losses at the collection NA. The measured diameter was found to be slightly larger for the wet cell, as expected from the preceeding argument; by about 0.2um. The focus sensitivity was +0.29um diam/um focus. Typical edge plots are shown in Fig 4. The marked 'knee' in the slope of the edge that occurs for positive focus offsets is not fully undestood but its asymmetry with focus position is probably due to the interaction of diffraction effects with spherical aberration in the objective. However the discontinuities in the slope were found to disappear when a large area detector was positioned immediately behind the mask in place of the normal collecting optics.

It was found that by fitting a 0.9NA objective with a coverslip correction ring the 'knee' could be made to occur for negative focus offsets by adjustment of the correction ring. The slope of the focus sensitivity was also reversed so that a positive focus offset gave a decrease in measured diameter. For a particular correction ring setting the 'knee' occured at the in-focus position, in which case the diameter showed reduced sensitivity to focus position. However, the in-focus diameter was found to be relatively insensitive to the level of coverslip correction.

Discussion.

The problems associated with the use of an aperture in chrome for calibration of the RNF profiler have been discussed. Due to diffraction effects the measured diameter of the aperture is dependent on the particular configuration of launch NA, collection NA and blocking NA, as well as focus position; in the latter case spherical aberration effects the result also. The use of an aperture for calibration is therefore only valid under strictly controlled conditions.

A chrome aperture of annular form is under development which is expected to show less sensitivity to diffraction effects. An average of the internal and external diameters of the annulus will constitute the reference dimension since this will have reduced sensitivity to axially symmetric aberrations,(2), blocking NA and focus. This is because line-spacing rather than line-width will be the measurement parameter. However, as in high resolution microscopy, the presence of an asymmetric aberration such as coma will be detrimental.

Finally, similar calibration discrepancies have been observed in the scanning beam method for fibre diameter measurement. This technique is often employed for control purposes during fibre pulling. Calibration is usually by means of a series of opaque wires of known diameter. Edge response effects in this environment are under investigation.

References.

(1) M.J.Downs, N.P.Turner, "Application of optical microscopy to dimensional measurements in microelectronics", SPIE vol 368, 1983 (Microscopy - Techniques and Capabilities).

(2) C.P.Kirk, "Aberration effects in an optical measuring microscope", Appl Opt. vol 26, no 16, pp 3417-3424, 1987.

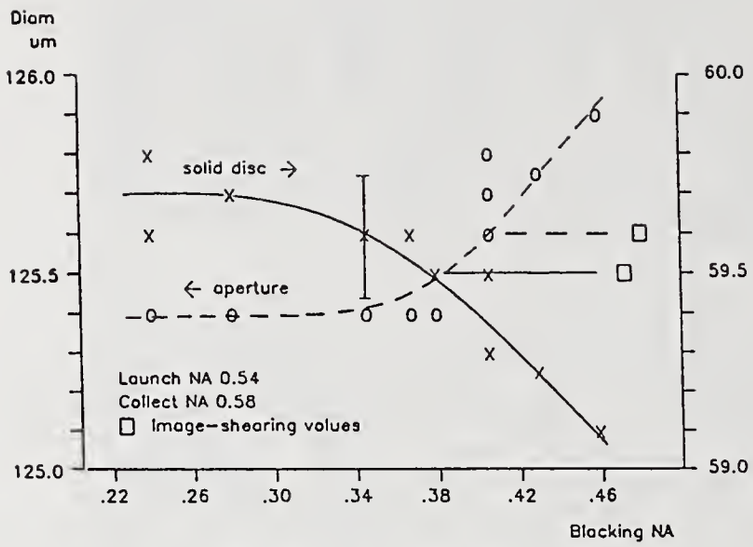

Diameter vs Blocking NA

Fig 1

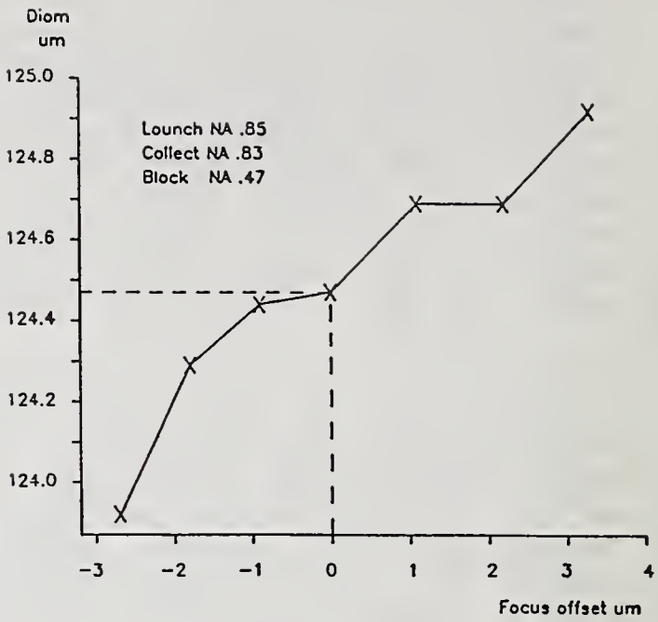

Aperture diameter vs Focus Offset

Fig 2

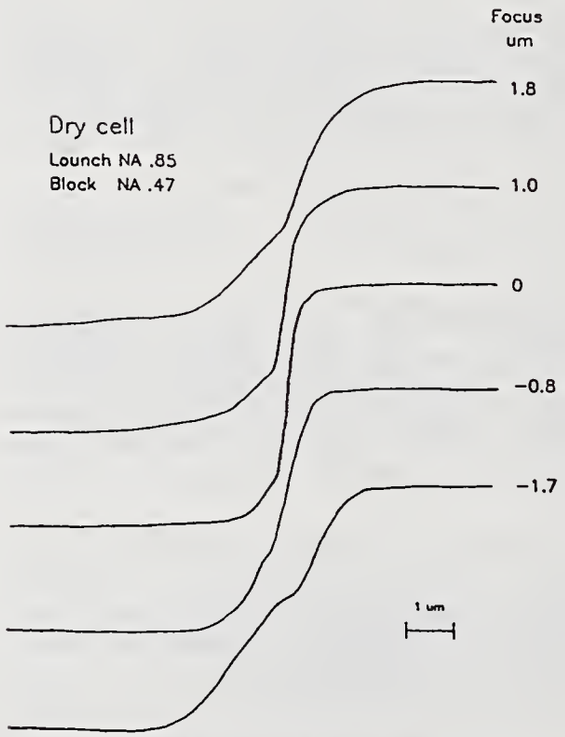

Aperture edge response

Fig 3

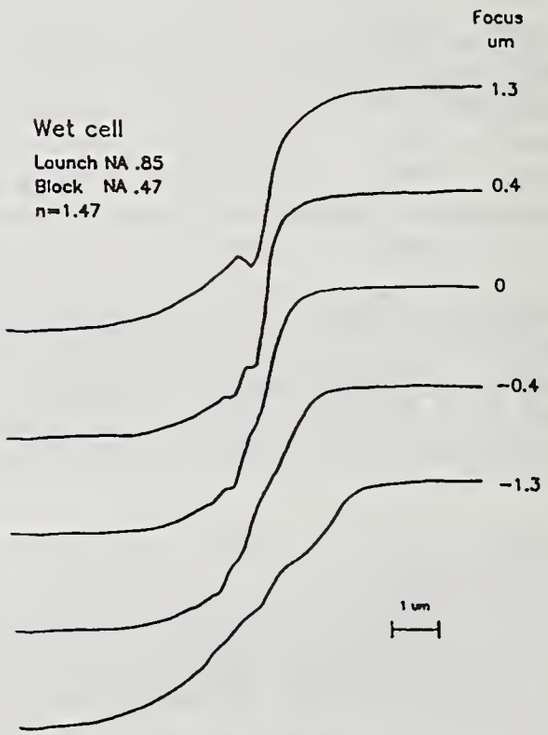

Aperture edge response

Fig 4

AN ELECTRONIC INDUSTRIES ASSOCIATION INTERLABORATORY COMPARISON TO RESOLVE DIFFERENCES IN MULTIMODE FIBER NUMERICAL APERTURE MEASUREMENTS

A. H. Cherin and E. D. Head
AT&T Bell Laboratories
Atlanta, Georgia 30071

D. L. Franzen and M. Young
National Bureau of Standards
Boulder, Colorado 80303

M. Hackert
Corning Glass Works
Corning, New York 14831

INTRODUCTION:

An industry-wide study among members of the Electronic Industries Association (EIA) was conducted to document and reconcile differences between various numerical aperture (*NA*) definitions and measurement methods. Results on twelve multimode graded index fibers indicate that systematic differences exist among commonly used far-field and index profile techniques. The differences can be explained by a wavelength dependent factor and the choice of *NA* definitions. Conversion factors have been developed to relate the various measurement methods and definitions.

BACKGROUND:

The *NA* of a graded index multimode fiber is an important parameter that describes a fiber's light gathering ability. It is used to predict launching efficiency, joint loss at splices, and micro/macrobending performance. The maximum theoretical *NA* is a graded index multimode fiber is defined as:

$$NA_t = \sin\theta_m \tag{1}$$

where θ_m is the largest meridional ray angle, in air, that will be guided by the fiber. In terms of the fiber's index profile,

$$NA_t = \sqrt{n_1^2 - n_2^2} \tag{2}$$

or

$$NA_t \approx n_1 \sqrt{2\,\Delta} \tag{3}$$

where

$$\Delta \approx \frac{n_1 - n_2}{n_1} \quad \text{for} \quad \Delta << 1$$

n_1 is the maximum refractive index of the core and n_2 is the refractive index of the cladding. *NA* can be determined from a far-field radiation pattern measurement on a short length of fiber. The far-field method is described in EIA Fiber Optic Test Procedure (FOTP) 47. Using this test procedure, the far-field radiation intensity pattern, $I(\theta)$, of a fiber is acquired and the NA_{ff} is defined as the sine of the half-angle where the intensity has decreased to 5% of its maximum value. For a given wavelength, the relationship between the 5% far-field numerical aperture, NA_{ff}, and the maximum theoretical numerical aperture, NA_t is given by:[1]

$$\frac{I(\theta)}{I(0)} = 0.05 = \left[1 - \frac{NA_{ff}^2}{NA_t^2}\right] \tag{4}$$

or

$$NA_{ff} = 0.975\, NA_t \tag{5}$$

Standards groups are aware that differences exist between NA_{ff} and NA_t determined by index profile measurements. Methods currently in use for determining a fiber's refractive index and refracted near-field, RNF, (EIA FOTP 44). In addition to the difference that is accounted for in equation 5, the different test methods are commonly implemented at different wavelengths, and *NA* is a function of wavelength. Most far-field measurements are made using an incandescent lamp and interference filter at a wavelength of 850 nm; the NA_{ti} obtained from transverse interferometry is measured using a 540 nm line from a mercury lamp; and the NA_{rnf} obtained from refracted near-field measurements is measured with a 633 nm HeNe laser. In this work, the dependence of *NA* upon wavelength has been measured and a wavelength dependent factor relating the difference measurement techniques is obtained.

INTERLABORATORY COMPARISON AND RESULTS:

An industry-wide round robin comparison was conducted among nine U.S. and Canadian laboratories to document the differences among the various methods. Twelve graded index multimode fibers designated A through L were studied in the comparisons. The most popular core sizes were used—five 50, four 62, one 85 and two 100 micrometer diameter fibers. NA_{ff} was determined using the recommendations of FOTP 47 while NA_{rnf} and NA_{ti} were determined by FOTP 44 and 29 using equations (2) or (3). Average results from the participants are given in Tables I and II. Nine laboratories submitted far-field results at 850 nm; six submitted

refracted near-field results at 633 nm; and one laboratory submitted transverse interferometry results at 540 nm. Using the far-field method, the wavelength dependence of *NA*, in a range from 520 to 1550 nm, was also obtained for several fibers and is shown in Figure 1. The NA difference between 850 nm (NA_{ff} wavelength) and 540 nm (NA_{ti} wavelength) is 2.7%, while the difference between 850 nm and 633 nm (NA_{rnf} wavelength) is 1.3%.

CONCLUSIONS:

The differences existing in the industry among various *NA* measurement methods may now be explained: Measurement wavelength and the definitions applied to the curves account for most of the offsets. Correction factors may be applied to the properly calibrated RNF and TI numerical aperture measurements to give the same results as far-field measurements. To obtain 850 nm NA's, 633 nm RNF data should be reduced by approximately 4% while 540 nm TI data should be reduced by approximately 5%. The relatively large offsets observed in the the interlaboratory comparison for RNF measurements cannot be explained; perhaps better methods for calibration are needed.

REFERENCES

1. A. H. Cherin, "An Introduction to Optical Fibers," McGraw-Hill, 1983, p.135.

TABLE I

NA_{ff} and NA_{fi} Results

Fiber; Dia.,μm	NA_{ff}	SD_{ff},%	NA_{fi}	% Difference, $\frac{NA_{fi}-NA_{ff}}{NA_{ff}} \times 100$
A, 62	0.285	1.4	0.298	4.4
B, 62	0.285	1.4	0.296	3.7
C, 50	0.226	1.3	0.238	5.0
D, 50	0.226	1.3	0.237	4.6
E, 100	0.291	1.4	—	—
F, 50	0.206	1.9	0.213	3.3
G, 62	0.279	1.4	0.289	3.5
H, 85	0.268	1.9	0.284	5.6
I, 100	0.305	1.6	—	—
J, 62	0.286	1.4	0.300	4.7
K, 50	0.228	1.3	0.240	5.0
L, 50	0.188	1.6	0.204	7.8
Average	—	1.5	—	4.8
Number of Participants	9	—	1	—

TABLE II

NA_{ff} and NA_{rnf} Results

Fiber	NA_{ff}	NA_{rnf}	SD_{rnf},%	% Difference, $\frac{N_{rnf}-NA_{ff}}{NA_{ff}} \times 100$
A	0.285	0.307	5.9	7.2
B	0.285	0.309	7.4	7.8
C	0.226	0.239	6.7	5.4
D	0.226	0.240	6.3	5.8
E	0.291	0.321	7.8	9.3
F	0.206	0.223	4.9	7.6
G	0.279	0.301	6.3	7.3
H	0.268	0.293	7.5	8.5
I	0.305	0.340	7.4	10.3
J	0.286	0.307	6.8	6.8
K	0.228	0.246	6.1	7.3
L	0.188	0.203	5.4	7.4
Average	—	—	6.5	7.6
Number of Participants	9	6	—	—

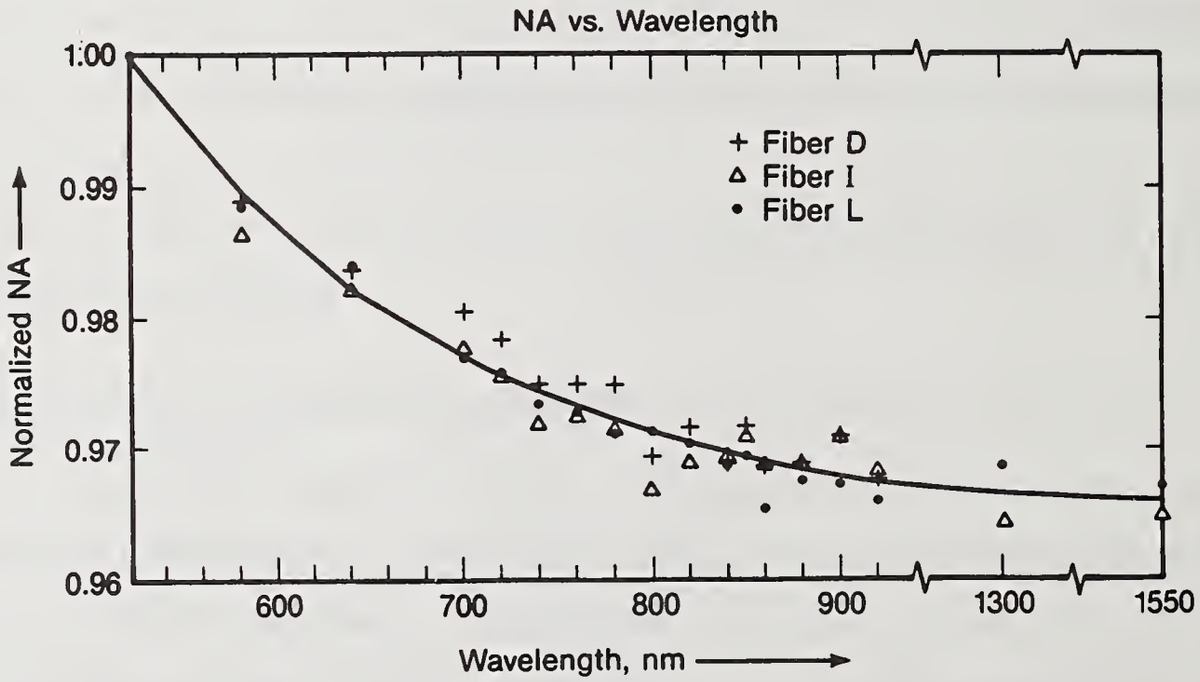

FIGURE 1

Novel Interferometric Dispersion Measurement System

A. O. Garg, M. A. Brandtner and C. K. Eoll

Siecor Corporation
489 Siecor Park (RD)
Hickory, NC 28603

Abstract

Several papers (including [1,2]) have been presented on the use of interferometry for determining the dispersion of various fibers at wavelengths beyond a 1000 nm. Most of the methods involve critical alignment procedures, during initial setup and at the beginning of each measurement, along with a considerable loss of transmitted power in the optical paths leading to and from the sample and reference fibers. Typically, such a system also generates a relatively noisy interferogram, so that its midpoint can be difficult to pinpoint. The midpoints of the interferograms for a set of wavelengths are used to find relative group delays which lead to dispersion values.

The system described here is comparatively easy to assemble; relatively few components require critical alignment procedures, and these procedures are needed only when the equipment is first set up. None of the components require alignment during normal dispersion measurements. The system also gives smooth interferogram envelopes whereby the midpoints can be accurately determined with a high degree of repeatability.

Dispersion Measurement System

Two 2x2 single-mode fiber optic couplers (optimized for 1300 nm and 1550 nm) and precision capillary units are used in a system with rigidly attached and encased optics. As a result, a minimum amount of careful alignment is needed to set up the interferometric system. Because capillaries and couplers are used in place of traditional beam splitters, postioners and lenses for coupling light to and from fibers and sources, no components need alignment during normal measurements.

The system (Figures 1 and 2) uses a tungsten-halogen light source directly attached to the monochromator. All four ends of each of the couplers (C1 and C2) have been connectorized. The polished end faces ensure optimum coupling efficiencies. The output of the monochromator is fed into one arm (I1) of a 2x2 coupler (C1). The output of the monochromator consists of a semi-precision unit housing the coupler end (I1). The second input end (I2) of the coupler (C1) is attached to a He-Ne laser which is used for alignment purposes during initial setup. (It is otherwise switched off). The output ends (O1 and O2) of the coupler (C1) are fed through precision capillary units to sample and reference fibers, respectively. The sample fiber is directly coupled to the input end (I3) of coupler (C2) using another precision capillary unit. The output end of the reference fiber is mounted in a

stepper motor controlled stage. Using lenses, the beam from the reference fiber is collimated and then focused on the input end (I4) of the second coupler (C2). The output end (O3) of the second coupler (C2) is attached to a precision detector assembly housing an InGaAsP photodiode. The other output end (O4) of this coupler (C2) is mounted in another detector assembly housing a silicon photodiode which detects the output of the He-Ne laser.

A smooth interferogram envelope (Figure 3) is achieved by use of a small speaker, operating at low frequency, and loosely attached to the input arm (I4) of the coupler (C2). This causes the optical path length in the input arm (I4) to vary in an oscillatory fashion. As a result, for each position of the stepper motor controlled stage, a small section of the interferogram is repeatedly traversed so that the detection electronics can find a point on the relatively noise-free rms representation of the interferogram envelope. Similar techniques have often been used in differential interferometry [3,4,5].

In calculating dispersion, the raw relative delay data is differentiated numerically - no curve-fitting is used with the delay data. Instead, curve-fitting is used with the dispersion values. When this fit is restricted to a wavelength range of 40 nm or less, approximately centered on the wavelength of zero dispersion, a straight line is a good fitting function [6].

Measurements

Measurements were made on standard and dispersion-shifted fibers. Typical results are shown in Figures 4 and 5. These particular results have been confirmed by means of standard interferometric equipment as well as a Raman laser system [7]. The total possible error in the wavelength of zero dispersion provided by the new system appears to be less than +/- 0.5 nm.

The new system permits relatively fast interferometric measurements. A typical set of 200 measurements, involving 10 wavelengths and 20 automated steps per wavelength, provides the zero dispersion wavelength of a fiber in less than 12 minutes.

Conclusion

An interferometric dispersion measurement system which requires no critical alignment procedure during measurements has been developed. Results are highly repeatable, and the accuracy is good. The system has advantages in comparison to other interferometric dispersion measurement systems.

References

1) L. G. Cohen and J. Stone, "Interferometric Measurements of Minimum Dispersion Spectra in Short Lengths of Single-Mode Fibre," Electronics Letters, Vol. 18, p. 564, 1982.

2) F. M. Sears, L. G. Cohen and J. Stone, "Interferometric Measurements of Dispersion-Spectra Variations in a Single-Mode Fiber", Journal of Lightwave Technology, Vol. LT-2, p. 181, 1984.

3) A. O. Garg and R. O. Claus, "Optical Fiber Path Differential Wideband Interferometer", Acoustical Society of America (Chicago, IL), April 1982.

4) A. O. Garg, "Application of Optical Fibers to Wideband Differential Interferometry and Measurements of Pulsed Waves in Liquids", Master's Thesis, Virginia Tech. (Blacksburg, VA), July 1982.

5) R. O. Claus and A. O. Garg, "Measurement of Pulsed Ultrasonic Waves in Liquid by Wideband Differential Interferometry", Acoustical Society of America (Orlando, FL), November 1982.

6) A. J. Barlow, "Techniques for the Calibration of Chromatic Dispersion Measuring Instruments", SPIE Vol. 841, Fiber Optic Network and Coherent Technology in Fiber Optic Systems II, p. 266, 1987.

7) C. Eoll, W. Lieber, M. Loch, H. Etzkorn and W. Heinlein, "Advances in the Dispersion Characterization of Different Single-Mode Fibers," Technical Digest of the 12th European Conference on Optical Communication, Barcelona, Vol. 1, p. 71, 1986.

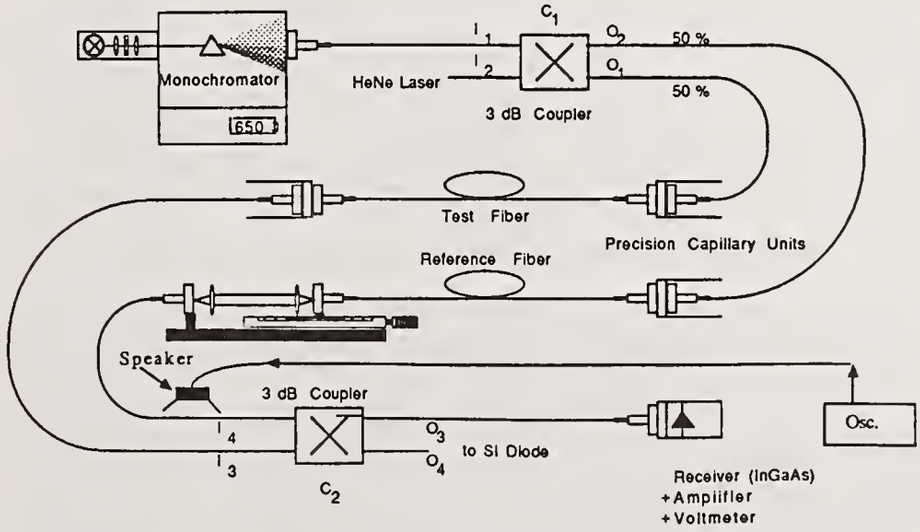

Fig. 1. Schematic Diagram of new interferometric dispersion measurement system

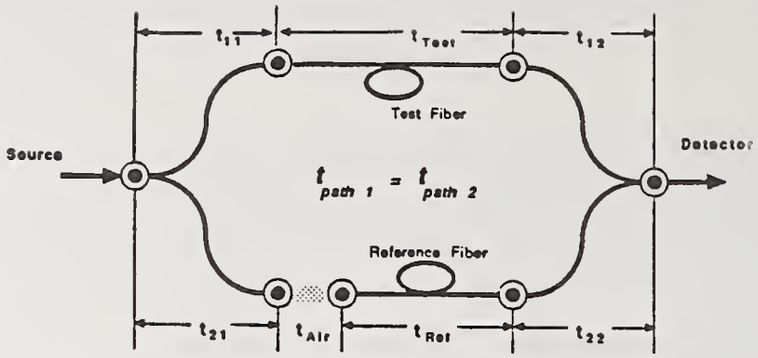

$t_{12} = t_{22}$

$t_{11} = t_{21}$

Fig. 2. Schematic Diagram of delay times along the main optical paths

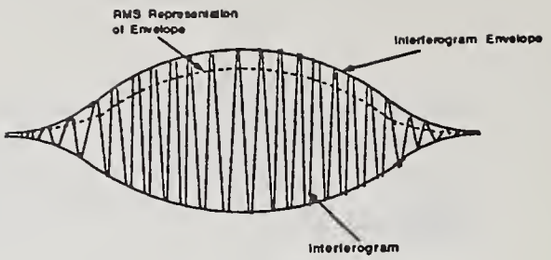

Fig. 3. Idealized interferogram

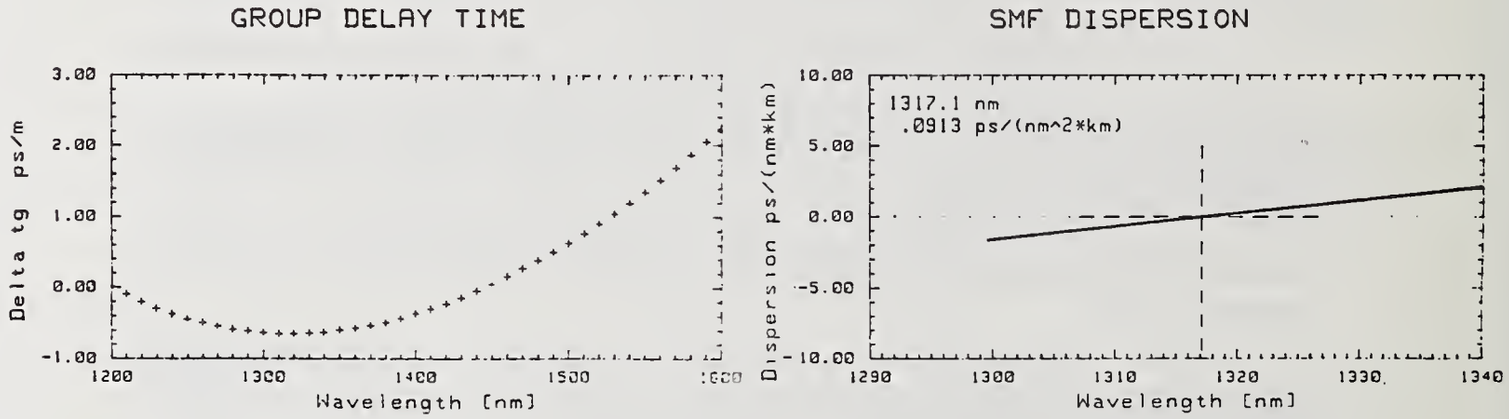

Fig. 4. Group delay and dispersion of standard matched-cladding fiber

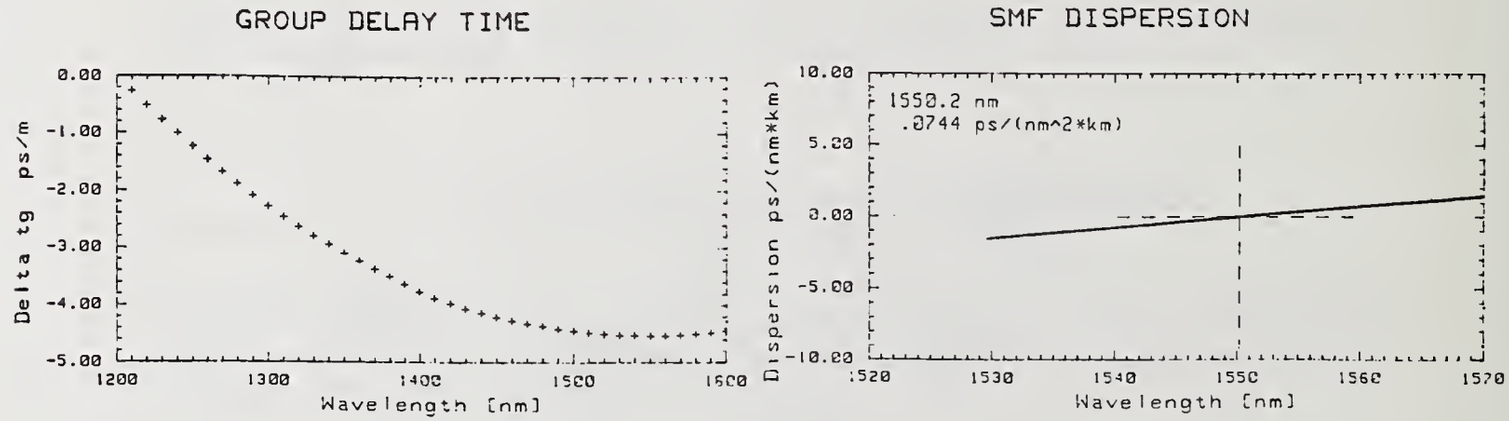

Fig. 5. Group delay and dispersion of dispersion shifted fiber

REFRACTIVE INDEX PROFILING - STATE OF THE ART.

K. W. RAINE, J. G. N. BAINES, D. E. PUTLAND.
(National Physical Laboratory, Teddington, Middlesex, U.K.)

INTRODUCTION.

Numerous techniques exist for obtaining the refractive index profile of optical fibres [1,2]; of these refracted near field (RNF) is the most commonly used. However, recent intercomparisons [3,4,5] indicate that accurate calibration can be a problem. In this "state of the art" paper we discuss mechanisms which can lead to inaccurate RNF measurements, how these effects can be minimised, and how axial interferometric measurements can be made with an uncertainty of ±1% and be used to calibrate RNF instruments using a multi-step index fibre. A comparison of measurements made by RNF and axial interferometry on several fibres is presented along with some conclusions drawn from recent intercomparisons.

RECENT REFRACTIVE INDEX PROFILE INTERCOMPARISONS.

At least three intercomparisons have been completed in the last year, these having been organised by Dr. P. Di Vita through the European Cooperation in Science and Technology (COST) consortium, by Ir. M. Hutjens of Philips at Eindhoven (Holland), and by Drs. D. Franzen and M. Young of NBS at Boulder (USA). In the latter intercomparison the object was the accurate determination of numerical aperture (NA) from the refractive index profile. The results of these intercomparisons are due to be published shortly and cannot be discussed in detail here. However, the general indications were as follows;

In the intercomparison organised by Philips there were 8 participants who measured a multi-step index fibre with a depressed cladding (mean δn=-0.006) and a largest step of about 0.018 for which measurements varied between 0.015 and 0.021. The results tended to group with particular makes of instrument. The depressed cladding caused vignetting in some instruments and was responsible for the lowest measured values.

The COST intercomparison involved 7 participants measuring 6 monomode fibres having maximum refractive index differences between 0.005 and 0.02; some had simple step index profiles and others depressed and/or raised annuli. The overall standard deviation of the results, which did not fit well to a normal distribution, was ±20%.

Finally the NBS intercomparison which involved 11 participants measuring 12 multimode fibres with maximum index differences between 0.015 and 0.030. The NA determined from RNF profiles varied by ±10% which corresponds to ±20% in peak index difference. Although some of this variability could be attributed to interpretation of index spikes and ripples, the systematic differences between laboratories indicated that calibration and measurement problems were an important factor [3].

THE USE OF AXIAL INTERFEROMETRY FOR ACCURATE CALIBRATION.

The main disadvantages of axial interferometry are the difficult and laborious preparation of the thin fibre slices and the poor spatial resolution of the technique. These make it unsuitable for rapid turn-around measurements and its use for measuring monomode fibres is limited. It does however measure refractive index differences in terms of the wavelength of light, providing measurements traceable to national standards and, with care, uncertainties of ±0.0001 in a refractive index difference of 0.015 on relatively large and uniform areas of refractive index

can be obtained. The technique therefore seems ideally suited to providing traceable calibrations, via a transfer standard fibre, for RNF instruments.

In implementing this method an essentially common path interference microscope is preferred; that is the ray paths through the imaging optics, sample and air paths should be the same for the two interfering light beams. This minimises the effects of aberrations, mechanical instability and air turbulence required when optical path differences (OPD) as small as 5nm are to be determined.

By placing a Mach-Zehnder interferometer between the objective and the eyepiece, the Zeiss Interphako interference microscope achieves common path operation throughout the imaging optics producing excellent stability and phase uniformity over the field of view. Operation of the interferometer allows a variable degree of shear to be introduced between the images formed by the eyepiece. Thus the fibre core of one image can be superimposed on the cladding of the second image, with cladding against cladding in an adjacent part of the field of view to provide a reference level. With a 100μm thick fibre slice the combination of an objective with an NA between 0.5 and 0.8 and a condenser NA of 0.3 provides an optimum balance between magnification, resolution (about 2μm) and image brightness.

The interferometer is adjusted so that in the absence of any phase objects the image field is uniform in intensity. A phase compensator, which changes the path length of one arm of the interferometer, can be adjusted so that the intensity is minimised or equalised across an imaged edge of a half shade plate. The phase plate is situated at an intermediate image plane and provides a more precise setting than can be obtained from the interference minimum. Further improvement and ease of operation is achieved by using a TV system and displaying the intensity profile alongside the normal image. With a 100μm thick slice this technique can give a single reading uncertainty equivalent to ±0.00005 in refractive index [6]. Using a phase compensator to measure directly the optical path removes uncertainties that can arise in interpreting the intensity distributions of the interferograms but makes measurements of a complete profile tedious. In addition the setting is less certain when made on a sloping intensity profile produced by regions of non-uniform refractive index. However, perhaps more importantly in this context, effort can be directed towards averaging the effects of slice imperfections which have been troublesome in previous work [7]. Measurements can be made with the image of the core sheared sequentially into the four quadrants of the cladding and repeated with randomly chosen starting positions. Possible errors due to imperfections in the interferometer are overcome by moving the sample stage so that the readings are taken at the same place in the image plane. Despite averaging the slices must be of good quality to produce an acceptable standard error of the mean.

The quality of the fibre slices can be checked by interference microscopy and self-Fizeau fringes which can be seen with the unaided eye in the capillary section using a He-Ne laser or low pressure mercury lamp. Once assured that the parallelism of the capillary is satisfactory the interference microscope can be used to shear the image of the fibre into the capillary to assess the quality of the fibre slice. As a second test the end faces of the fibres can be viewed with a microscope incorporating a Michelson interferometer objective. This will show end face flatness and any tilt of the fibre slice with respect to the capillary. Typically thickness variations less than 0.1μm can be achieved and deviations from flatness less than 0.05μm. The overall uncertainty in the OPD measurement due to slice imperfections is thought unlikely to exceed ±0.5% when the averaging measurement

procedure described above is adopted.

The thickness of the fibre slice can be measured using the z-axis measurement facility on the Vickers Fibercheck microscope. Precision focussing on the upper and lower surface of the slice is achieved by aligning two halves of a graticule image and an electronic readout of the displacement is given with an uncertainty of ±0.5μm (2σ). The instrument is calibrated using a thin silica slice whose thickness is known from interferometric measurements. The effects of slice imperfections are averaged as in the phase measurement which also reduces the random uncertainty. The overall uncertainty of the thickness measurement is considered to be ±0.2μm.

In summary, the overall uncertainty in the refractive index difference is systematic and can be estimated to be ±0.7% or ±0.0001 in an index difference of 0.015 (1σ).

REFRACTED NEAR FIELD.

The difficulties in making accurate RNF measurements are due to uncertainty in the calibration techniques and to making accurate radiometric measurements particularly when there are angle of incidence changes in the intensity distribution.

The most common methods of calibration involve using the oil-cladding index difference, a fibre of known NA and moving the blocking disk. Oils have large temperature coefficients of refractive index requiring the temperature to be known to better than 0.3°C and the refractive index of the cladding can be several parts in the 4th decimal place higher than that of bulk silica [6]. Use of a fibre of known NA relies on definitions, and on the interpretation of imperfections, ripple, spikes and dips in the refractive index profile. For the purpose of traceable calibration and obtaining the fullest understanding and confidence of measurement techniques it is more satisfactory if the value of the NA calculated from the profile agrees with that measured by far-field and vice versa. A direct refractive index calibration using a fibre measured by interferometry therefore seems to be the preferrable choice. It would provide traceability for and confidence in other methods perhaps preferred for convenience by other laboratories.

SOME RNF MEASUREMENT PROBLEMS.

Movement of the blocking disc only simulates movement of the cone of rays.This is subject to errors if the transmissivity of the collecting optics significantly varies with angle of incidence (considered by Stewart as a potential source of error [1]). This effect can be seen if an extra blocking disc is placed close behind the launch objective so that a hollow cone of light is focussed on to the end of the fibre. The size of this disc should just prevent the innermost rays intercepting the instruments blocking disc. Thus when the focussed spot is scanned across the fibre the output from the detector should be constant. Figure 1a shows instead an inverted profile which has the effect of reducing the profile height and the height of the oil-cladding step by at least 0.0005 in index. Figure 1b shows the strong polarization dependence and further emphasises the need to use circularly polarized light or light plane polarized at 45° to the scan direction. These error curves can then be used to produce correction curves as a function of index difference; the curve for our instrument is shown in figure 2. Alternatively the collecting optics should be designed to ensure the angles of incidence at air-glass interfaces are less than 30° or correcting optical coatings used, or, in the case of ellipsoidal collectors, an eccentricity of 0.71 ensures that angles of incidence are within a

few degrees of 45°; small changes in angle of incidence can then be made to have an insignificant effect.

We have also observed with our instrument that repeatable and consistent measurements are only obtained from the average of orthogonal scans and that the oil index level often needs to be determined a distance greater than 30μm from the oil-cladding interface. These effects seem to be due to the changes in annular light intensity distribution during a scan. The detector needs to be insensitive to this and should not be driven non-linear by high localised intensities which must not exceed 70μW/mm^2.
Thus to avoid possible detector non-linearities and position sensitivity of the detector a blurred spot is preferrable to a sharply focussed point or a well defined annulus. Even so, the badly focussed spot size will vary and vignetting at the detector must always be considered. These difficulties can be overcome by placing an integrating sphere in front of the detector, the focussed light now falling onto a diffusing baffle in the centre of the sphere. This effectively desensitises the detector to annular and angular distribution variations in the incident light. We have found its use beneficial to the production of level symmetrical profiles on step fibres and in reducing scan direction dependence. The reduced detection efficiency did not lead to signal-to-noise problems.

In an effort to ensure some measurement repeatability our RNF profiler was assessed and modified in light of the points discussed above. The movable blocking disc was repositioned so that there was agreement with the axial interferometric results on the calibration fibre (whose RNF profile is shown in figure 3) after the angle of incidence corrections had been applied. Comparisons between RNF and axial interferometry were then made on several other fibres, one having a step index and the others parabolic index profiles with no, or very small, on-axis index depressions. The calibration and refractive index of the oil were used to calculate the refractive index of the cladding which was also determined by phase contrast microscopy [8]. The NA of multimode fibres was evaluated from the smoothed curve fit profiles [9] and compared with the Far-Field values from the NBS intercomparison. The results are shown in table 1. RNF measurements are the average of at least four sets of orthogonal scans, which also reduced the random uncertainty to ±0.0002 (2σ). The refractive index of the oil was measured at 20°C on an Abbé refractometer and the oil temperature by a platinum resistance thermometer adjacent to the cell; during RNF measurements it was necessary to minimise temperature gradients by allowing the instrument temperature to stabilise (for a few hours) and the oil cell, after loading, to come to thermal equilibrium with the instrument.

Table 1 shows that sufficiently accurate results can be obtained by RNF measurements. Calibration via interferometry and the application of the described correction curve leads to a ±1% agreement on index difference over a range of fibres, a ±2% agreement on the cladding refractive indices and a +1% difference (average of 12 fibres) in the NA determinations.

CONCLUSION.

Accurate measurement and calibration of RNF instruments can be achieved with uncertainty of ±1%. Accurate operation may require in some cases that additional attention be paid to the collecting optics and detector, angle of incidence error curves produced and scan direction dependencies investigated. A direct refractive index calibration, traceable to national standards of length is possible using multi-step index fibres measured by axial interferometry. The fibre whose profile is shown in figure 3 is now available with a certificate of calibration. With accurate

refractive index and geometry calibration (also under investigation at NPL) an RNF instrument can provide measurements of profile height, profile shape, all of the geometrical parameters and the NA.

Table 1

Fibre type	Index difference		Cladding index		NA	
	RNF	AI	RNF	PCM	RNF*	FF
Multi-step	0.0184	0.0184	-	-	-	-
	0.0147	0.0148	-	-	-	-
	0.0037	0.0036	-	-	-	-
Single step	0.0162	0.0163	1.4577	1.4576	-	-
Multimode	0.0310	0.0307	-	-	0.293	0.286
	0.0292	0.0291	1.4576	1.4577	0.281	0.279
	0.0160	0.0160	1.4575	1.4575	0.209	0.206
	0.0196	-	-	-	0.228	0.226

notes
AI = axial interferometry
PCM = phase contrast microscopy
FF = far-field
* = corrected to 850 nm wavelength

REFERENCES.

[1] STEWART, W. J.:"Optical fibre and preform profiling techniques.", IEEE J. Quantum Electron. QE-18, 1451-1466, 1982.
[2] MARCUSE, D.:"Principles of optical fiber measurement.",Academic Press, Chapter 4, 1981.
[3] FRANZEN, D.L., YOUNG, M., CHERIN, A.H., HEAD, E.D., HACKERT, M., RAINE, K.W. and BAINES, J.G.N.,:"Numerical aperture of multimode fibres by several methods: Resolving differences.", Submitted to J. Lightwave Technology.
[4] Di Vita, P.:"Report on COST 217 intercomparisons on circularly symmetric single mode fibres.", To be published.
[5] HUTJENS, M.:"Round-robin results of fibre refractive index differences measured by the refracted near field (RNF) method.", To be published in J. Opt. Comm., 9, 4, 1988.
[6] RAINE, K.W., BAINES, J.G.N., KING, R.J.:"Comparison of refractive index measurements of optical fibes by three methods.", IEE Proc. J., 135, 190-195, 1988.
[7] WONSIEWICZ, B.C., FRENCH, W.G., LAZAY, P.D. and SIMPSON, J.R.,: "Automatic analysis of interferograms: optical waveguide refractive index profiles.", Appl. Opt., 15, 1048-1052, 1976.
[8] LOCKE, J., UNDERHILL, M.:"Automatic refractive index measurement of glass particles.", Forensic Science International, 27, 247-260, 1985.
[9] FORBES, A.:"Fitting a generalized parabola to data", NPL Report DITC 96/87, September 1987.

ACKNOWLEDGEMENT.

The authors would like to thank Ir. M. Hutjens and Dr. P. Di Vita for permission to discuss the results of the intercomparisons ahead of publication.

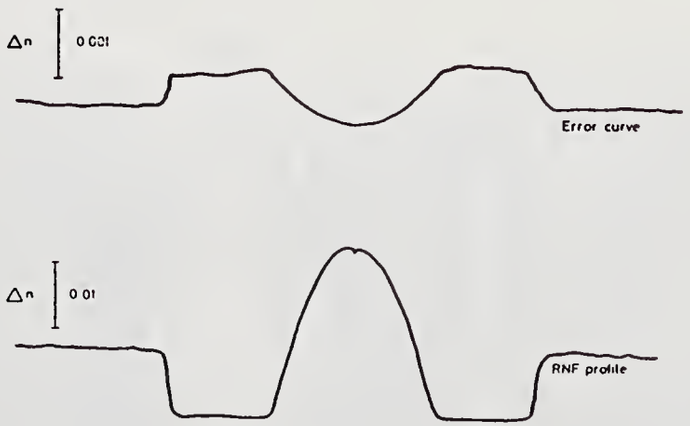

Figure 1a Refracted near field profile of 60/125 grade index multimode fibre with error curve

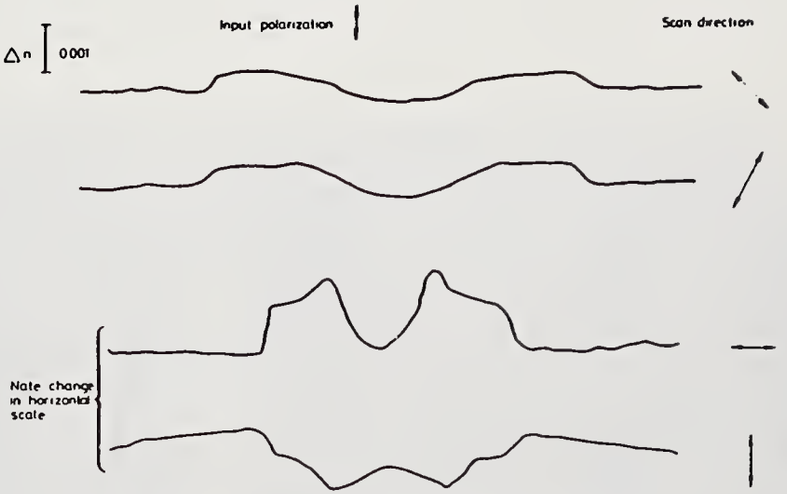

Figure 1b Error curves showing effect of changing the scan direction relative to the input polarization

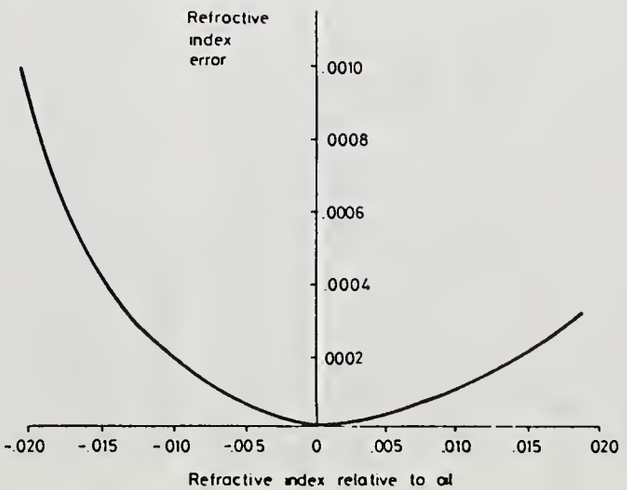

Figure 2. Error in measured refractive index relative to index of oil.

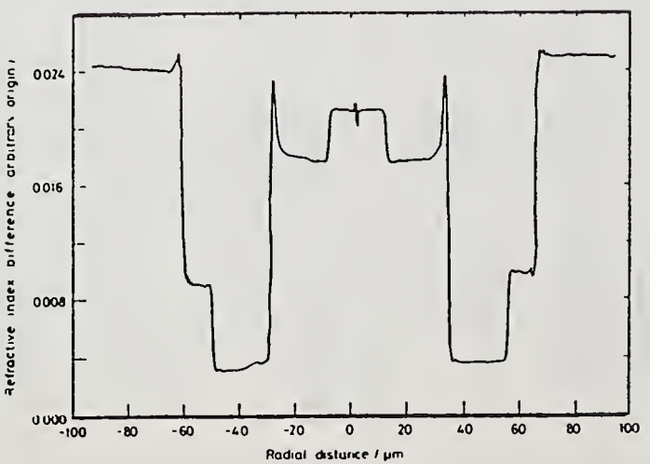

Figure 3 Refractive index profile of multi-step index fibre available as a calibration standard

RECONSTRUCTED REFRACTIVE INDEX PROFILE OF OPTICAL FIBER BY REFRACTED RAYS

Nobuo AMANO and Ken-ichi NODA

Faculty of Technology
Tokyo University of Agriculture and Technology
Koganei-shi, Tokyo, 184, Japan, telephone +81 423 81 4221

New microscopic computer tomography measurement method of optical fiber refractive index profile has been reported by the authors elsewhere [1]. In the first half of this paper, this microscopic CT technology is applied to polarity-maintaining optical fiber refractive index profile measurement. It is difficult to measure it by conventional method because of masking effect of the stress-giving area. In such a case, effectiveness of this method is demonstrated by showing experimental result.

In our previous paper, error estimation of this method which may be produced in the process of the ray to index-strip-integral transformation was not enough. So in the latter half the error estimation of this method is made through a computer simulation for a given input refractive index distribution.

In the computer X-ray tomography, an X-ray flux passes through an object, such as a human brain, and a received projection represents a strip integral of the absorption in the object. Unlike the X-ray, in most optical material, light does not suffer any absorption but is refracted due to the refractive index non-uniformity [2-3]. Therefore, a received projection represents a ray flux density distribution due to refraction. New and improved signal processing algorithm is needed. It is that the ray flux density distribution is transformed to the strip integral of the refractive index along the projection path, as described in Ref. 1.

This method has advantages that there is no need to prepare special samples, and only ordinary microscope and TV camera are used and is a non-destructive measurement. This is especially significant for nonaxisymmetrical distributed refractive index profile measurement. Effectiveness of this measuring system has been demonstrated by showing an example of measured

result on a dual core fiber who has two single mode cores in one cladding [1].

This time, elliptic jacket fiber was used as measured material as an example of the polarity-maintaining fibers. This fiber has nonaxisymmetrically located stress-giving portion near the core to produce large birefringence in the core. Although residual stress distribution in this kind of optical fiber has been measured using CT algorithm [4], refractive index profile measurement has not yet been reported. It is not possible to measure, using observed data from only one side of the fiber. Moreover, in general, stress-giving portion has lower refractive index than that of the cladding material and has large cross sectional area. So, it is difficult to measured the core profile by usual optical observing method, because non-uniform refractive index region distorts the image of the core when observed from the outside of the fiber.

In our measurement, the fiber immersed in the matching liquid is observed with a microscope and television camera, and 480 times 480 pixels of eight bits multilevel light intensity data are stored in a frame memory. The obtained data are averaged in the fiber longitudinal direction, to minimize noise due to dust, and other causes. This observation and averaging are repeated rotating the fiber by π/n at a time, where n is a projection number of CT. Then n intensity distribution data items are obtained in π radians of rotation, around the axis. The observed data are transformed to the index strip integral. At each rotation angle of view, the observation and calculations are performed. After repeating these procedures, the obtained all projections are space-filtered and back-projected to reconstruct the refractive index two dimensional profile [5]. n=100 was selected in the most measurements. An example of three dimensional plot of reconstructed refractive index profile is shown in Fig. 1. The measured profile along the major and minor axes are shown in Fig. 2. In these figures, a higher refractive index region of a small core is clearly demonstrated.

A computer-simulated experiments has been performed to estimate the error of the microscopic CT algorithm. Fig. 3 shows an example of simulation

result. In Fig. 4, an input refractive index profile for the simulation is given, by a broken curve, which has five concentric circle areas. There are four levels of refractive indexes, including a low level of equivalent of stress-giving portion. Fiber radius of 60 μm, core radius of 5 μm, observing area diameter of 150 μm are assumed. Reconstructed index distribution along the fiber diameter line is shown in Fig. 4 by a solid curve, and is compared with the input data. The reason why axisymmetric index distribution is selected as an input, is merely to make the error estimation easy.

Ray trace simulation is done as follows; white light ray flux enters into a hypothetical optical fiber having a given input index distribution, and light intensity distribution due to the illuminated light is calculated. The refraction and reflection at the boundary cylinders between neighboring concentric circle regions are obtained by Snell's law. The reflection and transmission coefficient at the boundary cylinders are obtained by Fresnel's law. The scattering at the boundary cylinders is ignored. Pixel number at the observing plane is 300 dots. The ray flux number is assumed to be 100 per a pixel. 30 000 flux in total are used in this simulation. The reconstruction is made by this method using these data.

In this simulation, variance of the error is 0.57. In this value, ray trace simulation error is also included. There are a little error of the artifact accompanying CT. Reconstructed profile by the simulation is very similar to that of the given profile, except near the stepwise index change portions. If the refractive index change is rapid, ray crossovers may cause a distortion of the reconstructed shape. But it is not so important because practical fiber has a relaxed index change as shown in the experimental result. The obtained variance is mainly attributed to the given stepwise index change.

In conclusion, an elliptic jacket optical fiber having non-axisymmetrically distributed refractive index, is measured by the microscopic CT, and index profile of small core surrounded by a large area of lower index

stress-giving portion is successively demonstrated. The error estimation through a computer simulation is made.

REFERENCES

[1] K. Toga, et al, Jour. Lightwave Techn. 6, 1, pp. 73-79, Jan. 1988.

[2] D. Marcuse, Appl. Opt., vol. 18, no. 1, pp. 9-13, Jan. 1, 1979.

[3] D. Marcuse, and H. M. Presby, Appl. Opt., vol. 18, no. 1, pp. 14-22, Jan. 1, 1979.

[4] T. Abe, et al, Electron. Lett., vol.21, no.1, pp.4-5, 1985.

[5] L. A. Shepp and B. F. Logan, IEEE Trans. Nucl. Sci., vol. NS-21, pp. 21-43, June 1974.

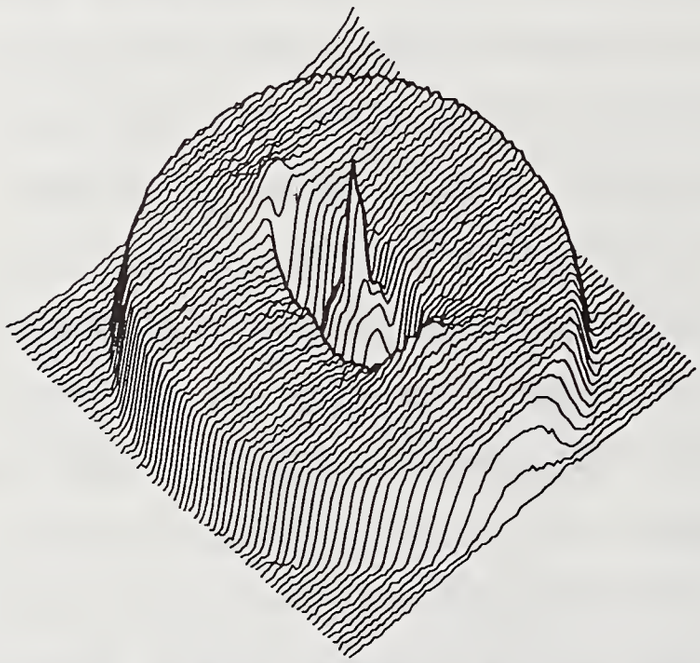

Fig. 1 3D plot of reconstructed index profile of the elliptic jacket fiber.

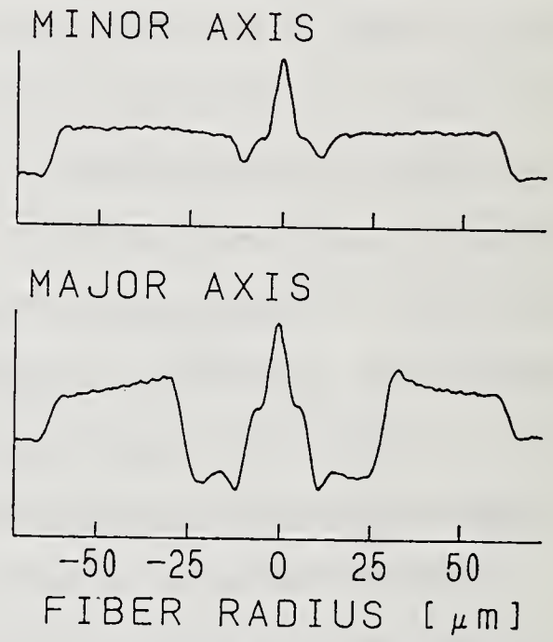

Fig. 2 Major and minor axial direction distributions of the elliptic jacket fiber refractive index.

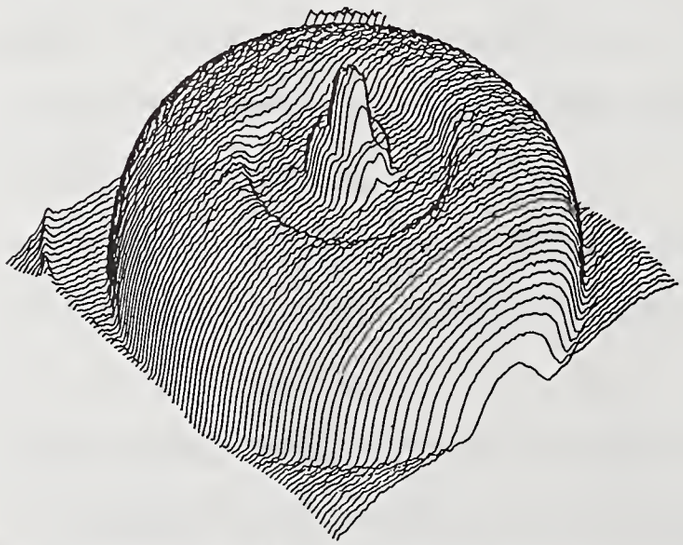

Fig. 3 3D plot of reconstructed refractive index profile by a simulation.

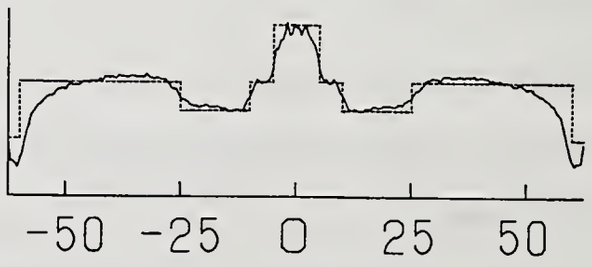

Fig. 4 Input (broken curve) and reconstructed (solid curve) index distributions along the diameter direction.

CALIBRATION OF OPTICAL FIBER PREFORM REFRACTIVE INDEX MEASUREMENT

D.A.Svendsen, G.Beresford and D.Marcus-Hanks

York Technology Limited, York House,School Lane,
Chandler's Ford, Hants SO5 3DG, United Kingdom.

Introduction

The measurement of the refractive index of optical fiber preforms by transverse illumination can achieve repeatabilities of better than 100 ppm in refractive index. For example, a measurement of a graded-index multimode fibre preform gave a core index difference of 0.01265, with a one standard deviation of 0.00008, based on 9 groups each of 9 measurements made over a period of several days. To fully realise this performance and provide the basis for substantial improvement, a calibration technique is required that offers of the order of 0.1% of typical index differences. The preform analyser obtains the index profile from the deflection function which is the change in refracted angle as a function of preform radius[1]. It is proposed that the angle measurement is calibrated rather than the index difference directly. Existing calibration techniques rely on measuring index differences known by some independent reference method; for example the interferometric measurement of a slice of the preform[2]. However, such techniques are generally destructive, unsuitable for routine use and may not give the required accuracy. The three different approaches to angle calibration described offer both convenience and high accuracy, and will be traceable to absolute standards using conventional index and dimensional measurements.

Calibration lens in air

A typical preform analyser consists of a light source, the preform immersed in index matching oil inside a cell, and a means of measuring the refraction angle as

The gradient at the centre of the tube is thus:

$$\left.\frac{d\Theta(y)}{dy}\right|_{y=0} = -2N1\left[\left(\frac{N2 - N1}{R1\ N2}\right) + \left(\frac{N3 - N2}{R2\ N3}\right)\frac{N1}{N2}\right] \qquad \text{(iv)}$$

It is possible to correct for the absolute index of the matching oil, and hence its temperature sensitivity, so that the deflection function depends only upon the silica/air interface. Figure 2 shows some typical results for the measured gradient for a 42mm diameter, 2mm thick wall, fused silica tube, both with and without temperature correction. Repeatabilities of well under 1 part in a 1000 have been achieved using standard tubes. The circularity and wall thickness variations of these tubes are being investigated to ensure that the required accuracy may be achieved by computation using expression (iv).

Prisms-in-cell

A less convenient, but potentially more accurate, alternative to the tube is a right-angle prism immersed in the cell. With the light source at tilt angle A to the normal of the hypotenuse face, the deflection function is given by:

$$\Theta = -B + \text{ARCSIN}\left[\frac{N2}{N1}\ \text{SIN}\left(A + B - \text{ARCSIN}\left(\frac{N1}{N2}\ \text{SIN}(A)\right)\right)\right] \qquad \text{(v)}$$

where the terms are defined in Figure 3. With silica index matching oil(N1=1.458) and a crown glass prism(N2=1.5196), the difference in refraction angles between the two exit surfaces is about 7 degrees (Figure 4) with a sensitivity to tilt of the prism of about 0.0015deg/deg ($\partial\Theta/\partial A$) and to prism angle error of .09deg/deg ($\partial\Theta/\partial B$). Thus a prism with angles accurate to better than 1arc.minute and tilt less than 3 degrees will meet the 0.1% required accuracy if the refractive index is known to 50 ppm. The absolute index of the oil and its temperature sensitivity may be eliminated by utilising an adjacent fused silica reference prism. Although the prism only gives one calibration angle unlike the other two methods, it has the advantage that it does not require the cell movement stage to be calibrated.

In addition, the significance of strain in all three calibration samples is being studied to ensure that the stress optic effect[3] does not degrade the absolute accuracy.

the preform traverses[1]. The simplest approach to angle calibration is to substitute a standard plano-convex lens for the cell and preform. The deflection function for normal incidence on the plane surface of the lens is then:

$$\theta(y) = \text{ARCSIN}\left(\frac{N2}{N3}\frac{y}{R}\right) - \text{ARCSIN}\left(\frac{y}{R}\right) \qquad \text{(i)}$$

where: y is the distance from the centre of the lens, R its radius of curvature, and N2,N3 are the refractive indices of the lens and air, respectively.
The gradient at the centre of the lens is thus:

$$\left.\frac{d\theta(y)}{dy}\right|_{y=0} = \left(\frac{N2 - N3}{R\ N3}\right) \qquad \text{(ii)}$$

The refractive index is known to better than 10ppm and so the gradient accuracy will be limited by the calibration of the cell movement stage, typically about 0.1%. Not only may the gradient be used to calibrate the measurement to the required accuracy, but the known shape of the theoretical deflection function allows the linearity of the instrument to be checked. Figure 1 compares the deviation of expression (i) from a linear function with that of an actual measurement. Short term repeatabilities of 1 part in 3000 and longer term of 1 part in 1000 have been achieved, hence coming close to the target of 0.1% accuracy.

The objection to this approach is that the cell must be removed which may introduce errors arising from the absence of the cell windows from the optical path.

Tube-in-cell

A hollow fused silica tube inside the cell gives a deflection function of the form:

$$\theta(y) = -2N1\left[\text{ARCSIN}\left(\frac{y}{R1}\right) - \text{ARCSIN}\left(\frac{N1}{N2}\frac{y}{R1}\right) + \text{ARCSIN}\left(\frac{N1}{N2}\frac{y}{R2}\right) - \text{ARCSIN}\left(\frac{N1}{N3}\frac{y}{R2}\right)\right] \qquad \text{(iii)}$$

where: y is the distance from the tube axis, R1,R2 are the outer and inner radii of the tube, and N1,N2,N3 are the oil,tube and air refractive indices respectively.

Acknowledgement

Thanks are due to the Directors of York Technology Limited for permission to present this paper.

References

[1] W.J.Stewart, "Optical Fiber and Preform Profiling Technology", IEEE J.Quant.Electron., 1982, Vol. QE-18, N010, p1451-1466.

[2] M.Carratt, C.Reinaudo, J.Auge, "Preform measurements and their industrial application", 1985, SPIE Proceedings, Vol.584, paper 584-19, p122-128.

[3] G.W.Scherer, "Stress-induced index profile distortion in optical waveguides", Applied Optics, 1980, Vol.19, No12, p2000-2006.

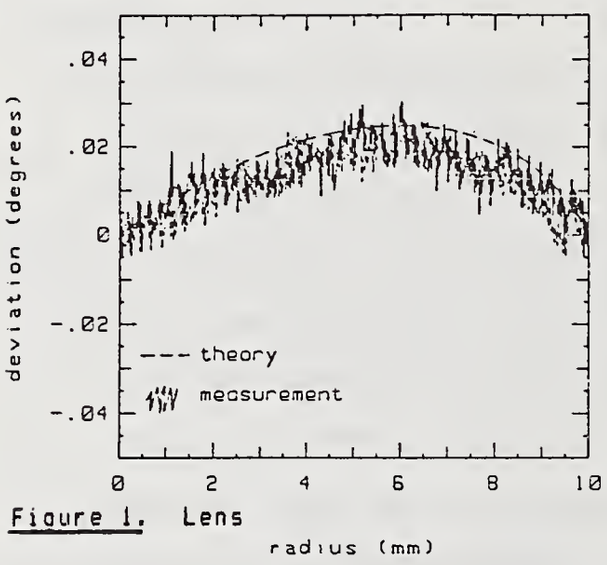

Figure 1. Lens

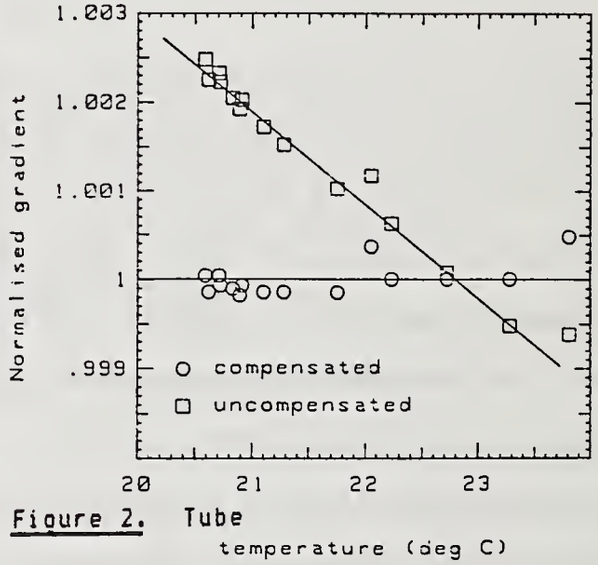

Figure 2. Tube

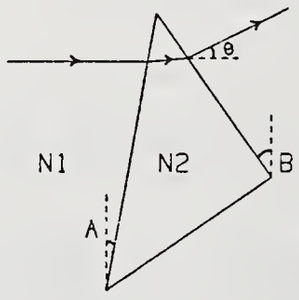

A = angle of tilt of prism

B = angle of exit face

θ = deflection angle

Figure 3. Prism

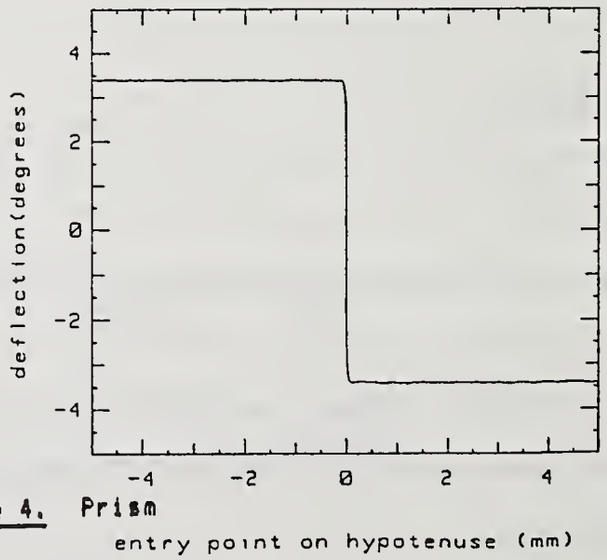

Figure 4. Prism

INTERLABORATORY COMPARISON OF FAR-FIELD METHODS FOR DETERMINING MODE FIELD DIAMETER USING BOTH GAUSSIAN AND PETERMANN DEFINITIONS

Timothy J. Drapela
National Bureau of Standards
325 Broadway
Boulder, CO 80303

In a previous interlaboratory comparison of measurement methods for mode field diameter (MFD) of single-mode optical fiber, participants assumed a Gaussian mode-field distribution [1]. Those results indicated good agreement (0.15 μm, one standard deviation) among the various methods for dispersion unshifted fibers at 1300 nm. The Gaussian distribution was a good assumption since 1300 nm was close to the cut-off wavelength. At 1550 nm, however, the Gaussian assumption is not valid, and significant offsets (0.7 μm) were observed between the one-dimensional far-field scan (FF) method and variable aperture far-field (VAFF) method. This is of concern, since these two methods are among the most widely used for routine MFD measurements. Anderson and Kilmer have shown that the "Petermann 2" definition, based on a second moment, gives good consistency among various measurement methods [2] [3]. Moreover, in those situations where mode profiles are not approximately Gaussian, the Petermann definition gives better prediction of splice loss than does the Gaussian.

This paper describes an interlaboratory comparison which includes the Petermann as well as the Gaussian definition and also considers measurements on dispersion shifted single-mode fibers. Participants in the comparison are members of the Electronic Industries Association and include most of the major fiber and cable manufacturers in North America.

Six single-mode fibers representing five different manufacturers were measured by the participants. Two fibers were dispersion shifted, while the remaining four were dispersion unshifted.

Seven participants used the FF method, in which laser diodes are used as sources and MFD is determined by acquiring the one-dimensional far-field radiation pattern. Five participants used the VAFF method, in which MFD is determined by measuring the relative power passing through a series of far-field apertures. Here, the source generally consists of a tungsten lamp and a monochromator. Details of the FF and VAFF methods can be found in EIA-FOTP 164 and EIA-FOTP 167, respectively.

Common to all methods were a test fiber length of 2.0 ± 0.2 m, a single 50 mm diameter loop to strip out possible second-order mode power, and, when necessary, some type of cladding-mode stripper.

Participants closely followed the guidelines of FOTPs 164 and 167. The FOTPs contain specific curve-fitting instructions for the Gaussian MFDs. Petermann MFDs were determined from far-field integrals without specification of a particular curve-fitting routine.

The results of the comparison are grouped into three categories: 1300 nm dispersion unshifted, 1550 nm dispersion unshifted, and dispersion shifted. This division seems quite natural when the average offsets between FF and VAFF methods are examined. For fibers in the same category, the relative offsets are approximately the same, without exception; relative offsets between FF and VAFF methods are given in Table 1 (small corrections have been made for variations in source wavelengths). The offsets are less for the Petermann definition for all fiber categories.

For unshifted fibers at 1300 nm, using the Gaussian definition, the results of the previous interlaboratory comparison were verified. An average standard deviation of 0.17 μm was observed, with only a small offset between average VAFF and FF results. The Petermann results did improve on this though, giving almost no offset and an average standard deviation of 0.11 μm, Fig. 1.

For the same fibers at 1550 nm, substantial offsets were observed between VAFF and FF results for the Gaussian definition. Petermann results gave significant improvement, reducing offsets to almost zero and giving an average standard deviation of 0.11 μm, as opposed to 0.32 μm for Gaussian, Fig 2.

With dispersion shifted fibers, the Gaussian results gave the largest offsets of all. Petermann results seemed to improve upon this, but only slightly. The average standard deviation was 0.5 μm for Gaussian and 0.35 μm for Petermann, Fig 3. The Petermann results of one VAFF participant were consistently within the range of FF Petermann results. We suspect the large VAFF/FF offsets are related to the small MFDs of dispersion shifted fiber. Smaller MFDs translate to more power at larger far-field angles. If the VAFF optics and associated detector do not have sufficiently uniform collection for large enough NA, then the measured far-field pattern will be truncated; this translates into a larger measured MFD. We believe, therefore, that the discrepancies observed for this fiber category have more to do with experimental apparatus than with the Petermann definition; this is currently being investigated.

REFERENCES

[1] D. L. Franzen and R. Srivastava, "Determining the Mode-Field Diameter of Single-Mode Optical Fiber: An Interlaboratory Comparison," J. Lightwave Technol., vol. LT-3, no. 5, p. 1073, Oct. 1985.

[2] W. T. Anderson, V. Shah, L. Curtis, A. J. Johnson, and J. P. Kilmer, "Mode-Field Diameter Measurements for Single-Mode Fibers with Non-Gaussian Field Profiles," J. Lightwave Technol., vol. LT-5, no. 2, p. 211, Feb. 1987.

[3] K. Petermann, "Constraints for Fundamental Mode Spot Size for Broadband Dispersion-Compensated Single-Mode Fibers," Electron. Lett., vol. 19, no. 18, p. 712, 1983.

Table 1. Average offset values, in μm, between VAFF and FF results, for the three categories of comparison fibers.

Category	Offset Between VAFF and FF Methods, μm (Ave. VAFF – Ave. FF)	
	Petermann	Gaussian
1300 nm Dispersion Unshifted	0.04	0.28
1550 nm Dispersion Unshifted	0.05	0.59
1300&1550nm Dispersion Shifted	0.52	0.92

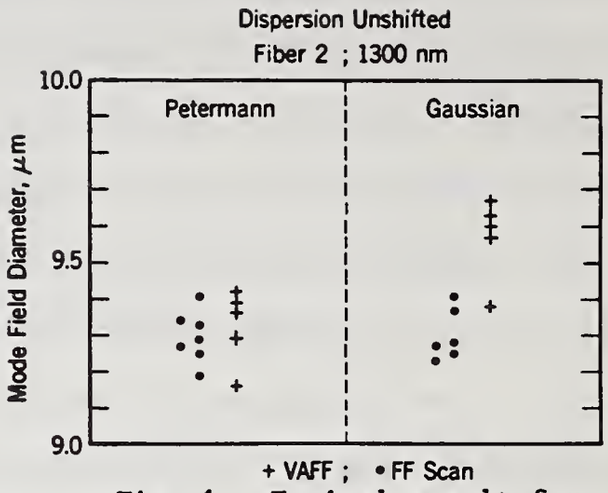

Fig. 1. Typical result for dispersion unshifted fibers at 1300 nm.

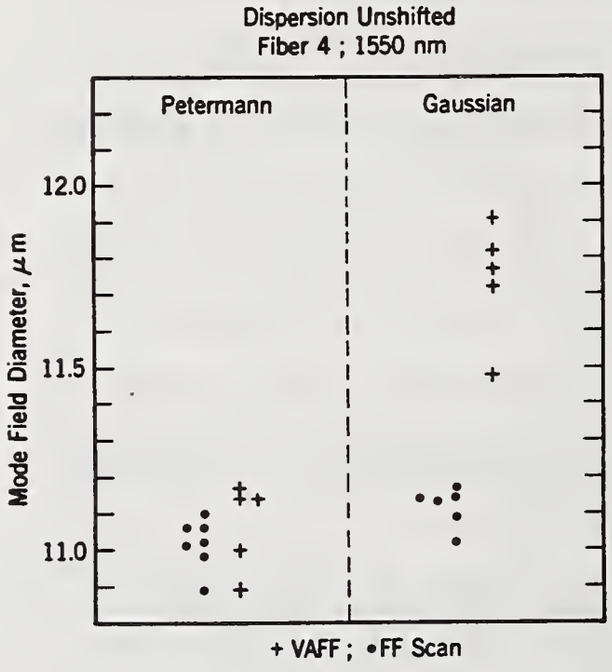

Fig. 2. Typical result for dispersion unshifted fibers at 1550 nm.

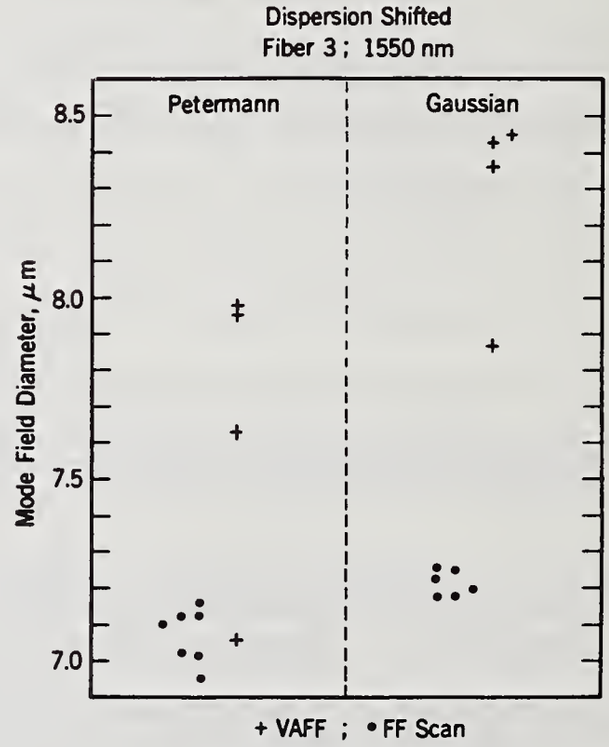

Fig. 3. Typical result for dispersion shifted fibers.

IMPROVEMENTS TO THE VAMFF SYSTEM FOR ACCURATELY MEASURING THE MODE-FIELD DIAMETER OF DISPERSION SHIFTED FIBERS

JERRY R. PARTON, PRODUCT ENGINEERING, MP-RO-2
CORNING GLASS WORKS, CORNING, NEW YORK 14831

Introduction Mode-field diameter (MFD) is an important parameter in the performance and specification of optical fibers[1]. This places a requirement on the industry to have accurate MFD measurement methods so that this parameter can be controlled and specified. Improved measurement accuracy will provide improved manufacturing process feedback, while facilitating better agreement throughout the industry.

Improvements to the variable aperture method in the far-field[2] (VAMFF) MFD measurement system are presented. The principle modification is the increase of the maximum numerical aperture (NA) of the system by increasing both the number and size of the apertures. By increasing the maximum NA from .2 to .4, sufficient power is collected from the tails of the far-field power distribution of dispersion shifted (DS) fibers to allow a more accurate measurement of these non-gaussian mode-fields. Without this modification, the .2 NA system can result in MFD error of up to 7% for some DS fiber designs. Agreement to within .1 μm is demonstrated between the new "High NA VAMFF" system and one-dimensional direct far-field scan measurements on DS fibers based on the Petermann II[3] definition of MFD.

Equipment The increased NA is accomplished by a spherical mirror focusing the light back through the aperture and onto the detector. The fiber and detector are each offset from the mirror's axis by .85 mm yielding a 1.7 mm fiber to detector separation (see Figure 1). The aberration introduced by

this offset does not negatively impact the system because the 300 μm detector diameter was appropriately chosen to collect essentially all of the power in the focused spot.

Vignetting is minimized by the close spacing of the components, and the remaining vignetting effect is compensated for by a geometric calculation of an effective aperture size. An additional benefit to using a mirror rather than a lens system is the absence of chromatic aberration, allowing the system to be used over a broad range of wavelengths. Twenty-one apertures, ranging from .03 to .40 NA, are used in the aperture wheel, providing good coverage between the largest and smallest apertures.

Calculation DS fibers, having more complex index profiles than standard step-index fibers, also have more complex non-gaussian field distributions. The Petermann II shape-independent definition of MFD is an accepted definition for the fundamental-mode spot size of DS fibers. Pask[4] has shown that this definition can be transformed to the far-field, from which point integration by parts yields the following expression for MFD:

$$MFD = 2\left(2/W_{ff}^2\right)^{1/2}$$

where $W_{ff}^2 = K^2\left[\sin^2\theta_m - (2/P_m)\left(\int_o^{\theta m} P(\theta)\sin\theta\, d\sin\theta\right)\right]$

$K = 2\pi/\lambda$
θ_m = half angle of largest aperture
P^m = power measured through largest aperture
$P^m_{(\theta)}$ = power measured through each aperture

The integral is solved numerically. This can be done by trapezoidal numerical integration, but depending on the form of the integrand and differential used, the result may vary across integrands by more than one percent. Recent tests have determined, however, that numerical integration

by Simpson's Rule is self-consistent across the same integrands to within .2%, and is centered between the errors of the trapezoidal methods. Use of Simpson's Rule can therefore give a slight improvement to agreement between laboratories.

Results The High NA VAMFF system has been compared to one dimensional direct far-field scanners in two separate forums. The first was the 1987 CCITT Study Group XV contribution 145 entitled Experimental Data for Mode-Field Diameter by the Variable Aperture Technique. These results are summarized in Table 1. The second comparison came from the 1988 NBS/EIA measurement round robin for MFD. These results are summarized in Table 2. In general, the MFD bias between the High NA VAMFF system and the various far-field scanners was less than .1 μm, with a VAMFF measurement standard deviation of approximately .05 μm.

Conclusions Modifications to the VAMFF system have made it possible to accurately measure the MFD of DS fibers by this technique. The primary modification is the use of a spherical mirror to collect power out to .4 NA. The calculation accuracy is also improved by using Simpson's Rule to carry out the numerical integration. Experimental results show excellent agreement between High NA VAMFF and one-dimensional direct far-field scanners. Therefore, the variable aperture technique, with its relatively short measurement time, can be used to accurately measure MFD of both standard step-index fibers, and dispersion shifted fibers.

Acknowledgments The "High NA VAMFF" system was initially designed and tested by R. A. Modavis and A. B. Bussard of Corning Glass Works.

References

[1]D. Marcuse, BSTJ, Vol. 56, No. 5, p. 703, 1977.

[2]J. Dick et al., OFC Technical Digest, paper WB3, 1984.

[3]K. Petermann, Electronics Letters, Vol. 19, No. 18, P. 712, 1983.

[4]C. Pask, Electronics Letters, Vol. 20, No. 3, p. 145, 1984.

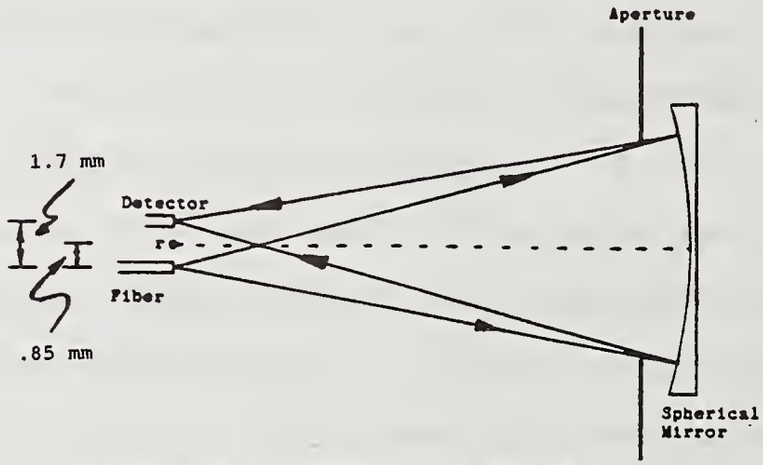

Figure 1 (not shown to scale)

High NA VAMFF Optical Path

Table 1 - CCITT Study Group XV, 1987
Mode-Field Diameter Contribution 145

Fiber	Wavelength (nm)	High NA VAMFF Mean (μm)	Far-Field Scan Mean (μm)	Bias (μm)
1	1550	8.338	8.374	-.036
2	1537	8.183	8.155	.028
			average bias =	-.004 μm

Table 2 - NBS/EIA 1988 Mode-Field Diameter Round Robin

Fiber	Wavelength (nm)	High NA VAMFF Mean (μm)	Far-Field Scan Mean (μm)	Bias (μm)
3	1550	7.06	7.07	-.01
4	1550	8.19	8.34	-.15
3	1300	5.77	5.83	-.06
4	1300	6.42	6.48	-.06
			average bias =	-.07 μm

ACCURACY OF MODE FIELD DIAMETER MEASUREMENTS IN SINGLE-MODE FIBRES FROM NEAR-FIELD TECHNIQUE

M. Artiglia, G. Coppa (°), P. Di Vita, M. Potenza
CSELT - Via G. Reiss Romoli, 274 - 10148 Torino (ITALY)

ABSTRACT

The accuracy of Transmitted Near-Field Intensity measurements for the determination of Mode Field Diameters in single mode optical fibres is discussed. The possible error causes are analyzed, with particular attention to systematic terms, and an evaluation of their effect is performed.

1. INTRODUCTION

One of the most important dimensional parameters for the design and the characterization of single-mode optical fibres is the Mode Field Diameter (MFD). Various techniques for the measurement of the MFDs have been proposed in the literature. Among these approaches, the one based on Transmitted Near-Field Intensity (TNFI) scanning is particularly attractive because it can be used also for geometrical measurements [1]. Aim of this paper is to carry out a comprehensive analysis, still lacking, on both the accuracy and the reproducibility of the technique to the end of providing valuable suggestions for its practical implementation. In particular, the delicate case of dispersion modified SM fibres is examined for its actual interest. It is well known that from a TNFI scan both Near-Field (NF) MFD and Far-Field (FF) MFD can be calculated from the relations [2]:

$$d_n = 2\sqrt{2}\left\{ \int_0^\infty r^2 E^2(r)\, r\, dr \Big/ \int_0^\infty E^2(r)\, r\, dr \right\}^{1/2} \qquad (1)$$

$$d_f = 2\sqrt{2}\left\{ \int_0^\infty E^2(r)\, r\, dr \Big/ \int_0^\infty (dE(r)/dr)^2\, r\, dr \right\}^{1/2} \qquad (2)$$

where r is the radial coordinate on the fiber endface and E(r) is the LP01 electric field. In order to evaluate the accuracy in the MFD determination, it must be pointed

---

(°) Present address:
POLITECNICO di TORINO - C.so Duca degli Abruzzi, 24 - Torino (ITALY)

out that such a measurement is performed in two steps. First, the TNFI pattern is acquired, successively the experimental data are numerically processed according to the defining equations. The TNFI acquisition is affected both by the measurement noise and by the diffraction effects on the image of the NF. Thus an analysis of the TNF optical system (supposed to operate in diffraction limited conditions and with a spatially coherent illumination) is needed in terms of the objective NA and of the dynamic range of the acquisition system, which are the quality parameters of the experimental set-up. Furthermore the numerical processing of experimental data can introduce additional errors that must be taken into account. All of these error causes will be discussed in the following.

2. ACCURACY OF THE NF MEASUREMENTS

The aim of a TNFI measurement is the determination of the width of a light intensity distribution, acting on a magnified image of it. The possible causes of errors are due to: accuracy in the positioning of the scanning motors, accuracy in the determination of the optical system magnifying power, use of a finite aperture to collect the TNF local intensity on the image plane (errors due to the finite aperture of the lens will be discussed in the following Section; errors introduced by unproper stripping of the fibre or by uncorrect lens focusing can be removed in principle and will not be discussed here). The accuracy of the traslation stages is within 1 μm on the image plane. Since the lateral magnifying power M is around 50X this corresponds to an error of $\pm$ 0.01 μm on the fibre end face. To determine the magnifying power M, a precision bar mask can be employed as optical object to calibrate the spatial scale on the image plane; taking again into account the accuracy of translation stages, the error on M can be evaluated around $\pm$ 0.1X, thus contributing a further $\pm$ 0.02 μm on the fibre face. It is interesting to note that the effect of the finite size of the (circular) collecting aperture can be exactly calculated as far as d_n is concerned. Calling D_n the measured NF MFD, one obtains:

$$d_n^2 = D_n^2 - 4\cdot\varepsilon^2 \qquad (3)$$

ε being the aperture radius on the fibre face. For example, if a 50 μm-core step-index fibre is employed to collect light on the image plane, this corresponds to a systematic error of + 0.05 μm (for a 9 μm-MFD). Such an exact calculation is not possible for the FF MFD d_f: then one should have to employ rather lengthy numerical procedures. A perturbative calculation at $O(\varepsilon^2)$ [viz. neglecting $O(\varepsilon^4)$ terms and

higher ones] for d_f shows that the exact d_f is equal to the measured one, a conclusion that can be accepted with a sufficient degree of confidence since a similar perturbative evaluation applied to d_n at the same order gives the same result of Eq.(3).

3. DIFFRACTION AND NUMERICAL PROCESSING EFFECTS

Diffraction effects due to the finite aperture of the TNF lens (assumed to have a NA = 0.65) have been taken into account calculating the image TNFI distribution by means of a diffraction integral over the system finite pupil. Noise effects have been simulated superposing to the image TNFI signal a random contribution according to the assumed dynamic range of the TNF set-up (40 dB). Then we have numerically calculated the NF and FF MFDs according to Eq.(1) and (2); suitable noise filtering techniques have been employed in performing numerical derivatives on "measured" quantities. To start the investigation, we have considered step index fibres, the simplest case. A first structure (representing a conventional fibre dispersion optimized @ 1300 nm) has a core diameter of 8 μm, a NA of 0.10 and theoretical MFDs d_n=13.45 and d_f=12.27 μm at 1550 nm. We found a systematic error of + 0.06 μm on d_n (due to the combined effects of diffraction and of the smoothing procedures employed) and of + 0.05 μm on d_f (similarly due to diffraction and numerical processing); the corresponding random contributions (due to noise) are $\pm$ 0.02 μm and less than 0.01 μm respectively. A second step structure with core radius of 4.4 μm and NA = 0.18, whose theoretical MFDs at the same wavelength as before are respectively d_n=7.51 and d_f=6.83 μm, has been considered as an example of a dispersion-shifted fibre. In this case the error on d_n is given by a systematic contribution of + 0.03 μm and a random term of $\pm$ 0.01 μm, while for d_f we have a + 0.09 μm systematic error and a random error lower than 0.01 μm. Finally, we considered a multi-cladding dispersion-flattened fibre (of total radius 7 μm and NA = 0.135) with d_n=8.54 and d_f=7.20 μm @ 1550 nm. Now d_n is affected by a systematic error of - 0.02 μm and by a sensible random contribution of $\pm$ 0.17 μm. Also in this case the MFD d_f is more stable, being affected by a systematic error of + 0.03 μm and a random term of $\pm$ 0.03 μm.

4. CONCLUSIONS

Taking into account the error causes discussed in Sections 2 and 3, the total MFD error for the considered structures is reported in Table I. Three kinds of systematic terms have been pointed out. A first one depends on the finite size of the detector. In practical cases this contribution is slightly less than 1%. A second systematic term is due to diffraction effects. Diffraction causes the presence of Fresnel rings

in the image NF, leading to an overestimation or an underestimation of the MFDs depending on the integration interval determined by the dynamic range and the lens NA of the set-up. Finally, processing techniques reduce noise fluctuations but can also reduce the information content about the intensity distribution. Operating at the best trade-off point between these contrasting effects, this leads, in general, to overestimate d_n and d_f of about 1%. In summary, after the elimination of the systematic errors, we can assess that the MFD determination accuracy from TNFI distribution measurements is within $\pm$ 0.05 μm for d_n and $\pm$ 0.03 μm for d_f in single-step structures. In more complicated refractive-index distributions (DF SMF) noise effects reduce the accuracy on d_n to $\sim \pm$ 0.20 μm, and on d_f to $\pm$ 0.06 μm, a less dramatic increase. In fact, the FF MFD d_f is less sensitive to these fluctuations because the smoothing procedures and noise filtering techniques are employed in Eq.(2) on both E(r) values and on E'(r) ones; for d_n, on the contrary, noise fluctuations, though smoothed out, are weighted by the factor r^2 (see Eq.(1)) and then are more effective. Surprisingly we have found that in TNFI measurements the accuracy on d_f is better than that on d_n. This fact confirms the validity of the CCITT reccommendation individuating in d_f the more convenient MFD definition to be used in SMF characterization.

REFERENCES

1 - G. Coppa, P. Di Vita, U. Rossi, El.Lett., Vol.19 (1983) pp.293-294.

2 - C. Pask, Electron. Lett., Vol. 20 (1984), pp. 144-145.

Table I - Total error on MFDs

profile	MFD	random	systematic
conv. step-i.	d_n	$\pm$ 0.05 μm	+ 0.09 μm
" "	d_f	$\pm$ 0.03 μm	+ 0.05 μm
DS step-i.	d_n	$\pm$ 0.04 μm	+ 0.08 μm
" "	d_f	$\pm$ 0.03 μm	+ 0.09 μm
DF multi-step	d_n	$\pm$ 0.20 μm	+ 0.03 μm
" "	d_f	$\pm$ 0.06 μm	+ 0.03 μm

INDEX OF AUTHORS

NBS-114A (REV. 2-8C)

U.S. DEPT. OF COMM. **BIBLIOGRAPHIC DATA SHEET** (See instructions)	1. PUBLICATION OR REPORT NO. NBS/SP-748	2. Performing Organ. Report No.	3. Publication Date September 1988

4. TITLE AND SUBTITLE

Technical Digest, Symposium on Optical Fiber Measurements, 1988

5. AUTHOR(S)

G. W. Day and D. L. Franzen, Editors

6. PERFORMING ORGANIZATION *(If joint or other than NBS, see instructions)*

NATIONAL BUREAU OF STANDARDS
DEPARTMENT OF COMMERCE
WASHINGTON, D.C. 20234

7. Contract/Grant No.

8. Type of Report & Period Covered

9. SPONSORING ORGANIZATION NAME AND COMPLETE ADDRESS *(Street, City, State, ZIP)*

Sponsored by the National Bureau of Standards, in cooperation with the IEEE Optical Communications Committee and the Optical Society of America.

10. SUPPLEMENTARY NOTES

Previous Symposia were held in 1980, 1982, 1984, and 1986. Technical Digests of those were published as NBS Special Publications 597, 641, 683, and 720.

☐ Document describes a computer program; SF-185, FIPS Software Summary, is attached.

11. ABSTRACT *(A 200-word or less factual summary of most significant information. If document includes a significant bibliography or literature survey, mention it here)*

This digest contains summaries of 42 papers presented at the Symposium on Optical Fiber Measurements, held September 20-21, 1988, at the National Bureau of Standards, Boulder, Colorado.

12. KEY WORDS *(Six to twelve entries; alphabetical order; capitalize only proper names; and separate key words by semicolons)*

fiber optics; instrumentation; measurements; optical fiber; reviews

13. AVAILABILITY

☒ Unlimited

☐ For Official Distribution. Do Not Release to NTIS

☒ Order From Superintendent of Documents, U.S. Government Printing Office, Washington, D.C. 20402.

☒ Order From National Technical Information Service (NTIS), Springfield, VA. 22161

14. NO. OF PRINTED PAGES

202

15. Price

USCOMM-DC 6043-P80

☆ U.S. GOVERNMENT PRINTING OFFICE:1988-576-212/85197

NBS Technical Publications

Periodical

Journal of Research—The Journal of Research of the National Bureau of Standards reports NBS research and development in those disciplines of the physical and engineering sciences in which the Bureau is active. These include physics, chemistry, engineering, mathematics, and computer sciences. Papers cover a broad range of subjects, with major emphasis on measurement methodology and the basic technology underlying standardization. Also included from time to time are survey articles on topics closely related to the Bureau's technical and scientific programs. Issued six times a year.

Nonperiodicals

Monographs—Major contributions to the technical literature on various subjects related to the Bureau's scientific and technical activities.

Handbooks—Recommended codes of engineering and industrial practice (including safety codes) developed in cooperation with interested industries, professional organizations, and regulatory bodies.

Special Publications—Include proceedings of conferences sponsored by NBS, NBS annual reports, and other special publications appropriate to this grouping such as wall charts, pocket cards, and bibliographies.

Applied Mathematics Series—Mathematical tables, manuals, and studies of special interest to physicists, engineers, chemists, biologists, mathematicians, computer programmers, and others engaged in scientific and technical work.

National Standard Reference Data Series—Provides quantitative data on the physical and chemical properties of materials, compiled from the world's literature and critically evaluated. Developed under a worldwide program coordinated by NBS under the authority of the National Standard Data Act (Public Law 90-396). NOTE: The Journal of Physical and Chemical Reference Data (JPCRD) is published quarterly for NBS by the American Chemical Society (ACS) and the American Institute of Physics (AIP). Subscriptions, reprints, and supplements are available from ACS, 1155 Sixteenth St., NW, Washington, DC 20056.

Building Science Series—Disseminates technical information developed at the Bureau on building materials, components, systems, and whole structures. The series presents research results, test methods, and performance criteria related to the structural and environmental functions and the durability and safety characteristics of building elements and systems.

Technical Notes—Studies or reports which are complete in themselves but restrictive in their treatment of a subject. Analogous to monographs but not so comprehensive in scope or definitive in treatment of the subject area. Often serve as a vehicle for final reports of work performed at NBS under the sponsorship of other government agencies.

Voluntary Product Standards—Developed under procedures published by the Department of Commerce in Part 10, Title 15, of the Code of Federal Regulations. The standards establish nationally recognized requirements for products, and provide all concerned interests with a basis for common understanding of the characteristics of the products. NBS administers this program as a supplement to the activities of the private sector standardizing organizations.

Consumer Information Series—Practical information, based on NBS research and experience, covering areas of interest to the consumer. Easily understandable language and illustrations provide useful background knowledge for shopping in today's technological marketplace.

Order the **above** *NBS publications from: Superintendent of Documents, Government Printing Office, Washington, DC 20402.*

Order the **following** *NBS publications—FIPS and NBSIR's—from the National Technical Information Service, Springfield, VA 22161.*

Federal Information Processing Standards Publications (FIPS PUB)—Publications in this series collectively constitute the Federal Information Processing Standards Register. The Register serves as the official source of information in the Federal Government regarding standards issued by NBS pursuant to the Federal Property and Administrative Services Act of 1949 as amended, Public Law 89-306 (79 Stat. 1127), and as implemented by Executive Order 11717 (38 FR 12315, dated May 11, 1973) and Part 6 of Title 15 CFR (Code of Federal Regulations).

NBS Interagency Reports (NBSIR)—A special series of interim or final reports on work performed by NBS for outside sponsors (both government and non-government). In general, initial distribution is handled by the sponsor; public distribution is by the National Technical Information Service, Springfield, VA 22161, in paper copy or microfiche form.

U.S. Department of Commerce
National Bureau of Standards
Gaithersburg, MD 20899